# Design and development of a turn-by-turn spectrometer in order to investigate micro-bunching instabilities at the Diamond Light Source Ltd.

Aiveen Finn

Department of Physics
Royal Holloway, University of London


A thesis submitted to the University of London for the degree of Doctor of Philosophy

October 2017

# Declaration

I, Aiveen Finn, hereby declare that this thesis and the work presented in it is entirely my own. Where I have consulted the work of others, this is always clearly stated.

Signed:

Date:

For my Dad,

Andrew J. Finn

To the Four Peaks

and

the Library Stairs

# Abstract

Micro-bunching instabilities (MBI) occur when an electron bunch exceeds a threshold current, resulting in bursts of coherent synchrotron radiation (CSR) which is more intense than its incoherent counterpart. This CSR is emitted within the millimetre wavelength range and thus acts as a source of terahertz radiation. Diamond Light Source is one of many third generation light sources that has observed MBI. The dynamics of MBI are not fully understood and therefore, in this thesis, a detection system has been designed and developed to investigate these instabilities, their dynamics and the spectral characteristics of the CSR bursts. Schottky barrier diodes (SBDs) function at these CSR wavelengths and benefit from fast speeds, low noise, excellent sensitivity and room-temperature operation. The spectrometer is composed of eight individually characterised SBDs, collectively covering a range of 33-1000 GHz and creating a spectrometer able to observe the individual bursts of CSR. The spectrometer was installed and commissioned at the Diamond Light Source storage ring, in order to be used to investigate the onset of CSR bursts. In particular, the effect of increasing bunch currents, increasing radio frequency voltage and different machine lattices and fill patterns on bursts of CSR was studied. From these investigations, the machine parameters at Diamond Light Source which result in bursts of CSR from MBI have been determined as well as their bursting nature.

# Acknowledgements

A huge thank you to Pavel Karataev (RHUL) and Guenther Rehm (DLS) for being my supervisors, guiding me through, pulling me out of rabbit holes and helping me achieve it all. It has been such a wonderful opportunity to be able to work with you both.

For all their advice, ideas, and kind ears, I would like to thank everyone at Diamond, in particular those within the Diagnostics Group (Michael Abbott, Chris Bloomer, Lorraine Bobb, Graham Cook, Sandira Gayadeen and Alun Morgan), Diamond Operations, Mechanical Engineering, the CSR/MBI Enthusiasts Group, Ed Rial, Isa Uzun and Ian Martin, in particular for his willingness to implement low-alpha conditions.

Thank you very much to everyone in the Physics Department at Royal Holloway who forever made me feel welcome and were always willing to help. I would like to thank Royal Holloway, University of London and Diamond Light Source for providing me with the funding and facilities necessary to carry out my research.

Individual thanks are due to William Shields, Ciprian Plostinar, Suzie Sheehy, Stewart Boogert, Stephen Gibson, Matthias Scholz, Johann Zemella, Peter Milne, Peter Huggard, Laura Corner and dare I be cheesy enough to say everyone I have met at conferences, schools, symposiums and workshops for their eagerness, interest, warmth and drive.

Finally, my biggest thanks go to Dad, Mum, Roy and Liam for their unwavering support and everything in between. I wouldn't be where I am today without you. I am eternally grateful.

*Tá an ghrian ag taitneamh go hard sa speir.*

# Contents

# List of Figures

# List of Tables

Chapter 1

# Introduction

## 1.1 Accelerators & Light Sources

Ernest Rutherford is often the person who is credited with igniting the investigations into the feasibility and creation of a particle accelerator. It was at the Royal Society in 1928 during his presidential speech when he said "I have long hoped for a source of positive particles more energetic than those emitted from natural radioactive substances". In due time particle accelerators were created.

These particle accelerators were built for high energy and nuclear physics research. However when the accelerators caused the particles to circulate, the particles were losing energy. This phenomenon was measured at General Electric (GE) by Blewett in 1946 [1]. The following year in 1947 at GE (70 MeV), synchrotron radiation (SR) was first observed [2]. To the researchers synchrotron radiation was a nuisance, an undesired by-product. Though only measured and seen in the mid-1940s, the theory had been developed at the end of the nineteenth century by Larmor and Lièнard. In 1897 Larmor derived the expression to determine the total instantaneous power emitted when a non-relativistic charged particle is accelerated [3]. A year later, Lièнard determined the relation for a relativistic charged particle travelling along a circular path. Thanks to these physicists, it is now known that when a relativistic charged particle is accelerated transversely, the power emitted instantaneously is

$$P_e = \frac{2}{3}\,\frac{e_0^2 c}{4\pi\varepsilon_0\rho^2}\,\gamma^4, \tag{1.1}$$

where $c$ is the speed of light in a vacuum, $e_0$ the charge of an electron, $\varepsilon_0$ is the vacuum permittivity, $\rho$ the bending radius and $\gamma$ the Lorentz factor. And so, this relation creates the backbone of synchrotron light sources.

It was realised that this SR could be beneficial to other types of experiments and in the late 1950's the first user experiments were underway at the Cornell 320 MeV synchrotron. These first user experiments were carried out parasitically using machines built for high energy physics, which became known as first generation light sources.

The second generation light sources are the original dedicated light sources. They are composed of dipole bending magnets as their source of SR and are able to host many beamlines from these dipole magnets. The creation of these second generation light sources caused a large increase in the use of SR for research and thus a surge in SR demand. One of the earliest second generation light sources began operation in the mid-1970s in Tokyo, called the SOR ring with an energy of 380 MeV [4].

As a result of the increasing demand for SR and the successful work with insertion devices, third generation light sources were constructed. These light sources are optimised for high brilliance but with a low emittance. They also used bending magnets to generate the SR but had started employing insertion devices too. Insertion devices are periodic arrays of magnets, permanent or electromagnets and come in several varieties including undulators and wigglers. As the electron beam travels through the array of magnets it oscillates transversely resulting in the emission of enhanced SR. It was as a result of the insertion devices that the higher brilliance could be achieved. These light sources, though still circular, had larger straight sections to allow for the insertion devices to be installed [4].

Traditionally one of the most important factors in building a synchrotron light source was the energy. Higher energy machines result in a higher flux and thus user experimental duration times decrease and more experiments can be conducted. In trying to build higher and higher energy electron storage rings, the limiting factor becomes the relationship between the energy loss and the energy desired. Nowadays with the world populated with light sources of different energies, the goal of high energy machines is no longer relevant, nevertheless the term 'higher' is a relative one. The type of research to be carried out depends on the level of energy required. Currently, medium energy machines,

like Diamond Light Source at 3 GeV, are the most common. No matter the energy, the radio frequency (RF) system is there to provide enough voltage for the charged particle beams to be accelerated (in the linear accelerator and booster ring) but also to replace the losses in the beam's energy (in the storage ring). In order to reduce the strain put on the RF system especially at increased energies the bending magnet field strength can be reduced, however this results in a machine with a larger footprint which ultimately increases the cost. Of course, depending on the advancements at the time, the bending radius may be limited by the strength of the currently available magnets. The relationship between the energy, $E$, of the synchrotron and the bending radius, $\rho$ is

$$E = e_0 c B \rho, \tag{1.2}$$

where

$$B\rho = \frac{p}{e_0}, \tag{1.3}$$

$B\rho$ is the magnetic rigidity and $p$ the relativistic momentum.

## 1.2 Diamond Synchrotron Light Source

Diamond Light Source (Diamond) is a third generation light source located in Oxfordshire, UK operating at 3 GeV. Diamond began user operation in early 2007 [5] as the United Kingdom's national synchrotron. Like many third generation synchrotron facilities, Diamond follows the common layout as shown in Figure 1.1. The four main sections involved in the acceleration are the electron gun, linear accelerator (linac), booster ring and storage ring. It is from the storage ring that the beamlines emerge.

At the electron gun the process begins, with electrons being emitted via thermionic emission into the linac where they are accelerated up to 100 MeV. The linac injects the 100 MeV electrons into the full-energy booster of circumference 158.4 m. It is within the booster that the electrons are ramped up to 3 GeV. The booster follows a racetrack design. In the straight sections are the RF cavities which 'boost' the energy of the electron beam during each revolution until the desired 3 GeV is reached. Thirty-six dipole magnets are used in the curved sections to bend the electron beam around the corners [6].

These magnets are electromagnetic and thus there is the capacity to adjust the magnetic field strength. This is extremely necessary when increasing the energy of the electrons because the electron beam is required to remain within the beampipe along the same path as before. By changing (increasing) the magnetic field with time as the energy of the electron beam increases, the booster can have a fixed path i.e. a constant orbit radius. Once at the applicable energy of 3 GeV, the electron bunches are injected into the storage ring where they circulate the 561.6 m long ring.

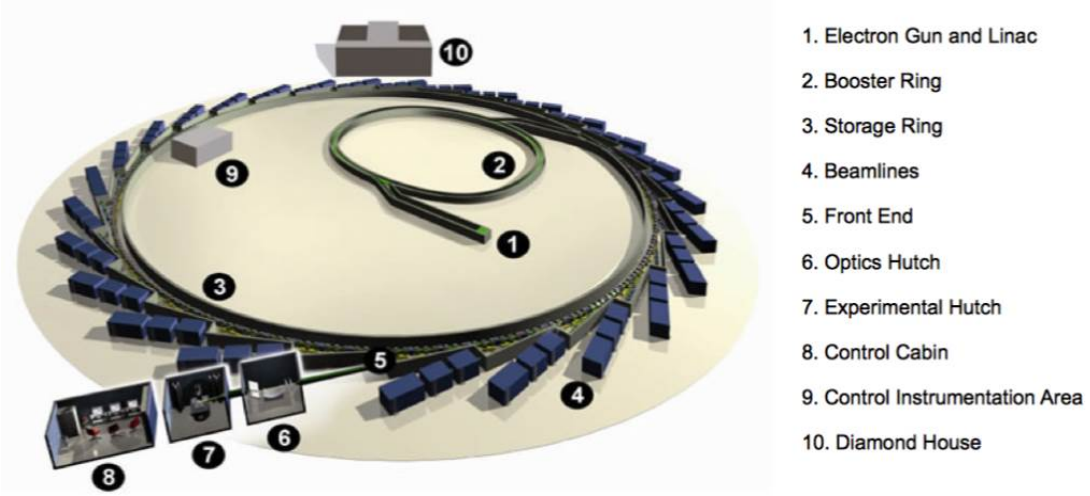


Figure 1.1: The layout of a typical third generation light source [6].

The storage ring is the largest component of a synchrotron light source. As the name suggests, the storage ring stores the electrons as well as accumulates the injected electrons from the booster ring. These electrons are travelling at relativistic speeds and follow the circular path of the ring. Throughout their journey the electrons lose energy in the form of photons, namely SR. The radiation emitted from the circulating electrons extends from millimetre wavelengths through visible to x-rays and is channeled into the beamlines at Diamond.

The RF system is paramount in the operation of a synchrotron light source. RF cavities give energy to the beam. Before the storage ring the RF system provides the beam with the means to meet the desired energy, 3 GeV in the case of Diamond. Once at the requested energy, the RF cavities within the storage ring put back energy that has been lost by the electrons due to SR. The RF cavities input this energy into the beam

by establishing an electric field across the accelerating gap. An alternating field is used, because the electrons must always see the field going in the same (forward) direction. As a result of this alternating field, the electrons become bunched. The bunching occurs because of what the electrons experience, i.e. which part of the alternating field. In the gun where the electrons are non-relativistic, the electrons with lower energies are slower and will therefore arrive later in the RF cavities. Correspondingly, they will experience more of the forward gradient and thus will receive a larger portion of energy. The higher energy electrons are faster and arrive earlier than the lower energy electrons. As a result, the difference in energy has been accounted for. Simply put, if electrons observe the forward

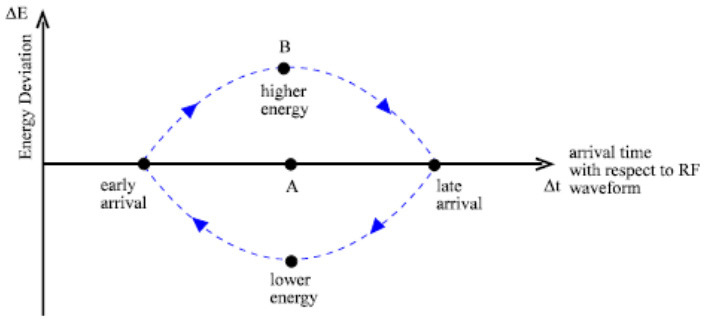


Figure 1.2: The arrival of particles with respect to the RF waveform, where A is the synchronous particle and B represents all other particles (Courtesy of [7]).

gradient they will be accelerated, while if they experience the decreasing gradient they will fall behind, thus forming bunches. The electrons after the gun are truly relativistic and thus will behave differently, specifically the higher energy electrons will have longer path lengths and will thus arrive after the lower energy electrons which are 'faster'. Moreover instead of bunching occurring in the remainder of the machine (linac, booster and storage ring) the bunch tails are cleared. Demonstrated in Figure 1.2, the synchronous particle (A) is one that is synchronous with the RF voltage and will thus not require any additional energy. It is the other particles (B) that will be affected by the RF voltage, because they are not completely in-sync with the RF waveform. As can be seen in the figure, the lower energy particles arrive earlier than the higher energy particles due to their differing path lengths travelled. At Diamond, a bunch is home to approximately $4 \times 10^9$ electrons. By the energy being kept constant (in the storage ring) a fixed orbit is maintained around

the storage ring. The RF cavities at Diamond are super conducting cavities with an RF frequency, $f_{rf}$, of 499.655520 MHz giving a bunch spacing of approximately 2 ns. Using Equation 1.4, the revolution frequency, $f_{rev}$ of Diamond is determined to be 533.820 kHz where $\beta c$ is the velocity and $\rho$ the bending radius of the storage ring. The harmonic number, $h$, of Diamond is 936 (Eq. 1.5) [8].

$$f_{rev} = \frac{\beta c}{2\pi\rho} \tag{1.4}$$

$$f_{rf} = h \cdot f_{rev} \tag{1.5}$$

This means that there are 936 places on the circumference where an electron could be put and would arrive synchronously [8]. These 936 locations are known as buckets which each can house a bunch of electrons. To prevent electrons undergoing unknown and unwanted collisions within the beampipe, the entire of Diamond from gun to beamline is kept under vacuum conditions of the order $2 \times 10^{-8}$ Pa.

Dipole magnets, quadrupole magnets and sextupole magnets, colour-coded green, red and yellow respectively are electromagnets which make-up a significant portion of the lattice implemented at Diamond as shown in Figure 1.3. The electromagnets operate at room temperature and are water-cooled. Dipole or bending magnets are used to control the beam orbit. They guide the beam of electrons along the desired orbit, traveling the arc of a circle. Since its commissioning forty-eight dipole magnets are used at Diamond [9] in order to combine all forty-eight straight sections that make up the Diamond storage ring. In late 2016, the Diamond storage ring lattice will be altered thus giving fifty dipole magnets connecting forty-nine straight sections [10, 11]. As well as guiding the electrons, dipole magnets also have another significant role, they are sources of SR. Quadrupole magnets are the primary focussing elements. These magnets contain four poles creating a field with a constant gradient in both the horizontal and vertical planes [4]. However, quadrupole magnets only focus in one plane at a time (while defocusing the opposite plane) [12], thus quadrupole magnets come in pairs where the first will focus in one plane and the second in the other plane. Sextupole magnets are composed of six poles and are used to control the chromaticities and x-y coupling within the ring. The chromaticity is defined as the tune spread due to the momentum [8] where the tune is the number of


Figure 1.3: Inside Diamond Storage Ring tunnel showing quadrupole (red) magnets, sextupole (yellow) magnets, dipole bending (green) magnet, the vacuum ion pumps and the ratchet wall.

oscillations around the closed orbit (synchrotron oscillations) for one complete revolution around the ring. Similar to quadrupoles, sextupoles are also used for focussing. The six poles generate a field which varies in amplitude as the square of the distance from the magnet's centre [4]. This variation in gradient allows for a variation in focussing with electron momentum (chromaticity). The arrangement of the magnets within a synchrotron is called the lattice and it is the lattice that determines the main features of the light source, including the emittance and transverse dimensions of the beam, as well as the amount and positions of the straight section for insertion devices.

In previous generations of synchrotron light sources, dipoles were the sole source of synchrotron radiation. However this is no longer the case, with the introduction of insertion devices. Insertion devices are composed of arrays of alternating polarity magnets. Most commonly a top jaw and bottom jaw house magnetic arrays which cause deflections of the electron beam as it travels between the jaws. It is the inclusion of said devices that resulted in third and future generations of lights sources being born. The two types of insertion devices used at Diamond are wigglers and undulators. The former generate

broadband emission in a fan-shaped photon beam, by 'wiggling' the electrons with deflections that are large compared to the natural emission angle of synchrotron radiation [4]. The radiation produced by a wiggler is similar to that of a bending magnet however the light is $2N_p$ times more intense [4], where $N_p$ is the number of periods. Undulators cause small electron deflections. These smaller deflections are comparable in magnitude to the natural emission angle of synchrotron radiation [4]. A narrow cone of light is produced from an undulator because the small deflections allow the radiation generated in individual undulator elements to interfere coherently and produce spectrum of discrete lines or harmonics.

Currently twenty-nine beamlines at Diamond are operational. Several beamlines obtain their SR from dipole magnets, however the main source of synchrotron light for the Diamond beamlines is an insertion device. Nevertheless, with regards beamlines the dipole magnets are always needed to separate the radiation from the electron beam by guiding the electron beam in an arc while the photon beam (SR) continues straight along a beamport and into a beamline hutch.

The front-end is the connection either side of the ratchet wall and is defined as where the beamline emerges from the storage ring to the point it enters the optics hutch after the ratchet wall of the storage ring. Most commonly beamlines are divided into three sections: optics hutch, experimental hutch, and control cabin. The optics hutch is the first room the photon beam enters after emerging from the storage ring tunnel. It is within this hutch where the radiation is prepared by focussing and filtering as required for the particular speciality of the beamline. This hutch contains a variety of mirrors and most importantly diffraction gratings or a crystal monochromator which selects the wavelength of light to be used in the upcoming experiments.

The experimental hutch houses the experimental apparatus, including detectors. It is here that the sample to be tested is placed. The prepared beam is directed onto the sample whereby the outcome of this reaction is captured via detectors centered around the sample. The detectors send the collected data to the control cabin. Within this final room, the control cabin, the data are analysed. The control cabin is usually the only room of the three where it is safe for a human to be while collecting data as the optics and experimental hutch contain the x-ray radiation. The optics and experimental hutches are

insulated to contain the radiation usually by lead walls, doors and ceilings.

The control system implemented at Diamond is EPICS, an Open Source package developed at many institutions worldwide [13]. It provides the user with real-time control for large scientific applications including particle accelerators. EPICS is used in both the control of the machine with its electron beam and all the components of the beamlines with their SR.

## 1.3 An Introduction to Micro-Bunching Instabilities

Electrons circulate the storage ring in bunches. However, when the charge of a single bunch exceeds a threshold current, it causes the bunch to filament [14]. These filaments or micro-bunches go on to emit coherent synchrotron radiation (CSR). What is special about this type of radiation is usually CSR occurs for wavelengths longer than the bunch length but in the case of micro-bunching instabilities (MBI), the wavelength of CSR can occur at wavelengths shorter than the bunch length. More specifically the wavelength of CSR is limited by the longitudinal bunch size but its wavelength must be longer than the bunch filament emitting the CSR. It must be reiterated that MBI only occurs when the criterion is met and thus a single bunch can filament, recombine to form one whole bunch again, filament, recombine again and again. MBI, the theory behind it and its applications are further discussed in Section 2.5.

## 1.4 Contribution to Current Research

The approach undertaken throughout this thesis is the design and creation of a detection system in order to investigate MBI in a turn-by-turn regime and thus to measure the spectral characteristics of the CSR produced at Diamond, which is one of the many light sources around the world that have observed MBI [15]. Other light sources include BESSY-II [16–18], SURF-II [19], NSLS-VUV [20–22], Advanced Light Source [23], UVSOR-II [24], MAX-I [25] and Canadian Light Source [26]. As a result of these international observations, MBI are being investigated on a worldwide scale with each research group employing varying techniques. In order to achieve our goal, a turn-by-turn

spectrometer has been developed. This spectrometer is a collection of detectors: seven of which are narrow-band and the eighth is a broadband detector. These detectors make up a detector array, or 'spectrometer', and have been individually characterised in order to thoroughly analyse the data they receive.

Schottky barrier diodes (SBDs) are the chosen detector type. The benefits that SBDs provide are immense and, from our point of view, dwarf the competitors, with average values of 250 ps speeds [15] and noise equivalent powers (NEPs) in the range of 1-45 pW$Hz^{-1/2}$ [27, 28], all operating at room temperature (or even cryogenic temperatures). These SBDs can detect from millimetre to sub-millimetre wavelengths and are hence often used as detectors in this wavelength range. The first known use of SBDs to observe bursting CSR was by Kramer at the VUV Ring [29]. SBDs benefit from excellent sensitivity ($10^3$ V/W) matched, for example, by the hot electron bolometer [15] and operate at high speeds [30] due to their semiconductor-metal interface. They can be terminated in a high (1 kΩ +) or low impedance (50 Ω) set-up to bring out either improved sensitivity with reduced speed or limited sensitivity with quicker speeds, respectively. SBDs perform at room temperature and thus they take up less space and are more economic, as a dewar is not required for cooling compared to the hot electron bolometer, for example. SBDs can also be frequency restricted by way of waveguides or filters, therefore it can be determined at which frequencies the CSR signals are being observed. Other room temperature millimetre detectors include pyroelectric detectors and golay cells. They benefit from large sensitivity regions ranging from millimetres to ultra-violet but can also be wavelength restricted by use of a filter or the windowing material. However, these detectors are inherently slow and easily affected by sound and mechanical vibrations. Moreover, they require a modulated signal as their detection systems lock-in to the changes observed. Naturally, the signal can be mechanically chopped prior to the detector, however the CSR emission especially the CSR bursts are not smooth nor continuous and thus to be mechanically chopped would alter the true signal emitted.

By employing a number of SBDs, a larger frequency range is probed and a clearer picture of what is happening during these CSR bursts can be realised. The Canadian Light Source has reported the use of three SBDs spanning 33-110 GHz [31], however the most amount of SBDs employed and first known recording of a detector array was

in 2015 by the author and colleagues [32]. (Currently a four YBCO detector system is under development at KIT [33]). In this work, the detectors used were individually characterised on the test bench with their respective horn antennas (if applicable) in the forward direction, as described in Section 3.4. Furthermore, this characterisation was carried out in free space that is to say an Erickson Waveguide power meter [34] was not employed but a Thomas Keating (TK) power meter [35]. By using a TK power meter a more realistic calibration was ascertained as the SBDs were not connected to a waveguide when in use but in free space in front of the beam viewport.

SBDs observe power and transmit their signal as a voltage. In the set-up utililsed here each of the eight SBDs are terminated into individual high impedance (10 k$\Omega$) voltage amplifiers to boost the signals by a factor of 100 before traversing the 30 m of cables to the data acquisition unit. A high input impedance is required to force the SBDs to operate with their famous sensitivity, but at the cost of a slower speed. The data acquisition system is composed of a simultaneous multi-channel digitiser which constantly outputs the data into a server. The server then carries out Fourier transforms on the incoming data. The framework acts somewhat like a soft lock-in amplifier, where the region of interest and bandwidth are specified. By using this acquisition method the expense of eight lock-in amplifiers, one for each detector, is not incurred. The technique of 'locking-in' allows for accurate measurements to be made of very small signals even if there is noise present many times larger than the desired signal. Lock-in amplifiers disregard any signal not at the reference and thus noise signals are eliminated. KIT, Germany have designed KAPTURE (KArlsruhe Pulse Taking Ultra-fast Readout Electronics), their own data acquisition system for ultra-short CSR emission via thin film and diode detectors [36]. It is a four channel, high accuracy acquisition system with the capability to observe each bunch in turn-by-turn mode [36]. KAPTURE is limited to one second's worth of data but to alleviate some of the issue caused by this, the storage ring is filled with many bunches of differing currents and in a modified filling patterns. Moreover, the data acquisition system portrayed within this thesis, is able to stream data continuously. However for the streamed data to be stored the only limit is the available storage. The speed of the detectors at 10 k$\Omega$ input impedance combined with the data acquisition system allows for turn-by-turn data capture. Bunch-by-bunch acquisition has been investigated but deemed

superfluous.

One of the popular methods for observing the CSR bursts as a result of MBI is to employ an interferometer. Interferometers use the principle of superposition in order to determine more about the source. The beam is split in two with one branch travelling a fixed path while the other's displacement is varied by way of a moving mirror. When the light branches interfere, their relationship can be constructive, destructive or a combination and it is from these interference relations that information about the source can be gleaned. The longitudinal bunch distribution can be determined using an interferometric set-up [37]. Interferometers have the advantage of higher resolution data compared to just using a fast detector like an SBD in a spectrometer set-up. However, interferometers have the disadvantage that they require more time (moving mirror) and thus result in smearing out of the CSR bursts during one interferometric reading. This means only a spectrum of the average of MBI emissions is ascertained. In summary SBDs provide fast results with lower spectral resolution while interferometers present higher resolution data but need longer time to obtain.

Most commonly a Michelson interferometer is employed with a bolometer [17, 20, 22, 23, 25, 31, 38–41]. However, interferometers with a variety of other detectors have also been used including a pyroelectric detector [42] and a quasi-optical SBD [42, 43]. Moreover, Martin-Puplett interferometers are also popular, almost identical to a Michelson but with a wire-grid polariser as its beam splitter. Though interferometers are favoured throughout the years, there has been interest in other techniques to learn more about the CSR from short wavelengths, including streak cameras [17, 39, 44, 45], electro-optical spectral decoding (EOSD) [46–51] and direct measurements using a variety of different detectors [23, 31].

In brief, the method of a multi-channel SBD array depicted within the pages of this thesis was chosen because of SBDs observation range, distinguished sensitivities, fast responses - ability to observe bursts as they happen, room temperature operation - reduction in cost and space, apparatus does not affect stability of beam and finally the more channels the wider frequency bandwidth for investigation.

## 1.5 Research Objectives

The aim of this research is to develop a fast spectrometer in order to investigate the spectral characteristics of MBI. Globally, MBI have been detected and many institutes are investigating their causes, dynamics, benefits and repercussions. The reason for this is MBI produce bursts of CSR, i.e. a source of THz radiation. Despite a huge amount of research having gone into the electromagnetic spectrum, there still exists the 'Terahertz Gap'. Though this gap is being filled in and will soon be a remnant from the past, it has resulted in a reduced knowledge about these frequencies, ill-defined boundaries and minimal sources. With the introduction of compressed electron bunches at synchrotron light sources, THz radiation can be created on demand providing another source of these wavelengths and a very intense one at that. By compressing the bunches the ratio of electrons to bunch size increases, leading to the bunches suffering from MBI and thus resulting in the bursts of CSR in the THz regime. Hence, a source of THz radiation has been born. It must be noted that without altering the length or charge of bunches, CSR is naturally produced at a synchrotron facility but shielded by the vacuum pipes. Additionally, by just reducing the bunch length to below the shielding of the beampipe (i.e. above the cut-off frequency), the shortened bunch lengths are also able to coherently emit and will not be damped by the vacuum pipe. It is by reducing the bunch lengths that allow for coherent THz radiation to be emitted.

Unfortunately, the coherent THz bursts above the threshold are intense and occur on fluctuating timescales with unstable intensities, hence the term instability. MBI have the ability to affect the performance of the synchrotron light source and can harm user experiments. Subsequently light sources usually endeavour to avoid the conditions that cause MBI. Nevertheless it must be mentioned that several light sources do provide specific user runs for the production of THz radiation including BESSY [52, 53], ANKA [39, 54], Metrology Light Source [55, 56], SPEAR3 [57] and Diamond [58]. These conditions, often referred to as 'low-alpha mode' are highly researched and strictly monitored for dedicated experiments and beamlines, with parasitic use by others.

Diamond undergoes two types of low-alpha runs in order to provide one specific beamline with shorter radiation pulses for time of flight and pump-probe experiments

giving a by-product of CSR THz radiation and another type of low-alpha mode to benefit a different beamline with intense THz radiation. Both these low-alpha user runs operate at a much reduced current, between either a factor of 15 or 30 lower than the current during a normal optics user run. The low intensity of the beam does not allow for many x-ray experiments to be carried out. If Diamond was able to increase the current of these low-alpha runs or operate this mode constantly without affecting the overall stability and the performance of the ring, all beamlines could make use of the beam in their individual ways simultaneously.

Occasionally other diagnostic equipment at Diamond has been altered in order to observe these bursts of CSR, namely the streak camera and BPMs (beam position monitors) [45]. However these pieces of apparatus are stretched to their limit to observe the longitudinal dynamic feature that is CSR bursting. A streak camera is designed to carry out time domain measurements and can be used to determine the length of an electron bunch. Most commonly it uses the visible part of the emitted synchrotron radiation. BPMs are primarily employed to determine the position of the electron beam within the vacuum beampipe for feedback and orbit correction systems. BPMs can also measure the beam current. In the paper presented by Martin [45], it is only the SBD array that is expressly designed to observe bursting CSR. Thus not only is the SBD array beneficial on its own but also complements the streak camera and other synchrotron diagnostics.

If more was known about MBI, it would be easier to harness their benefits thus resulting in a reliable source of THz radiation and brighter light for all. MBI have been and continue to be modelled by various institutes worldwide, however the accuracy of these simulations is always in question. With real experimental data gathered via the aforementioned SBD array as well other methods, these simulations can be compared against and their accuracy determined. Examples of theoretical work and modelling can be found in many of Stupakov's publications [59–61], Roussel [62], Klein [63], and simulations carried out in conjunction with measurements obtained at Diamond [64, 65] and ANKA [66].

In the synchrotron user community, lower emittance is always preferred. Thus with the continual movement for low emittance rings, MBI are becoming a limiting threshold. This is because in order to reach lower emittances, the beam size must be reduced and instabilities are amplified with a decrease in bunch length. After all, the emittance is

related to bunch size.

The novelty of this work is in the individual characterisations of each detector as well as the use of them in a combined eight channel array. The signal observed via this array is able to be continually monitored and the Fourier transformed data extracted continually. As a spectrometer, the data are obtained faster with lower resolution thus in contrast to the more popular interferometric method of slow capture but much improved resolution. As a result of the SBD the data captured can be used to understand more about the dynamics of this instability and hopefully will provide explanations and accurate models in due course.

Succinctly, this thesis portrays the theoretical background of this work gleaned from a variety of sources; both the method and results of the characterisations for each detector; the creation of the SBD array and its data acquisition system; the use of the spectrometer at Diamond and finally the information determined as a result of the analysis of the spectral data.

Chapter 2

# Theoretical Background

## 2.1 Synchrotron Radiation Properties

The electromagnetic radiation emitted when a charged particle is accelerated due to a magnetic field is called SR. As the particle moves in a curved path (thereby accelerated), the SR is emitted in a narrow cone centered around the direction of the particle's travel [4]. Most commonly it is the electron that is accelerated at synchrotron light sources. This SR is extremely intense and covers a large range of the electromagnetic spectrum from millimetre wavelengths, through visible and ultraviolet to both soft and hard x-rays. At synchrotron light sources, like Diamond, this SR is guided through tangential photon beamlines where it is used for a diverse mixture of scientific research including microscopy, x-ray diffraction, spectroscopy and timed pulse-probe experiments. SR can be used in a non-destructive way which is very important when using Diamond and other light sources to investigate ancient artefacts and masterpieces.

The total instantaneous power of radiation emitted from an electron moving at non-relativistic speeds can be derived from the Larmor formula [3, 67, 68]:

$$P_e = \frac{2}{3}\,\frac{e_0^2}{4\pi\varepsilon_0 m_0^2 c^3}\left(\frac{d\mathbf{p}}{dt}\right)^2, \tag{2.1}$$

where $\mathbf{p} = m_0\mathbf{v}$ is the electrons's momentum, $m_0$ is the rest mass of the electron, $\mathbf{v}$ the velocity of the electron, $c$ the speed of light in a vacuum, $e_0$ the charge of an electron, $t$ the (coordinate) time and $\varepsilon_0$ is the vacuum permittivity. From Equation 2.1 it is clear that

electromagnetic energy is only emitted when the electron's momentum changes as a result of an applied force [68]. This means that $\frac{d\mathbf{p}}{dt} \neq 0$. Furthermore, for the case of relativistic particles a Lorentz transformation is required where $dt = \gamma d\tau$ with $\tau$ representing proper time, thus giving [68]:

$$P_e = \frac{2}{3} \frac{e_0^2}{4\pi\varepsilon_0 m_0^2 c^3} \left[ \left( \frac{d\mathbf{p}}{d\tau} \right)^2 - \frac{1}{c^2} \left( \frac{dE}{d\tau} \right)^2 \right] \tag{2.2}$$

In a storage ring the electrons are being circularly accelerated and thus we only observe the perpendicular case. This means that the energy remains constant because though energy is being lost by the emission of SR, the RF cavities put back what has been lost and thus the second term of Equation 2.2 can be ignored to give:

$$P_e = \frac{2}{3} \frac{e_0^2}{4\pi\varepsilon_0 m_0^2 c^3} \left( \frac{dp}{d\tau} \right)^2 \tag{2.3}$$

$$P_e = \frac{2}{3} \frac{e_0^2 \gamma^2}{4\pi\varepsilon_0 m_0^2 c^3} \left( \frac{dp}{dt} \right)^2 \tag{2.4}$$

where $\gamma$ is the Lorentz factor,

$$\gamma = \frac{E}{E_0} = \frac{E}{m_0 c^2} \tag{2.5}$$

The change in momentum causes the SR, thus the last term of Equation 2.4 is the change in momentum that an electron experiences due to the dipole magnets as it travels through the entire storage ring. Accordingly, where $\rho$ is the bending radius,

$$\frac{dp}{dt} = \frac{\gamma m_0 c^2}{\rho} \tag{2.6}$$

Moreover, by combining Equations 2.6 with 2.4, the result brings us back to the familiar equation stating that power is instantaneously emitted when a relativistic charge particle is transversely accelerated, Equation 1.1, displayed again here:

$$P_e = \frac{2}{3} \frac{e_0^2 c}{4\pi\varepsilon_0 \rho^2} \gamma^4 \tag{2.7}$$

SR has two categories; incoherent and coherent radiation. Synchrotron light sources

generate both incoherent and coherent radiation. The difference between the two types of radiation is whether the waves of radiation are in phase with each other or not. Coherent radiation occurs when in phase at the same frequency and can thus cause interference. It will be further discussed in Section 2.2. However coherent synchrotron radiation (CSR) is usually shielded by the vacuum beampipe, that is to say it is suppressed by the chamber and thus cannot propagate nor escape [14, 23, 69]. In order for CSR to be emitted from one of the tangential beamlines, it must be at frequencies above the cut-off of the vacuum pipe, derived from an infinite parallel plates model with a separation of $h$ [14, 69]. The cut-off varies for each machine dependent on the Equation 2.8, where the cut-off frequency is $f_{cutoff}$, $h = 38$ mm the height of the vacuum chamber, $c$ the speed of light and $\rho = 7.13$ m the bending radius. The cut-off frequency of Diamond is estimated to be 54 GHz [15, 70].

$$f_{cutoff} = \frac{c}{2h}\sqrt{\frac{\rho}{h}} \tag{2.8}$$

Parameters of synchrotrons can be altered in order to allow CSR to have a shorter wavelength than the cut-off and thus not be hindered by the vacuum shielding. At Diamond and other light sources, this means the wavelength of CSR is in the millimetre range, thus producing coherent radiation in the GHz-THz range [15].

## 2.2 Coherent Synchrotron Radiation Properties

Coherence can be spatial (transverse) or temporal (longitudinal), dependent on the transverse bunch size or the longitudinal bunch size, respectively. The condition for complete spatial coherence can be written as in [71],

$$\lambda \gg 2\pi r_0 sin(\theta) \approx 2\pi r_0 \gamma^{-1} \tag{2.9}$$

where $r_0$ is the radius of a cylinder considering an electron bunch to have a even distribution over a cylinder, $\theta$ the angle of emission and $\gamma$ the relative energy [71]. Moreover, $r_0$ can be assumed to be the equivalent to the transverse bunch dimension, $\sigma_{x,y}$ resulting in

the condition for spatial coherence to be expressed as,

$$\sigma_{x,y} \leq \frac{\gamma\lambda}{4\pi} \tag{2.10}$$

On the other hand, temporal coherence occurs when the longitudinal bunch length is comparable to the wavelength of radiation being emitted, which results in the electrons emitting their radiation with the same phase. Throughout this thesis the relevant form of coherent synchrotron radiation is temporal coherence and accordingly from here on referred to simply as coherent synchrotron radiation.

CSR is known to come from the longer wavelength regions of the electromagnetic spectrum in particular the microwave regions. If these long wavelengths are longer than the transverse dimensions of the beampipe, they will not propagate through the vacuum pipe, and hence not be seen at beamports or beamlines [72]. Parameters and conditions of a storage ring can be altered to allow for CSR to be above the shielding cut-off (Eq. 2.8), allowing it to propagate, be emitted and observed.

In normal circumstances CSR arises when its wavelength is longer than the bunch length. This is because CSR can be generated if the wavelengths of radiation emitted by the bunch interact with the same phase and thus superimpose [73, 74]. When CSR is produced as a result of MBI, the wavelength can be shorter than the overall bunch length but must be the same size or longer than the structure (micro-bunch) emitting it. This implies that the wavelength of CSR can be much shorter than the total longitudinal bunch size. It is a steadfast rule, that the structure emitting the CSR must be comparable to or shorter than the wavelengths being emitted.

At a storage ring, CSR can be generated via two methods, both requiring the increase of charge density of the electron bunch. The first way squeezes the bunch in order to generate a bunch with an overall smaller longitudinal dimension, the shorter bunch can then go on to emit SR with wavelengths comparable to bunch length. As the bunch length and wavelength are of comparable size, the SR generated is CSR. The reduced size allows it to propagate throughout the vacuum pipe and therefore be emitted. This is the more gentle approach in which to create CSR at a synchrotron light source. Commonly, this procedure is used to yield shorter pulses of light for time-resolved and pump-probe

user experiments.

To go one step further, by compressing the bunch even more, micro-bunching instabilities (MBI) are achieved. As well as compressing the bunch, more electrons can be forced into a bunch to produce the same results because MBI are caused when a threshold single bunch charge density is exceeded. Once surpassed, the bunch separates into individual filaments or 'micro-bunches' and each of these filaments can go-on to emit CSR. So though, the CSR being emitted from the micro-bunches has a shorter wavelength than the original bunch length in truth its wavelength is comparable to the longitudinal dimension of the micro-bunch emitting it.

Not only is coherent radiation desired due to its emitted wavelengths and a side-effect of short pulses, its intensity goes as the square of the number of electrons in a bunch, $N_e$, as compared to incoherent SR which is just proportional to $N_e$. The derivation for this relation in one dimension is considered below [72]. The radiated field from a single electron is given, where $\omega$ is the frequency of radiation and $A$ an amplitude.

$$E_j \propto e^{i(\omega t+\varphi_j)} \tag{2.11}$$

The phase, $\varphi_j$ is defined as the position of the j-th electron with respect to the center of the bunch, where $z_j$ is the distance from the bunch centre [72].

$$\varphi_j = \frac{2\pi}{\lambda} z_j \tag{2.12}$$

It is assumed that the difference in path length from the beam cross-section to the observer is small with respect to the shortest wavelength of radiation emitted. The radiation field from $N_e$ electrons at a frequency of $\omega$ and phase $\varphi_j$ is expressed as a sum.

$$E_{total} \propto \sum_{j=1}^{N_e} e^{i(\omega t+\varphi_j)} \tag{2.13}$$

Thus the radiated power, $P(\omega)$, is proportional to the square of the radiation fields.

$$P(\omega) \propto \sum_{j}^{N_e} E_j \sum_{k}^{N_e} E_k^* \tag{2.14a}$$

$$P(\omega) \propto \sum_{j}^{N_e} e^{i(\omega t+\varphi_j)} \sum_{k}^{N_e} e^{-i(\omega t+\varphi_k)} = \sum_{j,k}^{N_e} e^{i(\varphi_j-\varphi_k)} \tag{2.14b}$$

For $j = k$,

$$\sum_{j=k}^{N_e} e^{i(\varphi_j-\varphi_k)} = N_e P_e(\omega) \tag{2.15}$$

where the power emitted from a single electron, $P_e(\omega)$ can be expressed in terms of $E_e(\omega)$, the field from one electron as:

$$P_e(\omega) = E_j E_k^* = \mid E_e(\omega) \mid^2 \tag{2.16}$$

Consequently Equation 2.14b becomes,

$$P(\omega) \propto N_e P_e(\omega) + \sum_{j=1}^{N_e} \sum_{k=1, j\neq k}^{N_e} e^{i(\varphi_j-\varphi_k)} \tag{2.17}$$

If each electron within a bunch is expected to have the same energy, then the total power emitted by a bunch is,

$$P(\omega) \propto N_e P_e(\omega) + P_e(\omega) \sum_{j=1}^{N_e} \sum_{k=1, j\neq k}^{N_e} e^{i(\varphi_j-\varphi_k)} \tag{2.18}$$

When $j \neq k$, that is the bunches are not the same, a form factor must be defined and implemented [75]. The total power emitted by a single electron bunch at a given wavelength is expressed below [73, 76],

$$P(\omega) = N_e P_e(\omega)(1 + (N_e - 1) f_\omega), \tag{2.19}$$

where $f_\omega$ is the form factor for the forward directed radiation and is only dependent on the longitudinal distribution. The bunch distribution must be taken into account especially as, the CSR power spectrum depends on the bunch distribution [72]. The form factor is given by the square of the modulus of Fourier transform of the longitudinal charge distribution [73, 74]:

$$f_\omega = \left| \int_{-\infty}^{+\infty} g(z) e^{ikz} dz \right|^2 \tag{2.20}$$

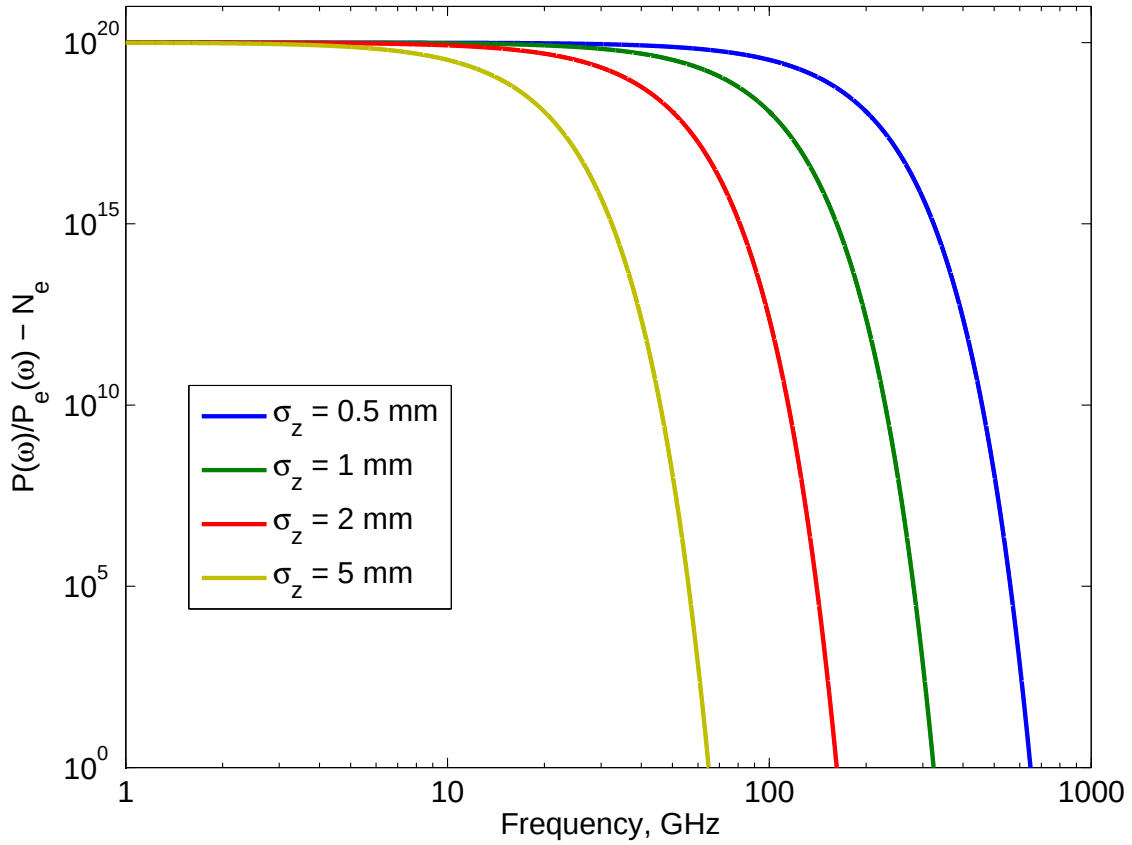


Figure 2.1: The amplitude of each coherent spectrum for a Gaussian bunch distribution ($N_e = 10^{10}$) with lengths 0.5 mm, 1 mm, 2 mm and 5 mm.

where $k = 2\pi/\lambda$ is the wavenumber. Assuming a Gaussian bunch distribution of,

$$g(z) = \frac{1}{\sigma_z\sqrt{2\pi}}\, e^{\left(-\frac{z^2}{2\sigma_z^2}\right)} \tag{2.21}$$

where $\sigma_z$ is the rms bunch length the form factor can be expressed as,

$$f_\omega = e^{-k^2\sigma_z^2} \tag{2.22}$$

The form factor is sensitive to the bunch shape and varies between $f_\omega = 0$ for incoherent emission due to an infinitely long bunch and $f_\omega = 1$ for coherent emission from a point-like bunch [58, 73, 74]. Illustrated in Figure 2.1, the amplitudes of coherent spectra where a Gaussian bunch distribution is assumed (Eq. 2.21) are shown for four different bunch lengths using Equations 2.19 and 2.22 as a function of frequency. At the lower

frequencies, all four curves appear to have the same amplitudes, with the discernment between bunches becoming more apparent with increasing frequencies. It can be seen that the longer bunches produce less higher frequency spectra than their shorter bunch counterparts. The y-axis denoted as $P(\omega)/P_e(\omega) - N_e$ can be considered as $N_e f_\omega (N_e - 1)$.

By plugging back in the values for the form factor into Equation 2.19 we obtain two relationships (Eqs. 2.23 and 2.24) depicting the total power in the case of incoherent and coherent radiation, respectively. As can be seen in Equation 2.24, coherent emission goes as the square of the number of electrons per bunch. This quadratic relationship is the signature of coherent emission.

$$f_\omega = 0 \Longrightarrow P(\omega) = N_e P_e(\omega) \tag{2.23}$$

$$f_\omega = 1 \Longrightarrow P(\omega) = N_e^2 P_e(\omega) \tag{2.24}$$

In the case of electron storage rings $N_e$ is usually in the order of $10^9$ - $10^{10}$ and thus for the case of coherence as $f_\omega$ approaches 1, the total power emitted is significantly large (Eq. 2.24) and the relationship can be clearly seen in data captured, which is later shown in this thesis.

## 2.3 Low Alpha Mode

Diamond has the ability to operate at a selection of different beam settings, which can be divided into two main categories. Table 3.1 displays the lattice and beam parameters for a variety of Diamond's different user modes. Normal user optics and low-alpha optics are the two main categories where the former is the most used setting and Diamond operates in this configuration approximately 98% of the time. Some user experiments at light sources require different machine conditions, frequently shorter electron bunches. Many light sources internationally, including Diamond, provide user runs with shorter bunch lengths [39, 52, 53, 56, 57]. This user mode is called low-alpha mode and gives rise to an assortment of different user experiments. These experiments include time-resolved or pump-probe experiments because a smaller electron bunch corresponds to a shorter x-ray pulse length. The reduction in bunch length also affects the wavelengths of radiation

produced and allows for the emission of CSR in the GHz to mid-infrared regimes [77, 78].

The natural bunch length, $\sigma_{z0}$ is proportional to the square root of the momentum compaction factor, $\alpha$ [44, 79, 80]. Thus, by reducing $\alpha$, hence the name 'low-alpha mode', the bunches become smaller, more compressed. Unfortunately, the reduction of $\alpha$ is not as simple as it sounds and provides many additional complications especially when many other ring parameters must be maintained including injection efficiency, longitudinal beam dynamics and lifetime of the stored beam [44].

The momentum compaction factor, expressed in Equation 2.25 is defined as the relative change in path length during one turn of the storage ring with respect to the relative change in the particle's momentum [81]:

$$\alpha = \frac{\frac{\Delta l}{l_0}}{\frac{\Delta p}{p_0}}, \tag{2.25}$$

where $\Delta l$ is the change in circumference travelled by the particle, $l_0$ the circumference of the storage ring, $\Delta p$ change in momentum of the particle and $p_0$ is the nominal momentum of the particle. Shown as a singular parameter, $\alpha$ can be expanded to allow for many more terms, usually as a power series with respect to the change in relative particle momentum, where $\delta = \frac{\Delta p}{p_0}$,

$$\alpha(\delta) = \alpha_1 + \alpha_2\delta + O(\delta) \tag{2.26}$$

Within this work, only the first two expansions are considered, where $\rho$ is the dipole bending radius, $\eta$ the dispersion and $\eta'$ its spatial derivative [44].

$$\alpha_1 = \frac{1}{l_0}\oint \frac{\eta_1(s)}{\rho}\,ds \tag{2.27}$$

$$\alpha_2 = \frac{1}{l_0}\int \frac{\eta_1'(s)^2}{2} + \frac{\eta_2(s)}{\rho}\,ds \tag{2.28}$$

The reduction of $\alpha_1$ is carried out by altering the lattice namely by minimising the dispersion in the dipoles as close to zero as possible. In order for the momentum aperture to remain at a reasonable size, $\alpha_2$ must also be reduced [44]. Naturally, for a most effective and thorough reduction of $\alpha$, further $\alpha$ values from the power series expansion should also

be reduced.

As well as the momentum compaction factor the RF voltage, $V_{rf}$, also influences the size of the bunch. The natural bunch length is inversely proportional to the $\sqrt{V_{rf}}$ [75, 79, 80]. Accordingly, for low-alpha modes, in order to reduce the bunch length, not only is $\alpha$ reduced but also the RF voltage increased. Byrd states the equation below [80] where $E$ is the beam energy and $f_s$ the synchrotron frequency:

$$\sigma_{z0} \approx \sqrt{\frac{\alpha E^3}{2\pi f_s V_{rf}}} \tag{2.29}$$

Typically, the operation of a synchrotron storage ring is how best to facilitate the users, thus a high flux and low emittance is the most sought after goal. Even when providing special beam conditions such as low-alpha mode these aims are still demanded. Nevertheless, not all criteria can be met. At Diamond, low emittance is maintained during low-alpha optics albeit not as low as during normal mode user operation. However to achieve a stable operation, the stored current and thus the flux cannot be kept at such a level. The beam current is reduced by a factor between 15 and 30, to ensure that the machine remains in stable operation and to avoid chaotic MBI. In the case of both Diamond low-alpha modes, the bunch current is set to 50 $\mu A$ whereby the bursting threshold is not exceeded in the case of the short pulse low-alpha mode (low-alpha pulse mode) and is surpassed for the mode of THz generation resulting in quasi-periodic bursts (low-alpha THz mode).

## 2.4 Beam Modes of the Diamond Storage Ring

At Diamond, normal user optics is defined as having a momentum compaction factor of $\alpha = 1.7 \times 10^{-4}$, with a maximum current of 300 mA and typical combined cavity voltage of 2.5 MV. Normal mode can deliver a selection of filling patterns including a standard fill with 900 bunches (of the 936 buckets) and a hybrid mode of 686 bunches with a high charge single bunch in the middle of the gap, both depicted in Figure 2.2. The figure represents the filling pattern used for each mode and the associated charge for each filled bucket. The most implemented of all the beam modes at Diamond is the normal user

mode with 900 bunches filled at 300 mA.

Low-alpha mode is the second category of beam mode varieties conducted at Diamond, where low-alpha mode means that the momentum compaction factor is reduced compared to normal user optics. The first implementation of low-alpha mode at Diamond was realised in 2008 [82], with the first user experiments the following year. Since the initial application of low-alpha modes at Diamond, two dedicated low-alpha user lattices have been created, each assigned to a specific beamline whose full details are displayed in Table 3.1. The most frequently operated low-alpha mode is for beamline B22, the Infra-red Beamline. This low-alpha mode is applied to obtain terahertz radiation. It uses $\alpha = -4.5 \times 10^{-6}$ with a fill pattern of 200+1 bunches and a current of 10 mA. The other low-alpha mode in operation is implemented to generate short pulses for the pump-probe and time-resolved experiments of beamline I06. The conditions are $\alpha = -1 \times 10^{-5}$ at 20 mA with a fill of 400+1 bunches. The fill patterns and associated bunch charges of these low-alpha modes are displayed in Figures 2.3.

## 2.5 Micro-Bunching Instabilities & its Applications

MBI have been a popular topic for many years especially in light of the creation of third generation light sources. With the detection of bursting CSR at light sources internationally, the theory of MBI came about. In 2002, Heifets and Stupakov [83] presented a theory to explain the bursting CSR, namely MBI. The theory proposed that the filaments or micro-bunches caused as a result of the instability were created by the SR from the beam acting back on the beam itself [23, 83]. The interaction between the beam and its wake-field is then amplified by the onset of CSR, where a wake-field is defined as the wavefront from a relativistically charged particle, scattering off boundaries e.g. the vacuum pipe, and thus affecting the motion of the charged particles behind, both parallel and perpendicular to their direction of motion. Therefore the growth and decay of MBI causes the bursting nature of the CSR emission detected. Within the same year, Byrd et al put forward the first evidence that these bursts of CSR are due to MBI [23], coinciding with Heifets and Stupakov's theory [83].

The longitudinal bunch distribution or charge distribution can be assumed to be

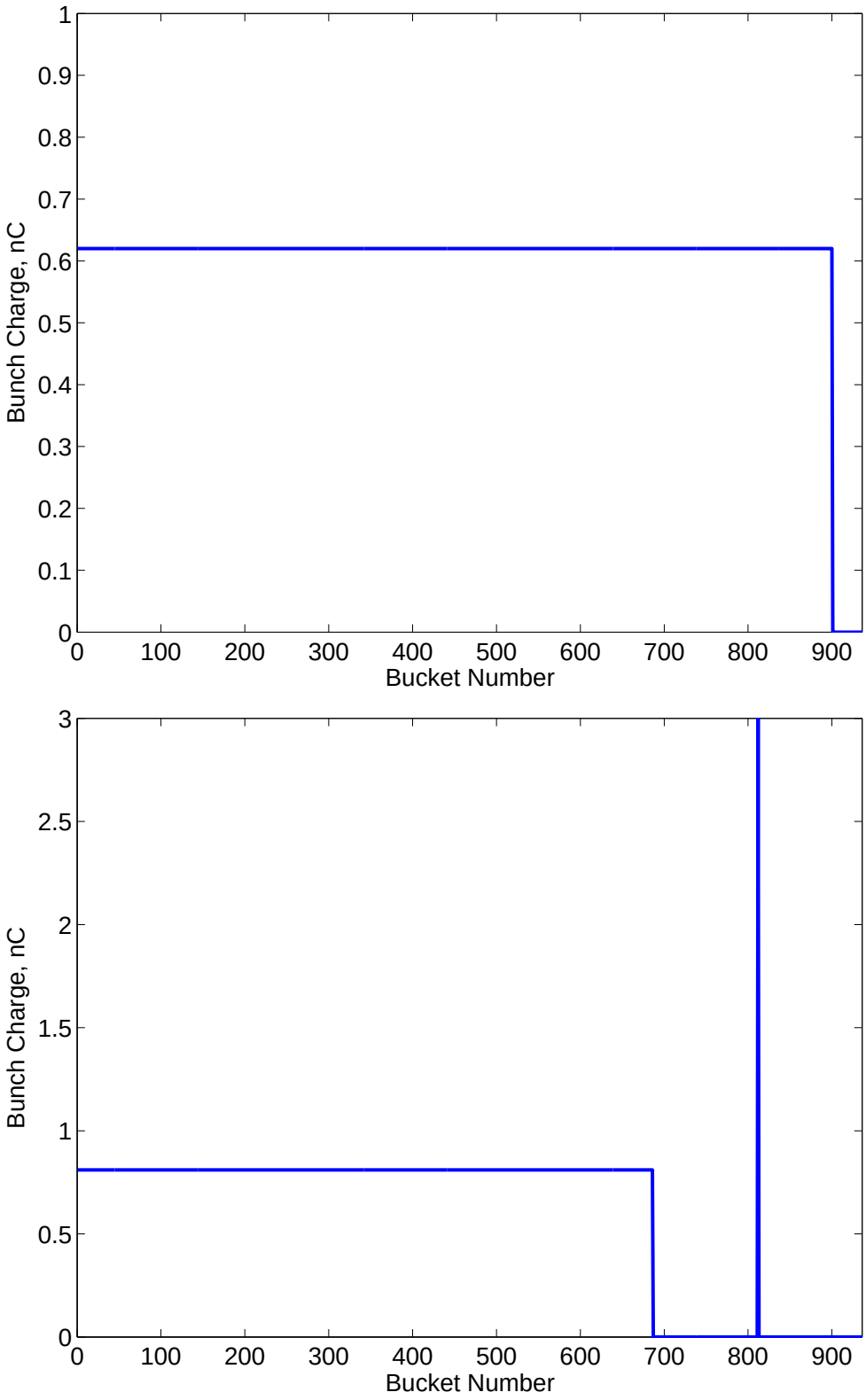


Figure 2.2: Filling pattern for Normal User Mode with 900 bunches with an overall beam current of 300 mA (top) and Hybrid Mode with 686 bunches and a high charge single bunch giving an overall beam current of 300 mA (bottom).

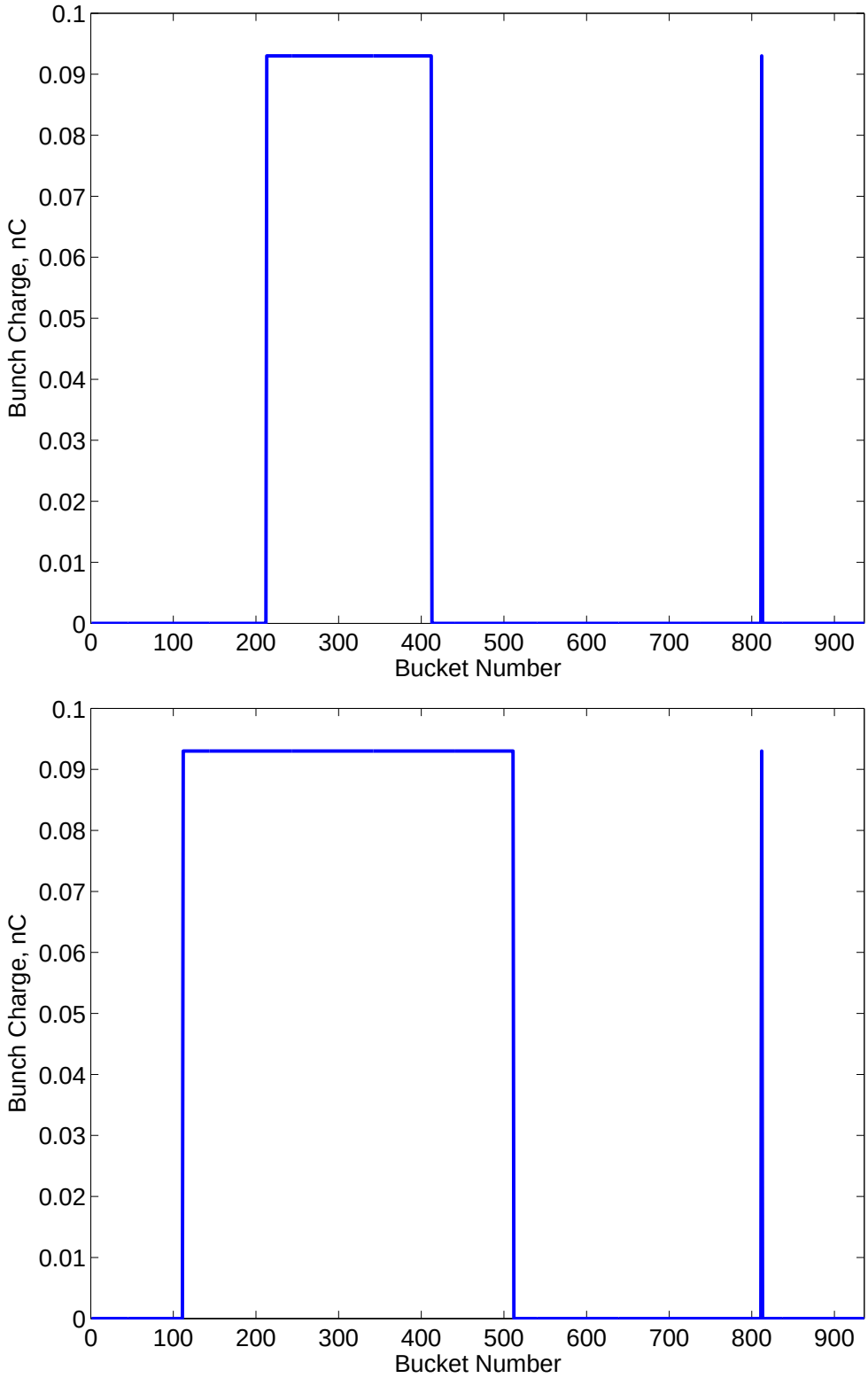


Figure 2.3: Filling pattern for Low-Alpha THz Mode with 200 bunches with an overall beam current of 10 mA (top) and Low-Alpha Short Pulse Mode with 400 bunches with an overall beam current of 20 mA (bottom).

Gaussian (Eq. 2.21) and is known to be so, at low currents [74, 81]. However a density fluctuation can result in a change of the distribution and thus effect the spectrum emitted. Below a threshold current, wake-fields can cause a density fluctuation and result in the static non-Gaussian deformation of a bunch [76]. When CSR is emitted, it must be when a change in the bunch shape/distribution has arisen and this can come about in two ways. The first is for the bunch to be compressed enough that when when the emitting wavelengths of radiation superimpose in phase they are sufficiently short and can be propagated through the vacuum pipe, and the second method involves MBI.

CSR is able to occur with wavelengths shorter than the bunch length yet it is not possible for the emitting structure to be larger than the wavelengths radiated. Hence it is established that the bunch as a whole is not emitting the CSR but rather sub-structures within the bunch, sub-structures known as micro-bunches. MBI can only occur when a threshold bunch current is exceeded thus allowing the interaction between the bunch and its wake-field be sufficiently strong to cause a density modulation. By increasing the bunch current, the more deformed the bunch becomes [76], i.e. the more the fluctuations affect and act upon the bunch causing more and more micro-bunches each emitting CSR. From the proposed model [83], Byrd et al derived a criterion which determines at what bunch current the MBI threshold will be met and thus at which point CSR bursts will occur [23]. For a Gaussian distribution this criterion states:

$$I_b > \frac{\pi^{1/6}}{\sqrt{2}} \frac{e_0 c}{r_e} \frac{\gamma}{\rho^{1/3}} \frac{\alpha \delta_0^2 \sigma}{\lambda^{2/3}}, \tag{2.30}$$

where $I_b$ is the average bunch current, $r_e$ the classical electron radius, $\gamma$ the beam energy, $\rho$ the dipole bending radius, $\alpha$ the momentum compaction factor, $\delta_0$ the relative energy spread, $\sigma$ the rms bunch length and $\lambda$ is the wavelength of radiation less than the vacuum chamber cut-off (Eq. 2.8). Using the values appropriate to Diamond during normal user operation $I_b = 0.46$ mA. Once above the threshold value the CSR *bursts*, which indicates that both the bunch's internal and hence entire structure are changing notably, on ever-changing timescales and that this truly is an instability. Initially above the threshold current the bunches are emitted quasi-periodically but the higher in current the bunches become the more random the bursting becomes. It is known that the compression of a

bunch can lead to a bunch interacting with its own wake-field because the compression of a bunch alters its charge density even if it is below the threshold value. When the bunches are short the CSR impedance dominates [76].

Although MBI are known for limiting storage ring operation and are implemented with a low intensity beam, this instability can open the door for many other possibilities and opportunities. From the point of view of the user, THz spectroscopy, Raman spectroscopy and Fourier Transform Infrared (FTIR) imaging are highly important in the areas of cancer diagnosis [84–86] and historic artefacts investigation [87, 88] as well as metal-organic frameworks research [89, 90]. In contrast to x-ray radiation, THz radiation does not harm the sample [91], hence its applications for human physiology and ancient relics. Naturally, the desire for stable CSR is paramount in order to allow many of these experimental techniques to proceed as they require a stable output signal in order to compare their signal received with and without the sample in question. As with many THz/IR beamlines, including B22 at Diamond, a comparison method is undertaken whereby the spectrum is observed with no sample present, then with a sample and finally the two spectra are compared. Therefore, it is paramount that the source remains constant to allow for accurate comparisons between the spectra.

Not only does the user benefit from the onset of THz radiation, but more diagnostics tools can be employed. The power spectrum of a bunch can be determined using FTIR spectroscopy [76], just as the data can be captured on a beamline for user experiments it can be obtained and used for monitoring the spectrum of the beam. Observing the spectrum of the CSR beam can also, of course, be determined using the eight channel SBD array as outlined within the pages of this thesis. Primarily used in stable beam conditions, streak cameras can be operated to determine the longitudinal bunch profile of the shortened bunches and even during a burst too [45].

Single shot bunch length measurements can be carried out by determining the temporal profile using the EOSD technique [46, 49]. Though recently implemented at storage rings [48] (originally used at linacs), it has proved successful. Changes in the bunch structure and sub-structure are able to be observed using EOSD with resolution to bunch lengths of 1.5 ps (rms) and bunch charges down to 30 pC in the case of ANKA [49] and even sub-picosecond lengths by others [47, 50]. As a result, EOSD allows for the de-

tection of MBI [49, 50]. EOSD and THz radiation also allow for the investigation into long-ranging wake-fields and examining bunch-to-bunch interactions [49]. Briefly described using EOSD on a desired bunch is as follows: the THz pulse from the bunch (or micro-bunch) must be stretched in time with the laser pulse lengthened to be the same as the THz pulse, the two then propagate through an electro-optical crystal probing the birefringence and after a series of wave-plates the amplitude modulation of the laser pulse represents the characteristics of the THz pulse [46, 50]. Using a spectrometer the laser pulse is analysed. Clearly, there are many stages involved in determining the longitudinal details but in spite of its high resolution and both the speed and precision, there is a lot of effort with regards the design and implementation of the system.

Using the CSR THz emission, unstable bunch oscillations can be detected as they happen [76]. Determining unstable bunch oscillations improves with shorter and shorter bunches and thus CSR producing bunches are ideal [76].

Chapter 3

# Experimental Hardware

This chapter provides an in-depth description of all the components and systems used in order to employ the detector array as a spectrometer to observe the bursts of CSR at Diamond. The equipment used on the test bench for the design and development of the array is described. As part of the commissioning the optimal positioning of the spectrometer was determined as well as the growth of the beam travelling longitudinally. Accordingly the commissioning of the spectrometer is reported below.

## 3.1 Millimetre-Wave Diagnostic Beamport

Within the Diamond storage ring tunnel, there is a beamport that has been dedicated to the investigations of CSR and by extension CSR from MBI [92, 93]. The beamport transports the SR from dipole magnet B06 to the silica viewport window as illustrated in Figures 3.1 - 3.4. The first image depicts the beampipes of the appropriate storage ring cell where the separation of the tangential beampipe from that of the radiation's pipe is shown. Figure 3.2 again shows the path of the radiation and the electron beams, but now consisting of all components of the cell including the dipole magnet B06 which is the source of radiation for the beamport. Figure 3.3 documents the journey of SR throughout the radiation beampipe from just after the source to just before emission from the viewport. The total distance travelled in the beampipe is approximately 3.5 metres, whereby the radiation initially travels in the same plane as the electron beam and at approximately one metre from the viewport window the radiation is parallel but vertically lower than the

Table 3.1: The main parameters of the Diamond storage ring for different user modes [6, 44, 75, 78].

| **Parameter** | **Normal User Mode** | **Low Alpha Mode** | | **Hybrid Mode** |
|---|---|---|---|---|
| | | **THz** | **Pulse** | |
| Beam current, mA | 300 | 10 | 20 | 300 |
| $\alpha_1$ | $1.7 \times 10^{-4}$ | $-4.5 \times 10^{-6}$ | $-1.0 \times 10^{-5}$ | $1.7 \times 10^{-4}$ |
| $\alpha_2$ | $1.9 \times 10^{-3}$ | $-2.3 \times 10^{-5}$ | $-2.2 \times 10^{-5}$ | $1.9 \times 10^{-3}$ |
| $\sigma_z$, ps (rms) | 15.8 | 3.5 | 3.5 | 16.8 |
| $\varepsilon_x$, nm rad | 2.7 | 3.9 | 4.4 | 2.7 |
| Number of bunches | 900 | 200+1 | 400+1 | 686+1 |
| RF Voltage, MV | 2.5 | 3.4 | 3.4 | 2.5 |

electron beampipe due to a periscope design in the beampipe indicated by Figure 3.3. The final figure (Fig. 3.4) shows the emission of radiation from the viewport window and the table for mm-wave investigation with the SBD array.

The radiation arises within the dipole bending magnet, B06, and travels along its dedicated radiation leg towards the beamport and out the silica window (Figs. 3.1 and 3.2). Throughout the path of the radiation while within the beampipe, there are many apertures. These apertures are standard at Diamond and do not affect the x-ray radiation which is desired most amongst its users. Nevertheless, these apertures can and do hinder the mm-wavelengths because of their larger opening angles.

### 3.1.1 Diamond Storage Ring

As discussed previously, Diamond is a 3 GeV synchrotron light source with 24 cells. It benefits from a 561.6 m circumference storage ring [94] and approximately 499.7 MHz RF frequency, resulting in 936 buckets with a bunch spacing of approximately 2 ns. By adjusting lattice and other machine parameters Diamond is able to operate with a variety of different filling patterns and bunch sizing. Table 3.1 displays some of the current types of beam modes available for user runs at Diamond. Most commonly, Diamond runs with the normal user optics. Twenty-nine beamlines are currently operational at Diamond with a further four in the construction or commissioning phases.

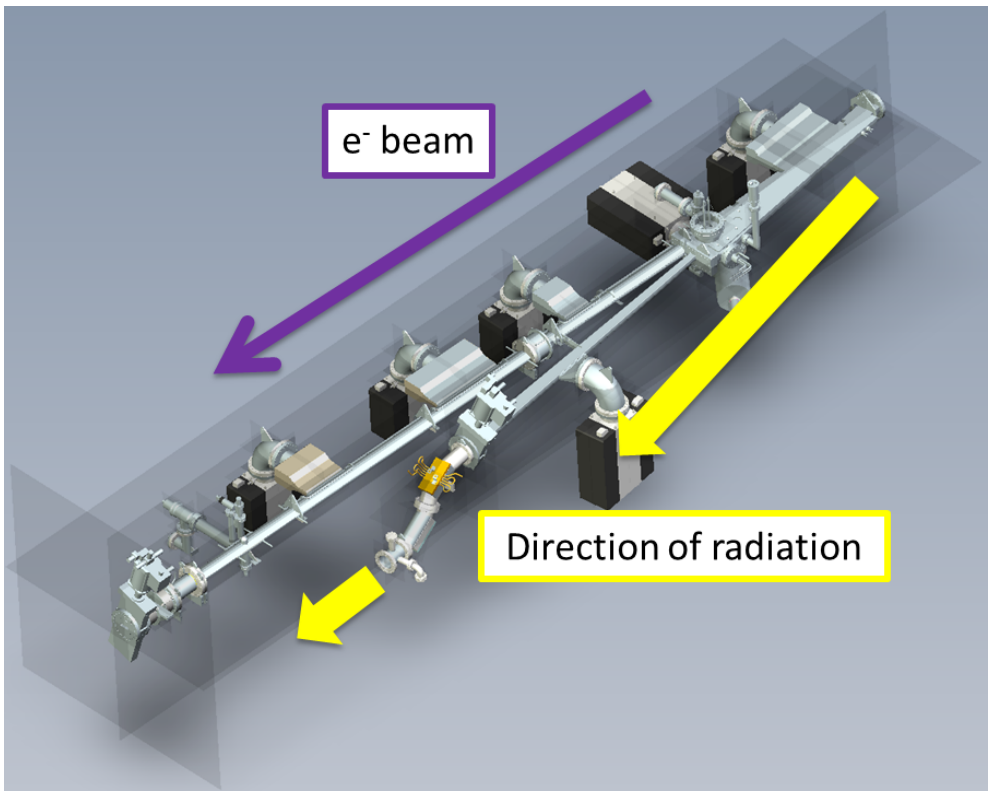


Figure 3.1: The relevant cell showing the direction and separation of the SR radiation and electron beam where the magnets have been removed for a clearer view.

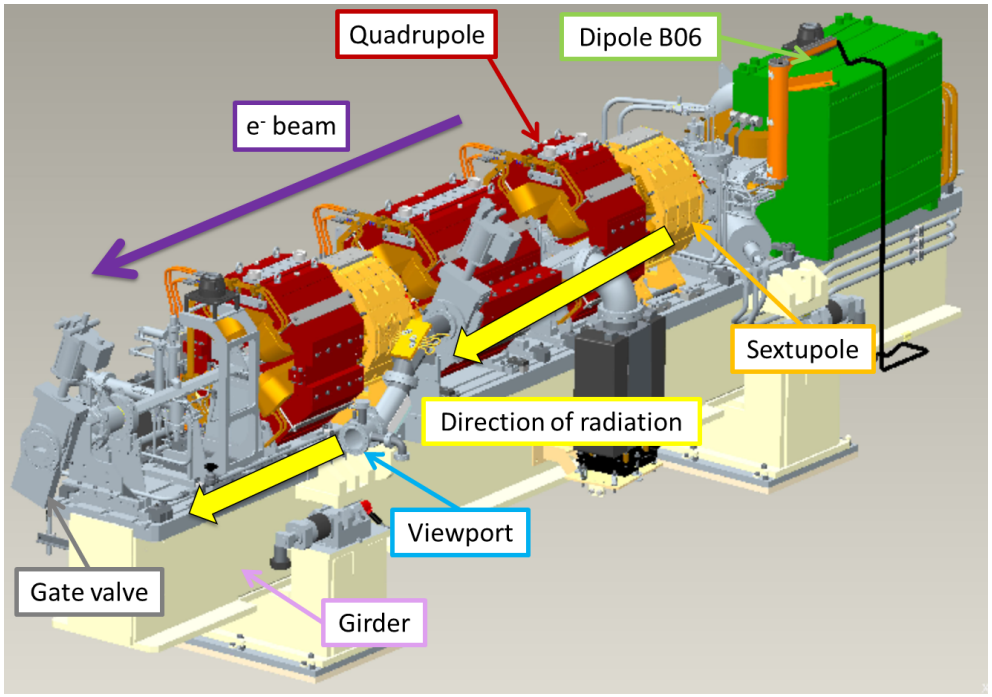


Figure 3.2: The entire cell of B06 with several key features labeled.

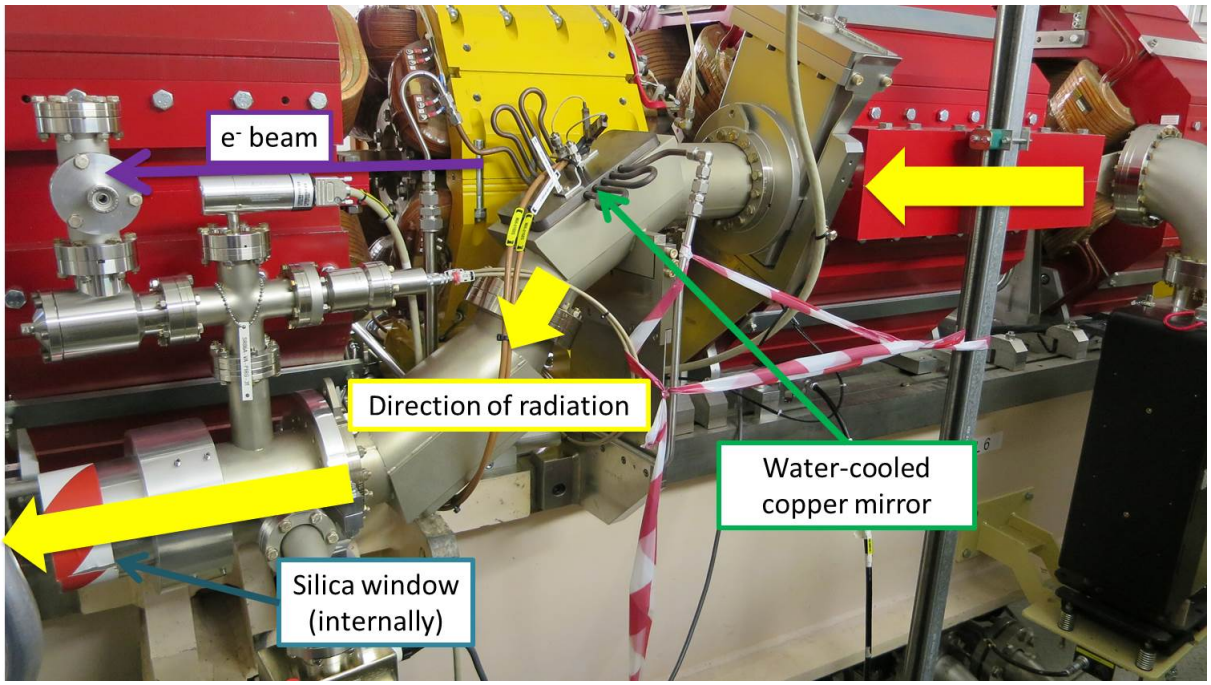


Figure 3.3: The path the radiation takes within the beamport from just after B06 to the silica window.

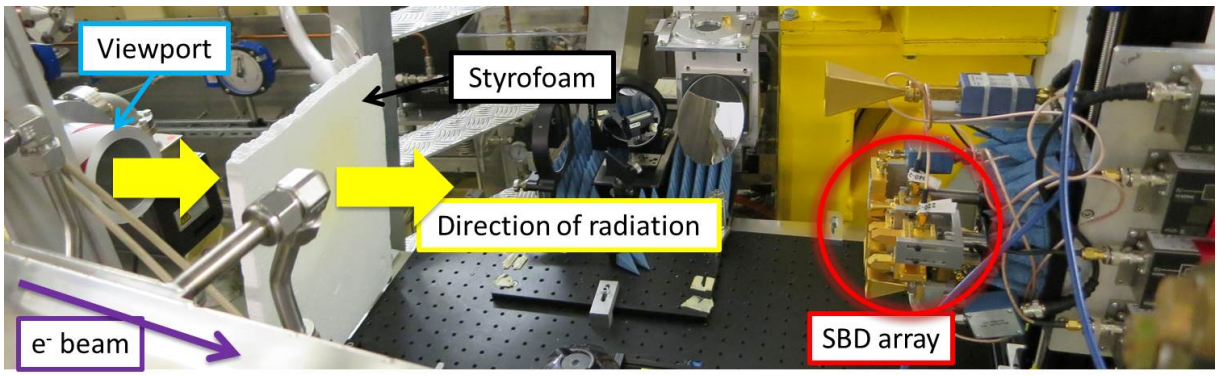


Figure 3.4: The detector array installed in the tunnel with respect to the viewport.

### 3.1.2 Synchrotron Radiation Generation at Diamond

When a charged particle travels along a curved path due to the presence of a magnetic field, SR is generated. In the case of a synchrotron storage ring, this emission of SR occurs as a result of dipole bending magnets or insertion devices. The dipole magnet B06 at Diamond provides the magnetic field to generate SR for the work presented throughout this thesis. At the time of writing (before installation of DDBA (double-double bend achromat) in late 2016 [10, 11]) all forty-eight dipole magnets, including B06, are of C-type design and length 0.900 m with a magnetic length of 0.935 m [94]. Thus the magnetic field strength can be calculated to be $\sim$1.4 T.

Diamond operates at 3 GeV with the bending radius, $\rho$ of the dipoles is 7.13 m [95]. By substituting these values into Equation 2.7, the emitted power from a single electron is $\sim$1.1 $\mu$W. This power is emitted across the entire EM spectrum produced at Diamond.

### 3.1.3 Radiation Transport & Manipulation System

The SR naturally separates from the electron beam as the electrons continue along the curved trajectory dictated by the dipole magnet, while the SR unaffected by the magnetic field continues straight ahead, tangential to the electron beam and its pipe. This is shown in Figure 3.1 where only the beampipes are on view for clarity. In Figure 3.2 the entire cell is illustrated including the relevant dipole magnet (radiation source) where the path of the electron beam versus the radiation is presented with respect to the true set-up. In order to alter the path of the desired radiation, but primarily to absorb and thus remove the x-ray radiation, water-cooled copper mirrors are employed to guide the mm and visible radiation through the periscope towards the beamport's exit as illustrated in Figure 3.3. It can also be seen that the radiation travels parallel but vertically lower than the electron beampipe (Figs. 3.1 and 3.3). The beamport concludes with a fused silica window after which and directly in front of the silica window, the SBD array is installed as shown in Figure 3.4. Like the storage ring, the beamport is kept under vacuum conditions.

Ray tracing inside the dipole magnet was carried out to determine the source of the dipole radiation, courtesy of Hammond and Rawcliffe [96]. With regards the wavelengths of interest, they are all combined in the horizontal plane and thus an average or

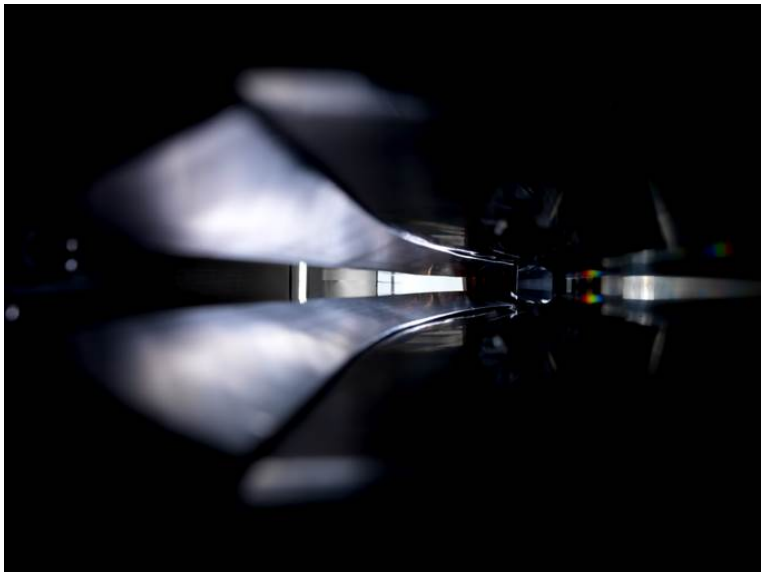

Figure 3.5: View of the lower and upper slit absorbers as seen by the SR [6].

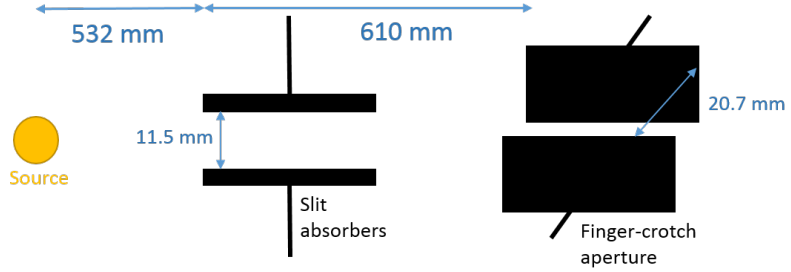


Figure 3.6: A simplified schematic of the first vertical and horizontal apertures after the generation of SR at the source within the bending magnet.

midpoint between the two extreme rays was taken as the source point. It is from this determined midpoint that longitudinal measurements were determined. The first and most severe limit is caused by the slit absorbers creating a vertical aperture of 11.5 mm at a distance of 532 mm from the source point. These curved metal absorbers, depicted in Figure 3.5 as if viewed by the radiation, travel the length of the dipole vessel protecting the downstream magnets and machine from radiation damage in the vertical plane. To accommodate the fan of radiation the dipole vessel itself expands in the horizontal plane. The crotch absorber and finger absorber create the first horizontal limit, with a diameter of 20.7 mm at 1142 mm from the source point. A simplified schematic is shown in Figures 3.6 where only the source, an initial placing of the slit absorbers and finger-crotch aperture are shown. The crotch absorber is the beginning of the solid divide between the electron beam and the photon beam and protects the downstream equipment especially

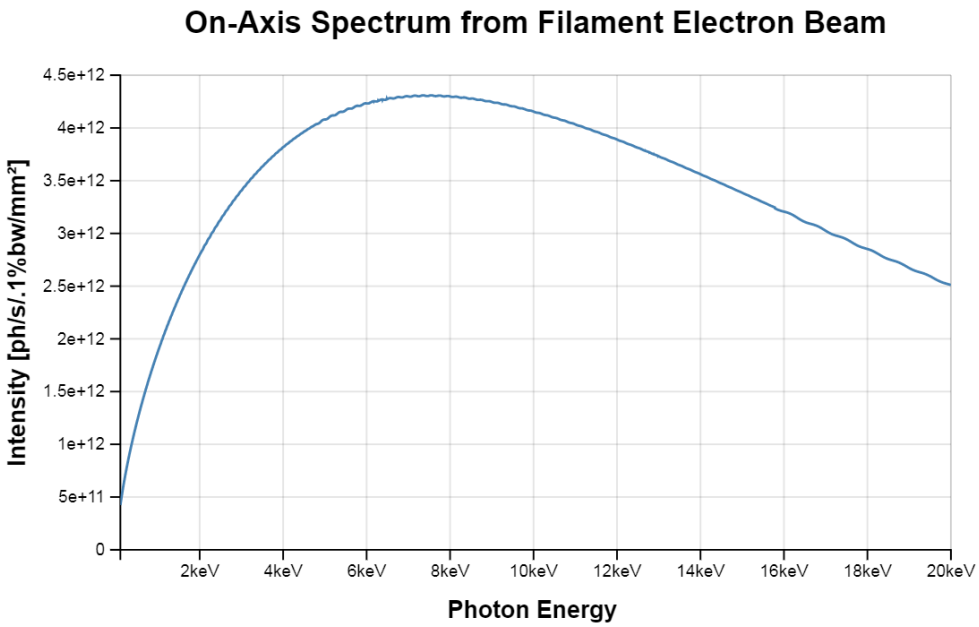


Figure 3.7: The spectrum of SR generated by an electron beam travelling through a dipole magnet at the Diamond Light Source, displayed as intensity against photon energy.

the magnets. As the name suggests the crotch absorber is positioned in the crotch of the dipole vessel. After passing through the finger-crotch aperture, the dipole radiation travels into the radiation leg. The radiation leg maintains a fixed vertical height of 33 mm while its horizontal dimension extends slowly from 39 mm and then it joins the vacuum valve. The vacuum valve connects the radiation leg to the beamport.

### 3.1.4 Viewport for Millimetre-Wave Transmission

With a diameter of 89 mm and thickness of 6 mm [75], a fused silica window supplied by Torr Scientific Ltd is placed at the end of the beamport. As stated by Shields [75], the thickness of the silica window is very important due to the refractions and reflections that occur as a result of it and of course its effect on the spectra observed.

It must be noted that the dedicated beamport has not been designed specifically nor optimally for millimetre and sub-millimetre wavelengths. The analogy often used is to describe the beampipe as a waveguide, nevertheless caution must be exercised. In many ways, using this analogy the beamport can be described as an over-moded pipe. This problem of complexity increases with the number of modes propagating through a structure and is referred to as being over-moded. In this context a mode can be defined

by Feynman as, a pattern of motion which has completely sinusoidal movement at any point, with all points oscillating at the same frequency, albeit some points may move more than their counterparts [97]. Neglecting the beampipe's influence, the impact of the slit absorbers have the most significant (negative) effect on the mm- and sub-mm-components of SR. The presence of these slits is to protect the downstream machine from unwanted x-rays however, in the millimetre and sub-millimetre regime the radiation beam is affected. The main effects are the diffraction and reflection of the beam.

As mentioned in the previous section, the first and most significant aperture after the source of radiation is caused by the slit absorbers creating a vertical limit of 11.5 m, the next limit experienced by the radiation is horizontal with diameter 20.7 mm. These apertures, shown in Figure 3.6, do not interfere with the x-ray radiation produced at Diamond, however they affect the longer wavelength radiation regions of relevance in this work. The effect is greater for the longer wavelength regions because they have a higher divergence than that of the x-rays and thus significant portions of the radiation can be cut due to the apertures. Moreover, the apertures are of comparable size to the wavelengths of interest. For example the 11.5 mm aperture is comparable to approximately the 9 mm wavelength of 33 GHz and thus diffraction can be expected. For two different frequencies observed by the detector array, 33 GHz and 220 GHz, the effect of the radiation as it interacts with the vertical aperture created by the slit absorbers and then the horizontal finger-crotch aperture was investigated.

In the case of 33 GHz, Figure 3.8 shows the radiation prior to any aperture. It is Gaussian - an even uniform shape and has a smooth intensity in both horizontal and vertical dimensions. As expected there is a peak of intensity in the central position, indicating that the intensity is strongest at this point with a value of just below $1 \times 10^9$ ph/s/.1%bw/$mm^2$. Figure 3.9 contrasts greatly with the previous figure as it depicts the 33 GHz radiation after the vertical aperture with height 11.5 mm, similar to the 9 mm wavelength of 33 GHz. The intensity in the vertical position forms a narrow peak reaching slightly higher than the $1 \times 10^9$ ph/s/.1%bw/$mm^2$. This peak has sidebands showing that diffraction has occurred, though at significantly lower orders of magnitude. In the horizontal plane there has also been an effect on the radiation. The intensity of radiation reaches an increased value of $1.5 \times 10^9$ ph/s/.1%bw/$mm^2$, however not at the central po-

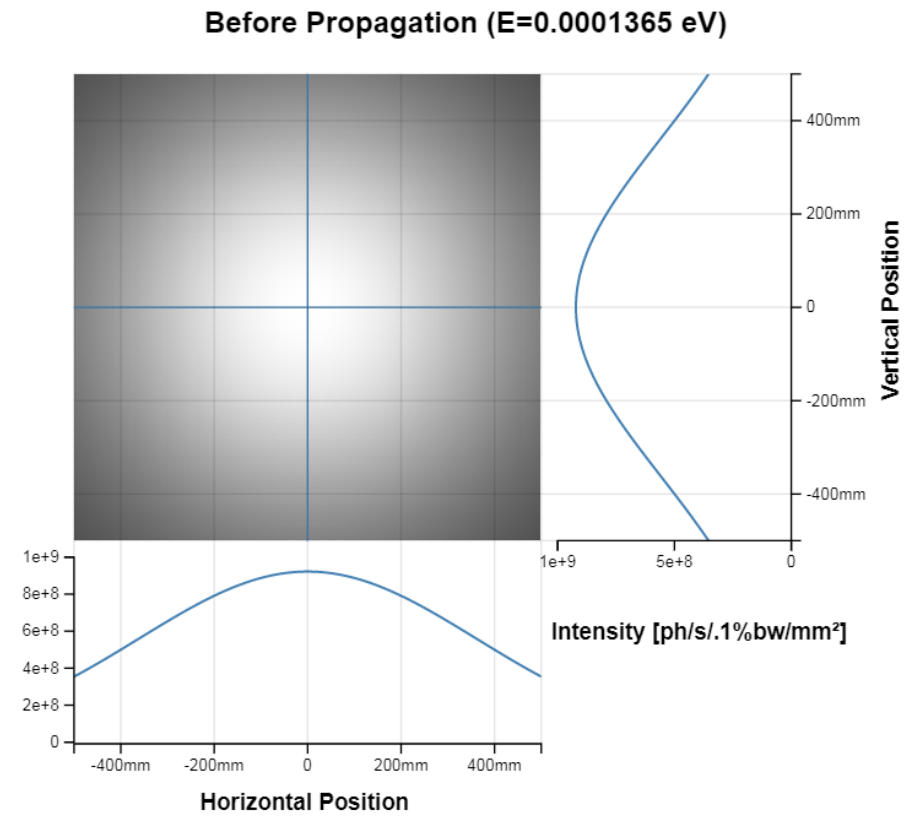


Figure 3.8: The intensity of the 33 GHz radiation prior to any apertures.

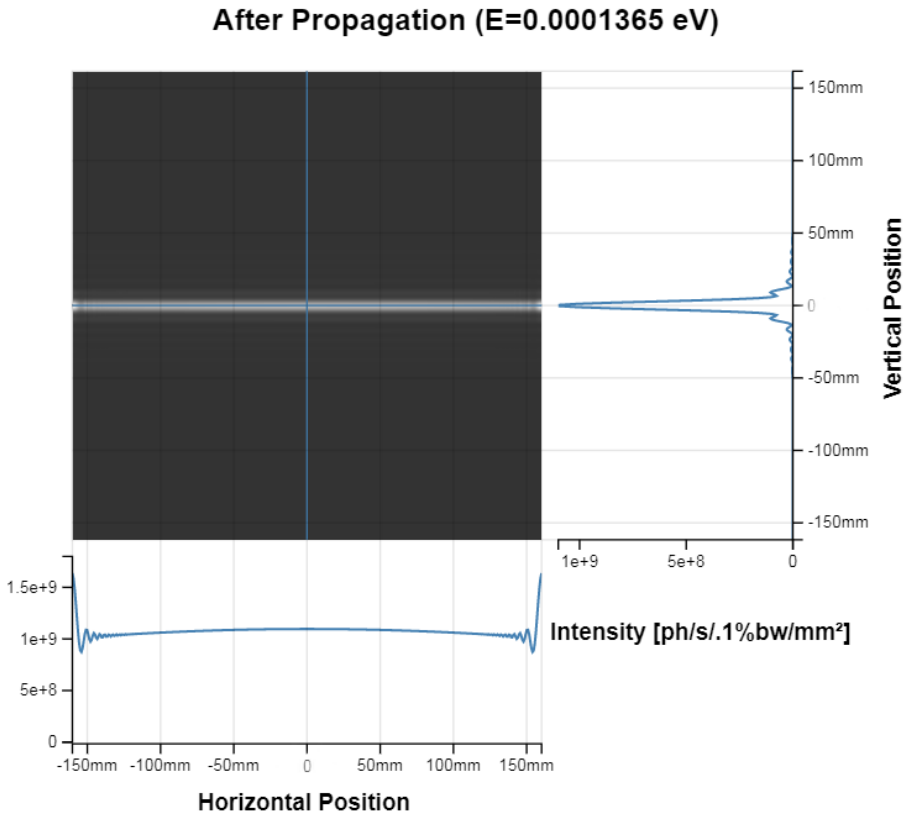




Figure 3.9: The intensity of the 33 GHz radiation immediately after the vertical aperture created by the slit absorbers, where the effect in the horizontal and vertical planes are also detailed.

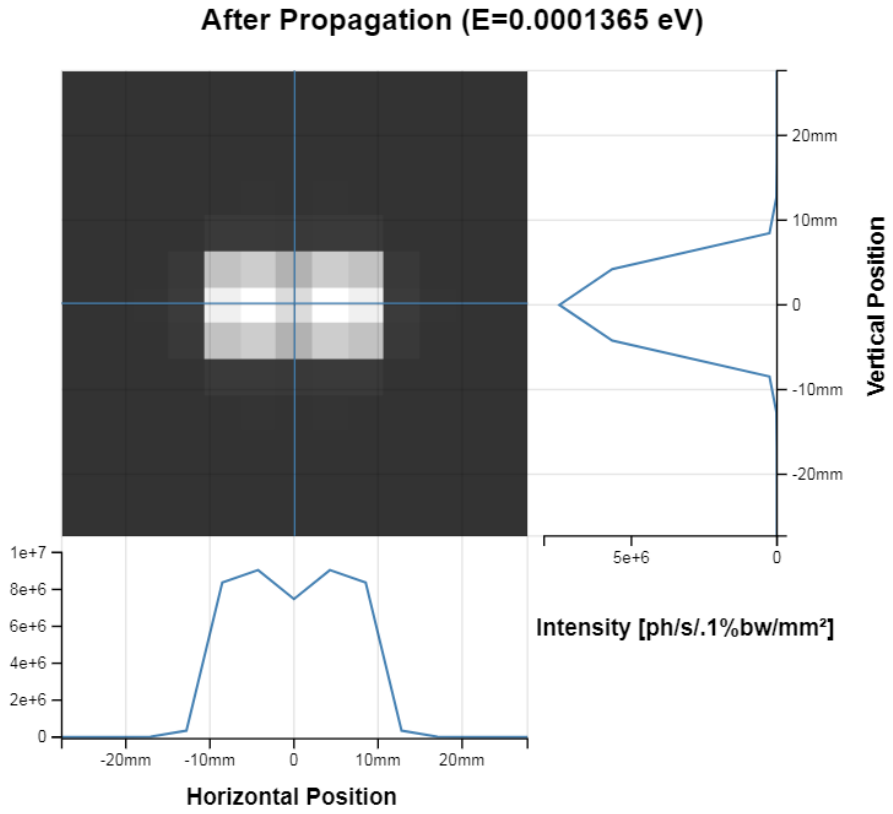


Figure 3.10: The intensity of the 33 GHz radiation immediately after the horizontal finger-crotch aperture, where the effect in the horizontal and vertical planes are also detailed.

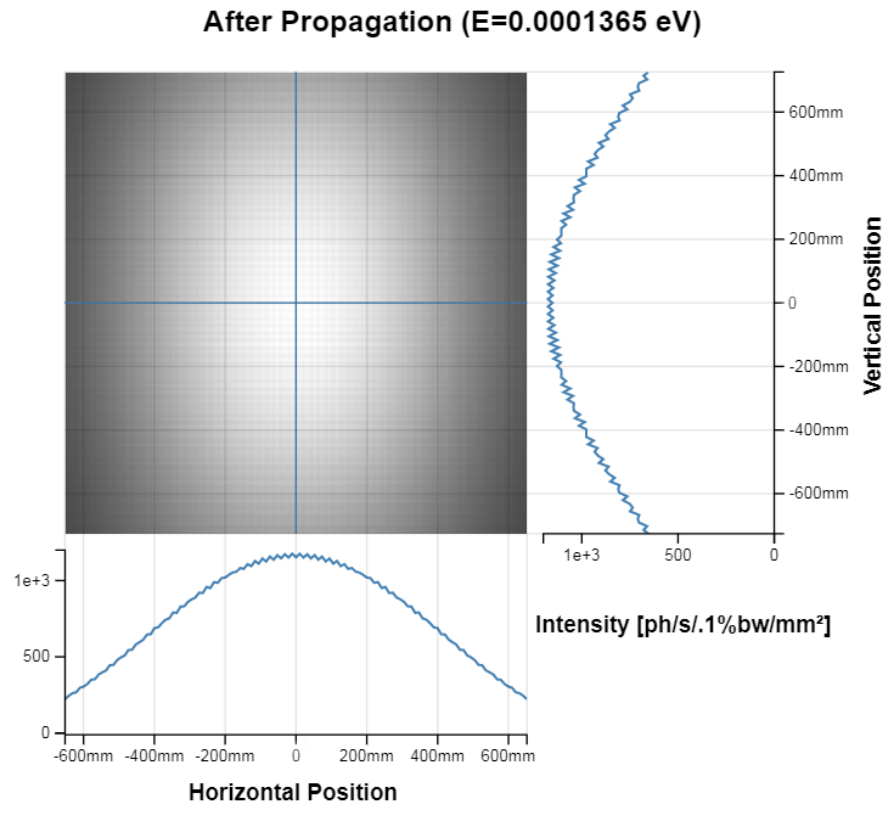




Figure 3.11: The intensity of the 33 GHz radiation at the viewport which is approximately 3.5 m from the source, where the effect in the horizontal and vertical planes are also detailed.

sition which remains slightly above $1 \times 10^9$ ph/s/.1%bw/$mm^2$. The intensity across the horizontal plane, also suffers from diffraction as can be seen by the numerous sidebands. With the introduction of the horizontal finger-crotch aperture 610 mm after the slit absorber aperture, a significant change in signal is observed, with sharp narrow peaks in both the horizontal and vertical fields. It must be noted that Figure 3.10 has a lower resolution compared to its counterparts because of the limits of the simulation. Figure 3.10 shows that the overall aperture through which the SR can travel is significantly reduced and thus there is a decrease in photon intensity. The vertical plane still has a peak but no sidebands, however it can be assumed that this is due to the lower resolution. Its peak is approximately $9 \times 10^6$ ph/s/.1%bw/$mm^2$. The horizontal plane produces two peaks close to each other with an intensity above $9 \times 10^6$ ph/s/.1%bw/$mm^2$. The final figure for the SR propagation at 33 GHz is Figure 3.11, where the radiation is depicted 3.5 m after the source and thus after the two main apertures. It can be seen that the beam has expanded again in the approximate 2.4 m since the horizontal aperture with a more gentle curve spread over a large range in both planes. However, the curves contain structure and are thus not smooth like they were prior to the apertures. The intensity has decreased by six orders of magnitude to approximately $2 \times 10^3$ ph/s/.1%bw/$mm^2$ rather than the original $1 \times 10^9$ ph/s/.1%bw/$mm^2$. It is paramount to note that due to the complex nature of the beampipe in these simulations only the initial vertical and horizontal aperture were considered.

A similar investigation was carried out with 220 GHz radiation, corresponding to a wavelength that is a factor of nine smaller than 33 GHz. As expected and depicted in Figure 3.12, the beam is narrower and also has a Gaussian distribution. It reaches a maximum intensity of $4 \times 10^{10}$ ph/s/.1%bw/$mm^2$ at its peak, which again is the central position. The effect of the vertical aperture can be seen to have a significant affect on the radiation intensity in Figure 3.13. It may have been assumed that because the aperture is less comparable to the wavelength of 220 GHz (compared to 33 GHz), a reduce effect would have occurred. This is not the case, if not it is the contrary. The intensity in the vertical plane has a split peak with smaller peaks in the centre, similar to beats. In the horizontal plane, the radiation retains its Gaussian shape. the peak intensity reached is again higher than prior to the propagation through the apertures. Finally, at the viewport

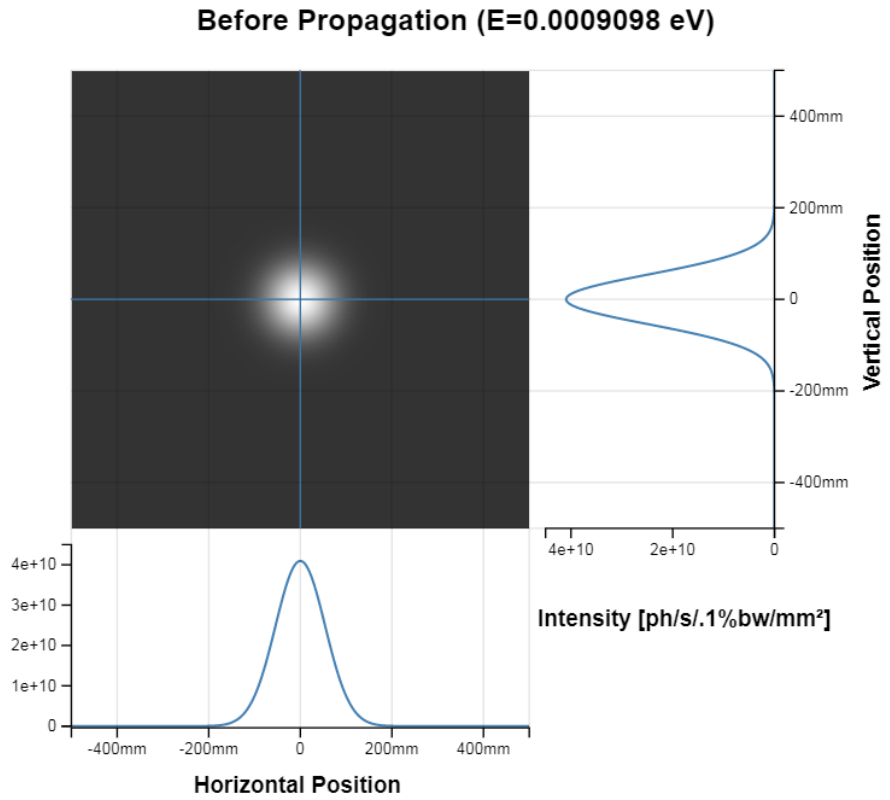


Figure 3.12: The intensity of the 220 GHz radiation prior to any apertures.

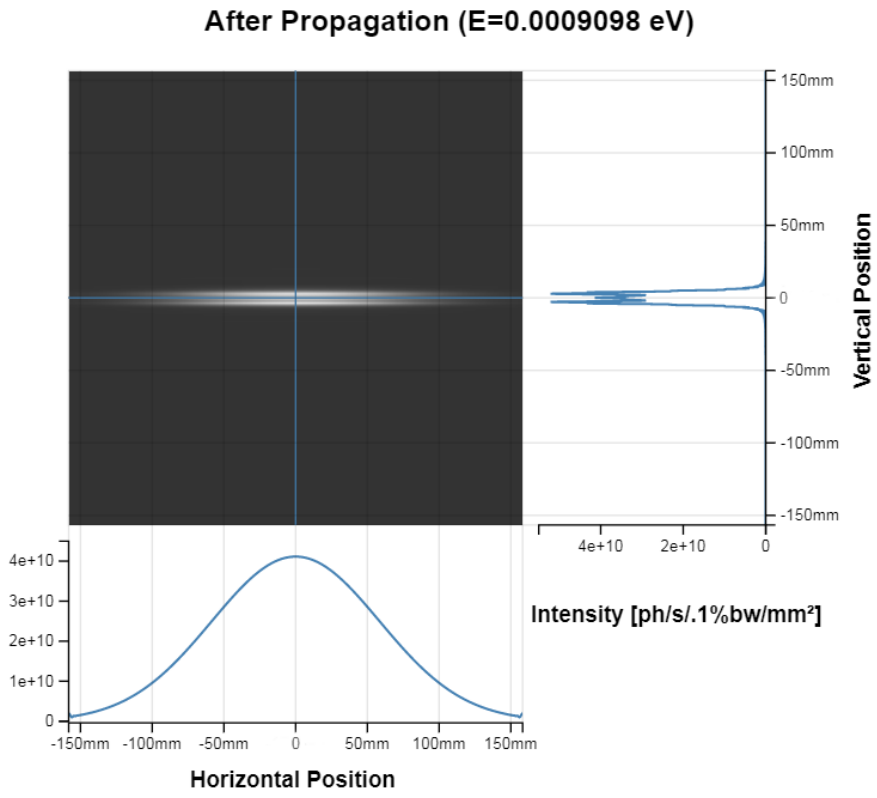


Figure 3.13: The intensity of the 220 GHz radiation immediately after the vertical aperture created by the slit absorbers, where the effect in the horizontal and vertical planes are also detailed.

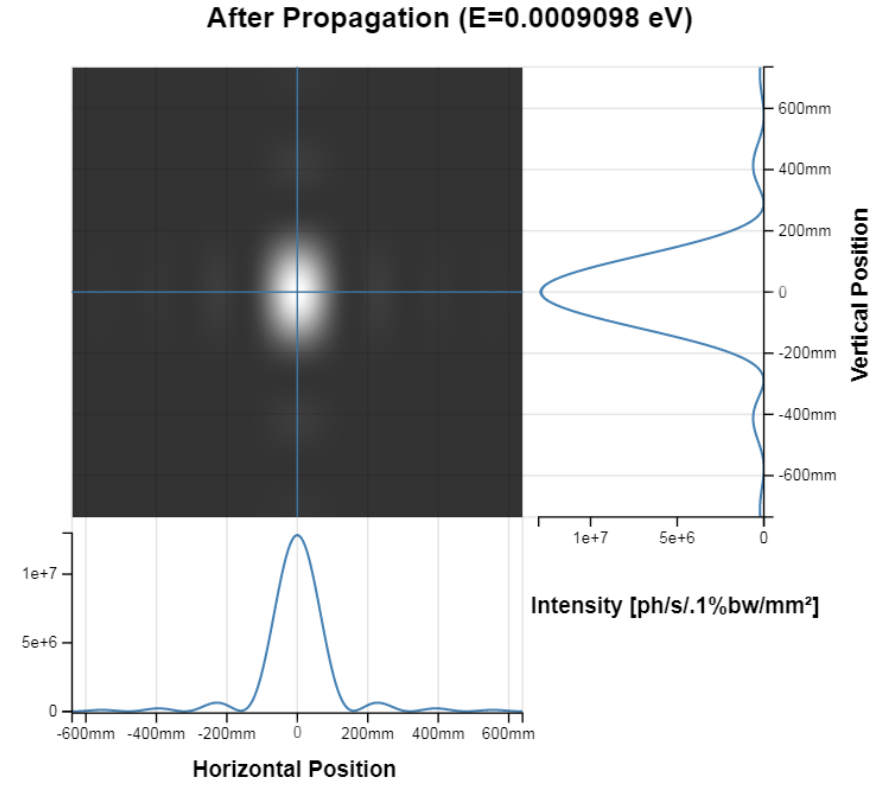




Figure 3.14: The intensity of the 220 GHz radiation at the viewport which is approximately 3.5 m from the source, where the effect in the horizontal and vertical planes are also detailed.

after propagation through both the vertical and horizontal aperture, the radiation intensity is $3 \times 10^7$ ph/s/.1%bw/$mm^2$ at the peak in both vertical and horizontal positions. This equates to a reduction in intensity by three orders of magnitude. What is interesting to note is that in the case of 33 GHz, the reduction was twice that, i.e. six orders of magnitude. This vast difference must be to do with the difference in wavelength and that the wavelength of 33 GHz is more comparable to the aperture sizes, resulting in more diffraction and impact on the radiation. The radiation profile for 220 GHz at the viewport has a Gaussian shape, with gentle and small sidebands. Though already known, it has been shown in this section (Fig 3.8 - 3.14) that the frequencies of the detector array will all be impacted by the vertical and horizontal apertures.

## 3.2 Detector Array & Data Acquisition System

A spectrometer is a piece of apparatus used to detect and analyse wavelengths of the EM spectrum. The spectrometer has been created in such a manner that all eight SBDs are as close together as possible to observe the most signal simultaneously [92] as depicted in Figure 3.15 with some blue pyramidal foam present to minimise the possibility of reflections. In order to eliminate the risk of shadowing all entrance apertures are in one plane. Due to the polarisation nature of waveguides, the horn antennas and hence detectors must be aligned correctly in order to observe the E-field. The detectors will be discussed later in Section 3.3.1.

As shown in Figure 3.4, the detector plate is installed in open air in front of the silica window, not further than 1 m away [92]. The detector array plate is attached to a three-way motion set-up in order to move the spectrometer in the x-, y- and z-planes and thus to optimise the signal obtained in the different channels. Directly after the viewport window there is a sheet of polystyrene, which is used to block unwanted frequencies that may affect the measurements, namely visible wavelengths of light and infrared while allowing THz and mm-wavelengths to pass through [92]. Though not required by the SBDs, the polystyrene has remained installed when it was used to protect pyroelectric detectors from visible frequencies. The transmission spectrum of a polystyrene sheet is shown in Figure 3.16. It is clear to see that it is effective at allowing the frequency

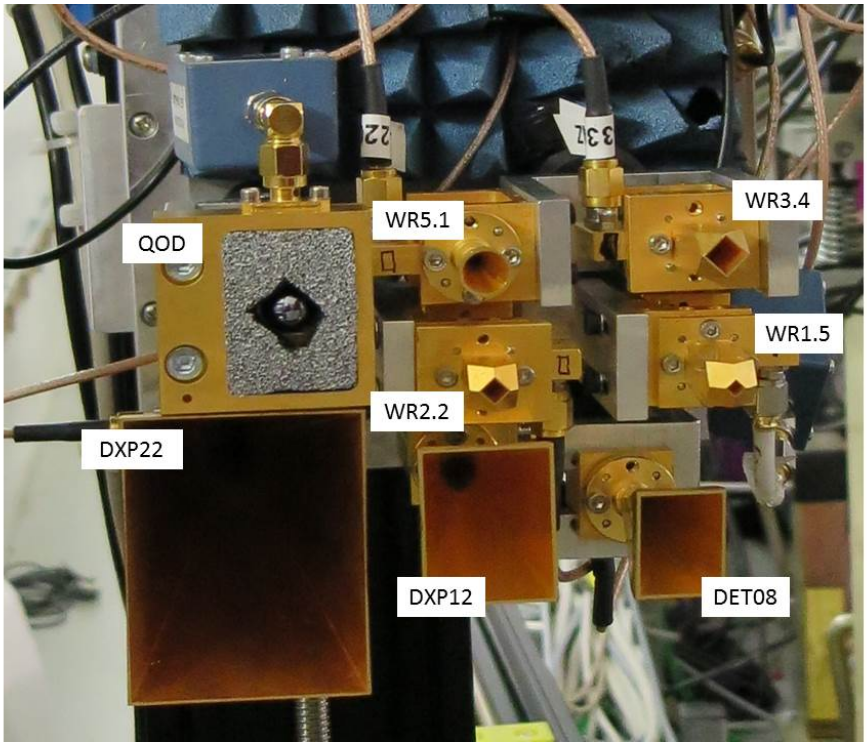


Figure 3.15: Layout of detector array plate with all with labels denoting the model of each detector and horn combination.

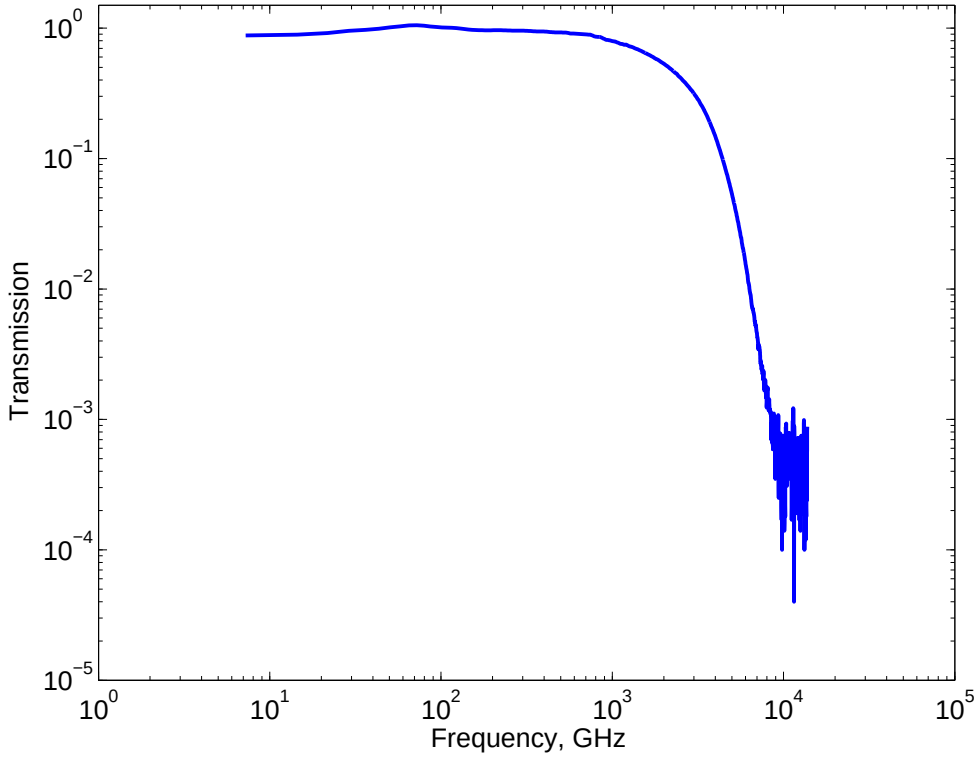


Figure 3.16: Relative transmission of sheet of polystyrene, courtesy of Arne Hoehl [98].

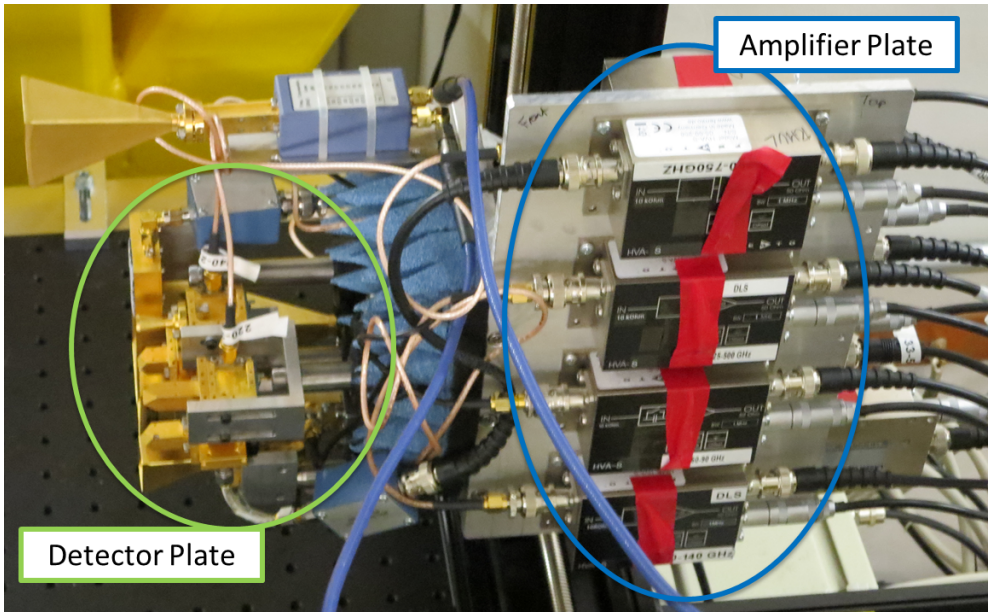


Figure 3.17: The two plates of the SBD array attached together perpendicularly and fixed to one arm of the motion stage.

bands of the detector array through. Furthermore, there are no spectral absorption features observed and across the relevant ranges the transmission is fixed.

To ensure the SBD operates in a high impedance set-up, each detector is terminated in its own voltage amplifier with an input impedance of 10 kΩ. These amplifiers are custom made by FEMTO, Germany (HVA-S Switchable Gain) and have a dual purpose because they provide a high impedance set-up but also boost the signals. The latter is important because these signals must traverse approximately 30 m of cable and would become very noisy as the signal is being attenuated. As discussed in Section 3.2.1 below, to accommodate a good signal-to-noise ratio around the revolution frequency, the cable capacitance must be low as the input impedance is high. In order to lower the capacitance shorter cables were used, thus a plate housing the amplifiers was attached to the detector array allowing for minimal cable length [92]. The perpendicular attachment between the detector plate and amplifier plate is shown in Figure 3.17. Following the voltage amplifiers the signals are carried out of the tunnel, where they are fed into a simultaneous 16-channel sampling digitiser.

### 3.2.1 Cable Capacitance

As a result of this high impedance regime, the capacitance of the cables becomes very significant. There are two methods to alter the effect of capacitive loading of the cables, both of which were employed here. The primary and most drastic change was to choose shorter cables. By removing the original cables and implementing shorter ones, the sensitivity was improved by a factor of four. The secondary alteration was to use cables with a lower capacitance. The desire for a low cable capacitance is especially important when dealing with large impedances because of the relationship between the two as depicted in the RC time constant. This time constant, also known as $\tau$ is the time for the decay of a voltage in an RC circuit and is expressed as

$$RC = \tau = \frac{1}{2\pi f_{cut}}, \tag{3.1}$$

where $f_{cut}$ is the cut-off frequency. Figure 3.18 simply depicts the diode, cable and voltage amplifier as a circuit diagram. The central part of the diagram, represent an RC series circuit, where the capacitor (C2) with capacitance (C2) represents the cable's capacitance and the resistor (R1) with resistance (R1) symbolize the input impedance of the amplifier. The desired signal to measure is the voltage across the resistor, $V_{R1}$, and for it to be as close to the input voltage $V_{(RC)in}$ however the voltage across the capacitor, $V_{C2}$, affects this. According to the following relation $V_{R1} = V_{(RC)in} - V_{C2}$, thus the larger the voltage across the capacitor is, the less $V_{(RC)in}$ is equal to $V_{R1}$. From the expressions of $V_{C2}$ and $V_{R1}$ in Equations 3.2 and 3.3, it can be seen that when $R1 = C2$, some voltage is lost across the capacitor with the rest of $V_{(RC)in}$ becoming $V_{R1}$. However, when $R1 << C2$, $V_{C2}$ becomes equivalent to $V_{RC-in}$, thus $V_{R1}$ becomes negligible. This is most significant in high impedance regimes because the discrepancy between the resistance (impedance) and the capacitance is at its largest.

$$V_{C2} = V_{(RC)in}(1 - e^{-t/R1C2}) \tag{3.2}$$

$$V_{R1} = V_{(RC)in}e^{-t/R1C2} \tag{3.3}$$

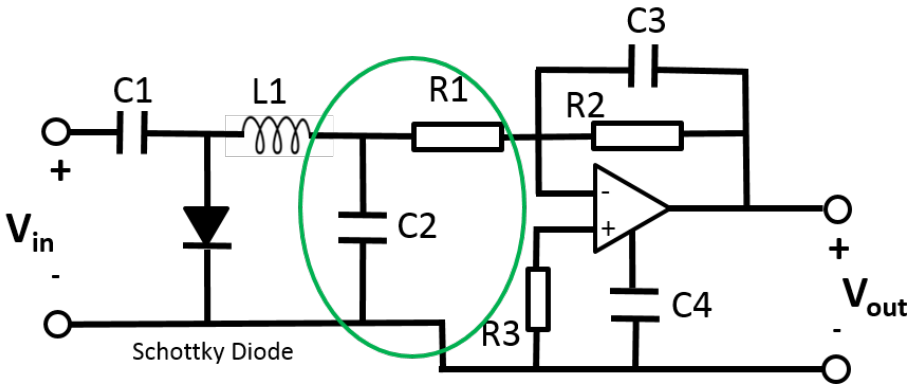


Figure 3.18: A circuit diagram showing the diode, cable and amplifier, where the RC series circuit (low pass filter, highlighted in green) simply represents the circuit between the SBD diode and the input impedance of the voltage amplifier.

The cables used were of length 0.25 m with capacitance 96 pF/m, giving an RC time constant of $2.4 \times 10^{-7}$ s. The junction capacitance of the SBDs implemented is approximately 35 fF, significantly less than the cable capacitance of 24 pF. The diodes themselves also contribute capacitance in the form of junction capacitance. However, the cable's capacitance is much larger than the diode's junction capacitance and thus makes the junction capacitance negligible and the cable capacitance significant.

### 3.2.2 Installation of Detector Array

The table for millimetre investigation had previously been installed at Diamond. It is placed at appropriate height with respect to the beamport fused silica window as shown in Figure 3.4. Its entire surface is a breadboard upon which a three-way motion set-up is attached. The first step was to install the detector array, upon the motion stages procured from BiSlide Velmex Inc. This was executed by fixing the detector plate directly onto the mounting plate of the stages enabling the amplifier plate attached to the detector plate to be perpendicular as shown in Figure 3.17. Though the stages have a wide range of movement along the x-, y- and z-axes, due to the close proximity to the storage ring itself movement at particular points is limited. It must be noted that originally the detector array only contained six detectors, covering the range of 33-500 GHz. Due to preliminary results a seventh detector was purchased in order to probe higher frequencies. This new addition covers the range of 500-750 GHz. The quasi-optical detector (100-1000 GHz)

was also added to the array when it was not required anymore by its previous experiment.

The amplifier plate was fixed at right angles to the detector plate in order to keep the cable lengths between the detectors and amplifiers at a minimum. Power supplies were connected to each of the amplifiers and then plugged into nearby sockets. The data signals from the amplifiers were fed into a patch panel which would allow the signals travel to a corresponding patch panel in the appropriate Control and Instrumentation Area (CIA).

### 3.2.3 Preparation of Detector Array

A variety of raster scans were obtained in a range of beam conditions. These scans involved the detector array collecting data in the x-y plane at various z positions, where z is the axis determining the longitudinal distance from the beamport window. The aims of the scans were to determine the beam growth as it goes farther and farther from the beamport and also to view the beam as a whole (Section 4.4).

From these raster scans the optimal position for the detector array to be placed for each longitudinal position was ascertained using the mean (Fig. 3.19, top) and standard deviation (Fig. 3.19, bottom) across all eight detectors. The images show the average signal or standard deviation of the mean of the eight SBDs at each xy position for one z location. Examples of the original raster scans used to establish the mean and standard deviation are shown in Figures 4.20 and 4.21. The optimal position was determined by taking into account each of the eight detectors and what they observed at the different positions with each detector normalised to itself. Determining the ratio between the mean (Fig. 3.19, top) and standard deviation (Fig. 3.19, bottom) shows where the least variance is (Fig. 3.20, top). To ensure that this was the correct approach, several more stringent ratios were investigated including the mean over the cubed standard deviation (Fig. 3.20, bottom). However from Figure 3.20 (bottom), it can be seen that the only suggested area where all detectors saw the same amount of signal was where none were observing signal and can therefore be concluded that only the mean over standard deviation need be taken into account.

Accordingly, for other non-raster scan experiments namely current ramps, the SBD array was placed at these optimal positions, one place for every longitudinal (z) position. For the longitudinal position of z=-330 mm, i.e. furthest from the source, the (x,y) coor-

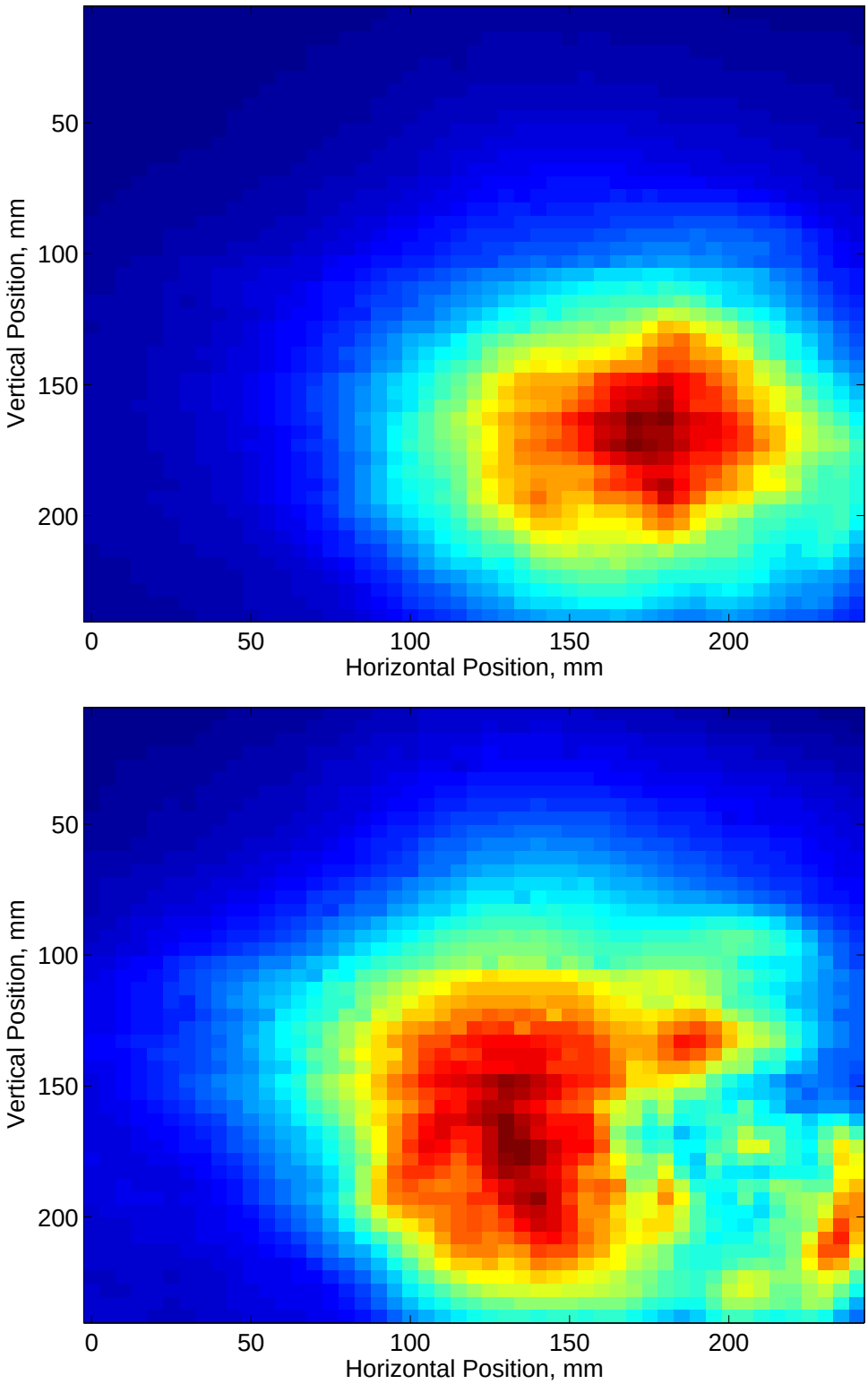


Figure 3.19: On the top image, the mean signal over all eight SBDs is depicted, where red shows the higher agreement of mean values across all the SBDs. On the bottom image, the standard deviation with respect to the mean for the eight SBDs, where blue represents the lowest standard deviation of the mean across all the SBDs. The horizontal and vertical positions are with reference to the SBD plate position.

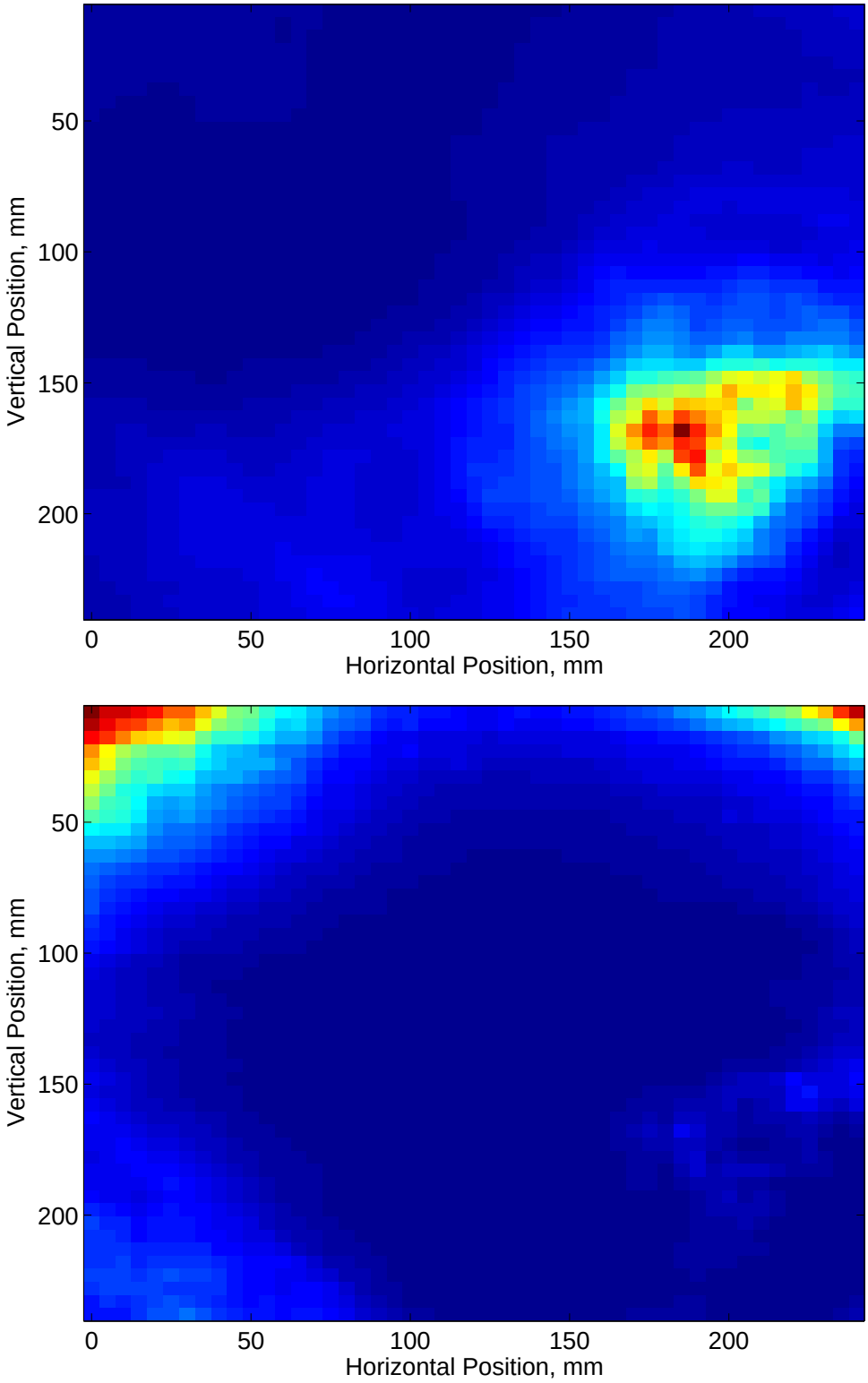


Figure 3.20: On the top image, the ratio of mean over standard deviation, where red depicts the smallest differences between the mean and its standard deviation. On the bottom, the ratio of mean over cubed standard deviation, again with red showing the smallest differences between the mean and its standard deviation. The horizontal and vertical positions are with reference to the SBD plate position.

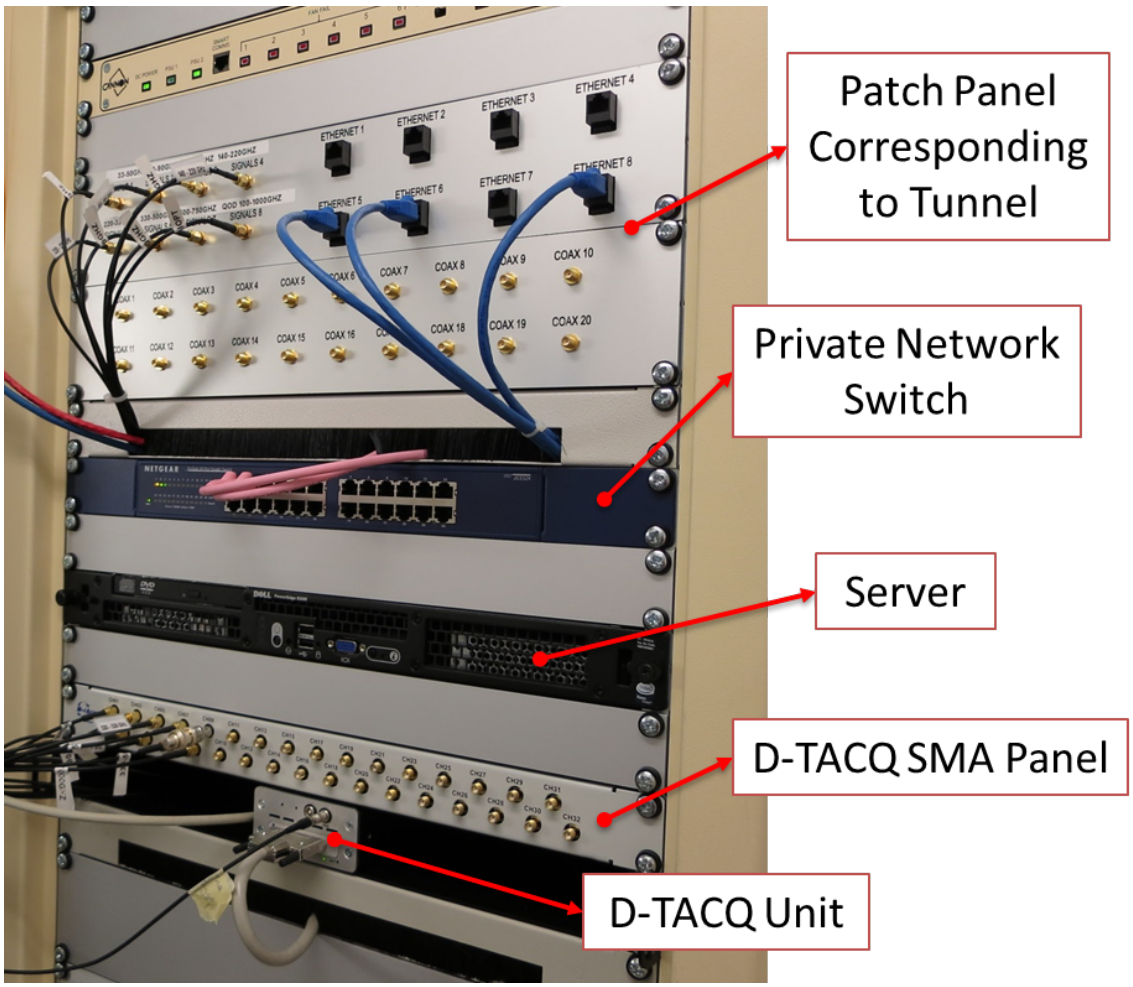


Figure 3.21: A view of the relevant rack in the CIA, housing the data acquisition hardware.

dinates were found to be (185 mm, 168 mm), where the units in all cases are defined by the motion stages.

Due to the nature of these raster scans, they are time consuming and thus could not be carried out all the time. Moreover, the scans showed reproducibility and thus when data were obtained just at one position a map of the beam could be determined showing what the array would have seen had it carried out a raster scan.

### 3.2.4 Data Acquisition System & Capturing Data with SBD Array

The apparatus for the data acquisition includes a 16-channel simultaneous sampling 1 MSPS digitiser from D-TACQ Solutions Ltd., a server and network switch, all displayed in their rack in Figure 3.21. The data are streamed continually from the detectors directly into the ADC (analogue to digital converter). The ADC then sends them to the server whereby the

Area Detector Framework is operating in conjunction with EPICS. The procedure carried out by the data acquisition system is given in the schematic in Figure 3.22. Set by the Area Detector Framework the ADC feeds in $10^5$ samples at a time. The framework is capable of assessing sixteen channels (16 x 100000) and thus the first step carried out is to reduce the data collected to eight channels, one for each detector (8 x 100000). This framework is primarily used to deal with images nevertheless, here it carries out Fourier transforms along every ten stacks of data, where a Fourier transform is expressed below,

$$X_k = \sum_{N-1}^{n=0} x_n e^{i2\pi kn/N} \tag{3.4}$$

A region of interested (ROI) is then chosen. The ROI is set up similar to a lock-in amplifier whereby the framework *locks* into the revolution frequency of the ring, 533.820 kHz. By locking-in, very small signals can be detected despite the presence of noise, as a side note the amount of data to be transferred decreases. As the digitiser has a sample rate of 1 MSPS, the Nyquist frequency lies at 500 kHz where the Nyquist sampling theorem states the sampling frequency must be at least twice signal's highest frequency to allow for the signal to be accurately reconstructed. Consequently, there is only 33.820 kHz of a gap between Nyquist and the chosen 'lock-in' frequency. To counteract this issue, the sampling rate of the digitiser was reduced and thus allowed for a larger difference between Nyquist and the revolution frequency. The optimal sampling rate was decided upon by taking into account the revolution frequency, the doubled revolution frequency, the tripled revolution frequency and each of their corresponding aliases. As depicted in Figure 3.23, for a range of sampling clock dividers ('*clkdiv*') by plotting the distance between the aliased revolution frequency bin and Nyquist bin, then to the doubled revolution frequency bin and finally the distance to the tripled revolution frequency bin, a point of intersection can be determined. This point of intersection signifies that the Nyquist frequency bin occurs at the same point of the double revolution frequency bin for a certain *clkdiv*. As there was no intersection involving the red curve, for this selection of clock dividers the only bins to consider are the aliased revolution frequency bins to the Nyquist bin and the aliased to the double revolution frequency bin. The cross-over is shown in more detail in Figure 3.24 and can be seen to be between *clkdiv* equal to 112 or 113. This resulted

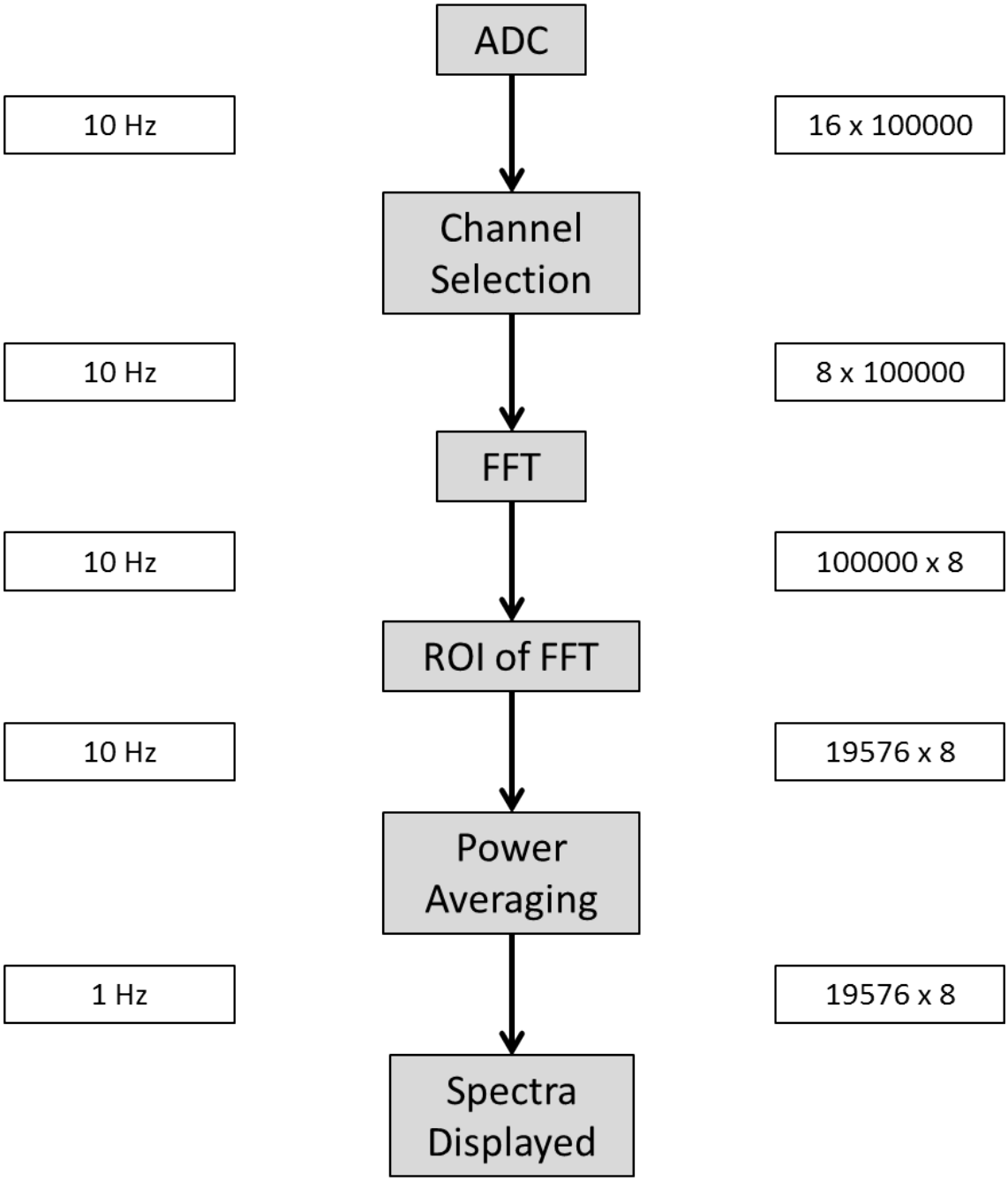


Figure 3.22: A flow-chart showing the steps of the Area Detector Framework implemented for the data acquisition system of the eight channel spectrometer for a sampling frequency of approximately 892857 Hz where the sample frequency is denoted on the left and the size of the data arrays on the right.

in a *clkdiv* of 112 being chosen and this gives a sampling frequency of 892857.1429 Hz, presented in Equation 3.5. This reduction in sampling allows for a much wider bandwidth of 87391.43 Hz as opposed to 33820 Hz when $clkdiv = 100$. Naturally with the change in sampling frequency, the ROI must be edited in order to capture the larger amount of signal now available.

$$\frac{100 \times 10^6}{clkdiv} = \frac{100 \times 10^6}{112} = 892857.1429\ Hz \tag{3.5}$$

As power is the only parameter conserved in noise, power averaging was implemented. Power averaging is executed upon every ten $19576 \times 8$ data arrays resulting in 1 Hz resolution, illustrated by Figure 3.25. The averaging is done on frequency data but over time.

Data were captured when no beam was present in the ring in order to obtain a noise floor for each of the diodes and to make sure nothing else was being picked up by the SBD array. Depicted in Figure 3.26 the signal obtained (or lack there of) by the SBDs with no beam (lines) was comparable to that seen when the SBD array was meant to be acquiring signal but due to a insignificantly low beam current signal could not be observed until a threshold was surpassed (dots).

The position of (185, 168, -330) mm was the optimal and thus most used location for the detector array to be placed, unless raster scans were being carried out. The synchrotron light source was set to the desired conditions; single bunch or multi-bunch, normal user optics or low-alpha optics and the SBD array collected the data. The signal observed from the viewport was guided into the detectors via their horn antennas or silicon lens in the case of the QOD, it was then converted into a voltage and travelled by coaxial cables to their respective amplifiers. The FEMTO amplifiers housed on the amplifier plate adjacent to the detector plate, boosted the signals by a factor of 100. These amplified voltages then traversed $\sim$30 m of coaxial cables whereby each detector's cable was patched into the SMA plate of the digitiser. The D-TACQ digitiser samples the data continually and feeds them directly into a nearby server via gigabit ethernet. The server carries out preliminary processing. After this, the user collects the data and executes the thorough analysis.

The major benefit stemming from the implementation of this data acquisition sys-

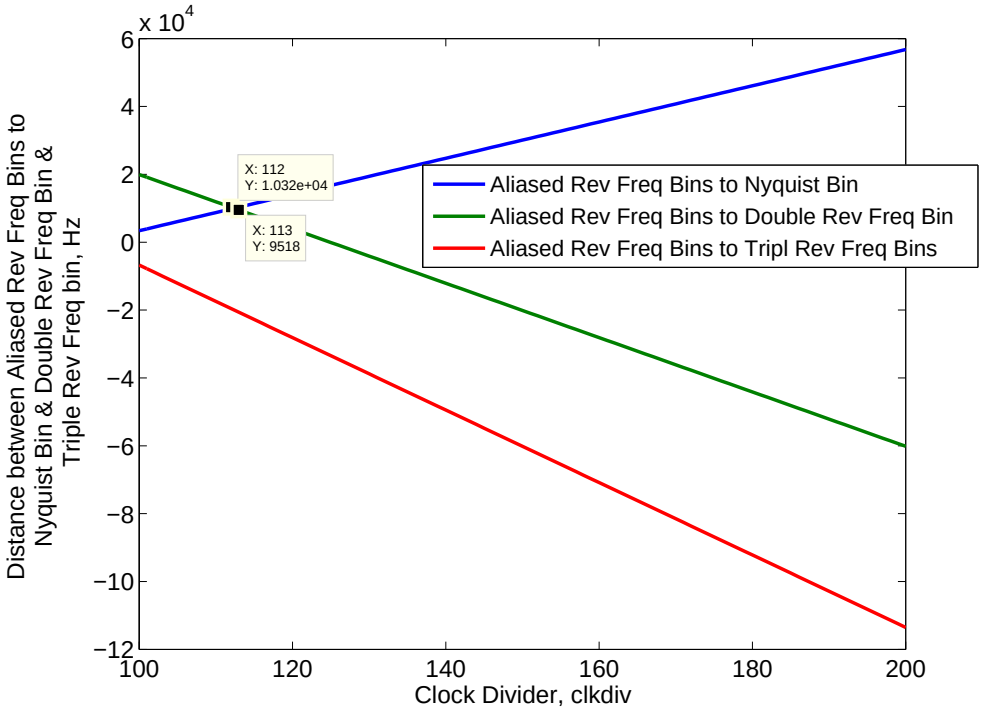


Figure 3.23: The distance between aliased revolution frequency (rev freq) bins to Nyquist.

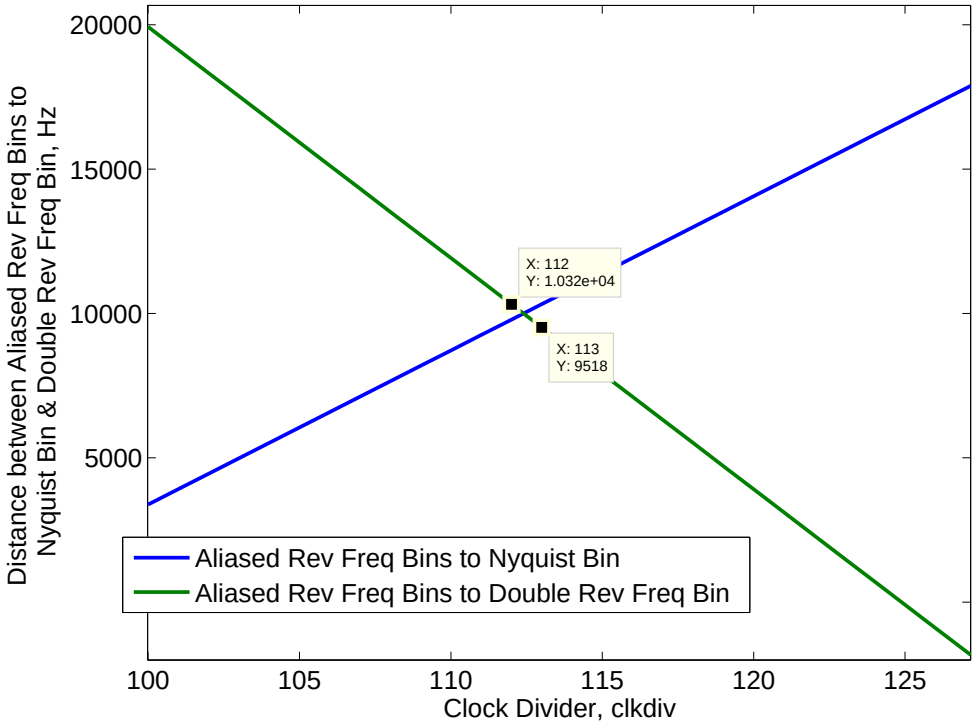


Figure 3.24: A closer look at the crossing between the aliased and double aliased frequencies.

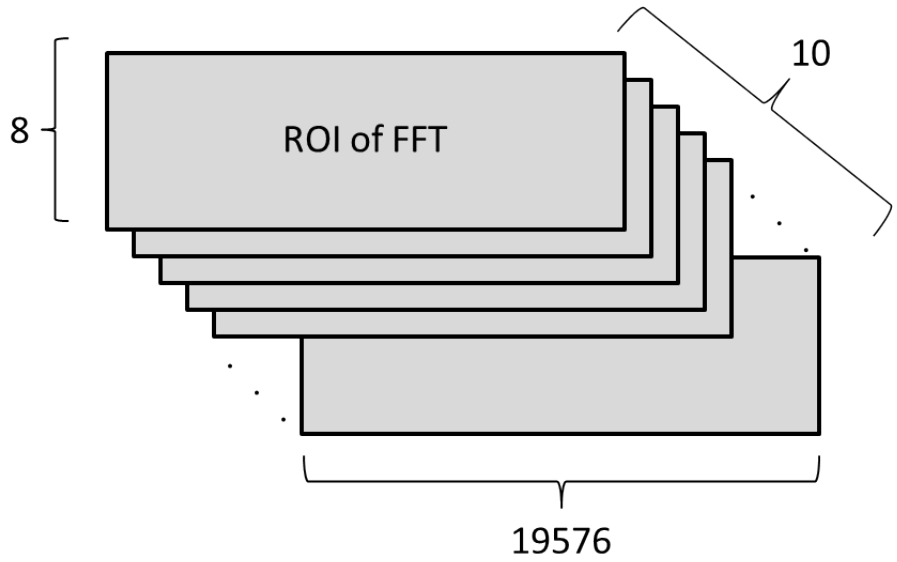


Figure 3.25: A sketch of the power averaging carried out over every ten stacks of 19576 x 8 arrays of the ROI of the Fourier transformed data.

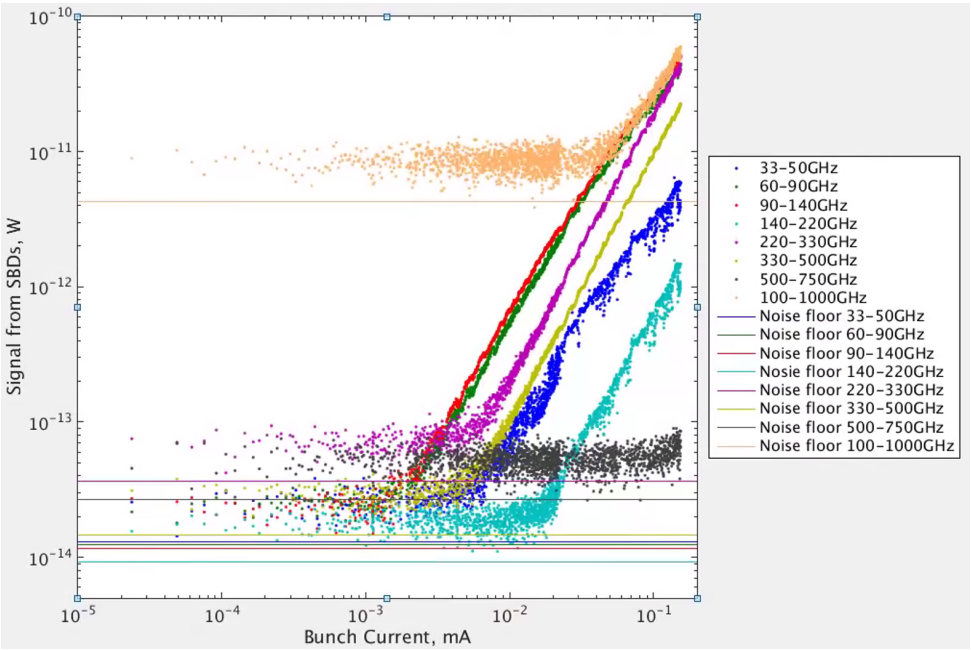


Figure 3.26: Signal obtained by each detector of the SBD array when the beam was present (dots) and the determined noise floor for each of the eight detectors (lines).

tem is the ability to quasi-live stream the Fourier transformed data, meaning that any changes to the spectrum can be seen almost exactly when they occur. This feature was useful not only for this work, but also in confirming hypotheses to the operation of the ring. The effect of moving collimators and insertion devices on the millimeter spectrum could be determined via the SBD array and its acquisition system, the results of which are shown in Section 4.10.

#### *a)* Comparison of Signal at DC and Revolution Frequency

There are two possible locations where the Framework can 'lock-in' and thus retrieve the signal from the diodes. These locations are at DC and the revolution frequency of the ring (533.820 kHz). As stated above in Section 3.2.4, the latter was chosen because of the signal-to-noise ratio (SNR) at that point. SBDs as well as other diodes suffer from 1/f (flicker) noise. Therefore at increasingly lower frequencies the noise experienced by the diode is enhanced.

#### *b)* Magnitude & Power Averaging

Prior to the power averaging feature being installed, magnitude averaging was carried out. Magnitude averaging signifies that a mean was taken of the magnitudes of the signal. The power averaging feature squares the data, averages the result and then takes the square root. Power averaging is preferred because power is the only parameter conserved in noise. With respect to the results portrayed throughout this thesis, the majority of the data was obtained when the power averaging feature was enabled. However, whenever magnitude data is shown, it will be clearly specified.

## 3.3 Detectors

Two types of detectors are employed in this work. Both sensitive to millimetre and sub-millimetre wavelengths, they are Schottky barrier diodes (SBDs) and a Thomas Keating absolute power meter. The former make up the spectrometer and thus observed the CSR from Diamond's B06. The Thomas Keating power meter was used on the test bench to

characterise the bench apparatus and most importantly each of the SBDs. In this section the diodes are described as well as the detectors' applications in the presented work.

### 3.3.1 Schottky Barrier Diodes

The SBD is the key piece of apparatus for this research, procured from Millitech Inc. and Virginia Diodes Inc. (VDI), USA. SBDs have a metal-semiconductor junction whereby a metal contact is deposited upon the semiconductor [99]. It is as a result of their semiconductor-metal junction that gives them ultra-fast switching because the junction does not possess any minority carriers and thus does not need to wait for the recombination of them [30]. Their current-voltage (IV) characteristics are explained by Equation 3.6.

$$U_{DC} = n\,U_T\,ln\Big(\frac{I_{DC}}{I_S}+1\Big)\;+\;R_S\cdot I_{DC}, \tag{3.6}$$

where $U_{DC}$ is the junction voltage, $n$ the ideality factor, $U_T = \dfrac{k\,T}{e_0}$ the thermal voltage, $k$ the Boltzmann constant, $T$ the temperature, $e_0$ the electron charge, $I_{DC}$ the diode current, $I_S$ the (reverse) saturation current and $R_S$ the series resistance. Assuming a room temperature of 300 K, $U_T$ equals approximately 26 mV. The ideality factor ranges from 1-2 where unity is the most ideal. A well-made diode should have an ideality factor of less than 1.20 [99].

Named after the German physicist, Prof Walter Schottky, these diodes are best known for their fast response [30, 100], low noise and excellent sensitivity. Operating at room temperature, SBDs are sensitive to mm- and sub-mm-wavelengths and hence are often used as detectors within this wavelength range [92]. SBDs are able to observe a wide range of frequencies in the GHz - THz regions however their bandwidths can be restricted as a result of their packaging, e.g. waveguides. The detector diodes that have been chosen are housed within waveguides and fed signal using horn antennas. This naturally limits their frequency range with a hard cut-off at the lower frequencies and reduced effectiveness at higher frequencies. As a result of their waveguide packaging, these SBDs are sensitive to polarisation. SBDs perceive the electric field (E-field). When terminated with a low impedance (typically 50 Ω) the SBDs operate at a much faster speed approximately 250 ps [15] but at the cost of lower sensitivity. Using Ohm's Law of $V = IR$, we know

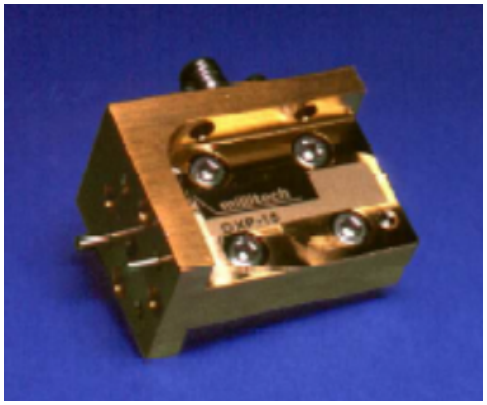

Figure 3.27: Image of a DXP detector from Millitech [101].

Figure 3.28: Image of a DET detector from Millitech [102].

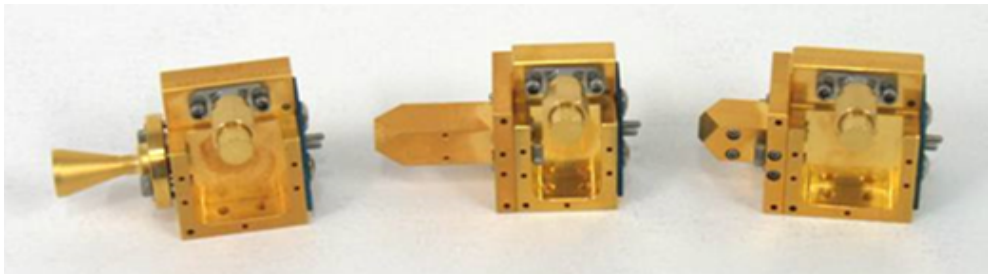

Figure 3.29: Three VDI detectors (WR5.1ZBD, WR3.4ZBD, WR2.2ZBD) with their accompanying conical and diagonal horn antennas [103].

that when an SBD experiences a higher resistance (input impedance) a larger voltage will have to be drawn compared to if a smaller resistance was present for the same current and so for the same input signal the output depends on the impedance encountered. In the set-up as described in this thesis, the SBDs are connected to a high impedance (10 kΩ) and thus achieve a higher sensitivity at the compromise of a slower speed [92]. Two examples of the Millitech Inc. SBDs employed in this thesis are shown in Figures 3.27 and 3.28 (without their antennas), where the casings around the diodes are gold-plated and the SMA connections are visible. Three of the frequency restricted VDI detectors and accompanying horns are shown in Figure 3.29, with the broadband QOD displayed in Figure 3.30.

SBDs are non-linear devices and are well known for their square-law detection Within the square-law region, the diode responds to the square of the voltage across the junction so the detected signal is a function of power [104]. At low input power levels, SBDs detect within the square-law region however at a certain criterion the detection re-

Figure 3.30: An image of the quasi-optical detector from VDI [103].

gion will undergo a transition from square-law to linear. The top image of Figure 3.31 shows the stages of signal detection for a typical diode at a given input impedance. The criterion that changes the detection regime from square-law to linear occurs is if too much power is inputted (commonly >-10 dBm) i.e. when the junction voltage ($U_{DC}$) is greater than the thermal voltage ($U_T$) which is usually 26 mV. It is known that the input impedance affects the input power to output voltage relationship. The effect of the square-law detection on the operation of the SBD array means that the signal being observed has to be below this 26 mV to allow the diode to detect as expected. With an increase in load impedance the sensitivity of a diode also increases as illustrated in the bottom image of Figure 3.31 for a Millitech Inc. diode. The responsivities for five alternate values of load impedance are plotted showing the relationship of impedance and responsivity. For further examples of a Schottky diode square-law response see [105–111], where they are well described.

Eight zero-biased SBDs, each covering a specific frequency band with stated ranges from 33-1000 GHz were employed. Of the eight detectors chosen, seven are housed within waveguides. The eighth detector is a broadband quasi-optical detector (QOD) with a silicon lens [92]. The three detectors with the lower frequency ranges are supplied by Millitech Inc., while the remaining five detectors are from Virginia Diodes Inc. Table 3.2 shows the properties of the chosen SBDs. The waveguide ranges contrast from the stated frequency ranges because the former is determined by the dimensions of the waveguide itself. The fundamental mode cut off (transverse electric mode, $TE_{10}$) and the lower cut off of the frequency of the next mode are classed as the waveguide range within this work

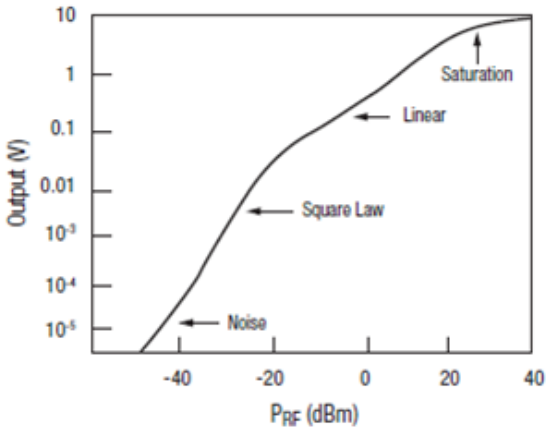


**Figure 12. Detector Output Characteristics**

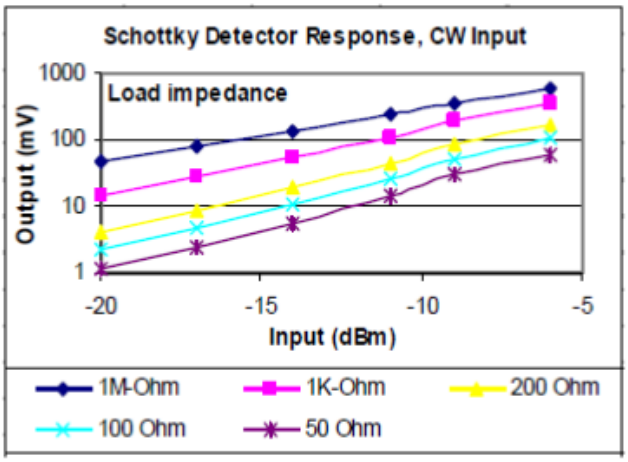


Figure 3.31: Relationship between input power and output voltage [101, 106], where the lower figure is supplied by Millitech Inc., our detector manufacturer.

and are further referred to in Section 3.4.4 and Figures 3.45 - 3.50. The stated range is a subset of the true frequency range.

### *a)* Horn Antennas

Worldwide there are a huge variety of horn antennas available. Horn antennas are used in the emission and reception of radiation, normally in conjunction with waveguide feeds. The radiation patterns for emission are identical to those of reception. In this work, horn antennas are used for the emission during bench tests, and signal reception for all tests and experiments. The three types utilised in this work are the pyramidal horn antenna (Fig. 3.32, top), the conical (Fig. 3.32, bottom) and the diagonal horn antenna. With

Table 3.2: SBD Specifications

| | Model | Stated Range GHz | Waveguide Range GHz | NEP pW/$\sqrt{Hz}$ |
|---|---|---|---|---|
| 1 | DXP-22 [101] | 33-50 | 26.36-52.73 | 632.46 |
| 2 | DXP-12 [101] | 60-90 | 48.41-96.81 | 1998.55 |
| 3 | DET-08 [102] | 90-140 | 73.82-147.64 | 6324.56 |
| 4 | WR5.1ZBD [103] | 140-220 | 115.79-231.59 | 13.2 |
| 5 | WR3.4ZBD [103] | 220-330 | 173.69-347.38 | 17.6 |
| 6 | WR2.2ZBD [103] | 330-500 | 295.28-590.55 | 9.1 |
| 7 | WR1.5ZBD [103] | 500-750 | 393.70-787.40 | 15.2 |
| 8 | QOD [103] | 100-1000 | (silicon lens) | 50-115 |

regards the RF source and its associated amplifiers and frequency multipliers for the calibration (described below Section 3.4.1), only pyramidal horn antennas have been implemented. Seven of the eight SBDs require horn antennas to guide the radiation from free space through the waveguides and across the diode to detect. Pyramidal horn antennas are implemented for the SBDs covering the lowest frequency ranges (33-140 GHz), one conical horn antenna is used to cover the range 140-220 GHz and finally three diagonal horn antennas are employed for the three detectors from 220-750 GHz. The cause for the variety of horns is due to limited availability of the manufacturers, primarily as a result of the difficulty and delicacy needed to machine horn antennas for high frequencies.

Each horn antenna design handles the radiation in a different way and thus each must be individually taken into account. The most appropriate method of doing this is by using the affective aperture, $A_{eff}$ [113–115],

$$A_{eff} = \frac{\lambda^2}{4\pi} G, \tag{3.7}$$

where $G$ is the absolute power gain and $\lambda$ the wavelength of radiation being observed or transmitted. The gain of an aperture can be determined using the equation below [114].

$$G = \eta \frac{4\pi A_{dim}}{\lambda^2}, \tag{3.8}$$

where $\eta$ is the efficiency of the horn antenna and can be defined as the ratio of the effective aperture ($A_{eff}$) over the dimensional aperture ($A_{dim}$) [114]. The dimensional aperture is

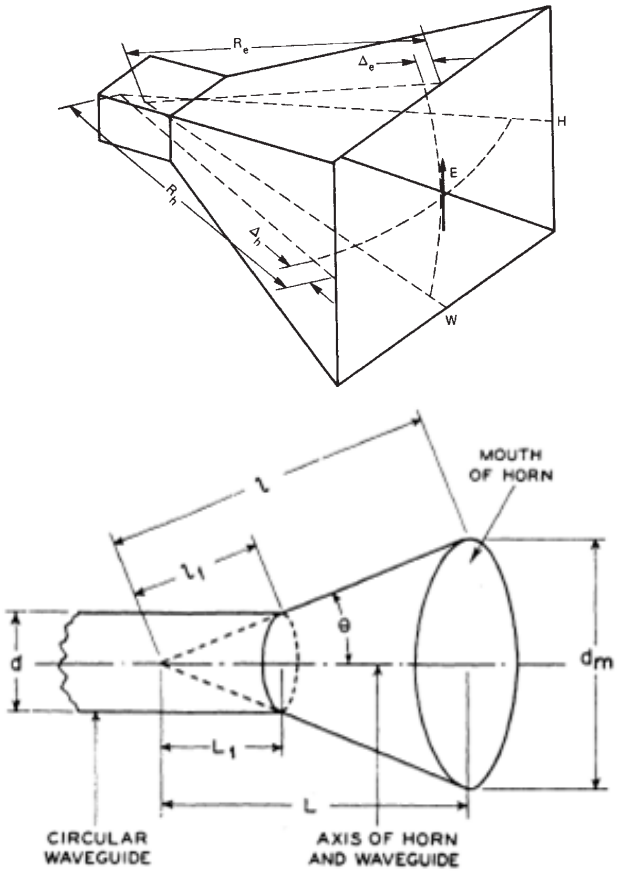


Figure 3.32: Geometry of a pyramidal horn antenna (top) and conical horn antenna (bottom) using the source notation [112, 113].

the area at the opening of the horn, no matter if it is a diagonal, conical or pyramidal horn antenna. It is known that the effective aperture of a conical horn is 52% of the actual aperture when the horn has been designed optimally [113]. Furthermore, with an increase in length of the horn while keeping the aperture area constant this ratio can increase up to 84% for very long horns. In Table 3.3, the comparison between the dimensional and effective apertures are shown, whereby the pyramidal and conical horn antennas all display a value similar to that given by King [113]. Optimal diagonal horn antennas have been known to have an efficiency of 0.81 [114] and thus, are deemed more effective relative to their size than conical or pyramidal horn antennas. The WR2.2 diagonal horn antenna gives a ratio (0.89) close to that of 0.81. Implausibly, the other two diagonal antenna give efficiencies greater than 1. The efficiency of an antenna is dependant on the gain (Eq. 3.7) and the dimensions of the horn's aperture ($A_{dim}$). The beamwidth and consequently gain measurements have been supplied by the company. The aperture

Table 3.3: Horn Antenna Apertures

| **Model** | **Shape** | $A_{dim}$, $m^2$ | $A_{eff}$, $m^2$ | $A_{eff}/A_{dim}$ |
|---|---|---|---|---|
| SGH-22 [117] | Pyramidal | $2.31 \times 10^{-3}$ | $1.15 \times 10^{-3}$ | 0.50 |
| SGH-12 [117] | Pyramidal | $6.85 \times 10^{-4}$ | $3.41 \times 10^{-4}$ | 0.50 |
| SGH-08 [117] | Pyramidal | $2.95 \times 10^{-4}$ | $1.47 \times 10^{-4}$ | 0.50 |
| WR5.1 [103] | Conical | $5.54 \times 10^{-5}$ | $2.99 \times 10^{-5}$ | 0.54 |
| WR3.4 [103] | Diagonal | $3.14 \times 10^{-5}$ | $3.34 \times 10^{-5}$ | 1.06 |
| WR2.2 [103] | Diagonal | $1.30 \times 10^{-5}$ | $1.15 \times 10^{-5}$ | 0.89 |
| WR1.5 [103] | Diagonal | $5.76 \times 10^{-6}$ | $6.49 \times 10^{-6}$ | 1.13 |

where $A_{eff}$ is with respect to the central frequency of the waveguide range, Eq. 3.7.

dimensions have also been provided by the manufacturer but have been verified by the author. Moreover, the waveguide dimensions of the WR2.2 horn have been measured with a ZEISS AxioVision Optical Microscope [116] and is in keeping with what is expected. Therefore it can be deduced that the gain values are the cause of the 100%+ efficiency, attributed to the rounding of values as the gain is supplied with only two significant figures and no error.

### *b)* IV Curves of SBDs

A diode is a non-linear circuit element. An ideal diode will allow current to flow in the forward direction but will block any current trying to travel in the reverse direction. This relation between current flowing through a diode and the applied voltage across its terminals is the main characteristic of a diode. SBDs also exhibit this characteristic IV curve, however it is slightly different from the more common pn-junction curve. The IV relation is depicted in Figure 3.33 for both pn- and Schottky barrier diodes where the variation between the two can be observed and also expressed as in Equation 3.6 for SBDs. Diodes with a pn-junction have a turn-on voltage of approximately 0.7 V while SBDs' turn-on voltage is at 0.2 V, which can be seen relatively in Figure 3.33. Moreover, Schottky diodes have a lower breakdown voltage compared to their pn-junction counterparts. This is due to SBDs containing a metal-semiconductor junction unlike the semiconductor-semiconductor junctions of pn-junction diodes. Moreover, zero-bias SBDs are the most sensitive type as they require a very low forward voltage to operate.

In order to establish that a diode is healthy, the IV curve can be measured and fitted

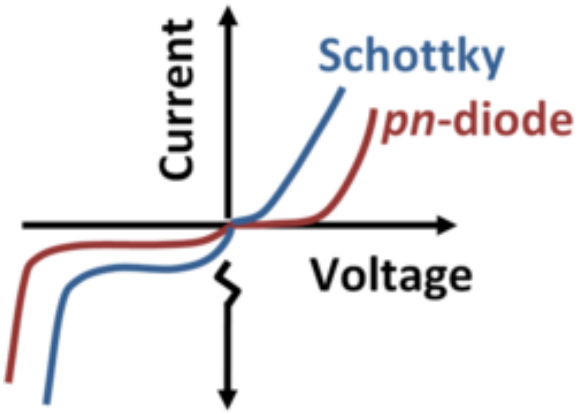


Figure 3.33: Typical IV curve of a Schottky barrier diode compared to a pn-junction diode. (Courtesy of [118])

with a model (Eq. 3.6), i.e. parameters $n$, $I_s$ and $R_s$. This test was regularly carried out to ensure each SBD was not affected by other radiation in the storage ring tunnel. In Table 3.4 and Figure 3.34, a data set for all of the eight diodes is displayed and fitted with the model. It must be noted that though all the diodes used are zero-bias detectors there are two distinct 'families' of diodes present - the Millitech and VDI diodes shown in Figure 3.34 (top) and (bottom), respectively. The lower frequency Millitech Inc diodes have much smaller saturation current, $I_s$, values when compared to the VDI family. Nevertheless, SBDs have much larger values of $I_s$ as against pn-diodes on the whole and zero bias SBDs in particular require a large $I_s$ in order to have enough ability to reach high currents at low voltages. The high frequencies that the VDI diodes reach require large $I_s$ values. Within the Millitech family, the DET08 exhibits a faster growth compared to the DXP22 and DXP12, this can be attributed to the fact that the DET08 is a newer model, works at higher frequencies and is possibly making use of a modified SBD. It is apparent from the results in Table 3.4 that with an increase in $I_s$ there is an increase in $R_s$. The large value of $R_s$ for WR5.1ZBD, WR3.4ZBD, WR2.2ZBD, WR1.5ZBD and QOD can be attributed by the presence of an electrostatic discharge (ESD) safety circuit namely the resistor component. All VDI detectors used contain ESD circuits [119] either built directly into the detector unit or as separate additions. For completion, the Millitech Inc. detectors do not contain any ESD safety circuits and thus their experimentally determined parameters are true to the diode itself [120].

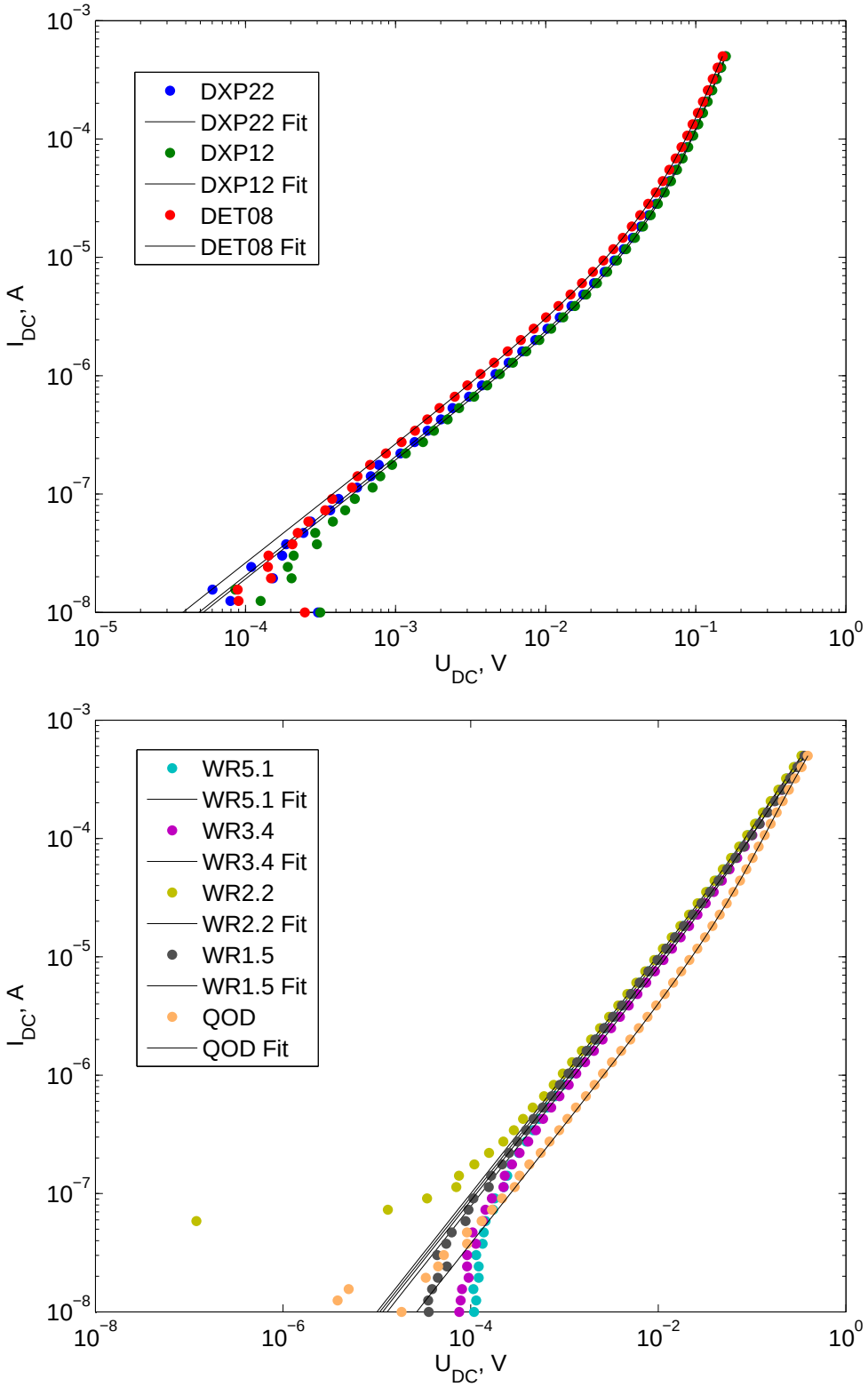


Figure 3.34: Fitted IV curves for the 33-140 GHz detectors from Millitech Inc. (top) and 140-1000 GHz from VDI (bottom).

Table 3.4: Parameters of the SBDs as determined experimentally.

| **Model** | **Stated Range GHz** | $n$ | $I_s$ $\mu$**A** | $R_s$ $\Omega$ |
|---|---|---|---|---|
| DXP22 | 33-50 | 1.23 | 6.54 | 37.7 |
| DXP12 | 60-90 | 1.22 | 6.09 | 37.5 |
| DET08 | 90-140 | 1.23 | 8.42 | 40 |
| WR5.1ZBD | 140-220 | 1.66 | 75.2 | 507 |
| WR3.4ZBD | 220-330 | 1.73 | 56.8 | 499 |
| WR2.2ZBD | 330-500 | 1.61 | 84.9 | 513 |
| WR1.5ZBD | 500-750 | 1.94 | 81.0 | 535 |
| QOD | 100-1000 | 1.88 | 22.3 | 480 |

### 3.3.2 Thomas Keating Power Meter

The Thomas Keating power meter is a broadband detector requiring modulated signal as shown in Figure 3.35. The aperture is of dimensions 65 mm $\times$ 40 mm and sensitive to to approximately 20-3000 GHz. It is between the window panes of the TK power meter where the detection occurs. In between the two window panes, a closed air cell exists within which is a thin metal film [121]. The absorption of the radiation beam causes variations in the temperature of the cell and hence changes in the pressure of the cell. These pressure variations are detected via the pressure-transducer in the TK head and recorded. It is known that approximately 50% of the incoming beam is absorbed by the thin metal film in the window [121]. The remainder of the incident beam is reflected or transmitted through the cell. In order to minimise reflections caused by the windows, the TK head must be used at the Brewster's angle. Brewster's angle is defined as the particular angle of incidence at which light is reflected from a surface completely polarised and is 55.5$^\circ$ [121] in the case of the TK's windowing material. The emitted beam from the RF source is polarised due to the waveguide and the E-field has the same orientation as the polarised field. Thus, the orientation of the waveguide (and hence horn antenna) determines about which axis Brewster's angle is used.

The main benefit of the TK power meter is that it can be calibrated by directly inputting a known modulated signal via the BNC connections on the side of the TK head. As a result of this, the TK power meter can then be used to characterise the source (on the test bench) and therefore used in the characterisation of the SBDs also.

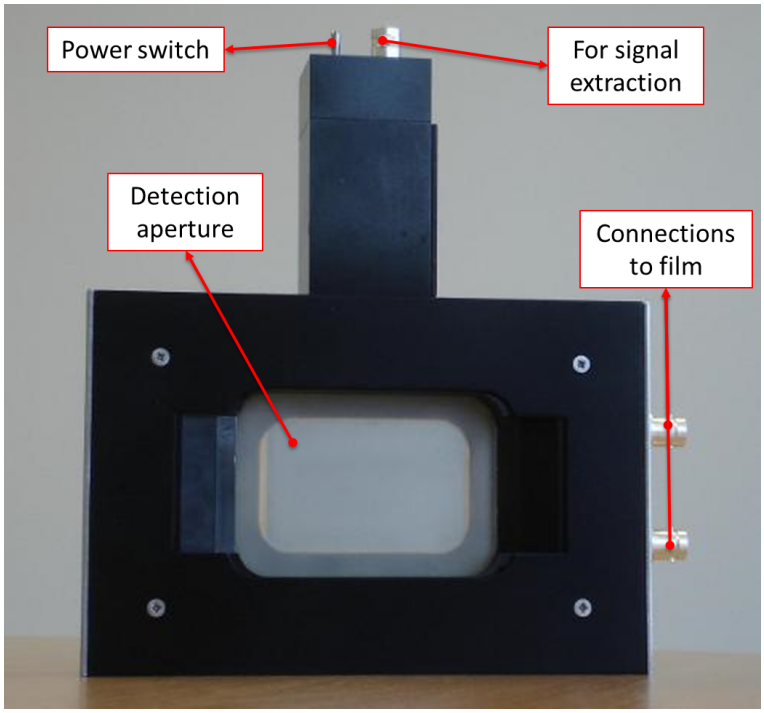


Figure 3.35: A photo of the Thomas Keating power meter [35], showing the detection aperture, BNC connection for signal output on the top and two connections on the side for the film.

## 3.4 Test Bench

The test bench is the optics table housing all the equipment necessary for the creation and quantification of the detector array as displayed in Figure 3.36. In this section the use and evaluation of the primary components is described. Following from the characterisation of the test bench apparatus itself, the detector array was developed and tested. The results are included below.

### 3.4.1 RF Source

The Ka band emitter (26.5 GHz - 40 GHz) is the radio frequency (RF) source used on the test bench to produce a signal with which the SBDs are quantified. The RF source employed is shown in Figure 3.37. The emitter employs a Gunn diode to produce the output frequency. The Gunn diode within this emitter produces frequencies in the range of 13 GHz - 20 GHz and, before it is transmitted from the source unit, the signal passes through a doubler, thus creating a Ka band emitter. This emitter has two methods to vary

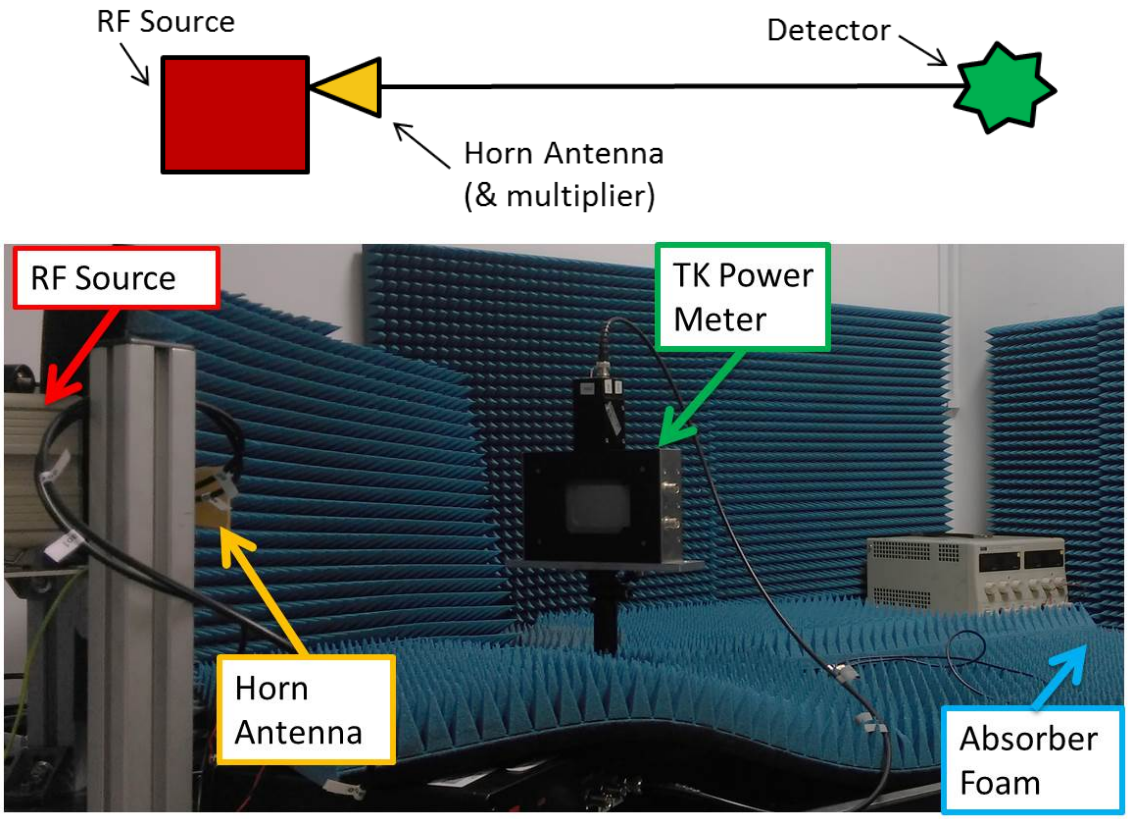


Figure 3.36: A schematic and photograph of the Test Bench set-up.

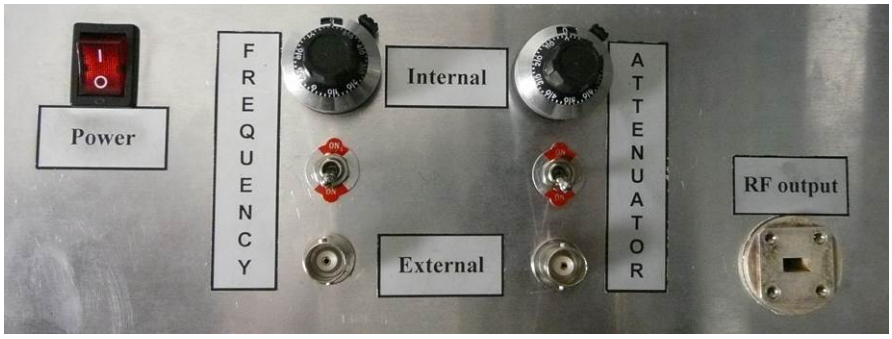


Figure 3.37: Ka Band Emitter

Table 3.5: Frequency Multipliers

| Model | Type | Input Frequency | Output Frequency |
|---|---|---|---|
| MUD-15 [122] | Doubler | 25-37.5 GHz | 50-75 GHz |
| MUT-10 [122] | Tripler | 25-36.67 GHz | 75-110 GHz |
| WR5.1X3 [103] | Tripler | 46.67-73.33 GHz | 140-220 GHz |

the output frequency and attenuation. The output frequency can be determined by the control voltage dial or by inputting a DC voltage via a BNC connection from an external source and the same for the attenuation. The primary method employed was to use a waveform generator to input the voltage for both output frequency and signal attenuation. By using the BNC connection for signal attenuation, the output frequency signal can be modulated. In Figure 3.37, the front panel of the emitter can be seen, along with the dials, BNC connectors and the waveguide connection for the frequency output.

In order to achieve the desired frequency ranges, various frequency multipliers were utilised. The properties of the multipliers are show in Table 3.5. Due to the nature of multipliers, the strength of the signal declines when passing through one (or more). To counteract this continual decrease in signal, an amplifier was used to boost the output power. The amplifier utilised is an AMP-15 from Millitech Inc. with an input frequency of 50-66 GHz and a gain of 22 dB. The combinations of frequency multipliers and power amplifiers are depicted in the schematic diagrams of Figure 3.38, where the orange circles indicate the RF source itself, the blocks the multiplier employed and finally ending with a pyramidal horn antenna. When the frequency is being increased by a factor of six an amplifier is used, shown as a cyan triangle. As for the detector array, horn antennas were employed by the RF source and its relevant multipliers. All of the horn antennas used by the RF source were of pyramidal design.

Each multiplier from Millitech Inc. was accompanied by a data sheet. The power output for each frequency value was given for the stated constant input power. The conversion losses for both MUD-15 and MUT-10 were calculated from these values. Both the experimental data according to Millitech Inc. and the results gathered by the author were combined, as presented in Figure 3.39. It can be seen that there is a good agreement between the data sheet results and those determined on the test bench.

Before detector characterisation could be carried out, the RF source itself had to be

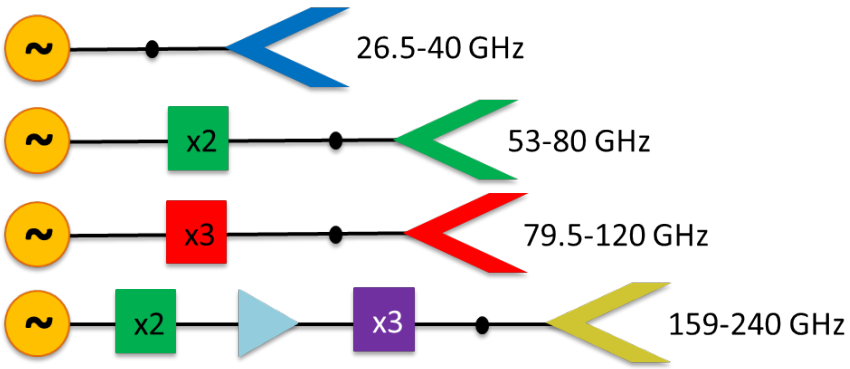


Figure 3.38: Block diagrams of the combinations of source, multipliers, amplifier and pyramidal antenna.

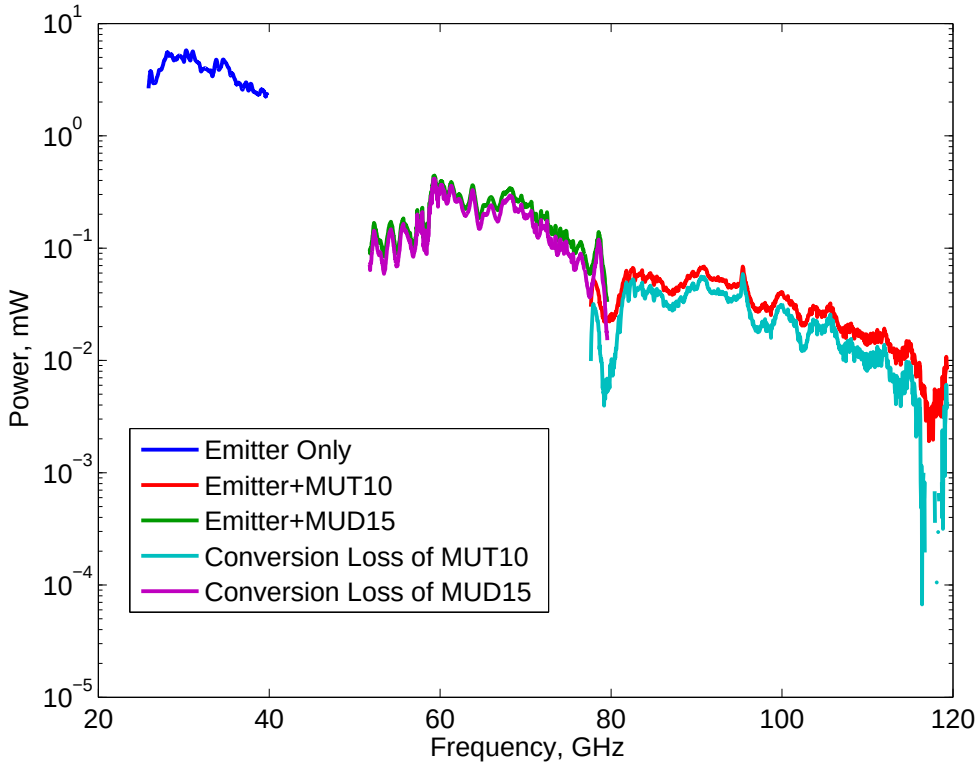


Figure 3.39: Ka band emitter with fundamental, doubler and tripler attached with their respective results from the data sheets.

investigated. Employing a waveform generator, voltage values were fed into the source and the corresponding output frequency identified by the spectrum analyser. Horn antennas were used to transmit the signal from the RF source and then to receive it into the spectrum analyser. For a known voltage inputted into the RF source, the spectrum analyser read the output frequency. From these tests, the resulting relationship between the input voltage and output frequency is depicted in Figure 3.40. This knowledge was then built into the code used on the test bench. Due to the range of the spectrum analyser, the full range of the RF source was unable to be examined. Nevertheless, the remaining values were extrapolated from the experimental data.

To determine the attenuation, the fundamental horn (SGH-28) was attached to the RF source and at a continual output of one frequency value the signal was read by the TK while the voltage controlling the attenuation was altered. Thus the attenuation was ascertained for incremental increases in the inputted voltage. The established attenuation as a function of the inputted voltage is shown in Figure 3.41, where it can be seen that there is a sharp drop off in signal strength after 1 V. The voltage controlling the frequency output was inputted as a square wave using a waveform generator to ensured the signal remained modulated.

The stability of the frequency output was determined using the spectrum analyser with the RF source employing the doubler at an output frequency centered on 79.855 GHz. The consistency of the output frequency was measured in two different cases. In the first, the time required by the source to 'heat up', thus stabilising the output, was found to be 20 minutes. Once warmed up, the consistency of the output could be ascertained for the second case. Six 'snapshots' were taken to illustrate the constant change in the frequency output. Furthermore, an average was also taken over one hundred sweeps. These seven data sets were plotted in Figure 3.42 where it can be seen that the frequency output has an error of $\pm$ 2 MHz resulting in a relative error of 0.005 %, which is excessively low.

### 3.4.2 Test Bench Layout

In the primary set-up, the TK power meter or SBD was placed on the optics bench using a rail system. The RF source stood alone on a stage inline with the rail 50 cm in front of the detector. Depending on the frequencies being investigated a selection of frequency

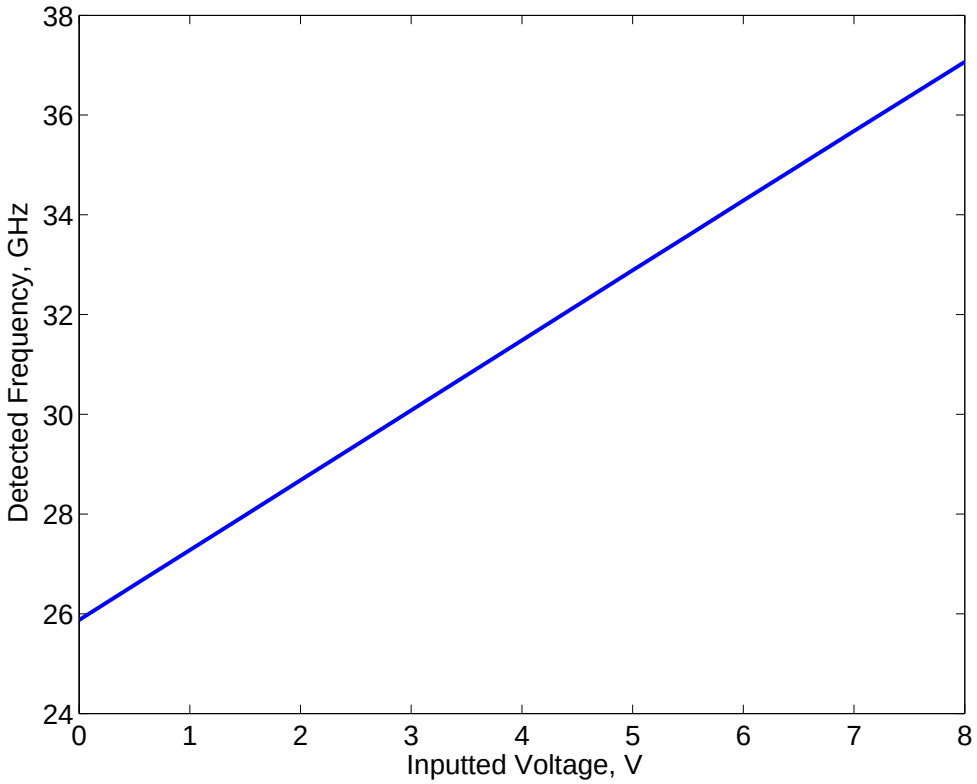


Figure 3.40: Frequency output measured from spectrum analyser when waveform generator inputs control voltage.

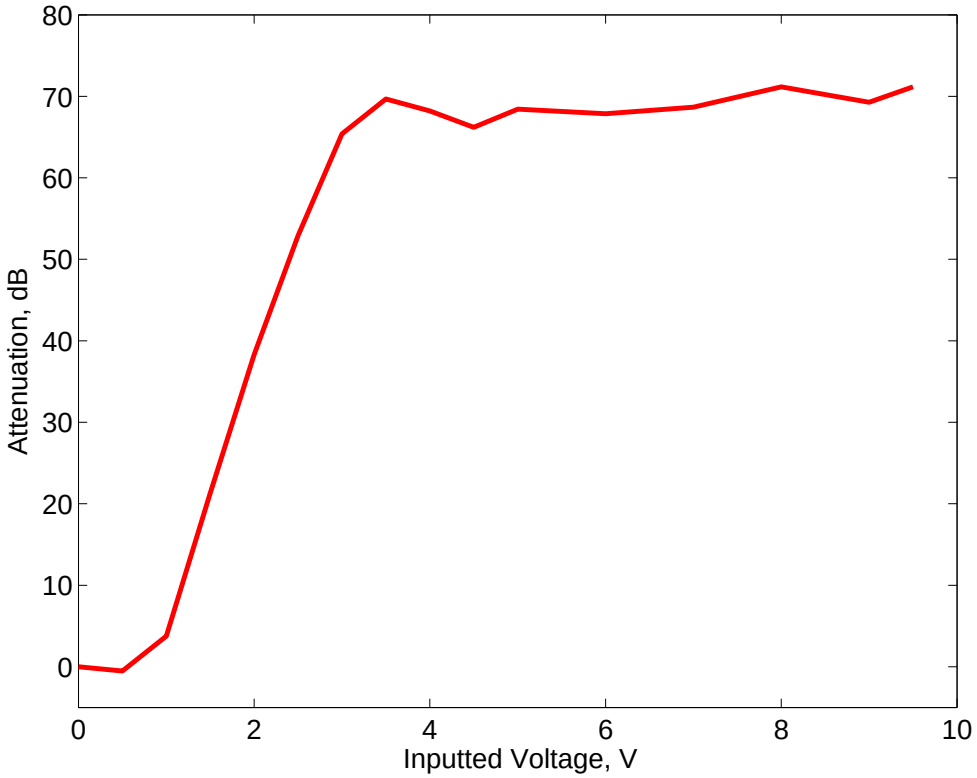


Figure 3.41: Attenuation curve of emitter as measured by TK power meter.

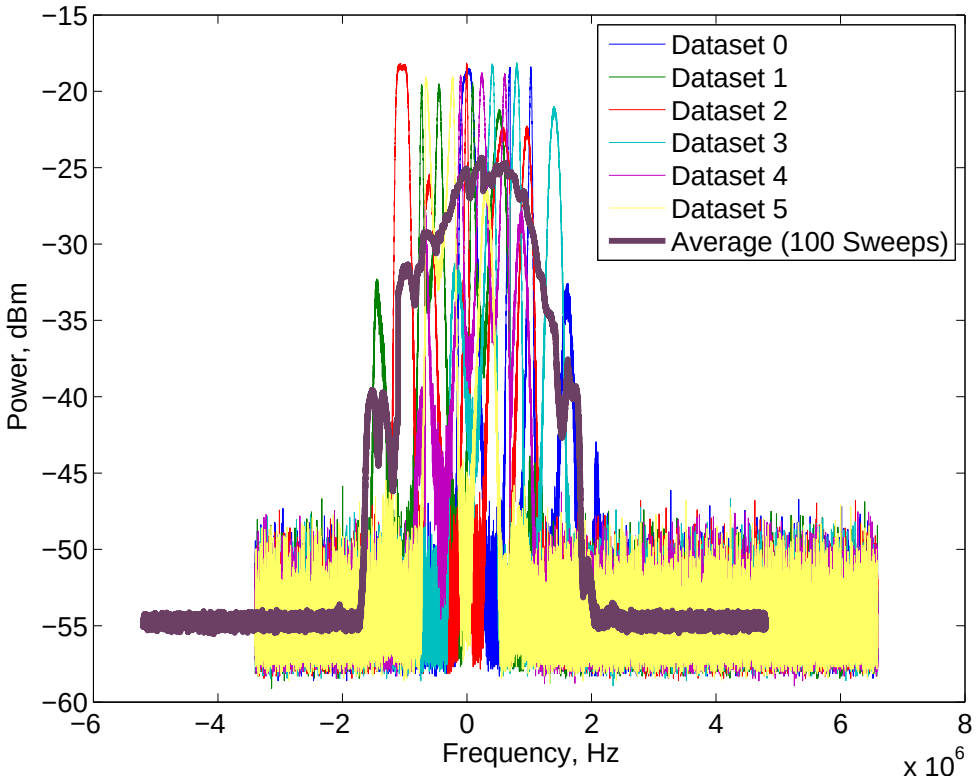


Figure 3.42: Frequency stability of the Ka band emitter showing the $\pm$ 2 MHz instability.

multipliers, power amplifiers and a horn antenna were attached to the RF source. Via its BNC connections, the RF source was connected to a waveform generator. The waveform generator was used to input a DC voltage to alter the frequency output and a square wave to electrically chop the output signal. When required the power amplifier was connected to a voltage supply delivering 9 V to the amplifier. The signal from the TK and SBDs was fed via a coaxial cable from their respective coaxial connector into an ADC with a high impedance. The ADC used for reading the data from the TK and SBDs has two input channels, both with a high impedance but only one channel with an amplifier to boost the signal of the TK. The signal from the SBDs does not require further amplification in the lab. The ADC was supplied with 5 V from a power source, and the data were fed into a computer via USB. As shown in Figure 3.36, the optics bench and the area around the set-up were covered with blue pyramidal absorber foam to minimise the reflections of the mm-wavelengths [112].

### 3.4.3 Data Acquisition on the Test Bench

A private network was created within the lab, encompassing the ADC to readout data, the waveform generators for voltage control and modulation and the computer running MATLAB. All hardware could be controlled using MATLAB. For each data collection, a calibration would be conducted and then a frequency sweep carried out, so that the calibration was fresh and thus more reliable. A software lock-in centered on the modulation frequency (17 Hz) was used to mimic a lock-in amplifier.

### 3.4.4 Main Test Results

Initially, the TK power meter was calibrated and using this information the RF source was quantified over the entire range of frequencies (26 GHz - 240 GHz) using the multipliers and amplifier [92]. This was carried out in several stages. First, a range of modulation frequencies were delivered to the TK and the response was monitored. Using Equation 3.9, where $P_0$ is the peak power, V the voltage inputted and $R_{film}$ the resistance of the TK aperture which was measured to be 166 $\Omega$, the sensitivity of the TK at each modulation frequency was calculated.

$$P_0 = \frac{V^2}{R_{film}} \tag{3.9}$$

By determining the sensitivity of the TK at a range of modulation frequencies and thus the noise, the optimal modulation frequency was identified. Figure 3.43 (top) depicts the sensitivity of the TK, by the voltage detected and the peak power from Equation 3.9, across a range of modulation frequencies. The curve is a smooth decay presenting an increased sensitivity for a lower modulation frequency. The noise was calculated using the standard deviation of the signal received by the TK and the relative sensitivity. Figure 3.43 (bottom) shows the relationship between the noise and modulation frequency as ever fluctuating. From the two plots of Figure 3.43 it can be seen that lower frequencies are more optimal as the TK seems to struggle at high frequencies. Hence, a modulation frequency of 17 Hz was selected as it agreed with the TK but also being a prime number it would be less likely to pick up any noise especially the mains at 50 Hz, that is to say that 17 Hz has minimal harmonics in common with the mains frequency. In Figure 3.44, the power of the signal from the RF source, its various frequency multipliers and horn antenna as

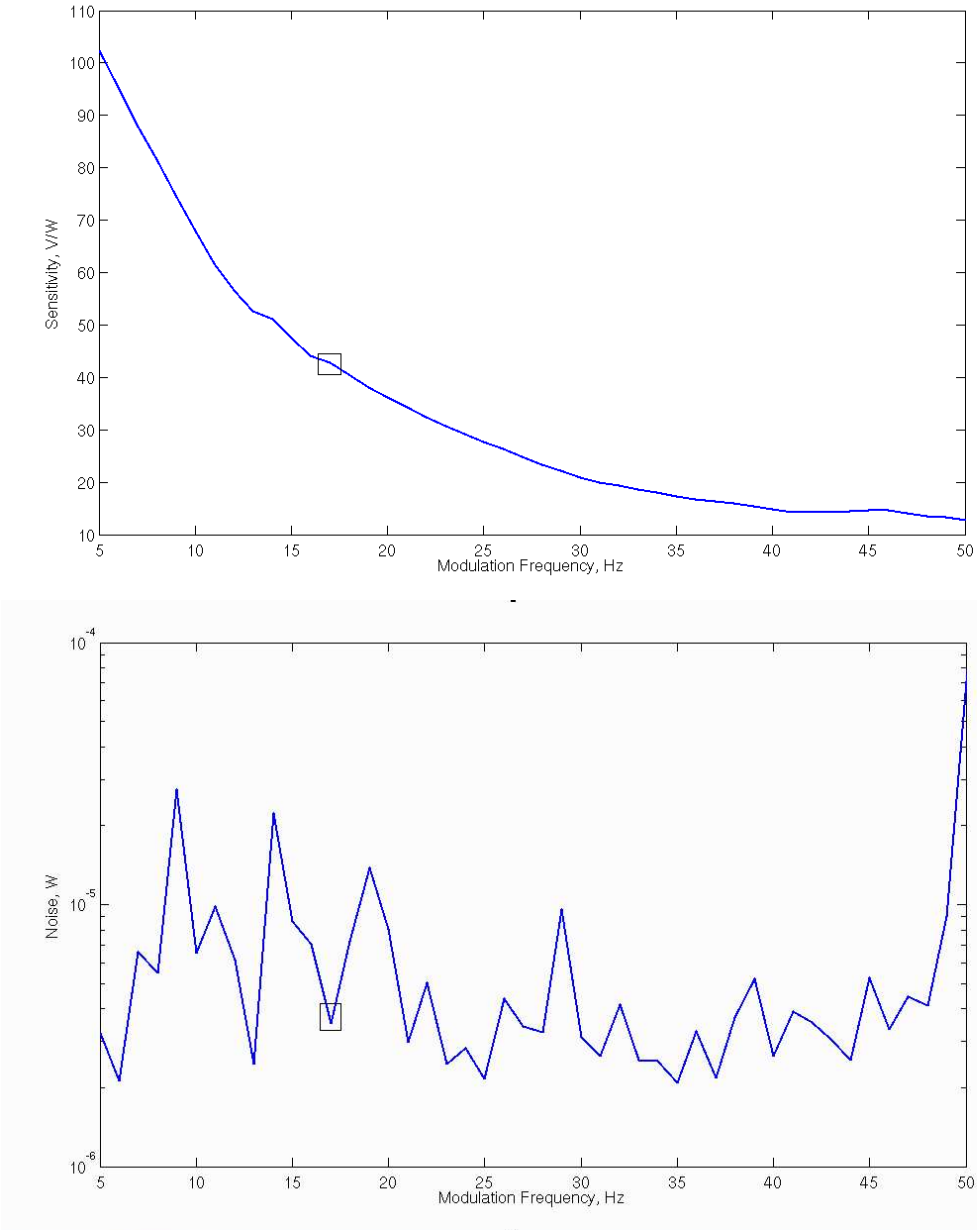


Figure 3.43: The sensitivity (top) and noise (bottom) of the TK detector with respect to a variety of modulation frequencies, where the chosen modulation frequency of 17 Hz is highlighted.

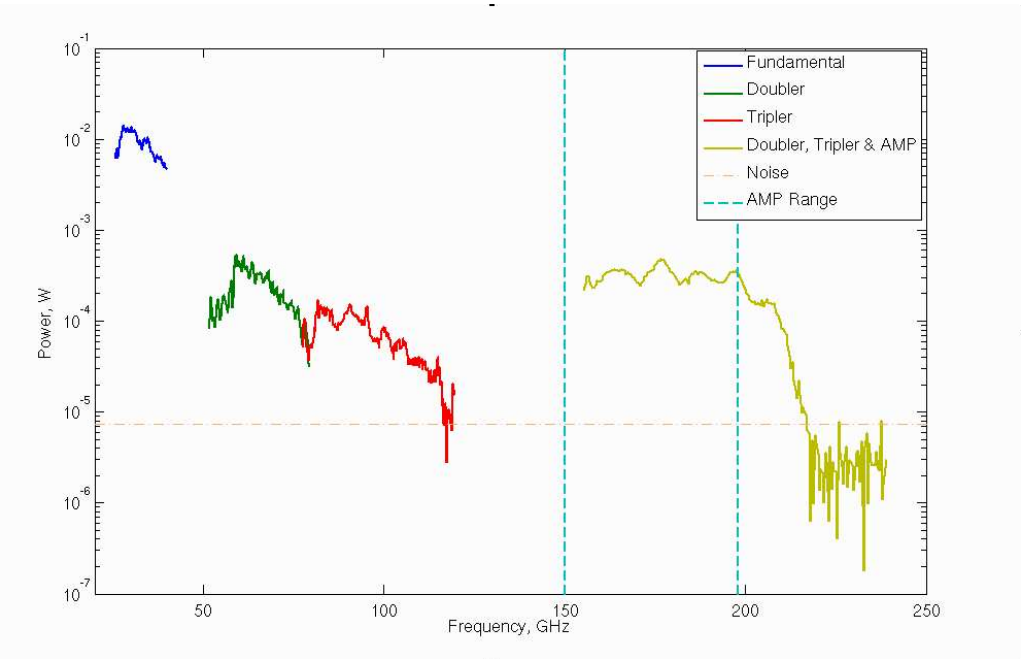


Figure 3.44: Power of signal received by the TK power meter for 26-240 GHz at a distance of 50 cm from the source with amplification on the doubler-tripler combination. The noise of the measurements with the TK as described within set-up.

received by the TK head is presented. The integration time was 1 second. The TK head and the emitter were at a set distance of 50 cm. Each frequency multiplier employed to achieve the desired range is portrayed as an alternately coloured curve. As expected due to the nature of multipliers the power of signal is reduced and thus the fundamental frequency band experiences the highest signal power. In order to minimise reflections, the area in and around the test bench was lined with pyramidal absorber. Furthermore the TK head was placed at Brewster's angle with respect to the source, 55.5° [121], to minimise reflections and thus standing waves between source and detector. The distance of 50 cm from the source was decided upon to ensure the detectors, in particular the SBDs would receive sufficient signal but would not be saturated.

The TK recorded the amplitude of the signal observed from the RF emitter. Within the software using the calibration factor, the power of the signal was determined. The TK was then removed and in its place was put an SBD and its specific horn antenna. This SBD was also positioned at 50 cm with both the emission and reception horns angled correctly. The amplitude of the signal received was sent as a voltage to the computer. Using the power determined by the TK for each frequency band, and signal amplitude actually

perceived by the SBDs, the sensitivities of the detector diodes could be ascertained.

To produce a more realistic value of sensitivity for each of the detectors and their corresponding horn antennas, a power density approach was undertaken. This technique was carried out because the aperture of the TK is large, especially in contrast to the physical apertures of the individual horn antennas. The power received by the TK from the RF emitter was expressed in terms of $W/m^2$ with reference to the TK's aperture. Thus by working with power densities ($W/m^2$) and sensitivities per area ($V/(W/m^2)$) a more dependable result was found.

Despite the source and combination of multipliers achieving frequencies higher than 240 GHz, due to the limited range of the amplifier, approximately 20 GHz of the 240 GHz occurs below the noise level as observed in Figure 3.44. Therefore, this cannot be used with regards the characterisation and thus the enforced upper limit of the set-up becomes 217 GHz.

The responsivities of the SBDs and their respective horn antenna partnerships as a function of frequency are depicted below (Figs. 3.45 - 3.50). They have been previously published by the author et al [92]. In each of the figures, the frequency multipliers and amplifier combination used to characterise the individual detector and horn antenna partnership is shown as well as the true waveguide limits (WG Cut-Off) as opposed to the industry's label and also the power amplifier range (AMP range), where applicable. The true waveguide limits are the fundamental (i.e. $TE_{10}$) mode cut-off of the waveguide and the lower cut-off of the frequency of the next mode. The true waveguide ranges are shown in Table 3.2 for each detector. It must be noted that the sensitivities determined from the power densities have been calculated for the detector and horn antenna combination in the forward direction.

DXP22 and its pyramidal horn antenna, SGH22, have the narrowest bandwidth of the SBD array. It is sold as a 33-50 GHz detector but in truth it can observe 26.36-52.73 GHz. From Figure 3.45, it can be seen that the sensitivity across the frequency range of DXP22 and its horn antenna is quite constant [92]. Nevertheless, the detector is still able to observe signal after the cut-off, albeit erratically. This is unsurprising as the lower cut-off of the next mode is not a hard cut-off and when dealing with higher modes it is more complicated to predict what will happen with respect to the power in the

waveguide.

Figure 3.46 depicts the sensitivity of the DXP12 detector and its SGH12 horn antenna. It is clear to see that there is a gradual decrease in signal observed with respect to an increasing frequency [92]. What is important to note is the comparable results for both the data obtained via the doubler (50-75 GHz) and the tripler (75-110 GHz). Similar to DXP22, the DXP12 still detects signal after the lower cut-off however it is with a much lower sensitivity per area.

The DXP22, DXP12 and DET08 detectors are all procured from Millitech Inc. It is usually correct to assume that the diodes used in equivalent models and thus from the same manufacturer are alike. Hence the sensitivity per area for DXP22 (with SGH22) and DXP12 (with SGH12) should be comparable but DET08 (with SGH08) could differ. This is the case. DET08 is a new model by Millitech Inc. and as a result it is likely to differ. In Figure 3.47, the shape of the curve differs strongly from DXP22 (with SGH22) and DXP12 (with SGH12) in Figures 3.45 and 3.46, respectively. DET08 and its pyramidal horn antenna have a peak sensitivity per unit area at 100 GHz.

WR3.4 has a true waveguide range of 173.69-347.38 GHz of which the current set-up can only probe the lower end. Depicted in Figure 3.49 is the sensitivity per unit area of this detector and its horn antenna fluctuate. There are two main points of change, the first is at and after the lower cut-off of the waveguide and then again as a result of the fall off from the power amplifier [92]. Measurements of the waveguide dimensions were performed in order to explain the unanticipated results of WR3.4ZBD. Both the horn and waveguide of the detector were surveyed using a Zeiss AxioVision Optical Microscope [116]. Between the expected and measured values there existed a 1-5 % error giving an average of 2.75 %, which is slightly larger than other comparisons of waveguide and horn dimensions. Moreover, the difference in measurement between the horn antenna's and detector's waveguides was 3 % in both dimensions, again larger than other comparisons. These discrepancies could attribute to variance in the sensitivity per unit area of WR3.4ZBD and its antenna.

The eighth detector, the quasi-optical detector (QOD), does not make use of waveguides nor horn antennas. It employs a silicon lens to guide the signal into a log-periodic antenna [123]. The range as stated by the manufacturer of the QOD is 100-1000 GHz.

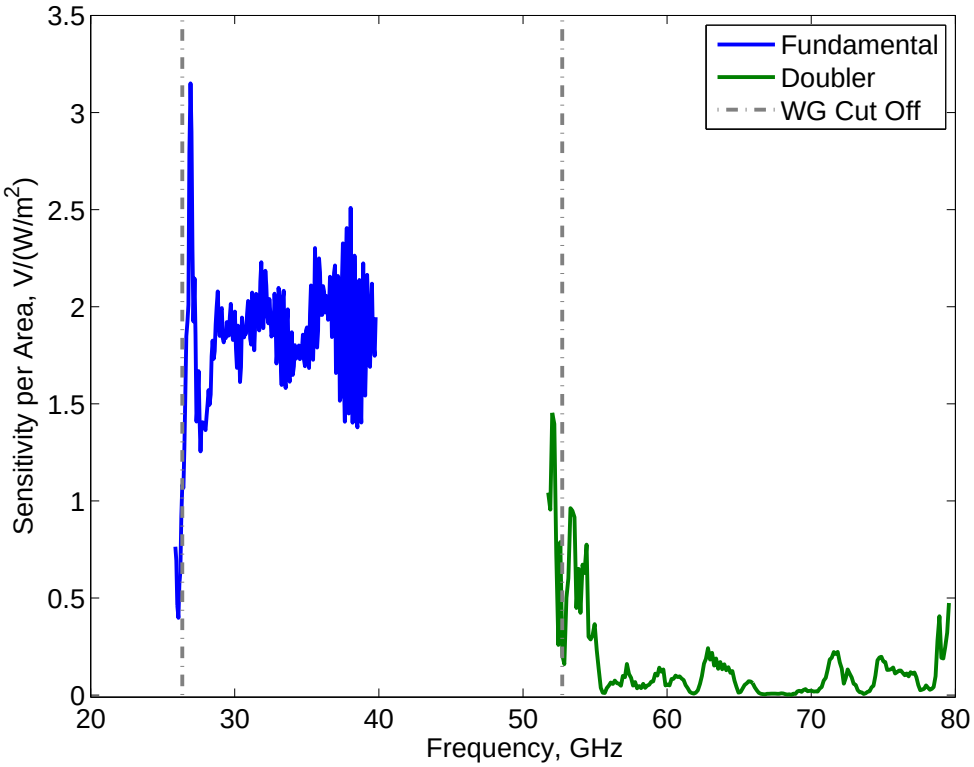


Figure 3.45: The sensitivity per unit area for DXP22 and its horn antenna (33-50 GHz).

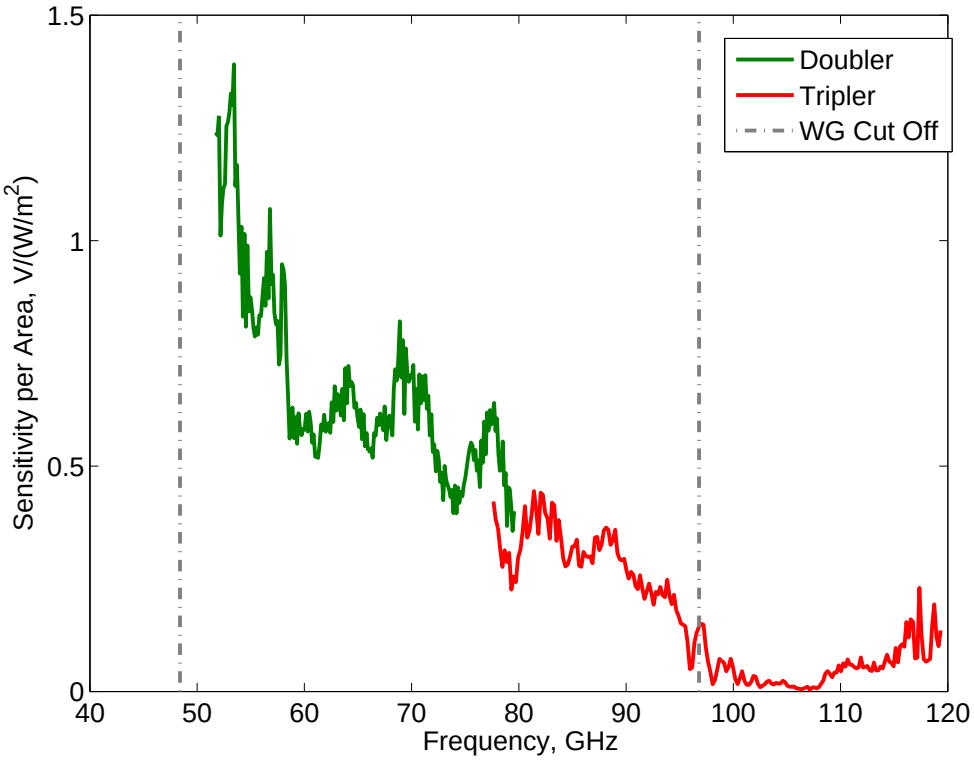


Figure 3.46: The sensitivity per unit area for DXP12 and its horn antenna (60-90 GHz).

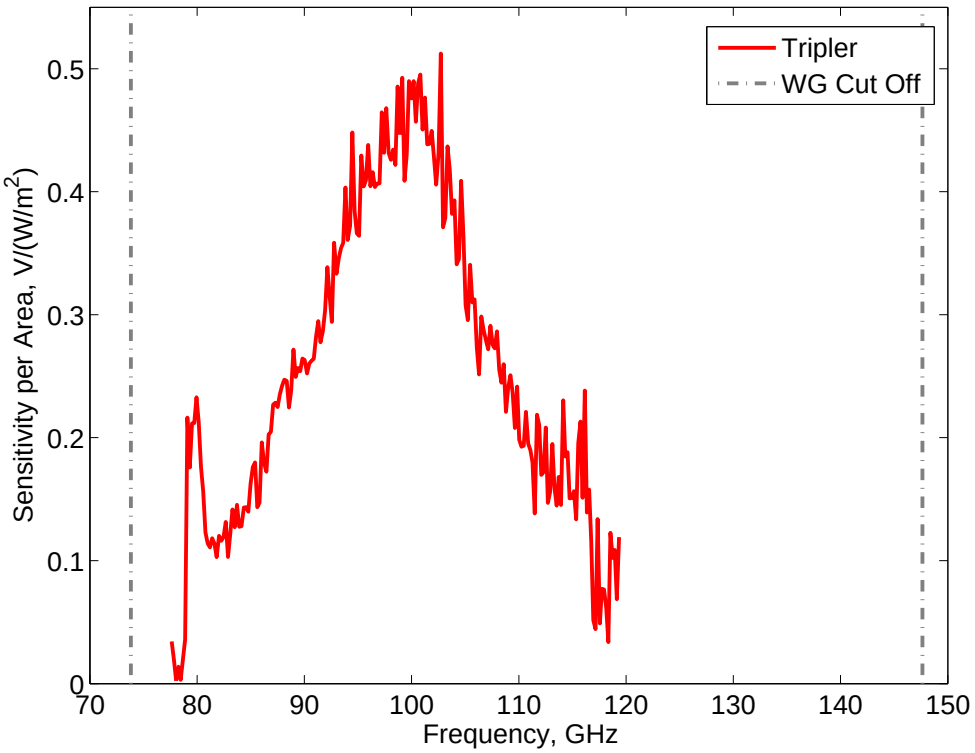


Figure 3.47: The sensitivity per unit area for DET08 and its horn antenna (90-140 GHz).

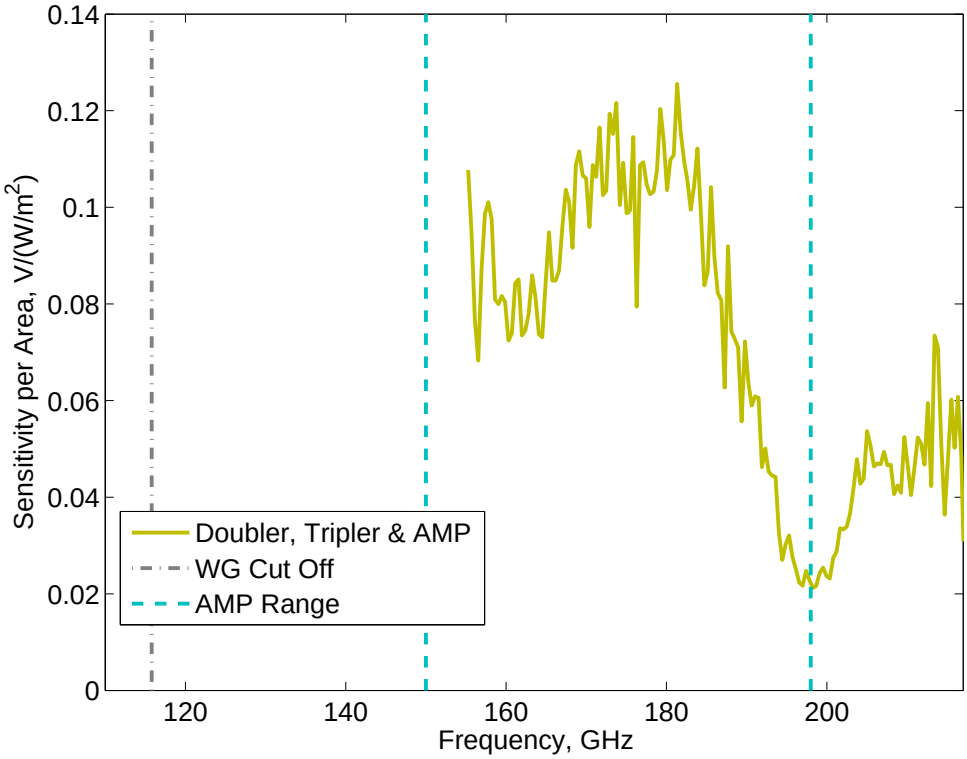


Figure 3.48: The sensitivity per unit area for WR5.1 and its horn antenna (140-220 GHz).

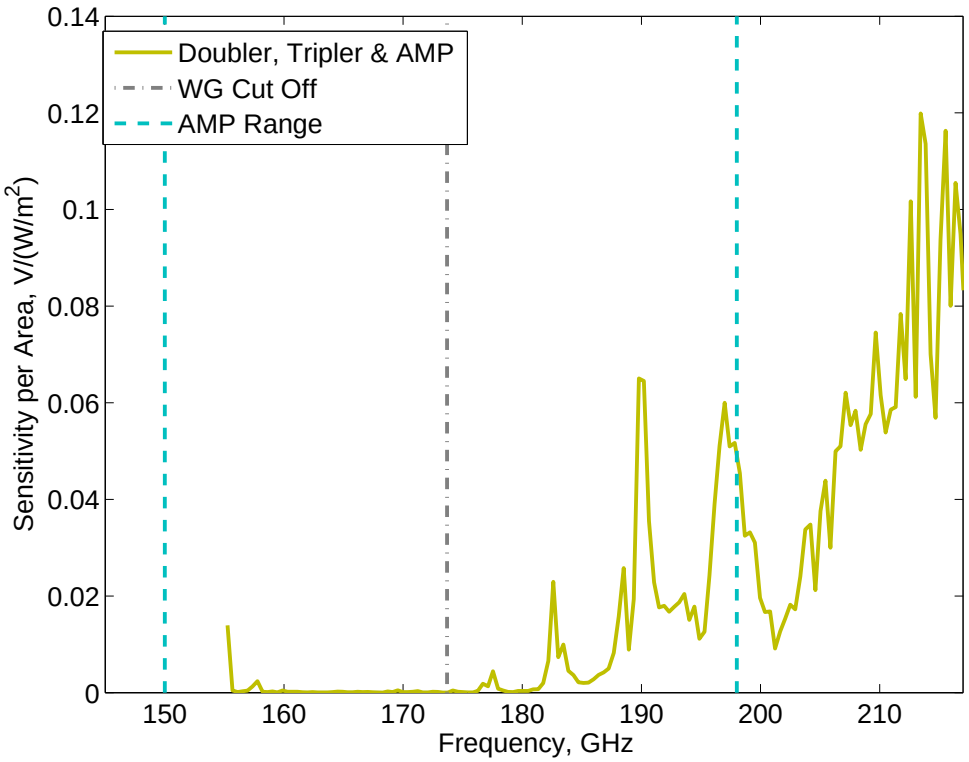


Figure 3.49: The sensitivity per unit area for WR3.4 and its horn antenna (220-330 GHz).

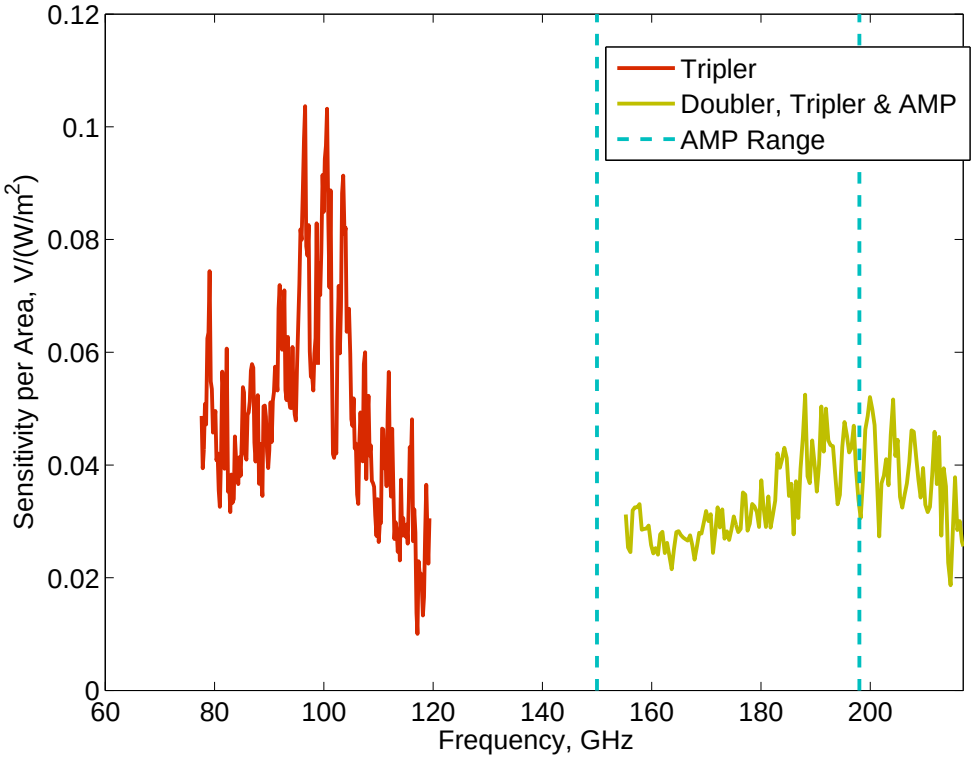


Figure 3.50: The sensitivity per unit area for Quasi-Optical Detector (100-1000 GHz).

However it must be noted that SBDs are able to see below this 100 GHz as demonstrated by the DXP22 and even lower but they are also able to probe higher than a 1 THz, usually in the region of 2 THz. It can be assumed therefore that the limits given by the manufacturer are the optimal operating frequencies for the manufactured detector. The silicon lens is 10 mm in diameter [123] and is thus comparable to the wavelengths at 100 GHz and below, as 10 mm corresponds to a frequency of 30 GHz. The QOD was subjected to the output signal of both the tripler and the combined doubler, tripler with power amplifier. The two set-ups are depicted by two differently coloured curves in Figure 3.50 where the red tripler signal has an overall higher amplitude with a shape comparable to that presented in Figure 3.47 for the DET08 with its SGH08. It can be seen in the figure, the sensitivity per unit area is variable and fluctuates. These fluctuations can be attributed to the silicon lens being of the same or similar size as the wavelength thus causing standing waves [92].

The remaining detectors with their corresponding horn antennas (WR2.2 and WR1.5) and the higher frequencies of already mentioned detectors could not be calibrated in the described set-up. However by way of providing sensitivity per unit area values and also as a means of comparison between the sensitivities given by the manufacturer and those determined by the methods described in this chapter, an inverse calculation was carried out to determine the remaining detectors.

The reverse determination of sensitivities per area was carried out in order to ascertain sensitivities per area for the uncharacterised diodes and also to establish how the results of the method described in this thesis compared with the manual given values. These values and those determined on the bench are shown in Table 3.6 for each detector and horn antenna where relevant. The sensitivity values experimentally determined in the fourth column of Table 3.6 are those used throughout the remainder of the thesis in order to calculate the power received by the SBDs from the beam of synchrotron radiation. Moreover, in the case of WR2.2ZBD and WR1.5ZBD the sensitivity values used are from the manufacturer. The higher frequency diodes had not been characterised on the bench because no relevant source could be attained. Furthermore, it must always be remembered that the sensitivities presented here are for the detector and its relevant horn antenna in a forward direction. This contrasts with the sensitivity values given in the detector man-

uals where the value is only valid for the detector itself. The discrepancies between the experimentally determined and manufacturer given sensitivity values are due to different experimental set-ups. In this thesis the detector and its horn in the forward direction were only investigated and the 'gold standard' implemented was the free space TK power meter as against a waveguide Erickson power meter for the manufacturers tests. The values issued by the company are for the model of the detector (without horn) and not specific to the individual detector. By using the effective area of a horn antenna, described in Section 3.3.1 *a)*, one can switch between sensitivities per area ($V/(W/m^2)$) and manual given sensitivities ($V/W$).

Table 3.6: SBD Sensitivity Comparisons

| | | Experimentally Determined | | Calculated from Manual | |
|---|---|---|---|---|---|
| **Detector Model** | **Stated Range GHz** | **Sensitivity Per Area V/(W/$m^2$)** | **Sensitivity V/W** Divided by $A_{eff}$ | **Sensitivity V/W** Given | **Sensitivity per Area (V$m^2$)/W** Multiplied by $A_{eff}$ |
| DXP-22 [122] | 33-50 | 1.78 | 1545.6 | 1200 | 1.38 |
| DXP-12 [122] | 60-90 | 0.55 | 1612.6 | 700 | 0.24 |
| DET-08 [122] | 90-140 | 0.25 | 1727.0 | 600 | 0.09 |
| WR5.1ZBD [103] | 140-220 | 0.07 | 2261.8 | 2000 | 0.06 |
| WR3.4ZBD [103] | 220-330 | 0.02 | 575.5 | 1500 | 0.05 |
| WR2.2ZBD [103] | 330-500 | — | — | 1250 | 0.01 |
| WR1.5ZBD [103] | 500-750 | — | — | 750 | 0.005 |
| QOD [103] | 100-1000 | 0.04 | 536.0* | 500 | 0.04* |

where * means $A_{dim}$ is used as QOD has a silicon lens, not horn.

Chapter 4

# Experimental Results

Once the detector array was installed at the beamport, experiments were conducted and data collected. The experiments were both to learn more about the detector array and also the characteristics of Diamond's beam in a variety of different beam modes. Throughout this chapter the analysis of the data captured using the SBD array at the B06 viewport of the Diamond Light Source is presented and discussed. It is paramount to note that Figures 4.10 - 4.18, 4.26 - 4.28 and Figure 4.32 are only showing the signal obtained directly at the revolution frequency of the ring and not the sidebands (from bursting). The signal observed at the revolution frequency is the steady state emission, while any variation goes into the sidebands where there is a bandwidth of more than 87 kHz. The detector is characterised by looking at the steady state. The instabilities are not well understood and thus looking at the sidebands of data would not be beneficial.

## 4.1 Reaction Time of the SBDs

To investigate the pulse shape and length detected by an SBD when observing a single bunch at Diamond a 13 GHz bandwidth oscilloscope with a sample rate of 40 GS/s was employed. Using this oscilloscope a single bunch as viewed by the WR5.1ZBD (140-220 GHz) can be seen in Figure 4.1, where it is the raw signal directly from the oscilloscope. The length of the pulse can be determined using the x-axis, while the y-axis depicts the magnitude of the signal as observed by the SBD. Repeated calculations show that the full-width half-maximum (FWHM) of the bunch as observed by the detector is

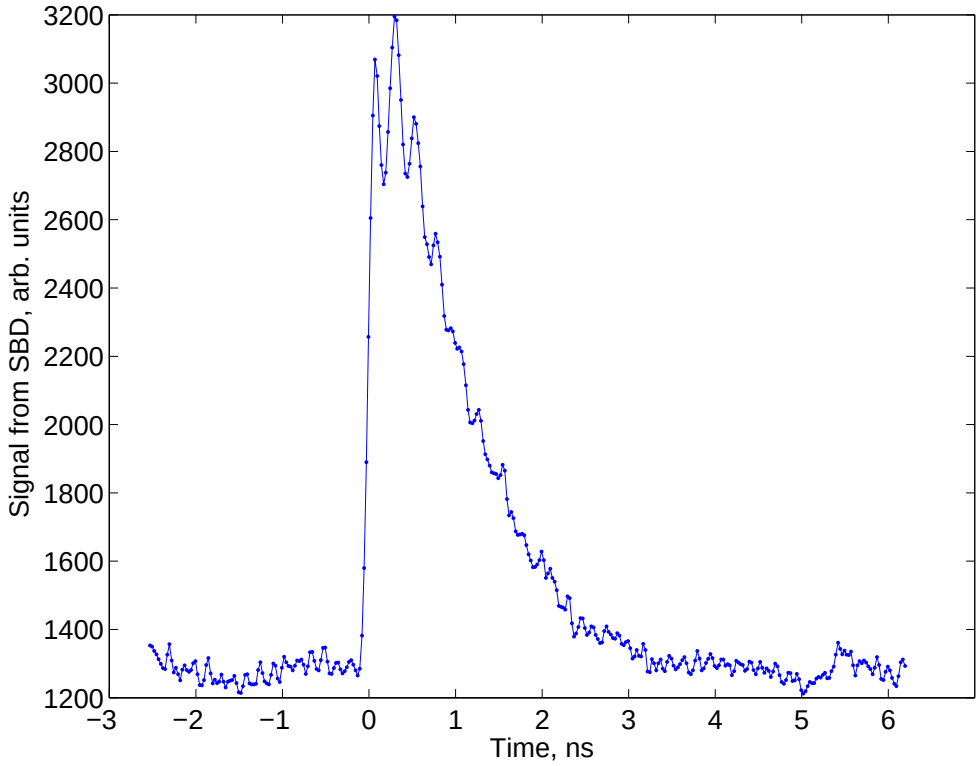


Figure 4.1: A typical signal from the WR5.1ZBD (140-220 GHz) detector by directly connecting to the 13 GHz oscilloscope.

1.1 ns. Therefore, it is verified that these detectors can operate in a turn-by-turn set-up.

In order to carry out further characterisation tests for the set-up, in particular looking at each SBD of the array simultaneously, an eight-channel 16 bit 1 GHz bandwidth oscilloscope was employed. Each of the SBDs were directly terminated into this oscilloscope which provided 50 Ω input impedance, thus the SBDs were in a low impedance set-up allowing for faster speed at the cost of lower sensitivity and the cable capacitance inconsequential. The lower impedance reduces the magnitude differences between R and C as discussed in Section 3.2 *a)*, resulting in the $V_R$ becoming closer to the value of $V_{in}$. As it is a 16 bit oscilloscope, signals below a millivolt could be determined however for a single shot or live data capture this could only be seen during a burst. In order to observe such low voltages when not bursting, averaging was carried out. Using the 1 GHz eight channel oscilloscope, there was worry that the pulse from each detector was being stretched. However when tested with an oscilloscope of much wider bandwidth (13 GHz) it could be seen that the pulse remained the same as before and thus concluded that the original oscilloscope had not been stretching the pulse. Moreover, it was deduced that the

cables were not altering the pulse shape either and that it was a true artefact of the diode itself. The diode has a significant shape of a sharp rise and a slow decay which can be seen in Figure 4.1.

This characteristic slow decay results in the diode not returning to the noise floor when observing between bunches. It had been noticed that when a train with consecutively filled buckets was present, the detector array did not show the breaks between the bunches. The diodes almost reached the noise floor when the same train had only every second bunch filled and definitely depicted the empty buckets when every fourth bucket was only occupied. Figures 4.2 and 4.4 illustrate the signal observed by all eight SBDs of the array, respectively when a 200 bunch continuous train was present and then with a train of 50 bunches where there are three empty bucket between each filled one. They show which buckets are filled and accordingly the amplitude of the signal observed by each detector. From these figures a slight rise time discrepancy can be observed, especially for the QOD, where upon initially observing signal the diode's response does not instantly jump to the true reading. This rise time disparity is shown for all detectors, to some measure in a screenshot in Figure 4.6 taken directly from the 1 GHz oscilloscope. Here the x-axis represent time (100 ns/div or 20 ns/div) and the y-axis the amplitude of the signal detected by each of the SBDs (1 mV/div or 200 $\mu$V/div). The left hand side subfigures depict in descending order detectors 33-50 GHz (yellow), 90-140 GHz (magenta), 220-330 GHz (cyan) and 500-750 GHz (green), while the right show the 60-90 GHz (white/green), 140-220 GHz (purple), 330-500 GHz (red) and 100-1000 GHz (orange). Two curves are shown for each detector with the top curve (ZX) representing a zoomed version of the lower (CX) in order to distinctly see the delay in rise time. However this rise time discrepancy is outweighed by that of the decay.

Figures 4.3 and 4.5 display data from the same capture as Figures 4.2 and 4.4, however the view is focussed in on the end of the bunch train in order to better observe. Illustrated in these zoomed figures (Figs. 4.3 and 4.5) ringing can be seen after the bunch trains cease, nevertheless the diodes are actually observing real signal here. As the ring is filled with minimal charge and the oscilloscope is sensitive, the latter is depicting the noise in the ring as bunches. In truth, this noise is actually buckets that have been filled but unintentionally. If operating at higher charge, the apparent ringing would be deemed

grossly insignificant. The two congregations of large spikes in Figures 4.2- 4.5, are due to cross talk from the external trigger of the revolution frequency of the ring. The periodicity of the 120 bunches is attributed to the booster and the filling technique employed at Diamond.

## 4.2 Bunch-by-Bunch Versus Turn-by-Turn

In order to determine the disparity, if any, between turn-by-turn observations and bunch-by-bunch, the eight detectors were terminated directly into the 1 GHz oscilloscope described above in Section 4.1. Operating the oscilloscope, a variety of different data sets were obtained including two bunch data where two buckets side-by-side were each filled with one bunch. Figure 4.7 shows the bunches at each revolution of the ring (x-axis) for 20 ms, where the positions of the recorded peak signals are at the 6th and 11th position, which are arbitrarily chosen place names. As a result, each of the two bunches can be seen as a band in the figure. The bursting behaviour of the two bunches shown in Figure 4.7 as observed by the same detector (140-220 GHz) is depicted in Figure 4.8. Throughout the data set of 20 ms, the bursting can be seen and is expected to be irregular and fluctuating, with amplitude variations of seven fold. While the data was being captured, it could be assumed that the bunches were unaffected by the other and behaved as individual bunches with no influence over the other. This assumption was later confirmed during analysis whereby cross-correlations indicated that there was no relationship between the neighbouring bunches. Cross-correlation of a discrete function can be defined as follows,

$$r_{ab} = a(t) \otimes b(t) = \sum_{-\infty}^{+\infty} a^*(t) b(t+\tau) = FFT(a) \cdot iFFT(b) \tag{4.1}$$

where $a$ and $b$ are discrete functions, $a^*$ is the complex conjugate of $a$, $t$ is time and $\tau$ is the displacement. The correlation of the two neighbouring bunches was not observed. This cross-correlation or lack thereof is presented in Figure 4.9, where a value of one (on the y-axis) would describe full correlation. The majority of the data show a correlation close to zero increasing to just above 0.1 at the most correlated point of these two bursting data sets. It can be concluded that due to the low values of correlation (0-0.1) the

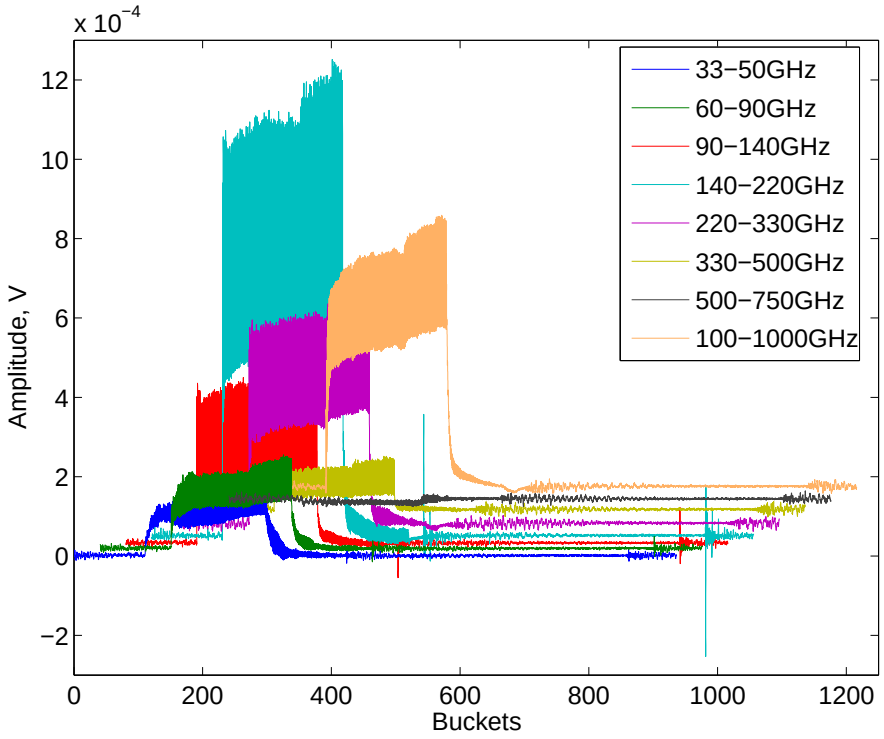


Figure 4.2: A continuous train of 200 bunches in low-alpha mode ($\alpha = -4.5 \times 10^{-6}$) averaged over 1000 sweeps. For a clearer view, the data has been staggered across the x- and y-axes.

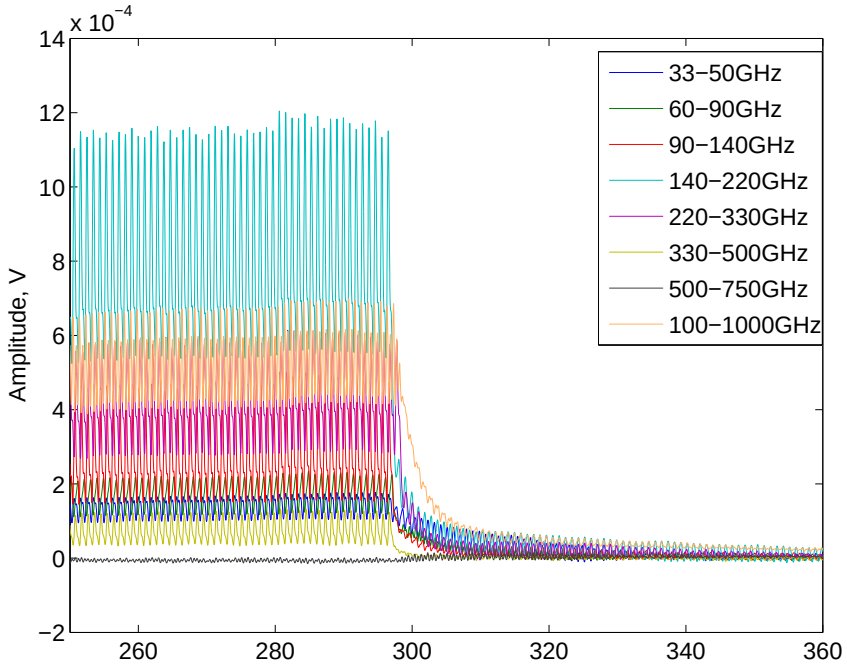


Figure 4.3: A zoomed image of the above figure, where all data has been aligned to (0,0), in order to highlight the signal observed after the continuous 200 bunch train and show that the signal does not decay adequately between bunches.

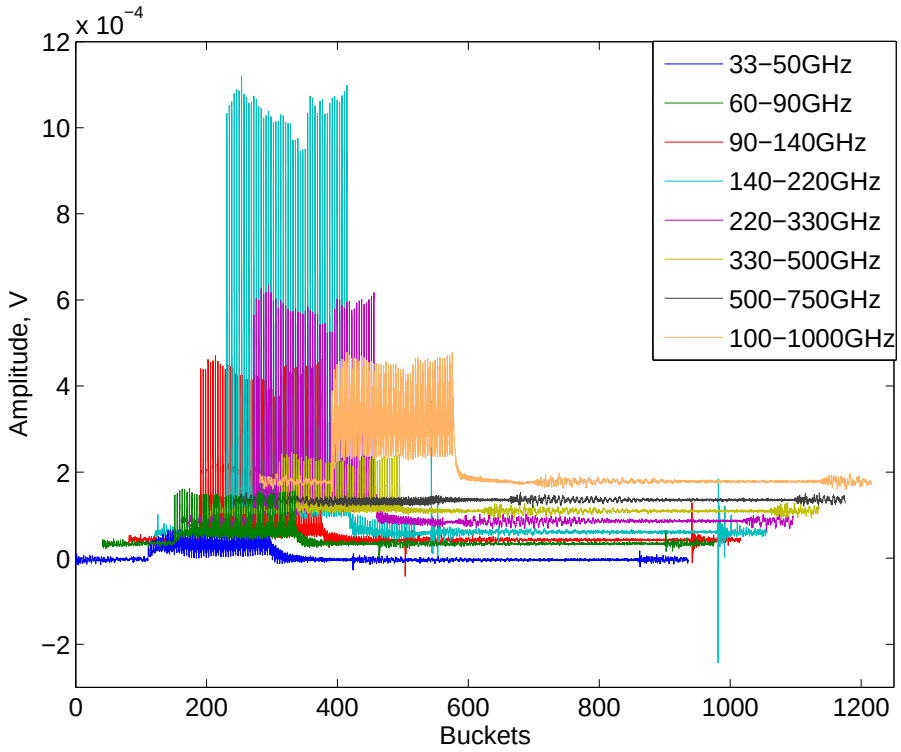


Figure 4.4: A multi-bunch fill of 50 bunches with three empty buckets between each filled bucket in low-alpha mode ($\alpha = -4.5 \times 10^{-6}$) averaged over 1000 sweeps. For a clearer view, the data has been staggered across the x- and y-axes.

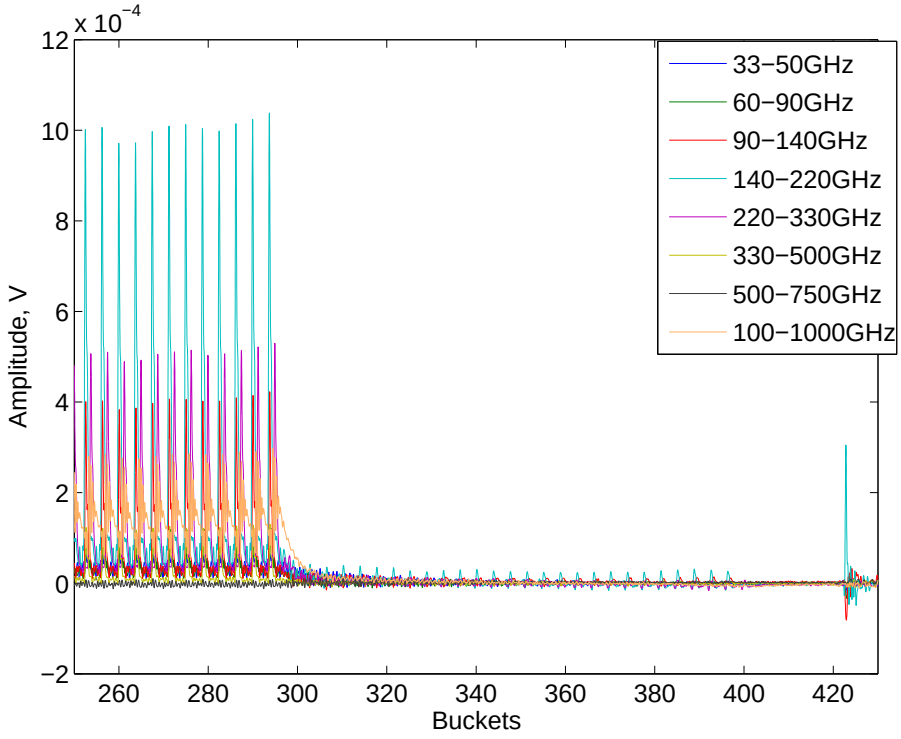


Figure 4.5: A zoomed image of the above figure, where all data has been aligned to (0,0), in order to highlight the signal observed after the 50 bunch train, the blips from the external trigger and to show the signal decays to zero between bunches.

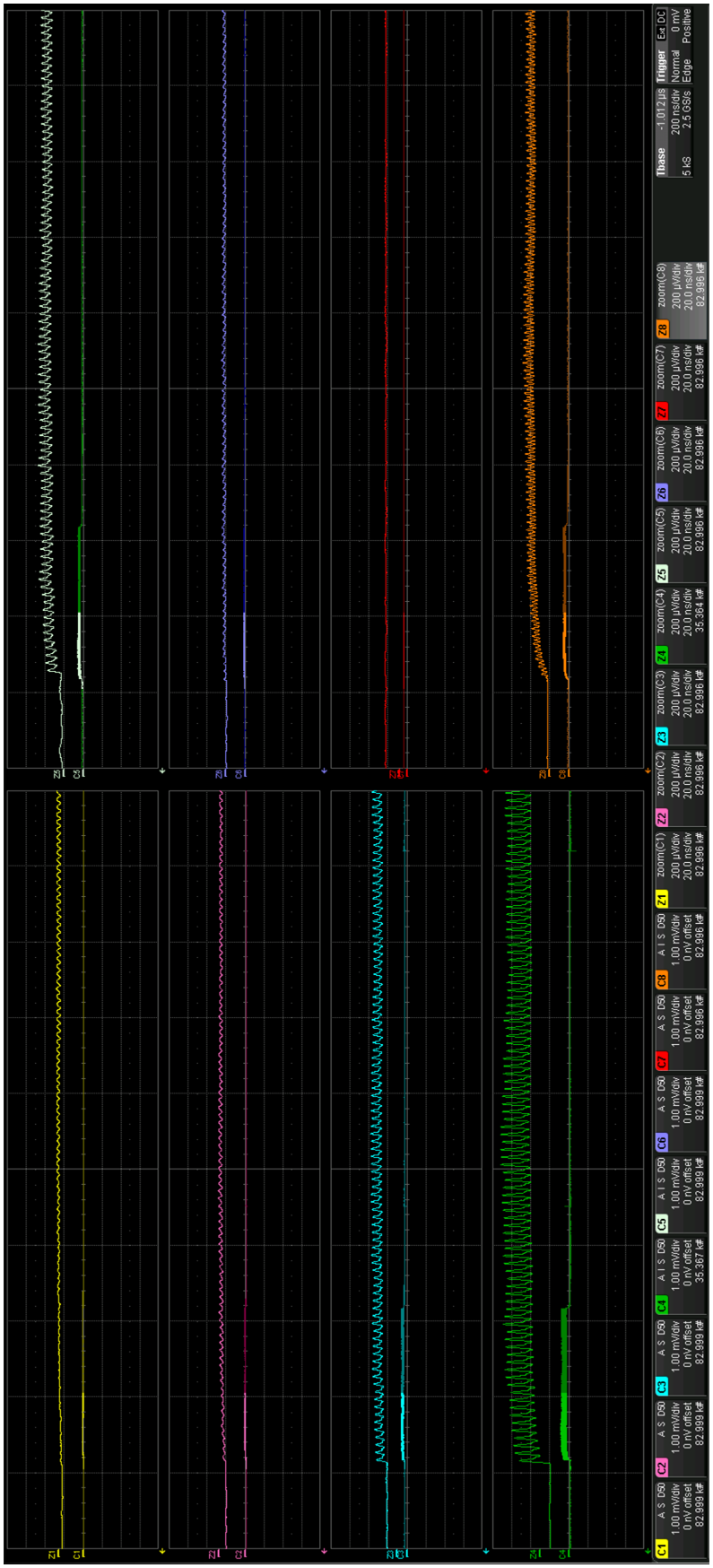

Figure 4.6: A view of the 1 GHz oscilloscope during a continuous train of 200 bunches in low-alpha mode ($\alpha = -4.5 \times 10^{-6}$) averaged over 1000 sweeps.

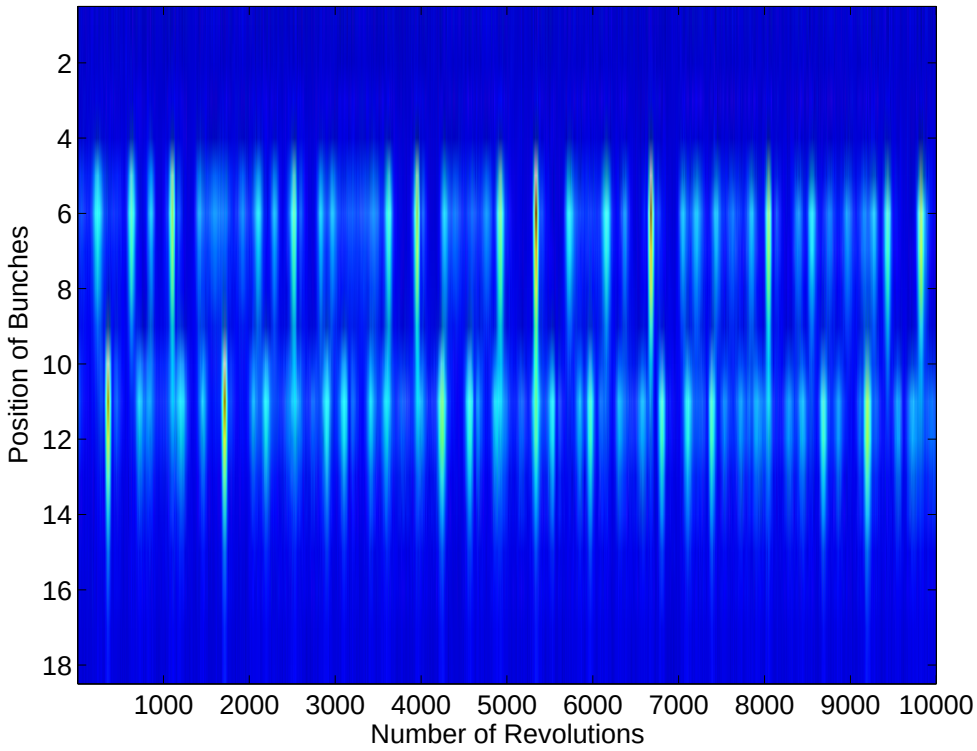


Figure 4.7: The two neighbouring bunches in the storage ring for each revolution as viewed by the 140-220 GHz detector during low-alpha mode ($\alpha = -4.5 \times 10^{-6}$).

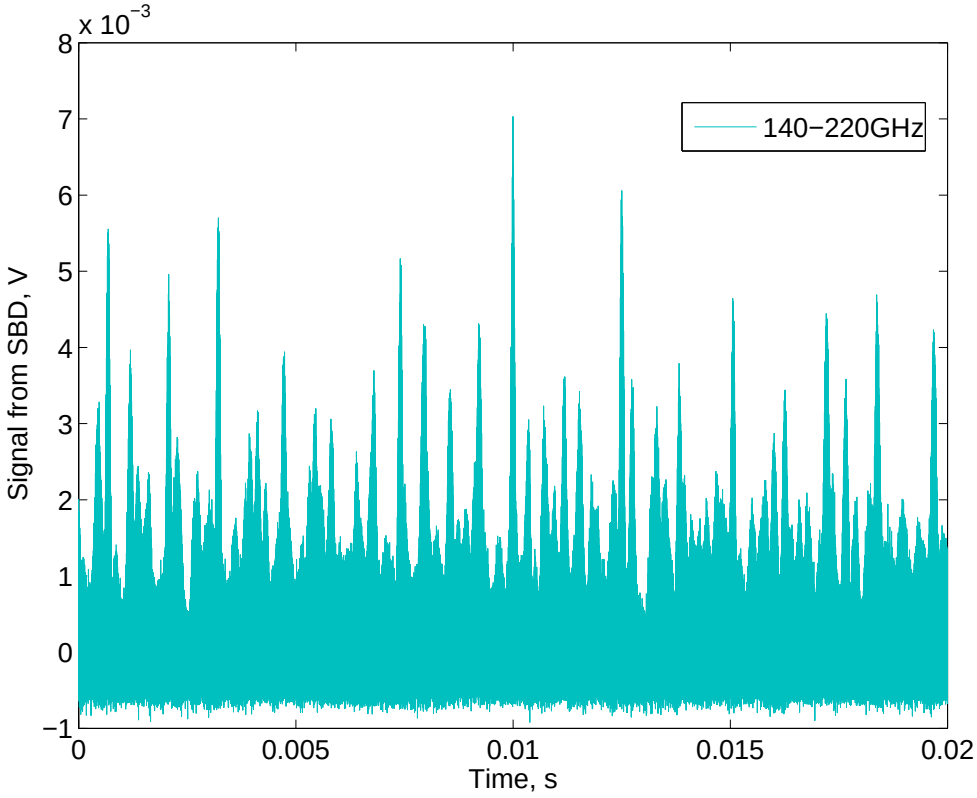


Figure 4.8: The bursting observed by the 140-220 GHz WR3.4ZBD for low-alpha mode ($\alpha = -4.5 \times 10^{-6}$) with two neighbouring bunches during the data capture of 20 ms.

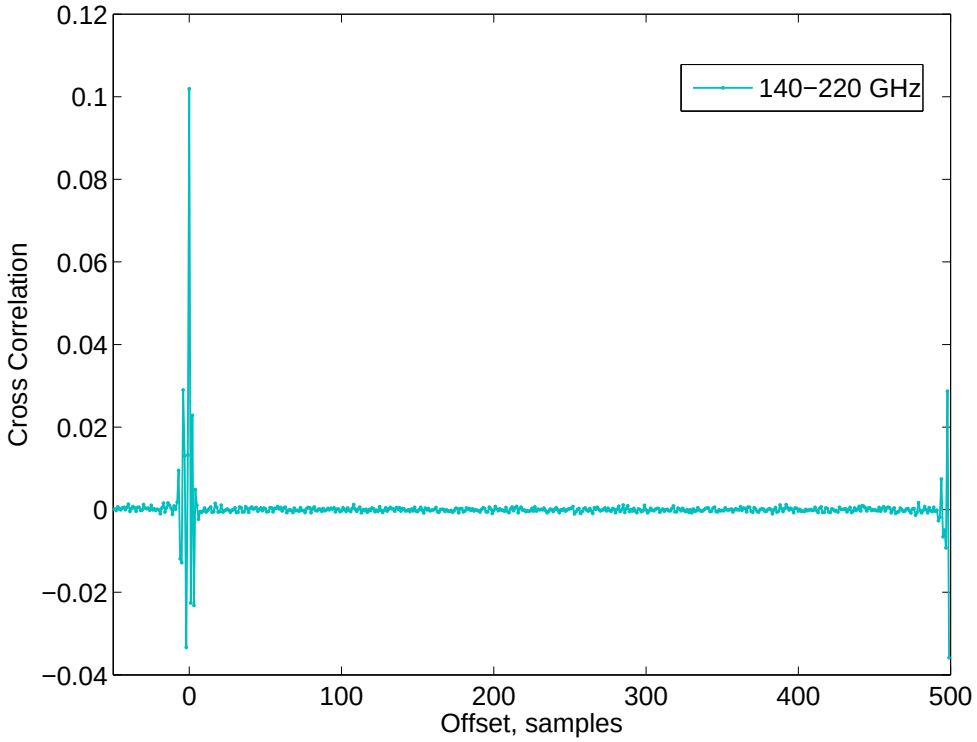


Figure 4.9: The correlation of the two neighbouring bunches with data collected by the WR3.4ZBD during low-alpha mode ($\alpha = -4.5 \times 10^{-6}$).

two bunches are independent of each other. Additionally this is indicated by the TMBF (Transverse Multi-bunch Feedback System) implemented at Diamond. The TMBF system acts on each bunch individually [124] in order to damp instabilities below 200 MHz. As the bunches are independent of one another, there is no need for bunch-by-bunch data acquisition.

Once the experiment with the oscilloscope was concluded, the original data acquisition system was re-implemented. Thus the eight detectors were connected to their individual voltage amplifiers with high input impedance and their signals fed into the multi-channel simultaneous digitiser.

## 4.3 Single Bunch Versus Multi-Bunch Fill

Each SBD is able to observe each electron bunch but is unable to differentiate between the bunches. As a result of this, single bunch mode is usually preferred. Henceforth, data were routinely and most commonly obtained when the ring was operating in single

bunch mode. However it must be remembered that SBDs are non-linear, continuous-wave devices and are best operated within their square-law region (Section 3.3.1). With respect to the data presented here, when a diode is in the square-law region (meaning quadratic of field) it is detecting linearly. This means that the relationship between power observed by the SBDs and the bunch current will be depicted as a quadratic relationship if the radiation is coherent, or a linear dependence if the radiation emitted is incoherent. Ergo, single-bunch mode may not be most applicable for these detectors and would most likely push the diodes out of the square-law, into the linear regime. This of course should only occur if the power is high enough to do this. Moreover in single bunch mode these higher powers could be reached sooner than in multi-bunch mode. As a result multi-bunch fills were investigated and a comparison between the two is aired throughout this section. Data have been taken in both multi-bunch and single bunch mode and under a variety of machine conditions most notably 'normal user mode' and 'low-alpha mode'. In each case current ramps were carried out with the bunch current starting in the noise floor of the detectors and slowly increased to and beyond the instability threshold. In the forthcoming figures, only the data captured at the revolution frequency (533.820 kHz) is depicted. As described at the beginning of the chapter, the signal at 533.820 kHz is the steady state emission while the signal from the rest of the bandwidth is the variation from steady state. The detector can only be characterised by looking at the steady state as too little is known about the activity in the sidebands. Looking at the figures within this section, the curve patterns remain the same throughout each mode. That is to say in normal mode, the detector observing the most to least power goes 100-1000 GHz, 90-140 GHz, 60-90 GHz, 220-330 GHz, 330-500 GHz, 33-50 GHz, 140-220 GHz and finally 500-750 GHz detectors, while in low-alpha THz mode the order is 100-1000 GHz, 220-330 GHz, 330-500 GHz, 90-140 GHz, 60-90 GHz, 500-750 GHz and a tie between 33-50 GHz and 140-220 GHz detectors. In each case, this can be attributed to what is observed by the diodes but then converted into power via the calibration factors as well as the location for each of the detectors in the array.

### 4.3.1 Single Bunch

As discussed above, a single bunch fill was assumed to be the correct choice for the SBD array because the discernment between bunches would be unavailable (and also unnecessary), thus data were taken in single bunch low-alpha mode ($\alpha = -4.5 \times 10^{-6}$). If the diodes were observing sufficient signal to remain within the square-law region, a current ramp would result in the power of CSR quadratically proportional to the bunch current. Figure 4.10 illustrates the signal observed by the detector array in terms of Watts with an increase of bunch current. A current ramp was carried out and the signals observed by the individual SBDs of the array are portrayed as different colours in the figure. Unsurprisingly the QOD (peach) reports the highest power thus denoting the most amount of signal detected, this is due to its wide bandwidth and lack of hard cut-off (waveguide). The next curve representing the detector observing the second highest amount of power is the 220-330 GHz (magenta) detector and is approximately two orders below that of the QOD's curve. The order of the coloured curves indicate the strength of signal observed across the variety of frequency bands. As expected and depicted in Figure 4.10, the result was not quadratic but decidedly linear. That is to say with an increase of bunch current, the power of signal observed by the SBDs followed a linear trend. A linear relationship should imply that the electron beam is emitting incoherently, however it is known that this cannot be true because the frequency bands of the detectors ensure they can only be observing in the GHz-THz region which is only created as coherent radiation at Diamond. The linear dependence occurred because even though the average power was kept low the peak power was too high and drove the diodes into the linear regime as outlined in Section 3.3.1. Consequently, to reduce the peak power a multi-bunch fill with an overall low beam current has been implemented. With this machine set-up, the square-law region of the diodes can be probed and the transition into the linear regime has been recorded also. It must always be remembered that SBDs are continuous wave devices by nature and thus depositing all the power from a single bucket within a couple of picoseconds, does not agree with it. This may seem at odds with detecting CSR bursts but the initial aim is to characterise the detector array and that is done with the steady state emission from the signal at the revolution frequency. Moreover when characterised and in use, bursting can still be seen when the overall peak power has been decreased and though the beam current

remains low, the bunch current can still be exercised. Multi-bunch could be considered more similar to a continuous wave than single bunch.

The power of signal observed by each of the eight SBDs during a bunch current ramp where the machine was in normal mode conditions with a single bunch fill is presented in Figure 4.11. With regards normal mode single bunch, the signal was primarily quadratic with respect to the current and at high bunch currents, became more linear. The figure shows this relationship, which is in keeping with the behaviour of SBDs, with an increase of input power the diodes begin to move into the linear regime. Nevertheless, the transition from quadratic to linear is not as smooth or gradual as it ought to be and this is no doubt due to the high peak power. It can be seen that this transition behaviour is not adhered to by the 500-750 GHz (grey) and QOD (peach) detectors, instead they undergo a large step-change at approximately 45 μA. This and other features of the seventh and eighth detectors are discussed in Section 4.9. All eight detectors observed a step-change in signal at approximately 85 μA, where the 33-500 GHz detectors noted an increase in signal while the 500-750 GHz detector (grey) and the QOD (peach) detected a decrease. As the diodes are not operating in their ideal region, the observations can not be definitively explained. Furthermore, normal mode current ramps too benefited from a multi-bunch fill.

### 4.3.2 Multi-Bunch

When using a multi-bunch fill, the bunch current must be kept low because if too high, the SBDs might again be driven into the linear regime. Furthermore, the lower in current reached the longer the current ramps become, allowing for as much data as possible to be captured. In normal user optics, it is straightforward to inject small amounts of current into the ring during a current ramp. A half-fill was used, meaning 468 buckets were filled. Nevertheless, reaching low enough currents in low-alpha mode is more arduous. The method implemented for low-alpha mode was to ramp up all the magnets as if injection was occurring but not fire the gun. This resulted in dark current being trickled into the storage ring. The approach was slow and meant that there was no control over the amount of bunches being filled. In order to reach higher currents in this ‘ultra-low’ current ramp, another method was also employed, by changing the amount of charge generated by the

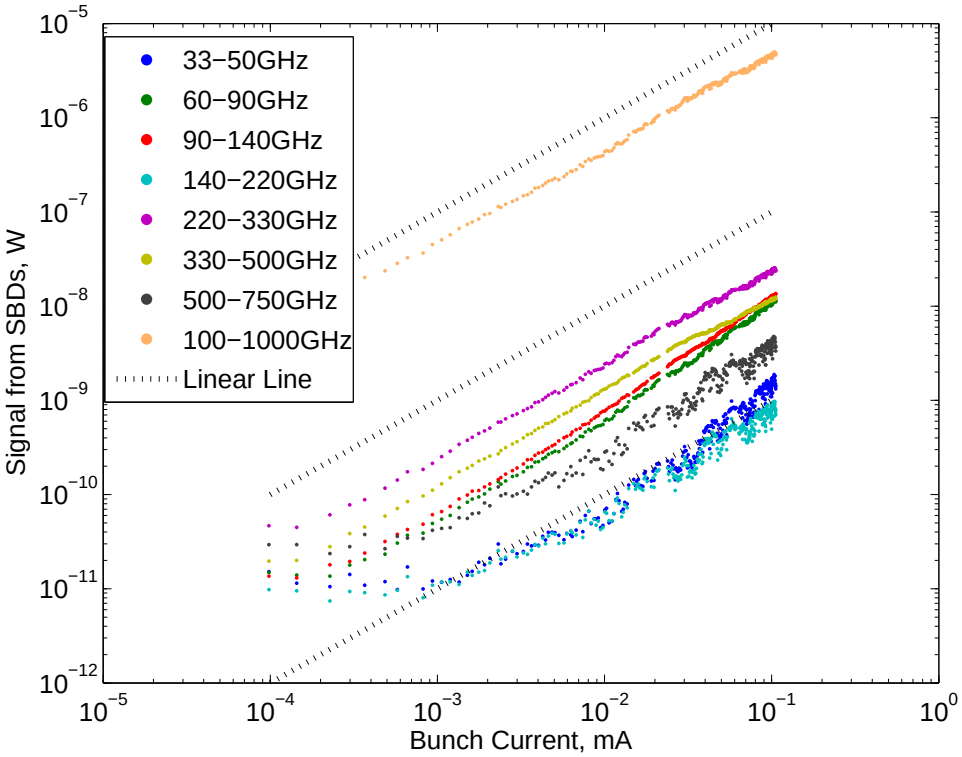


Figure 4.10: Signal observed at the revolution frequency of the ring via all eight channels of the spectrometer for **Low-Alpha THz Mode** ($\alpha = -4.5 \times 10^{-6}$) with a single bunch fill during a current ramp. A linear dependence can be observed.

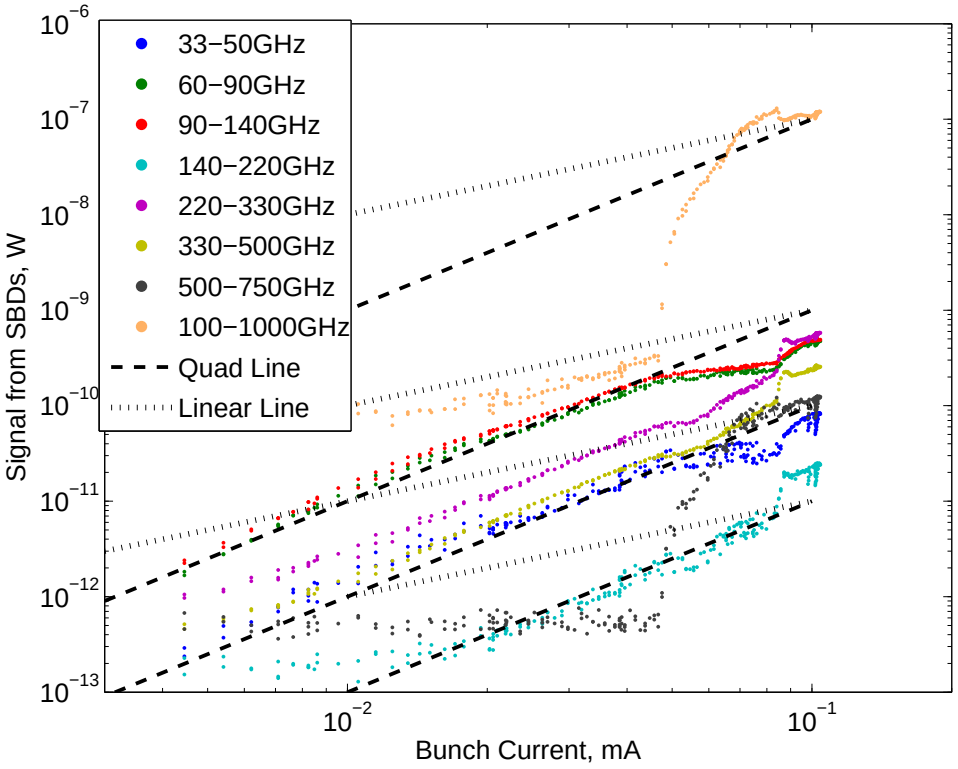


Figure 4.11: Signal observed at the revolution frequency of the ring via all eight channels of the spectrometer for **Normal Mode** ($\alpha = 1.7 \times 10^{-4}$) with a single bunch fill during a current ramp. Primarily a quadratic dependence is shown, with a tendency towards linear at higher bunch currents, as expected.

electron gun. This allowed for real current to be injected but the amount of current injected was severely reduced.

There are two interpretations on how to have a multi-bunch filling pattern in a storage ring. The first method is the most conventional approach at Diamond, whereby the buckets filled are all in one block called a train. The other method spreads out the individual bunches throughout the ring either individually or combined in a collection of smaller trains. Data obtained in multi-bunch mode were translated into single bunch mode by dividing across by the relevant number of bunches. It was also assumed that the amplitude of the signal is proportional to the number of bunches and thus the amplitude of the observed signal was also divided across by the relevant number of bunches. This assumption was shown to be correct as data captured with various multi-bunch fill patterns once 'translated' into single bunch data were equivalent to each other.

Presented in Figure 4.12 is the power of the signal as seen by the individual detectors of the SBD array, represented by a different colour, in normal mode with a multi-bunch fill during a current ramp. Six of the eight detectors (33-500 GHz) note a quadratic signal. The 500-750 GHz detector (grey) and the QOD (peach) do not appear to detect any significant signal and remain flat. It is assumed that this is because the diodes have not 'turned on' due to low levels of signal. This is in keeping with what is seen in figures, like Figure 4.14. Section 4.9 describes the behaviour of the higher frequency detectors in contrast to that of the 33-500 GHz detectors. In Figure 4.12, four of the curves are wide while the other four are narrow. The 60-90 GHz (green), 90-140 GHz (red), 220-330 GHz (magenta) and 330-500 GHz (gold) detectors begin with a wide curve but become more refined with an increase in bunch current and thus power detected. This implies that at a particular current only a restrictive range of power of the signal occurs. This is in contrast to the wide bands of the 33-50 GHz detector (blue) and the 140-220 GHz (cyan), which imply many more signal strengths are seen for a particular bunch current. It could be assumed that with the increase in bunch current, the curves of the other detectors would also narrow, but this does not seem to be the case as demonstrated by Figure 4.14. Moreover, these wide curves are only witnessed in normal mode. For the normal mode multi-bunch data (Fig. 4.12), both the QOD and 500-750 GHz detector observe no signal, a discussion of which is outlined in Section 4.9.

The relationship between an increase of bunch current and the power detected by the SBD array is also shown by Figure 4.13. However, as the data for this figure were captured during low-alpha THz mode, a variety of filling techniques were employed in order to achieve the necessary bunch currents. These different filling methods are depicted as different shapes. From these two figures (Figs. 4.12 and 4.13), it is clear to see that all of the detectors which observe a signal behave quadratically. Consequently, this means that the diodes were operating within the square-law regime and therefore the diodes were not observing excessive current to be driven into the linear detection regime as described in Section 3.3.1. Once again, the QOD detector (peach) appears to detect more power than the others, which is a direct result of its large bandwidth. The remaining detectors are grouped closer together, more than two orders of magnitude lower. Distinctly in the case of Figure 4.13, above 10 μA, some of the detector bands display an undulating signal. This is especially true of the 33-50 GHz (blue), 140-220 GHz (cyan) and 500-750 GHz (grey) detectors and the undulation increases with bunch current.

As expected, in both the modes, the relationship between the bunch current and signal power is clearly quadratic. It is a good time to remember that the signal shown in this section's figures is at the revolution frequency of the ring i.e. the steady state emission, and when the SBDs are operating in the square-law region, the diodes are detecting linearly. Additionally, for Figure 4.13, the relationship becomes more linear as the diodes are being driven from the square-law region into the linear regime due to the CSR emission increasing with bunch current in low-alpha THz mode. The pattern is, as expected a quadratic dependence, then the changeover and finally a linear dependence is observed in the figure.

### *a)* Multi-Bunch Train

In the case of normal mode, the ring was filled with 468 bunches with the current ramp converted to single bunch values. The results of this data capture are illustrated in Figure 4.14, where the bunch current is on the x-axis and the power of the signal as seen by each of the eight SBDs on the y-axis. Again, in order to achieve the desired range of bunch currents different filling methods were employed and are shown as the variety of different shapes. A half-filled ring was used in order for the lock-in amplifier to function

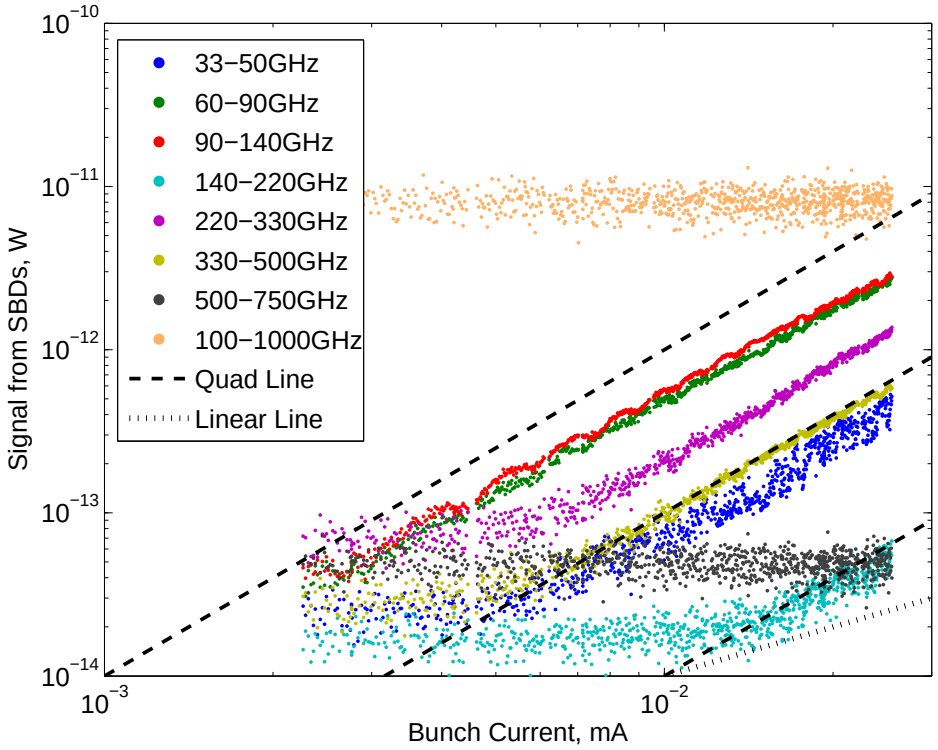


Figure 4.12: Signal observed at the revolution frequency of the ring via all eight channels of the spectrometer for **Normal Mode** with a multi-bunch fill during a current ramp. A quadratic dependence can be observed.

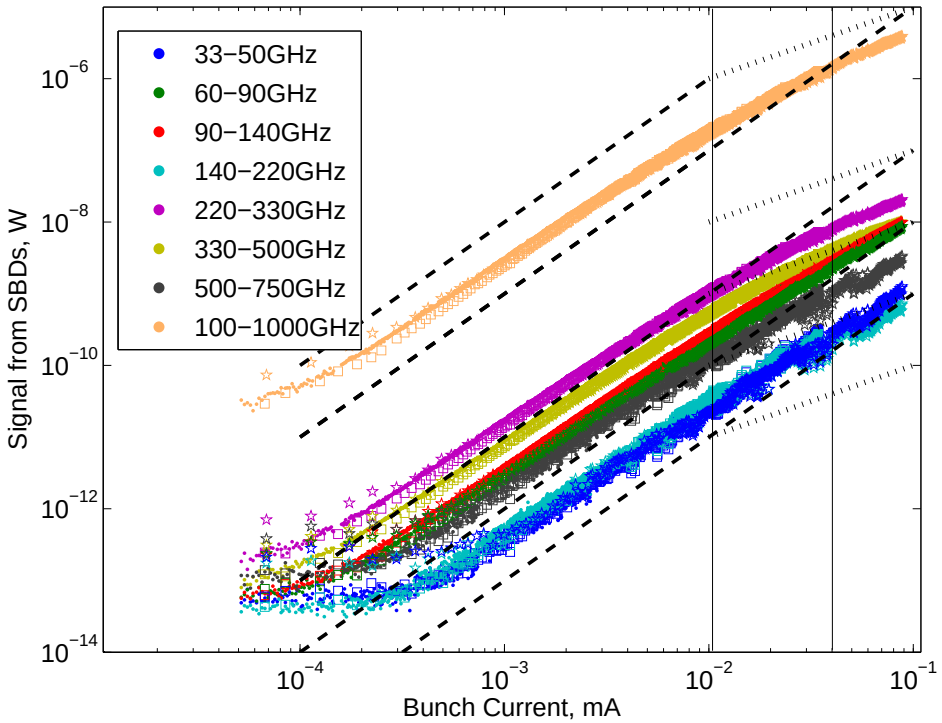


Figure 4.13: Signal observed at the revolution frequency of the ring via all eight channels of the spectrometer for **Low-Alpha THz Mode** with a multi-bunch fill during a current ramp using a variety of different filling methods, where each is shown as a different shape and the changes between the quadratic and linear regimes are marked.

because if the entire ring was filled, the acquisition system would not be able to lock-in to the revolution frequency of the ring. The lock-in technique requires a change of pattern with each revolution. With regards the low-alpha mode, for some of the filling methods undertaken to achieve small injection currents there was no control over the number of buckets filled. This instead was determined by the parameters of the booster, which has 120 buckets. As described above, Figure 4.13 depicts the signal observed at 533.820 kHz by all eight detectors during a multi-bunch train current ramp in low-alpha THz mode.

### *b)* Multi-Bunch with Different Fill Patterns

During low-alpha mode when the ring was filled with bunches not in one continuous train, a quadratic dependence between the bunch current and power is noted by the SBDs as portrayed in Figure 4.14 for normal mode and Figure 4.15 for low-alpha THz mode. Figure 4.15 shows that when the bunch current was increased in a ramp the SBDs detected a quadratic increase in the power of the signal and thus the emission was CSR. A variety of different filling patterns were used in this investigation, where half the ring was always left with empty buckets. Each filling pattern is depicted with a different shape in Figure 4.15. These filling patterns were 100100..., 111111111000000000..., 111000111000... and 100000100000...., where '1' signifies a filled bucket and '0' an empty one. The signal obtained by each of these alternative filling patterns gave very similar results, shown by the agreement between the curves representing the various filling patterns. Though the data are primarily quadratic, the changeover into the linear regime is noticeable as the detectors are exposed to excessive power.

Furthermore in low-alpha mode Figures 4.16 and 4.17 also show the relationship of power observed by the detector array with an increase in bunch current, where the former displays data from all eight channels and the latter just the observed power from three selected SBDs for a clearer view. These two figures display not just multi-bunch filling patterns both in a continuous train and not, but also include true single bunch data for comparison. As can be seen in both Figures 4.16 and 4.17, these alternative spread out multi-bunch patterns correspond with the train-filled multi-bunch patterns (dots, stars and squares), but contrast with true single bunch data (open circles). The single bunch data follows a linear trend unlike the quadratic relationship depicted by data taken in multi-

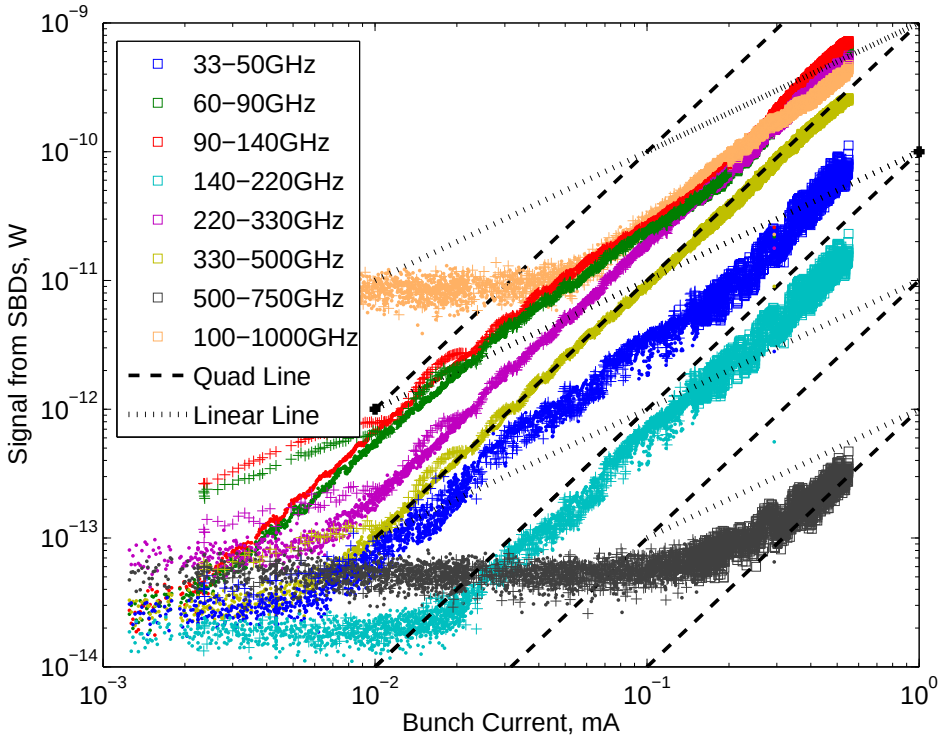


Figure 4.14: Signal observed at the revolution frequency of the ring via all eight channels of the spectrometer for **Normal Mode** with a multi-bunch fill during a current ramp for a variety of different filling methods where each method is depicted as a different shape. A quadratic dependence can be observed.

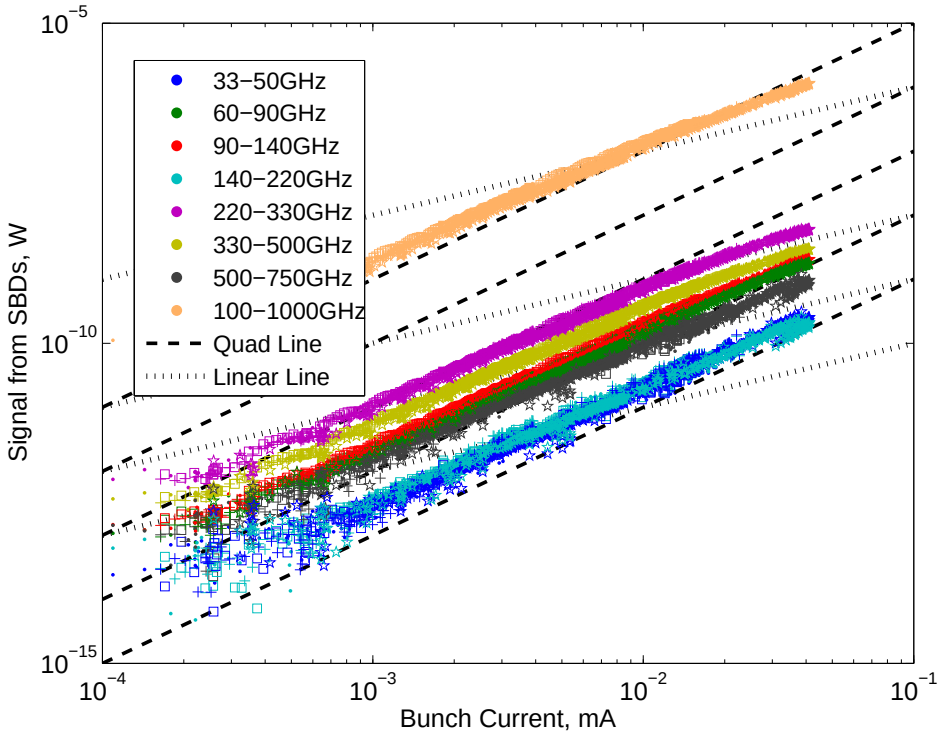


Figure 4.15: Signal observed at the revolution frequency of the ring via all eight channels of the spectrometer for **Low-Alpha THz Mode** during a current ramp for a variety of different non-train filling patterns where each pattern is given a different shape.

bunch mode. The disparity is most obvious at lower currents but as the current increases and the multi-bunch data are driven out of the square-law region, the single bunch data and multi-bunch data begin to match. This is expected, because in single bunch mode the diodes were subjected to too much power, as described in more detail in Section 4.3.3. Despite the contrast between the multi-bunch and single bunch data, the order of the detectors observing the most to the least power is still the same.

### 4.3.3 Comparison Between Single Bunch & Multi-Bunch Fills

When the true single bunch data was compared with the multi-bunch train data that had been translated into single bunch, the 'translated' data did not completely agree with data from true single bunch mode which is apparent in Figures 4.16 and 4.17, as the relevant data sets did not overlap adequately. It emerged that the peak power is most important because SBDs prefer to operate within the square-law region and are by nature continuous wave devices, thus high peak powers of signal being given to them in only a few picoseconds drives them into the linear region of detection. The significance of the detector rise-time or more specifically the decay time is inherent to the diode itself. Using the oscilloscope, it was seen that they recorded no signal between bunches when there was a couple of empty buckets present (Section 4.1). Moreover, the 1 GHz oscilloscope was not stretching the pulse shape. This was confirmed using the 13 GHz fast oscilloscope, also verifying that the pulse shape was true to the diode and not affected by the cabling either. The root for the discrepancy between multi-bunch of any method and single bunch, relates back to the peak power. It must be reiterated that normal mode single bunch does not suffer as greatly. That is to say normal mode single bunch and normal mode multi-bunch are more similar to each other than low-alpha single bunch and low-alpha multi-bunch as shown by comparing Figure 4.18 (normal mode) and Figure 4.16 (low-alpha mode). Both of these figures display the signal observed by the SBDs for an increase of bunch current for multi-bunch and single bunch filling patterns in the case of normal mode or low-alpha mode, respectively. Moreover, the former only depicts multi-bunch data when in one continuous train. The boost in signal at $\sim$1.5 mA can be attributed to the instability threshold. Though the multi-bunch and single bunch data for normal mode do not completely agree, there are strong similarities including the power levels detected

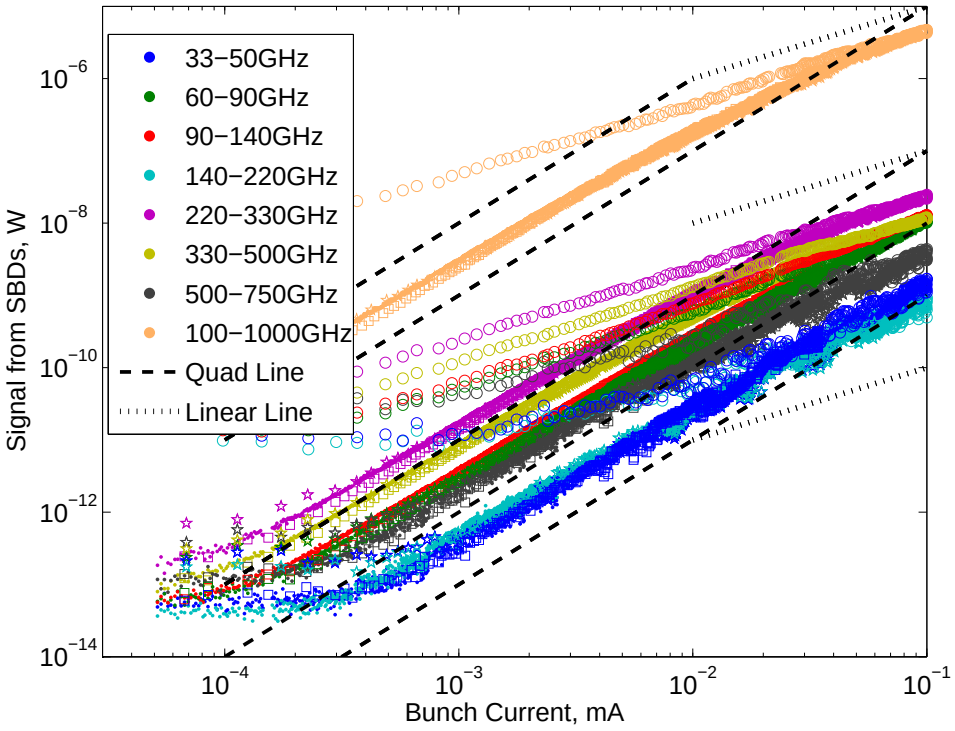


Figure 4.16: Comparison of true Single Bunch (open circles) and Multi-Bunch Train fill (dots, stars and squares) for all eight detectors during a current ramp in **Low-Alpha THz Mode**, where only the signal from the revolution frequency is depicted.

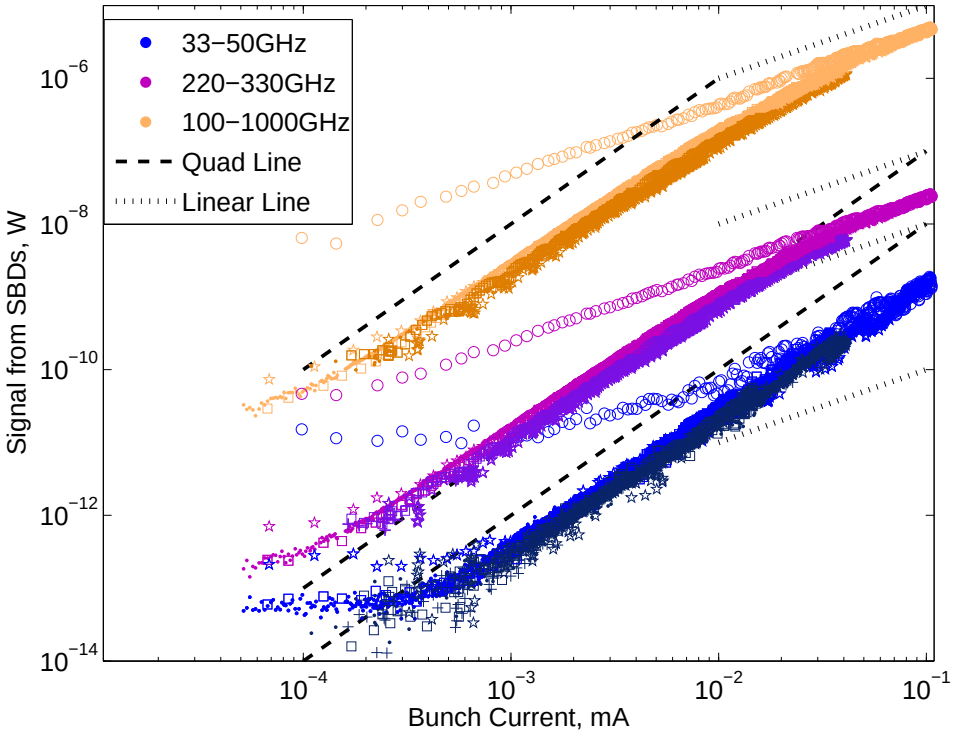


Figure 4.17: The signals depicted in the above figure observed by only three detectors for a clearer view, **Low-Alpha THz Mode** ($\alpha = -4.5 \times 10^{-6}$)where only the signal from the revolution frequency is depicted.

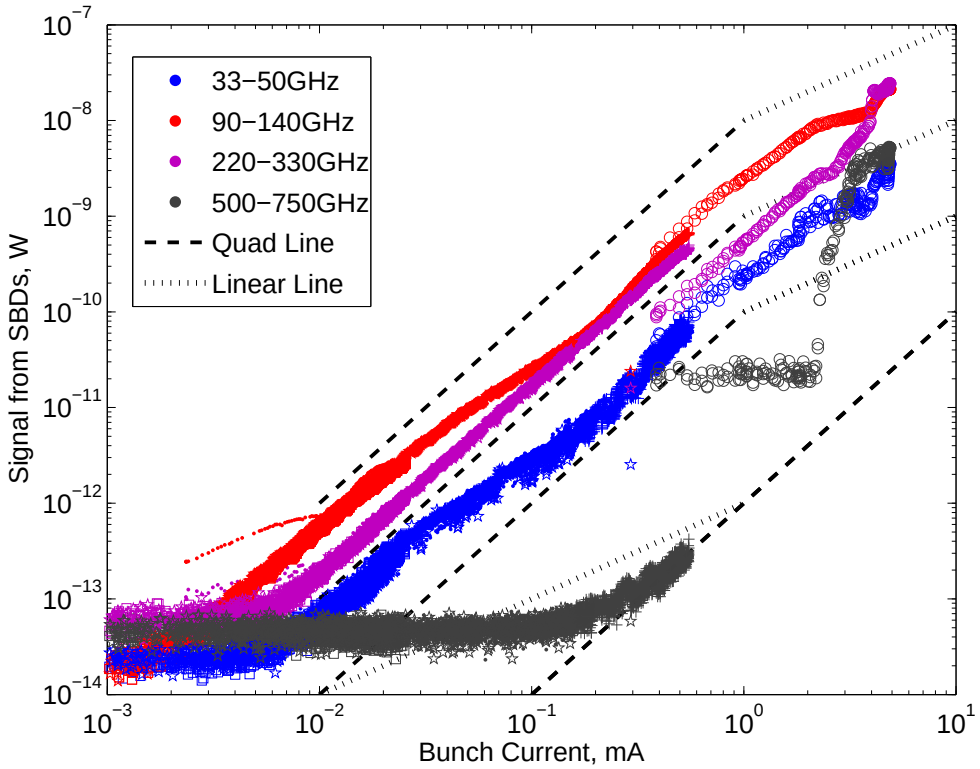


Figure 4.18: Comparison of true Single Bunch (open circles) and Multi-Bunch Train fill (dots, stars, squares, crosses) for all eight detectors during a current ramp in **Normal Mode**, where only the signal from the revolution frequency is depicted. For a clearer view, the signals shown above are only from four detectors.

and the relationship with the bunch current. It is clear to see that the true single bunch signal observed by the 500-750 GHz detector does not agree as well with the multi-bunch set compared to the other detectors, which is further mentioned in Section 4.9.2.

Low-alpha THz mode, which employs $\alpha = -4.5 \times 10^{-6}$, was used in these investigations primarily because the greatest discrepancies between true single bunch and 'translated' single bunch data was observed during low-alpha. Due to the nature of low-alpha, at lower currents stronger signals are more achievable than normal mode and low-alpha is more easily perceived by all detectors than normal mode.

## 4.4 Growth of the Beam

As a result of the three-way motion stages upon which the detector array was secured, raster scans in the xy-plane were carried out at four fixed longitudinal positions. These positions were decided upon by the limit switches of the longitudinal axis of the stage: z=0 mm, z=-100 mm, z=-225 mm and z=-330 mm, where z=0 mm is the location at which the detector array is closest to the source but still a distance of 730 mm from the silica window and thus z=-330 mm when farthest. By executing scans in several longitudinal positions, the growth of the beam from the beamport can be shown. Due to physical restrictions at certain longitudinal positions the detector plate was not always able to scan the full extent of the xy-plane and thus zero-padding was used.

The growth of the beam as seen by each detector for normal user mode and the two varieties of low-alpha mode are displayed in Figures 4.19- 4.23. Each sub-figure that makes up an entire figure shows the peak power observed by a detector at a particular position of the SBD array in the xy-plane denoted in terms of millimetres. This results in the overall beam shape that is seen by the 33-50 GHz detector in normal mode and all SBDs in both low-alpha modes. Each row of sub-figures represents the observations of one detector in the xy-plane at the four longitudinal positions. The first figure (Fig. 4.19) depicts the change of the beam size for the 33-50 GHz SBD as it moves with the array further from the beam source during normal user mode. Only the first detector (33-50 GHz) observes signal during normal mode and hence only it is shown. The beam growth for low-alpha THz mode is shown in Figures 4.20 and 4.21. The final two figures (Figs. 4.22

and 4.23) are relating to the growth of the beam for all eight channels of the SBD array for low-alpha pulse mode.

All eight detectors observe the low-alpha mode signals at every longitudinal position, contrary to the normal mode which is only clearly seen by the 33-50 GHz detector. These observations are expected because low-alpha mode is intended to result in CSR with wavelengths sensitive to the SBDs. Moreover, during normal mode the CSR produced is damped and shielded by the vacuum pipe and minimal CSR is generated in the millimetre regime.

In the band 33-50 GHz, the beam seen is as globular of Gaussian shape, exceptionally smooth during both THz and pulse low-alpha modes. Despite the lower operating currents of the low-alpha modes (10 mA and 20 mA), the peak power is much larger than during normal mode (300 mA). This is as a result of low-alpha modes being designed for THz emission by ensuring no damping of the CSR, as against normal mode where the CSR is shielded by the vacuum pipe. The 60-90 GHz detector also reports a globular, Gaussian shape in both low-alpha modes, though it is smaller by 50%.

Each of the detectors appear to have their own detection patterns, this can be explained by two reasons. The first is the design of the detector and its horn antenna. The three 33-140 GHz detectors are manufactured by Millitech Inc. and all have pyramidal horn antennas. The first two detectors observe a Gaussian distribution during the raster scans, while the 90-140 GHz detector displays a contrasting shape with two peaks. This can be explained by the model of the detector, whereby the 90-140 GHz detector is sold as a 'new and improved' model compared to the older model of the 33-50 GHz and 60-90 GHz detectors. The remaining waveguide detectors (140-750 GHz) are all made by VDI with diagonal horn antennas, except the 140-220 GHz detector which has a conical horn. The theory that the different detector-horn combinations are affecting the results cannot be qualitatively proved as only one type of detector and associated horn antenna was available for each frequency band. Nevertheless, the three horn antenna shapes have very similar detection patterns of a large lobe with small minor lobes.

The second reason and most credible cause is the interaction between the radiation and the inside of the beamport. The beamport contains two significant apertures - a vertical aperture of 11.5 mm and a horizontal aperture of 20.7 mm. In Section 3.1.4, the effect

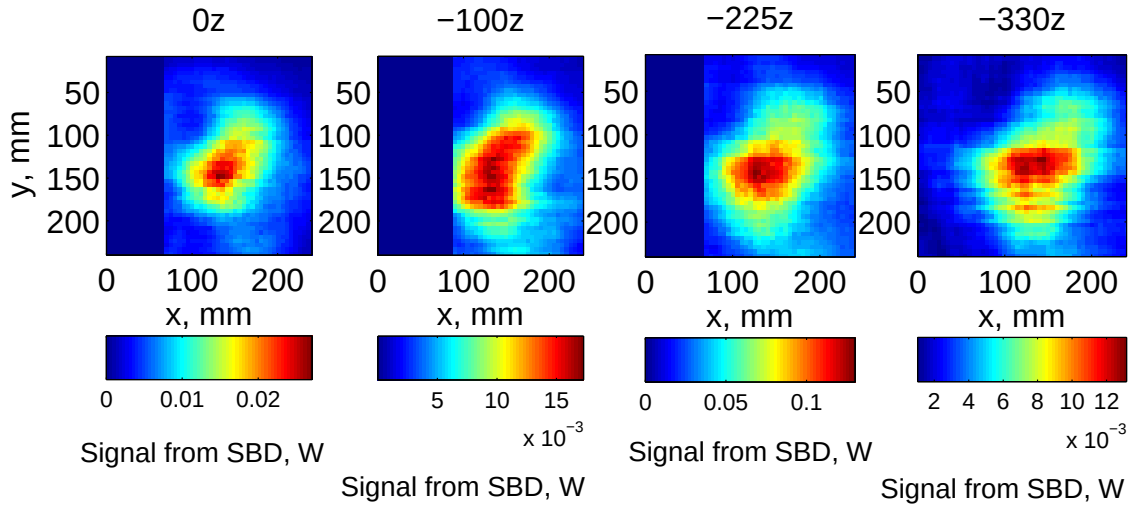


Figure 4.19: The signal observed during a raster scan at four various longitudinal distances from the source during **normal user mode user run** with 300 mA for the 33-50 GHz detector.

of the apertures within the beamport are outlined. The difference between the 33 GHz radiation (Fig. 3.11) and the 220 GHz radiation (Fig. 3.14) at the viewport demonstrates how differently the two frequencies behaved in the beamport. This gives proof that each of the detectors will observe different patterns because the radiation to which they are sensitive will have interacted differently with the beamport. Of course, the overall beam radiation (including mode of machine) will also have an impact combined with the detector and its horn antenna.

Internal bunch information can be gleaned from the raster scans also. The lower frequencies represent the bunch as a whole while the higher frequencies can report on the internal happenings of a bunch. For the detectors 220-750 GHz, it appears that patterns of peak powers observed could be solely due to diffraction, this has been shown not to be the case [125]. In the higher frequencies, the bursts from the micro-bunches can be seen on the raster scans as well as the effects from the apertures in the beamport (Figs. 3.11 and 3.14).

## 4.5 Spectral Power Density

Not only were the raster scans, described in Section 3.2.3, insightful for the growth of the beam and optimal positioning of the detector array, these scans have provided the

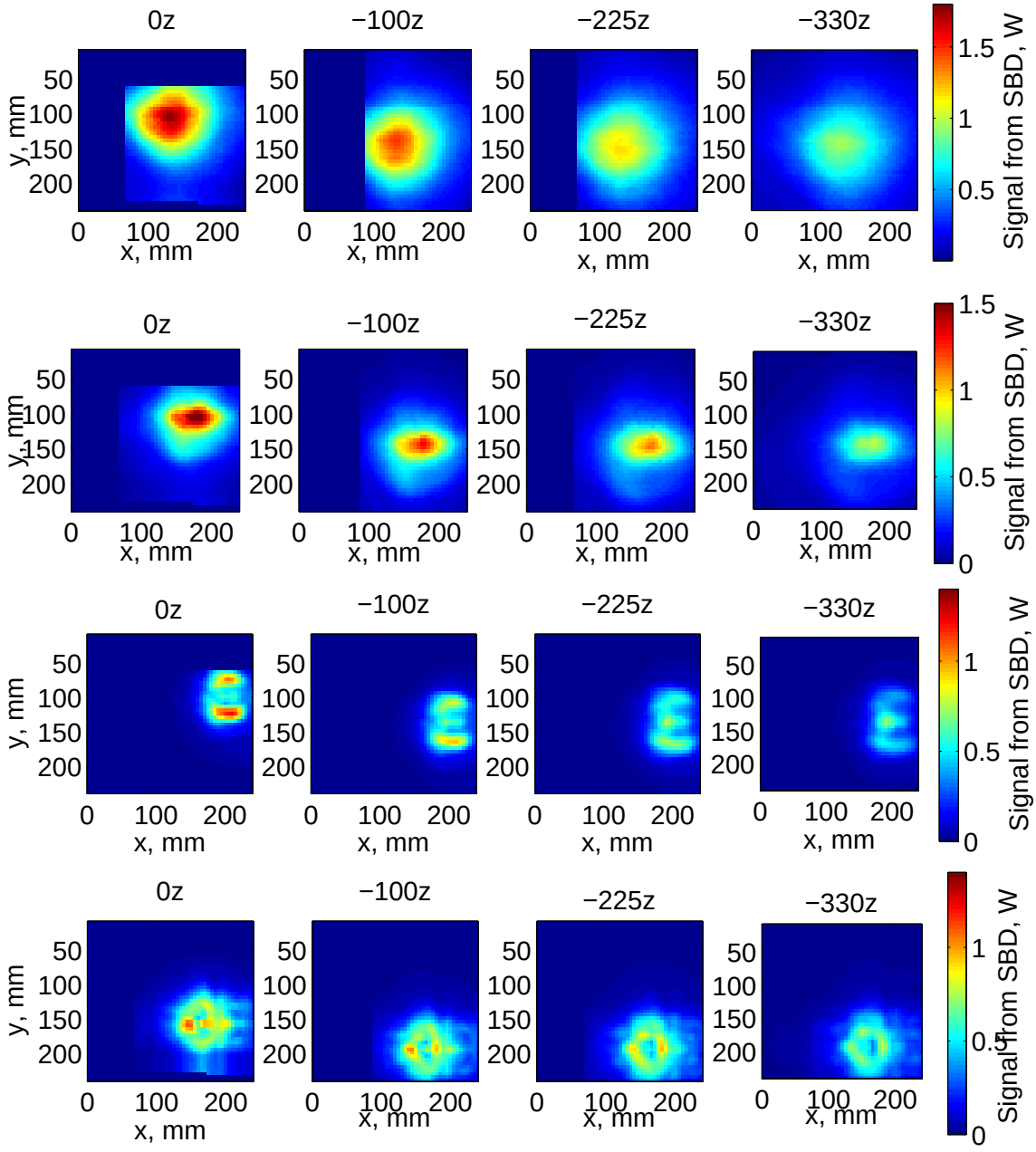


Figure 4.20: The signal observed during a raster scan at four various longitudinal distances (z=0, -100, -225 -330) from the source during **B22 low-alpha THz mode user run** with 10 mA for the 33-220 GHz detectors (33-50 GHz top, 60-90 GHz middle top, 90-140 GHz middle bottom, 140-220 GHz bottom).

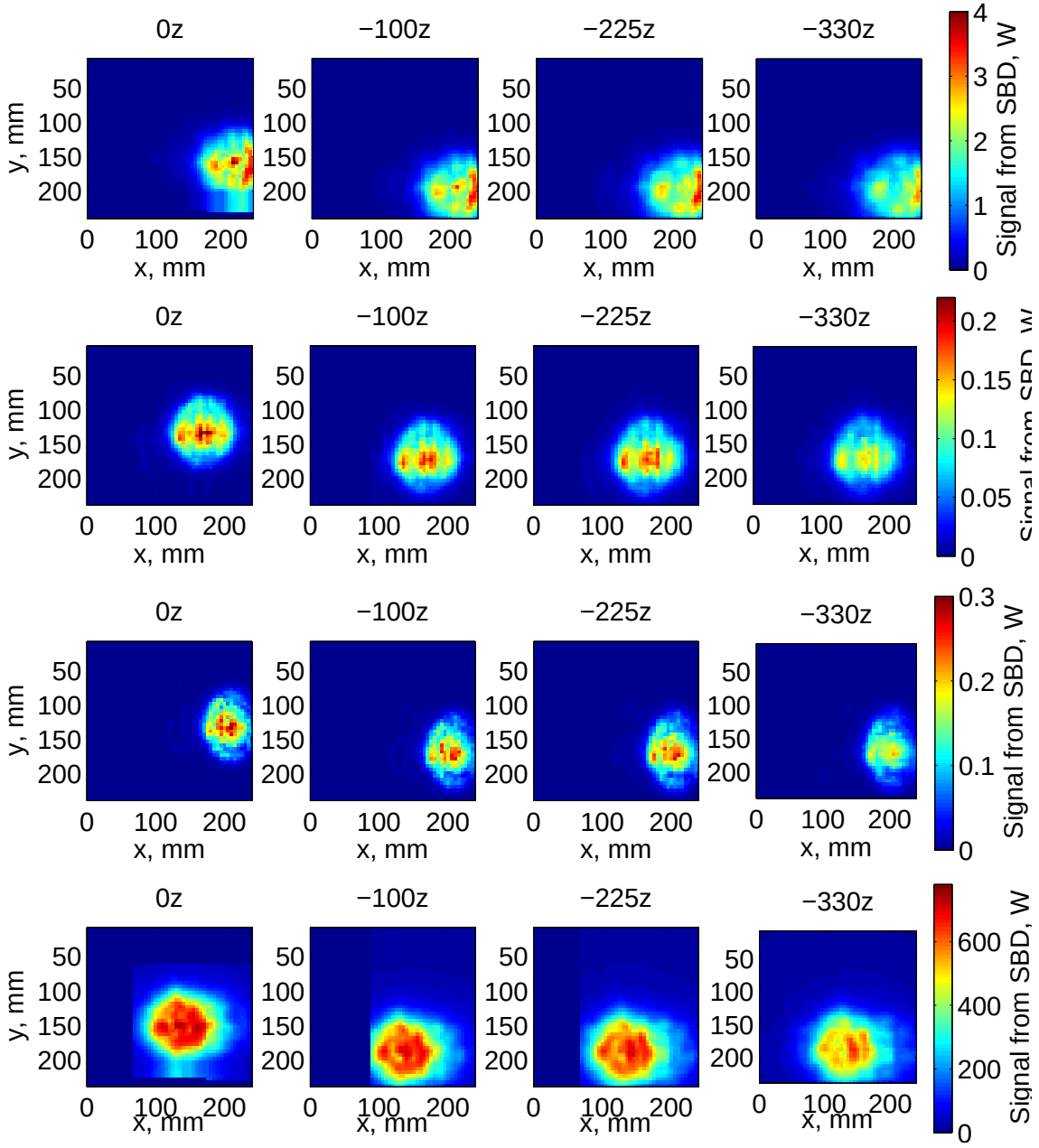


Figure 4.21: The signal observed during a raster scan at four various longitudinal distances (z=0, -100, -225 -330) from the source during **B22 low-alpha THz mode user run** with 10 mA for the 220-1000 GHz detectors (220-330 GHz top, 330-500 GHz middle top, 500-750 GHz middle bottom, 100-1000 GHz bottom).

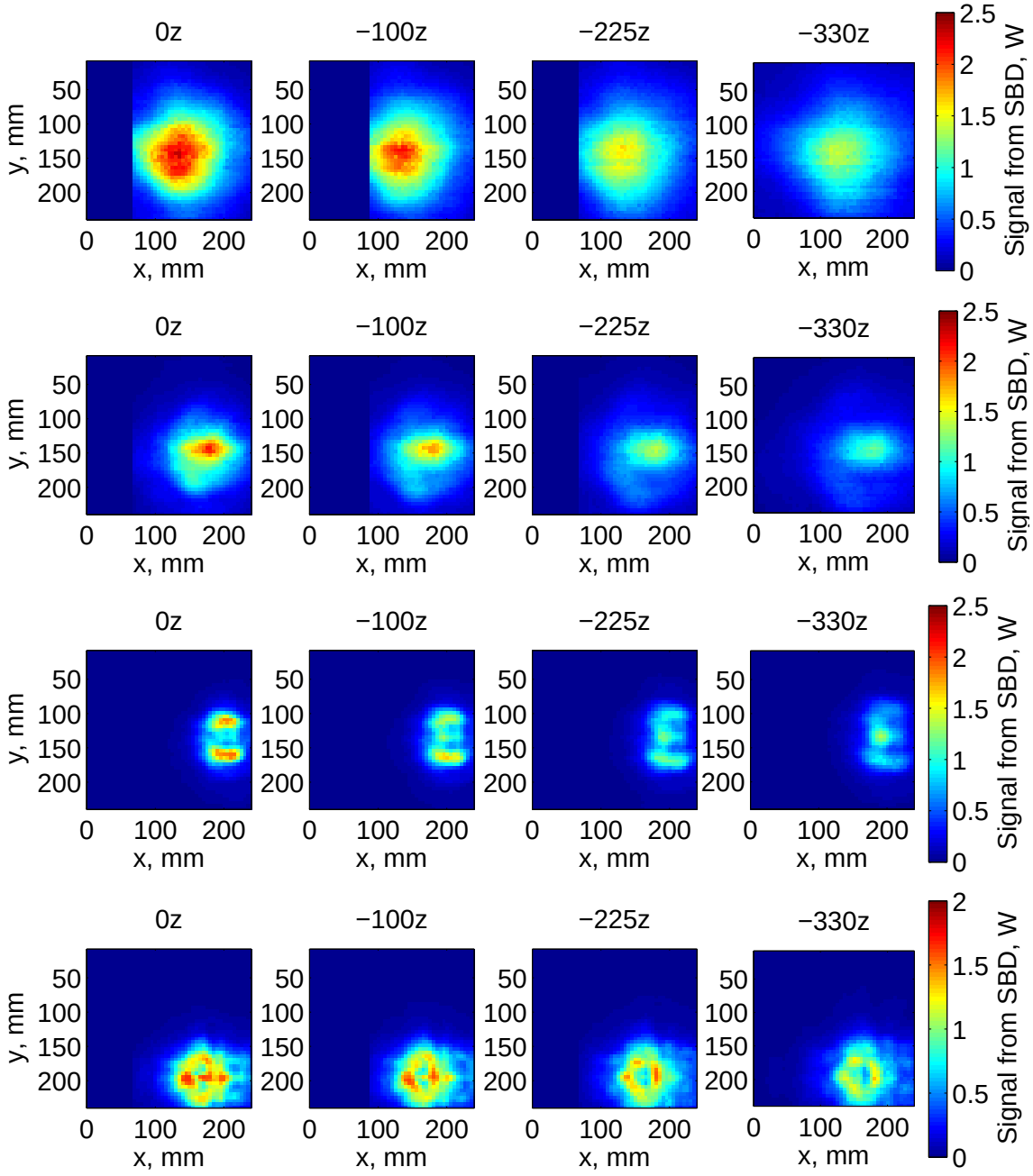


Figure 4.22: The signal observed during a raster scan at four various longitudinal distances from the source during **I06 low-alpha pulse mode user run** with 20 mA for the 33-220 GHz detectors (33-50 GHz top, 60-90 GHz middle top, 90-140 GHz middle bottom, 140-220 GHz bottom).

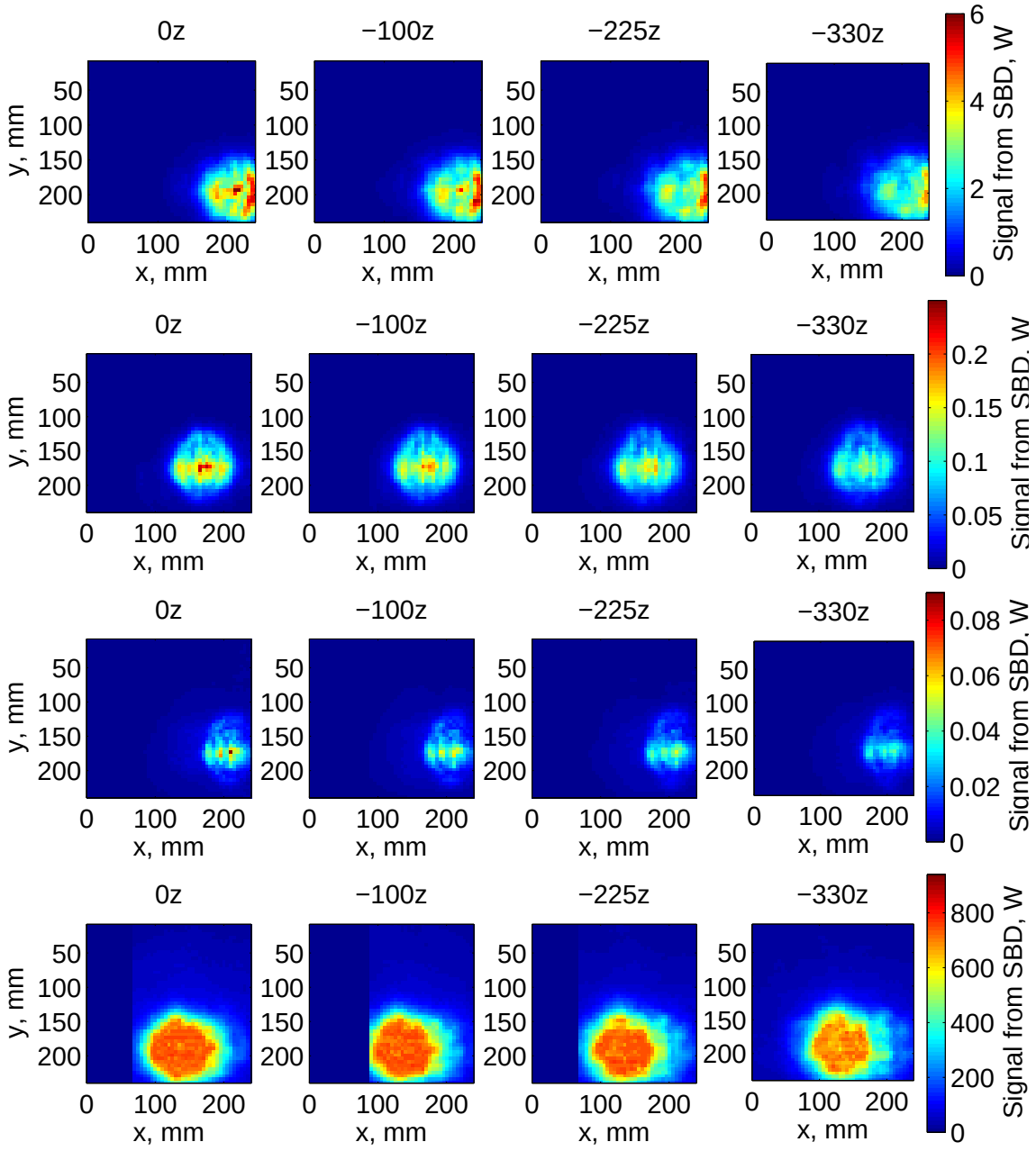


Figure 4.23: The signal observed during a raster scan at four various longitudinal distances from the source during **I06 low-alpha pulse mode user run** with 20 mA for the 220-1000 GHz detectors (220-330 GHz top, 330-500 GHz middle top, 500-750 GHz middle bottom, 100-1000 GHz bottom).

spectral power density of the beam. During different varieties of user runs carried out at Diamond, raster scans were executed. These scans could then be used to determine the spectral power density for each user mode. Data observed solely at the optimal location do not give an accurate enough picture as only one section of the beam is perceived. Hence, the spectral powers are gathered via raster scans where the whole beam is captured.

The spectral power densities are displayed in Figure 4.24 for normal mode with 300 mA, and the two varieties of low-alpha mode at Diamond, THz mode and pulse mode at 10 mA and 20 mA, respectively. The power density is shown for each of the modes as seen by the seven detectors (33-750 GHz) with respect to the central frequency of their true waveguide range. Two versions of low-alpha pulse mode are depicted because during one of the pulse mode user runs only one storage ring RF cavity (rather than two) was functional at Diamond and thus the ring was operated at a lower cavity voltage. Due to the lower cavity voltage of 1.7 MV, usually during low-alpha modes the combined voltage is 3.4 MV, the bunches were not as compressed as usual (Section 2.3). This gives rise to longer bunch lengths and a reduction in the amount of CSR produced compared to usual low-alpha pulse mode. On the streak camera, the pulse length for low-alpha pulse mode with one RF cavity was measured to be 4.2 ps [125], which is almost twice larger than the usual 2.4 ps zero current bunch length. The green curve in Figure 4.24 corresponding to the normal user mode displays a rise in power density for the seventh detector. It is known that the beampipe from B06 through which the radiation travels to the SBD array is not optimised for millimetre nor sub-millimetre wavelengths as presented in Section 3.1. It was considered that the limiting 11.5 m vertical aperture could allow for radiation in the 500-750 GHz band be passed through unhindered by the aperture in contrast to the other frequencies and this could account for the rise in power density in this band [126]. However, this hypothesis cannot be true as it is not supported by the low-alpha mode data. Despite this unexplained rise, it implies that the bunch distribution is not Gaussian as expanded upon in Section 4.9.2 [126].

It is expected that all low-alpha mode cases experience a higher power density [126] as low-alpha modes are designed to compress the bunches leading to CSR. Furthermore, since the SBDs are sensitive to mm wavelengths, accordingly they observe more activity at these wavelengths. As anticipated, low-alpha THz mode achieves the highest spectral

power density, due to the severe squeezing of the bunches and the bunches having high charge densities, thus resulting in MBI, collectively shown in Figure 4.24.

## 4.6 Ratios Between Neighbouring Channels

Despite the channels being treated separately and advertised with the stated frequency bands, it is known and has been discussed within this thesis (Section 3.3.1) that true frequency bandwidths are dictated by the waveguide dimensions themselves. Taking the frequency bandwidths as the hard cut off at the $TE_{10}$ mode and lower cut off of the frequency of the next mode, there are overlaps between the different neighbouring detectors (Table 3.2).

In Figure 4.25, the ratios of adjacent detectors are depicted for a 47 bunch train in low-alpha mode ($\alpha = -4.5 \times 10^{-6}$), whereby the sensitivities per area and effective apertures of each detectors are considered. It is clear to see that second (DXP12) and third (DET08) detectors have a steady relationship as well as the fifth (WR3.4ZBD) and sixth (WR2.2ZBD), with the former pairing having a ratio nearest unity. DXP12 and DET08 are both supplied from Millitech Inc., nonetheless DET08 is of a newer 'improved' design. The remaining four combinations of DXP22 and DXP12, DET08 and WR5.1ZBD, WR5.1ZBD and WR3.4ZBD, WR2.2ZBD and WR1.5ZBD show a growth (or decline) at lower currents but once above approximately 30 μA, where bursting occurs, the ratios level out. This incline can be attributed to the signals becoming greater than each detector's noise floor. The largest ratio (magnitude) is achieved by the WR5.1ZBD and WR3.4ZBD detectors which can also be determined across all low-alpha mode current ramps by eye, for example Figure 4.16.

## 4.7 Effect of the RF Voltage

As described in Section 2.3, the combined RF cavity voltage affects the bunch size; the natural bunch length is inversely proportional to the $\sqrt{V_{rf}}$. It is known that by reducing the size of the electron bunches, the emission of CSR can occur or the onset of MBI also resulting in emission of CSR, hence these effects can be brought about by altering the

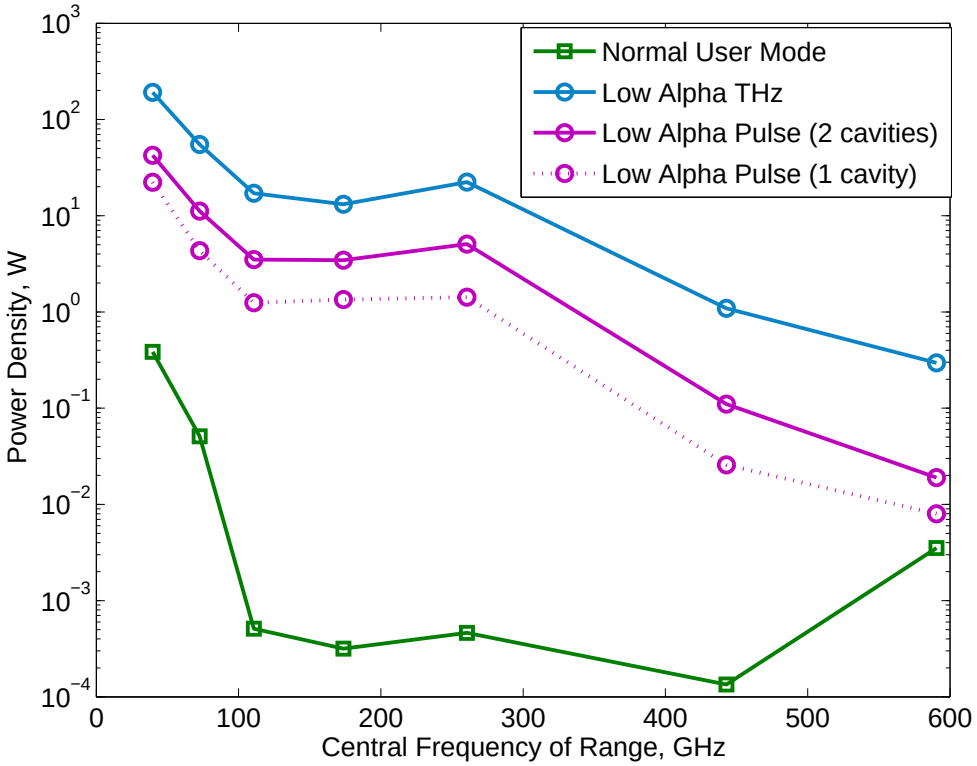


Figure 4.24: Spectral power density for the **Normal Mode** (green squares) and **Low-Alpha Modes** (blue and magenta circles) with respect to the central frequency of the true waveguide range for each of the seven frequency restricted detectors.

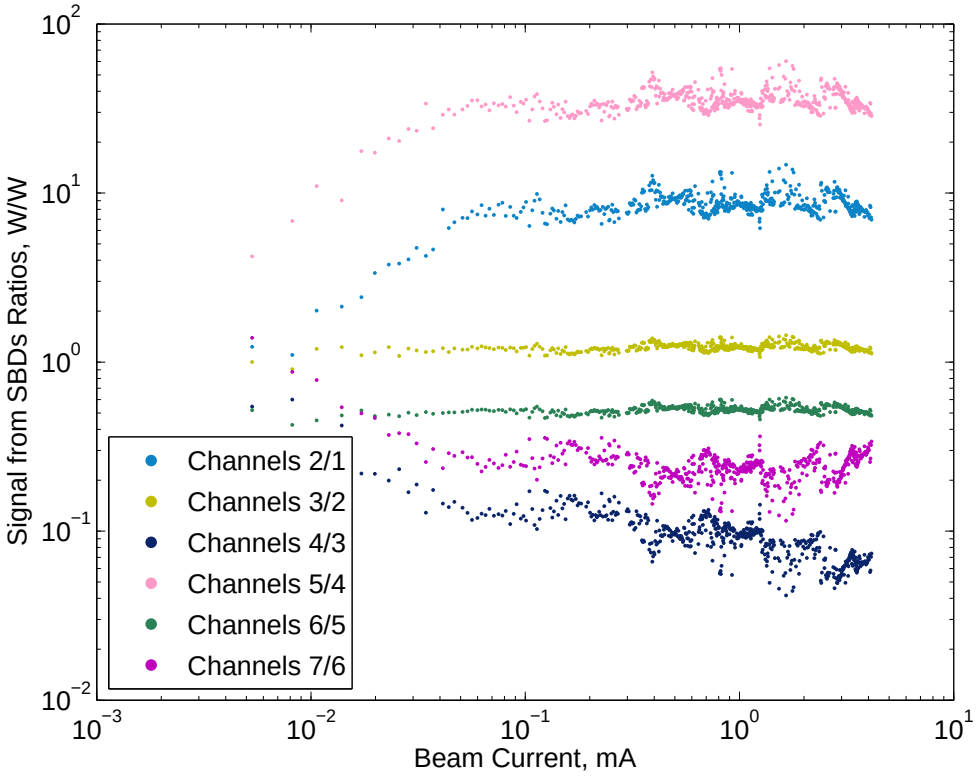


Figure 4.25: Signal ratios of the seven frequency restricted detectors and their neighbour.

momentum compaction factor, the RF voltage or both. In this section, the data obtained for a variety of different RF voltages for normal mode ($\alpha = 1.7 \times 10^{-4}$) with a single bunch is presented.

Figures 4.26 and 4.27 depict the signal observed by the detectors with a rise of bunch current during normal mode single bunch conditions. These current ramps were taken at four different values of the combined RF cavity voltage 2.2 MV, 2.5 MV, 3.0 MV and 3.4 MV, each represented by a different shape dots, squares, stars and crosses, correspondingly. From these figures, it can be seen that with an increase in combined RF cavity voltages the signals observed by the SBDs increase. The reason for this growth is because with smaller bunches, the possibility of the wavelength of radiation being comparable to the size of the bunch is more probable, thus allowing for increased amounts of CSR being radiated from the viewport. Also, by decreasing the bunch size, the bunch charge density can increase and if it goes beyond the threshold value, MBI occur leading to bursts of CSR. It is also observed that the higher the bunch current, the less distinction there is between the four different cavity voltages. It can be assumed that the reason for this is because once the bunch charge threshold has been surpassed, MBI is dominant.

The signals displayed in Figures 4.26 and 4.27 are accompanied by quadratic and linear lines in order to guide the eye. Each of the detectors especially for DXP22 (33-500 GHz), follow somewhat of a quadratic relationship between power and current, however on approach of the higher bunch currents a more linear dependance is achieved. It must be emphasised that these quadratic and linear relationships are not clear cut. The reason for this can be put down to the fact that the data was taken in true single bunch mode. In Section 4.3, the debate between single bunch and multi-bunch filling patterns was aired and though it was concluded that a lower overall peak power was paramount, it has to be remembered that low-alpha mode benefits greatly from multi-bunch and while normal mode does too, not to the same extent.

## 4.8 Decay in Low-Alpha Mode

When the SBD array was composed of only seven detectors, collectively covering a range of 33-750 GHz, low-alpha decay investigations were carried out. The ring was set with

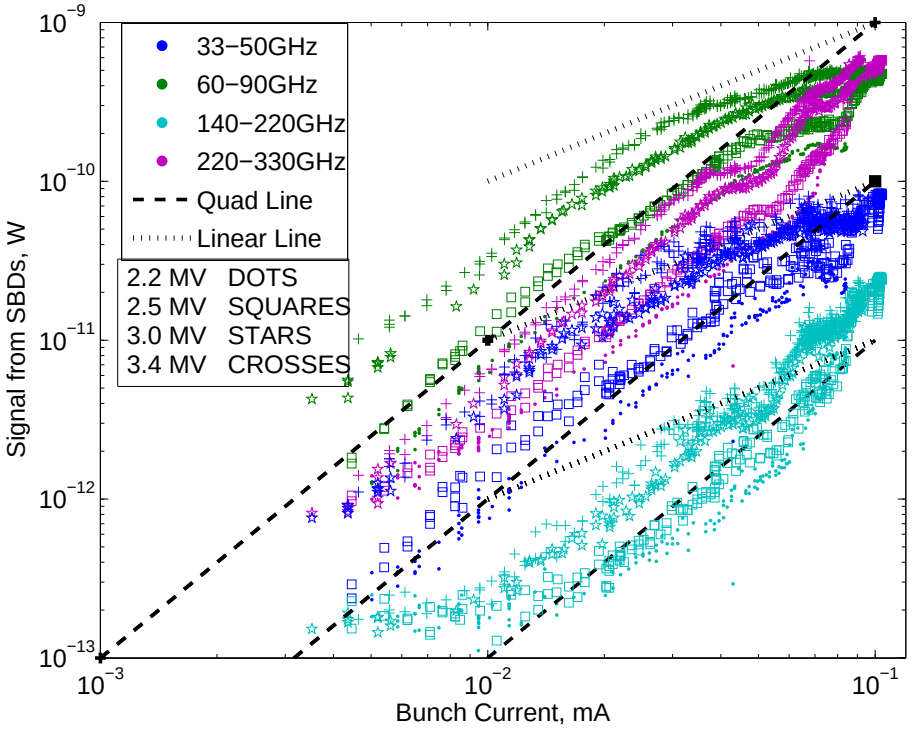


Figure 4.26: Comparison of different RF cavity voltages for SBDs 33-50 GHz, 60-90 GHz, 140-220 GHz and 220-330 GHz under Normal Mode Single Bunch conditions where the signal observed at the revolution frequency of the ring is displayed.

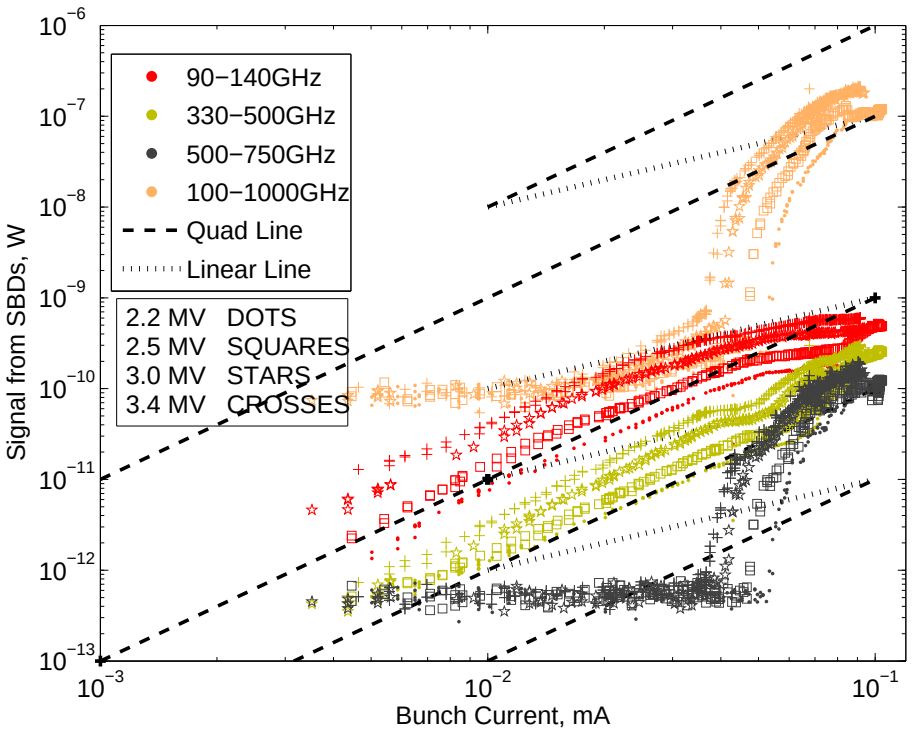


Figure 4.27: Comparison of different RF cavity voltages for SBDs 90-140 GHz, 330-500 GHz, 500-750 GHz and QOD under Normal Mode Single Bunch conditions where the signal observed at the revolution frequency of the ring is displayed.

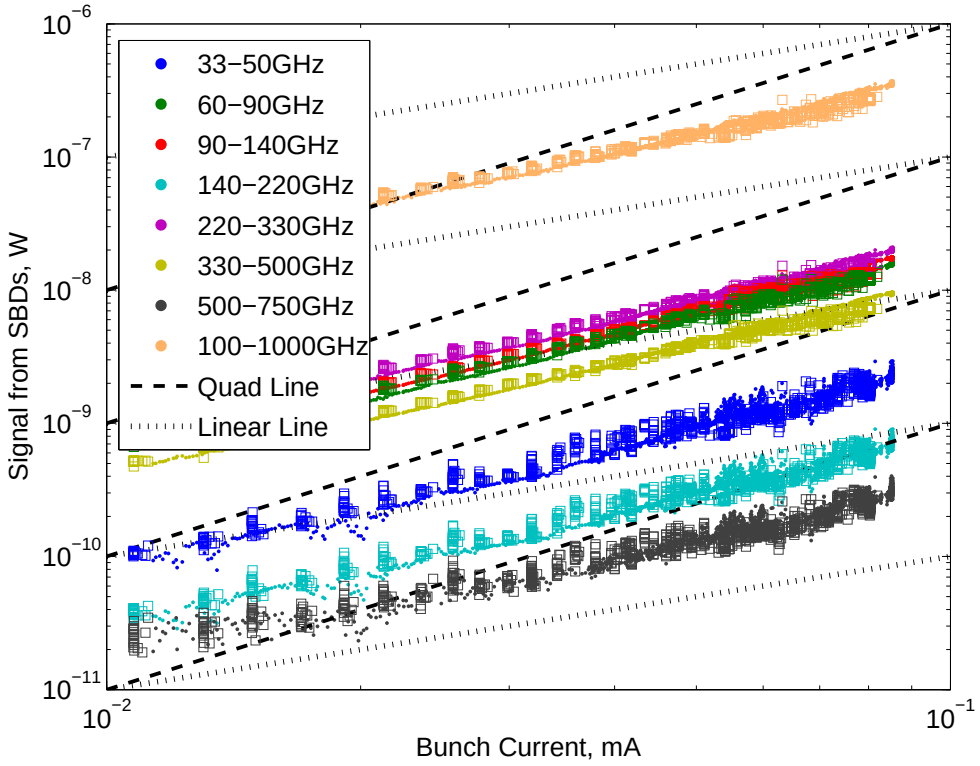


Figure 4.28: A comparison between a current ramp using injection (squares) and current decay using collimators (dots) for single bunch low-alpha mode ($\alpha = -1.4 \times 10^{-5}$) where the combined RF cavity voltage is 4 MV and the signal displayed was observed at the revolution frequency of the ring.

a comparatively 'large' momentum compaction factor for low-alpha mode at Diamond ($\alpha = -1.4 \times 10^{-5}$) and the SBD array placed at z=-70 mm. For a selection of combined RF cavity voltages (4 MV, 3.4 MV and 1.5 MV), a single bunch was injected into the ring with a current on average of 100 μA and the decay observed. Naturally the lifetime of a single bunch with tens of microamps of charge is very large and thus collimators were used to speed up the decay. Only the vertical collimators were slowly brought in evenly from either side and thus slowly scraped away electrons on the periphery. The horizontal collimators at Diamond are used to remove additional injected beam or beam that has been injected incorrectly and are kept much further away from the beam than the vertical collimators. It is known that collimators affect the impedance of the ring and thus can affect the spectrum of CSR (Sections 2.5 and 4.10). This experiment was to see the effect of the collimators on the CSR spectrum in low-alpha mode. In low-alpha mode because the bunches are short, the CSR impedance dominates [76] and therefore the effect of the collimators is negligible.

In order to compare the CSR observed during a current ramp against the CSR seen during a decay with collimators, a corresponding test was carried out to observe the result of a current ramp for each RF cavity voltage. Specifically a single bunch with low current was injected into the ring and slowly more current was added to it. During this current ramp data were continually obtained using the seven channel SBD array. Once at 0.09 mA the ramp was ceased and the decay began. As mentioned previously the vertical collimators were employed to quicken the decay. As with the ramp, throughout the decay the signal observed by each of the seven channels was recorded. When the data from the ramp (squares) were compared against those of the decay (dots), both cases produced comparable results. This is shown by the overlapping of the curves in Figure 4.28 for the case of 4 MV RF voltage with the SBD signal at the revolution frequency versus the bunch current. Due to these results it can be definitively known that the use of collimators to the decay a single bunch low-alpha mode with $\alpha = -1.4 \times 10^{-5}$ does not affect its spectrum. As mentioned above this low-alpha has a 'large' momentum compaction factor thus resulting in 'large' bunches and despite these bunches being 'large' the CSR impedance still dominates. Henceforth, it is deduced that it is true of low-alpha THz and pulse mode as both have significantly smaller momentum compaction factors and hence bunches.

In Figures 4.29, 4.30 and 4.31, the live spectra are shown during each decay for the three RF cavity voltages as detected by the SBD array. Each sub-figure represents what is observed by a specific SBD across the available bandwidth of 33 kHz for each value of bunch current. The most prominent signal observed by the detectors for each different combined cavity voltage is at the revolution frequency i.e. the lock-in frequency. On either side of the lock-in frequency are the sidebands which represent the bursting that is occurring. It can be seen in the figures that at higher currents there is a greater chance of the presence of sidebands as against the lower bunch currents. This is because a charge density threshold must be surpassed to result in CSR bursts. In all cases across all detectors, there exists the MBI threshold at approximately 50 μA.

As is always the case during a live stream of spectra, WR5.1ZBD (140-220 GHz) and WR3.4ZBD (220-330 GHz) observe signal first and continue to experience the most amount of activity within their detection range. On another note and to tie in with the

following section (Section 4.9), it can be seen in all three figures that the 500-750 GHz detector observes the least amount of signal compared to the other SBDs.

## 4.9 Observations with WR1.5ZBD (500-750 GHz)

The SBD array originally began as a six detector array ranging from 33-500 GHz. The seventh detector (500-750 GHz) was purchased after preliminary results showed that there was activity at the higher frequencies. The eighth and final detector added was the broad-band quasi-optical detector with a stated range of 100-1000 GHz. This was incorporated into the array when it had completed work on another experiment. Thus the SBD array now covers a large frequency range of 33-1000 GHz.

### 4.9.1 Higher Detecting Threshold

In Figures 4.11, 4.12, 4.14 and 4.27, the curves representing the QOD and 500-750 GHz detectors follow a similar trend as each other but contrary to the other detectors. With regards the above mentioned figures, the two detectors appear to have higher noise floors. In the case of Figure 4.27 when the detectors in question have obtained sufficient signals to be detected, they explode with a cubic dependance between $\sim$35$\mu$A-45$\mu$A. This is especially obvious for the 500-750 GHz detector, as the QOD does follow a quadratic relationship before the 'jump' to cubic. Similar behaviour is expressed in Figure 4.11 also, with the sudden change in detected signal occurring at approximately 45$\mu$A. The value of bunch current at which this change occurs is dependent upon a variety of factors including the combined cavity voltage where the higher the voltage the lower the bunch current is; the type of mode the machine is in, low-alpha mode calls for a lower bunch current than normal mode. Both a high combined RF cavity voltage and low-alpha mode result in the bunch becoming more compressed leading to emission of CSR. VDI manufacturers both the QOD and 500-750 GHz detector and therefore it is likely that both are made with the same type of Schottky barrier diode. Clearly this diode requires a certain threshold of power before detecting, notably higher than the other detectors in the array. This higher noise floor can be reinforced by the low-alpha case in Figure 4.13, where all diodes are detecting signal but at a higher power than Figures 4.12 and 4.14. The QOD has a much

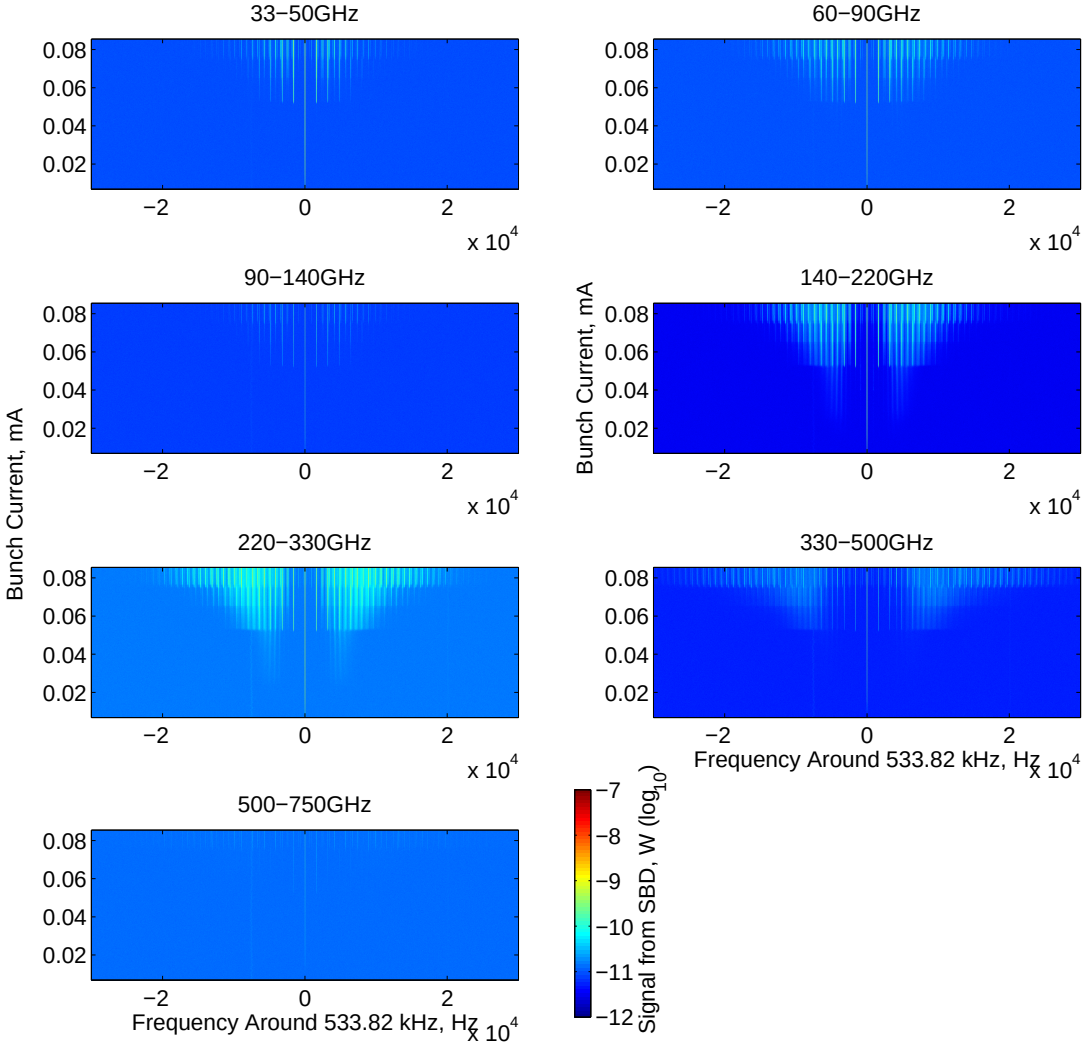


Figure 4.29: Using the vertical collimators for the decay of single bunch low-alpha mode ($\alpha = -1.4 \times 10^{-5}$) at a combined RF cavity voltage of 4 MV, as viewed by the seven frequency restricted SBDs.

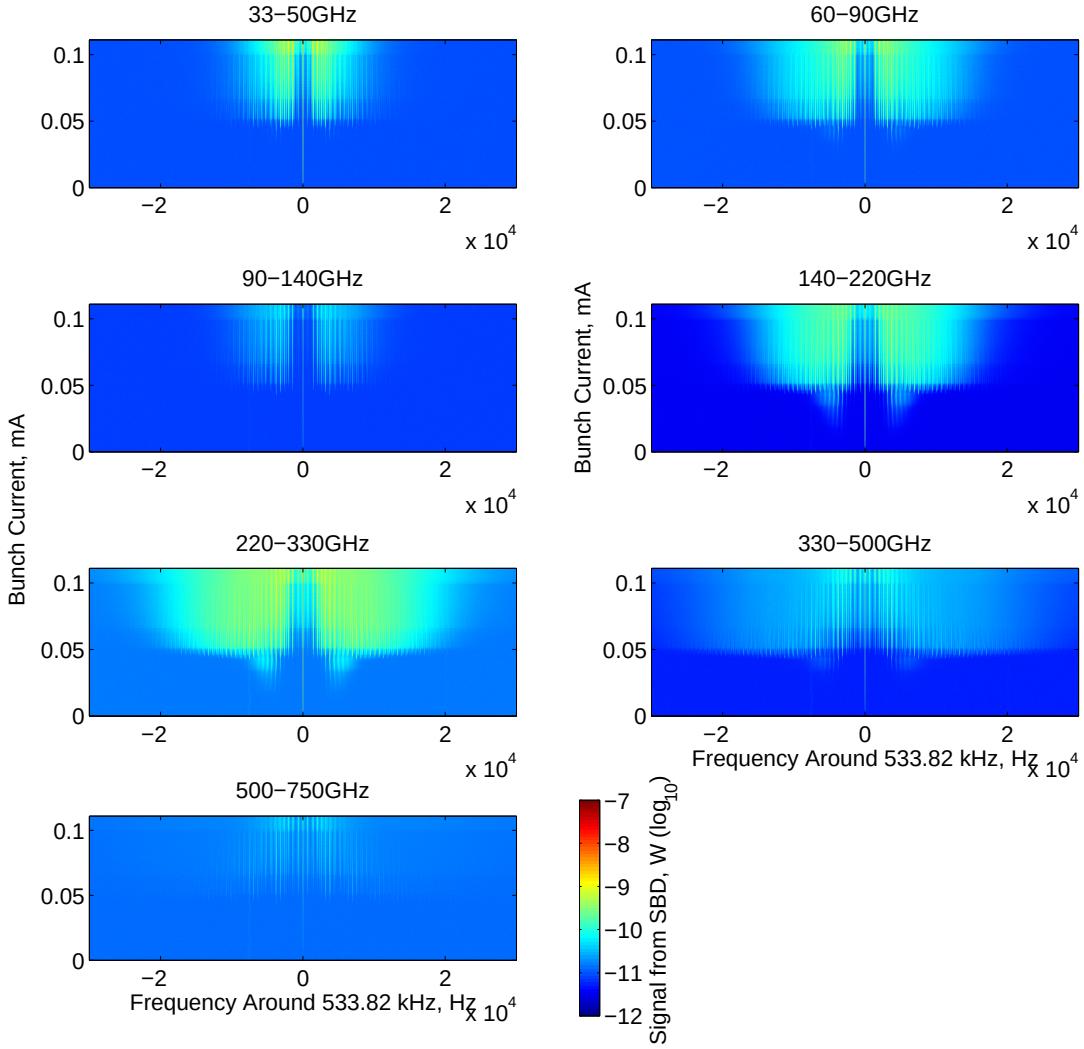


Figure 4.30: Using the vertical collimators for the decay of single bunch low-alpha mode ($\alpha = -1.4 \times 10^{-5}$) at a combined RF cavity voltage of 3.4 MV, as viewed by the seven frequency restricted SBDs.

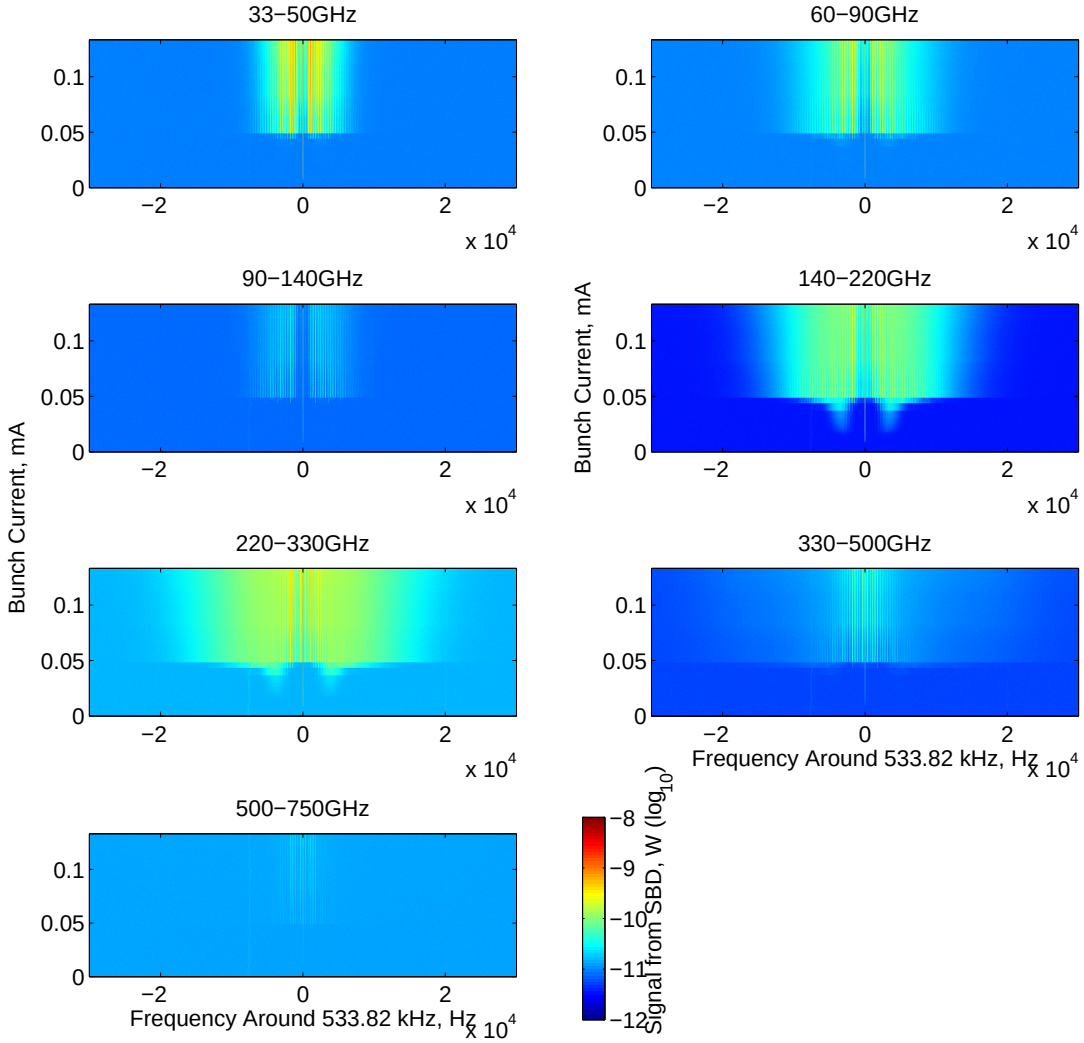


Figure 4.31: Using the vertical collimators for the decay of single bunch low-alpha mode ($\alpha = -1.4 \times 10^{-5}$) at a combined RF cavity voltage of 1.5 MV, as viewed by the seven frequency restricted SBDs.

larger bandwidth and thus should reach the threshold sooner during a current ramp, which is depicted in Figures 4.14 and 4.27. That is to say at lower bunch current values compared to the 500-750 GHz SBD, the broadband QOD should surpass its detection threshold. Moreover, it should be noted that both detectors undergo the 'jump' to cubic dependence for each RF voltage at corresponding bunch current values (Fig. 4.27).

### 4.9.2 Anomalies in Normal User Mode

During an experiment when the part-processed data are being streamed onto a control room computer, it is interesting to note that the 500-750 GHz detector is one of the four which detects the most amount of signal in normal mode, however in low-alpha mode it detects the least compared to the other SBDs [126]. This is not to be expected. The beam is expected to have a Gaussian distribution in normal mode (and low-alpha mode). Thus the detectors should be observing less and less the higher in frequency they are able to detect. The reason for normal mode observations is that the 500-750 GHz detector observes the signal coming from the tail of the bunch form-factor. Nevertheless the signal is strongly detected insinuating that the distribution is not entirely Gaussian [126] and perhaps that some density fluctuation is occurring. In Figure 4.24, the signal observed by the 500-750 GHz detector in normal mode is out of step with the other detectors observing normal mode and also with the 500-750 GHz detector for the other beam conditions. The inconsistency of signal detected by the seventh detector in normal mode versus low-alpha modes is discussed in the corresponding Section 4.5. Figure 4.32 illustrates the relationship between bunch current and signal detected by the WR1.5ZBD (500-750 GHz) detector in both normal mode and low-alpha THz mode during a current ramp. It is clear to see that the detector observes more signal in low-alpha mode than it does normal mode and also at lower currents in the case of low-alpha mode, nevertheless the contrast in detection is against the other detectors during the operation modes.

## 4.10 Additional Benefits of the SBD Array

As mentioned in Section 3.2.4, the SBD array has been advantageous in other applications. An investigation was carried out to determine the effect of THz emission during the

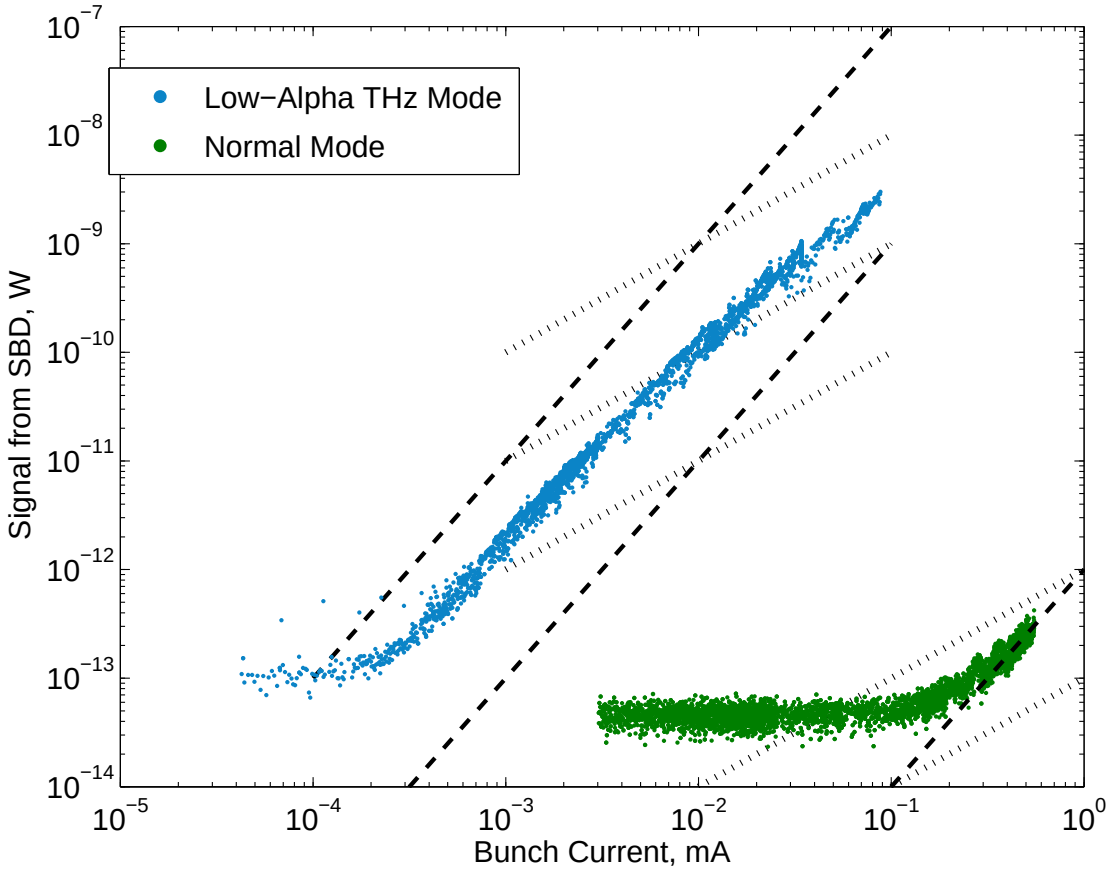


Figure 4.32: Relationship between signal at the revolution frequency of the ring observed by the 500-750 GHz detector and the bunch current for Normal Mode (green) and Low-Alpha Mode for THz (blue), where quadratic lines are dashed and linear dotted [126].

THz low-alpha mode user run ($\alpha = -4.5 \times 10^{-6}$), if another beamline was operating both of their insertion devices, the upstream and downstream undulators. The movement of insertion devices is known to effect certain SR frequencies. The investigation involved the use of the SBD array streaming on all eight channels into the control room of Diamond. While observing the frequencies detected by the eight SBDs of the spectrometer, the upstream undulator scanned through its opening distances at varying speeds and the same was done for the second undulator. The machine was operated in low-alpha THz user conditions throughout the experiment. During the continual observation, no change in the eight spectra could be seen live by eye. Moreover, by plotting the signal from each SBD and the undulator opening values of the undulators it was concluded that the movement of these undulators would not alter the frequencies or strength of signal during the THz low-alpha mode user run. Figure 4.33 shows the movements of the first insertion device of

beamline I06, with the signal observed via two channels (33-50 GHz and 220-330 GHz) in each case when set-up in low-alpha THz user mode (200+1 bunches and $\sim$10 mA).

The collimators of a storage ring are used in order the dispel additional current or the entire beam. They can be implemented to scrape excess electrons from the peripheries of the beam in either the horizontal or vertical plane. In a storage ring, electron bunches can interact with the beampipe resulting in wake-fields, which can act back on the bunch itself, thus affecting its beam dynamics. These wake-fields are due to the machine's impedance. Collimators are known to affect the impedance of a machine and therefore impact upon the SR in particular CSR as the latter is amplified by the wake-field and bunch interaction (Section 2.5). During operation, the collimators are kept away from the beam in order to limit the effect of impedance and are hence only called upon when required. It has been determined that only normal mode is adversely affected by the use of collimators, contrary to low-alpha mode which is not (Section 4.8). The reason can be attributed to when the electrons are housed in short bunches the CSR impedance dominates and thus the effect of the machine's impedance does not influence the spectra. While in the case of the comparatively long bunches for normal mode and even longer for a single bunch in normal mode, the CSR impedance is not as prevalent and thus the effects of other impedances impact upon the beam and thus the spectra.

An experiment was carried out to show and experimentally prove that the movement of collimators affected the THz spectrum of the SR during normal mode single bunch operation. It was seen when the vertical collimators were brought closer to the beam, the spectrum changed drastically and when moved apart the spectrum would be altered again. The largest variation in the spectra occurred when the vertical collimators were moved to and from having gaps of 3.5 mm to 4 mm. It is actually due to the impedance effect of the collimators that current ramps rather than decays were performed. To wait for the beam to decay is time-consuming especially when working on a user facility. A decay could not be expedited by scraping the beam with collimators as it would not result in a realistic outcome of what would have happened had the collimators not been present and thus not affecting the machine's impedance.

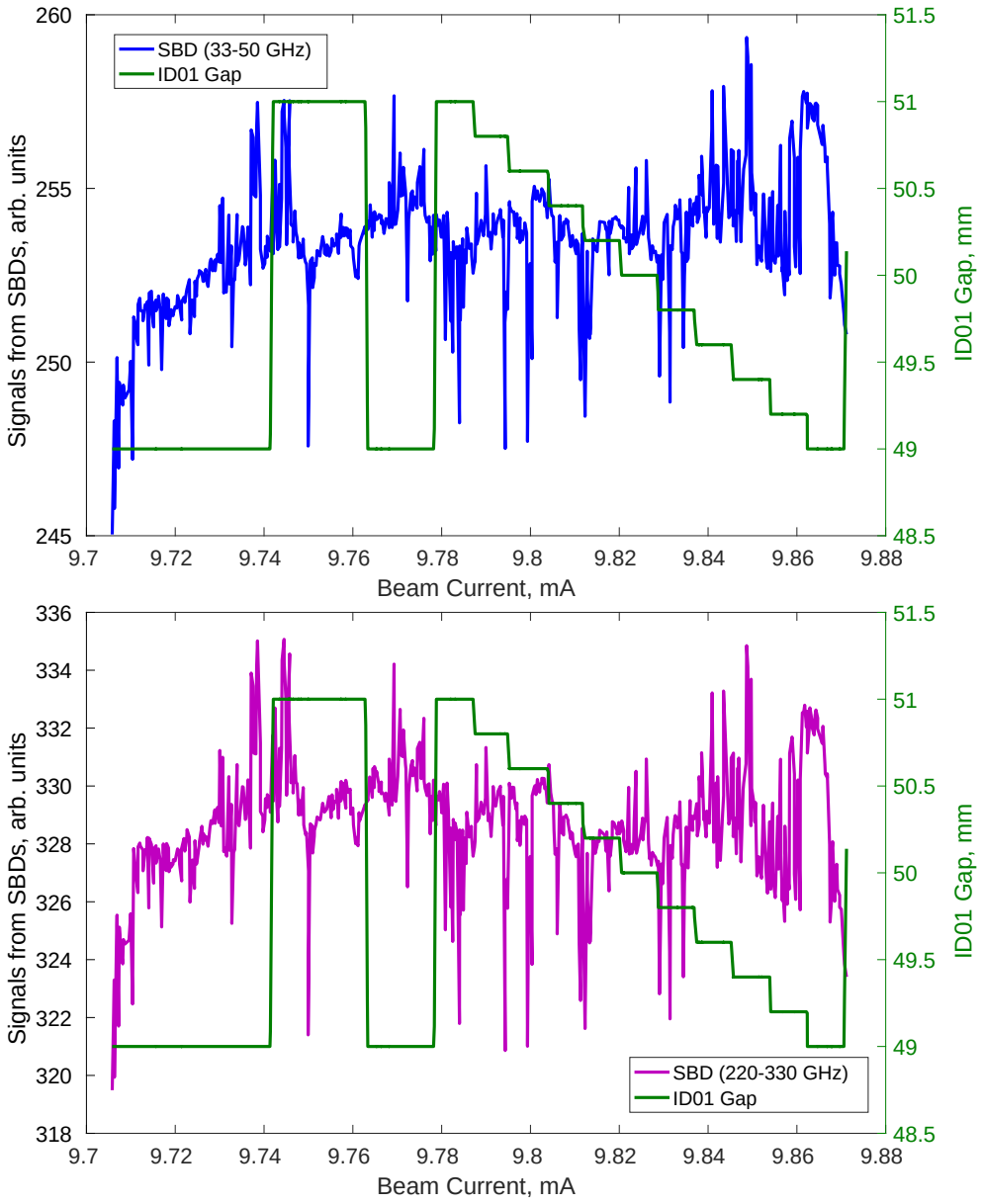


Figure 4.33: The signal observed via two channels of the SBD array (33-50 GHz top, 220-330 GHz bottom) during Low-Alpha THz user mode while moving the downstream ID (ID01) of beamline I06.

## 4.11 Bursting Observations

In the previous sections of this chapter, the data portrayed and investigated was based on that from the steady state emission. The steady state emission is the signal that occurs at the revolution frequency of the ring and also the frequency that is 'locked' into with the data acquisition unit. By looking at the steady state, the detector array could be further characterised and more known about the ring and the nature of the CSR produced. However, with true 'bursting' the MBI are really occurring within the sidebands and not at the revolution frequency. The data acquisition system has been set-up so as to have as wide a bandwidth as possible within the limits of the electronics, that is 87391.43 Hz either side of the 533.820 kHz revolution frequency of the ring. The instabilities observed within the sidebands are showcased in this section, they are not fully understood and it is hoped that soon their mystery will be a remnant of the past.

During an experiment, the data being captured could be seen in real-time in the form of spectrograms. Each spectrogram for each of the eight detectors displayed the signal determined at the revolution frequency (533.820 kHz) as well as that within the approximate 87 kHz of bandwidth either side. It was due to this continual data presentation that changes observed by each detector could be observed in real-time. One such observation is the order upon which each detector observes signal and this order is true of every experiment carried out in the same mode, that is to say either normal mode or low-alpha mode irrespective of the number of bunches. The first signals observed by the detectors are due to the revolution frequency of the ring. In the case of normal mode, the order of initial observation is first the 33-50 GHz detector, then the broadband 100-1000 GHz detector, the 60-90 GHz detector and finally the seventh 500-750 GHz detector. These four detectors 'turn on' very soon after one another with significantly more signal than the rest. The remaining detectors (90-500 GHz) require more signal before they are seen to be detecting. This can be shown for normal mode in Figure 4.34. It must be noted that the quasi-optical detector and the 33-50 GHz band detector do swap positions at a bunch current of approximately 77 $\mu$A. The sequence in which the detectors observe the signal from the revolution frequency sheds light on what is happening in the storage ring. The beam is expected to have a Gaussian distribution, which would hence result in the

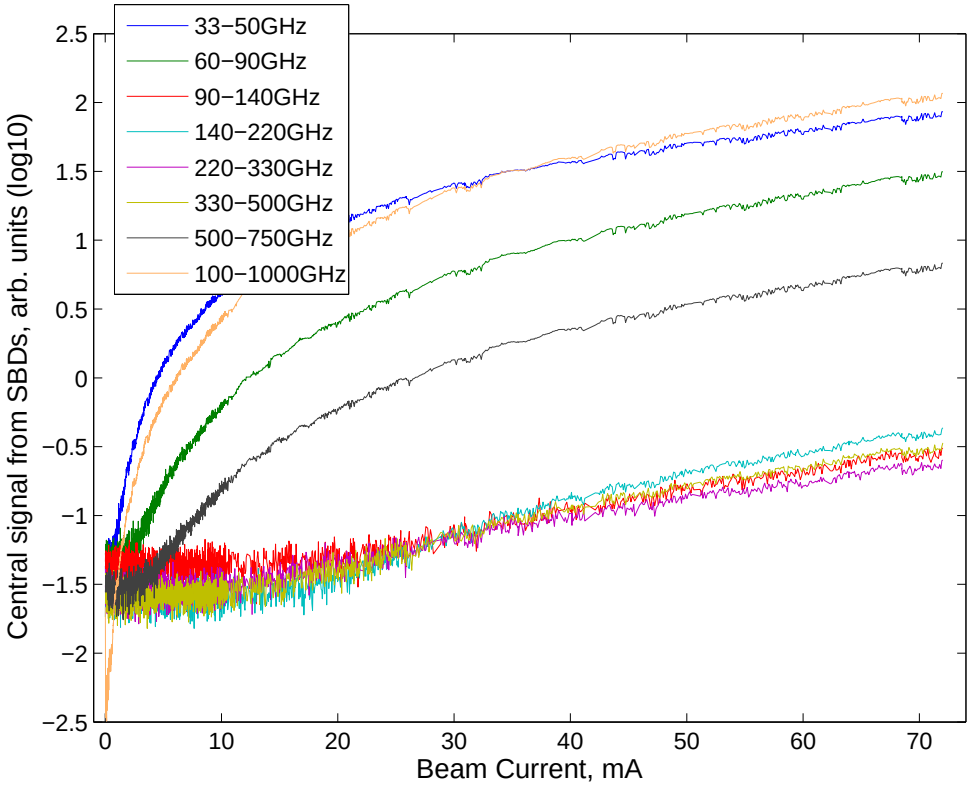


Figure 4.34: The signal observed at the revolution frequency by each of the detectors during a **normal mode** multi-bunch current ramp with each detector depicted as a different colour.

strongest signals to be found in the lower frequency ranges. The two waveguide restricted detectors observing the most are the 33-50 GHz and the 60-90 GHz bands which is in keeping with the Gaussian distribution. The quasi-optical detector is also observing significant signal and though stated to have a range of 100-1000 GHz frequency bandwidth, as discussed in Section 3.4.4, it is not a definitive range and the detector can detect both above and below its stated range. Moreover having a larger bandwidth means that it can accumulate more signal. The signal seen by the 500-750 GHz detector is due to the tail of the Gaussian distribution but as substantial signal is detected, it can be concluded that the distribution is not entirely Gaussian and this is also remarked on in Section 4.9.2. The observations by the 500-750 GHz detector can be supported by those of the quasi-optical detector.

Figure 4.35 depicts the signal observed at the revolution frequency (red) by each of the eight detectors and the signal from the sidebands (blue) under the beam conditions of normal mode multi-bunch. The blue sidebands are the collective signal from the 87.4 kHz

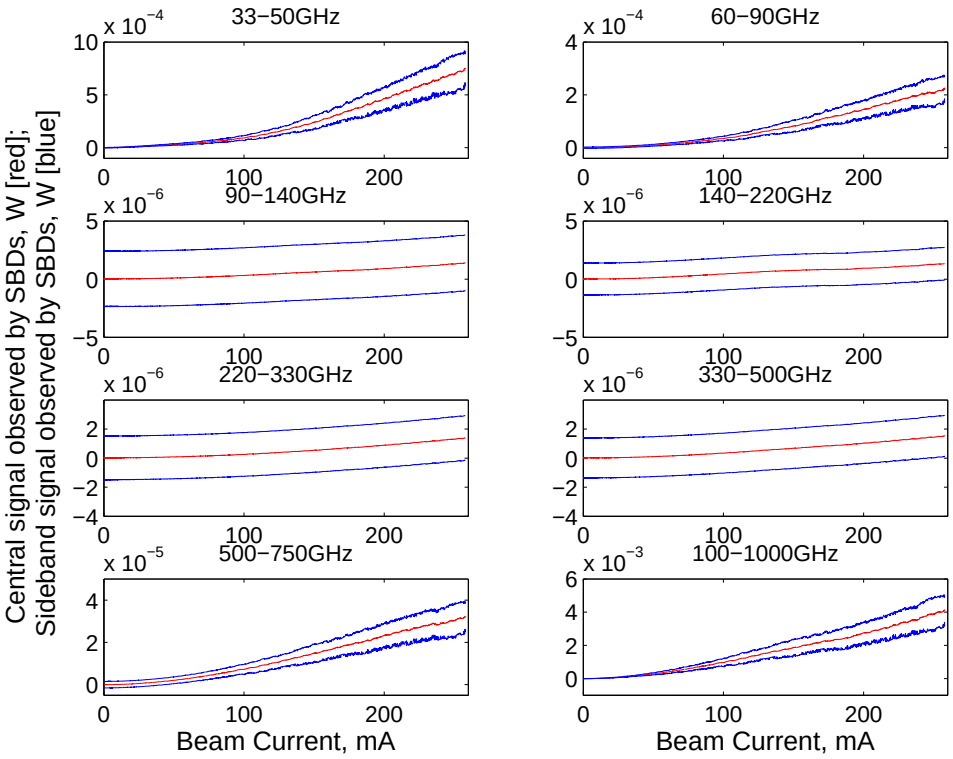


Figure 4.35: The signal observed at the revolution frequency by each of the detectors during a **normal mode** multi-bunch current ramp depicted in red and the activity in the sidebands under the same conditions depicted in blue against the beam current.

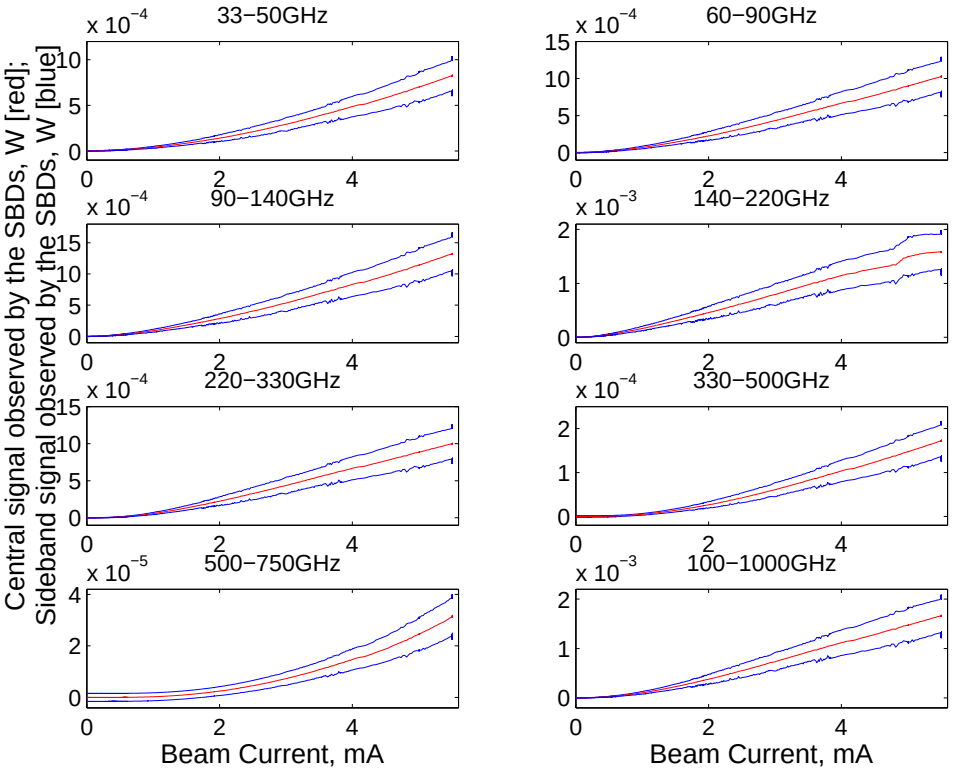


Figure 4.36: The signal observed at the revolution frequency by each of the detectors during **low-alpha THz mode** multi-bunch current ramps depicted in red and the activity in the sidebands under the same conditions depicted in blue against the beam current.

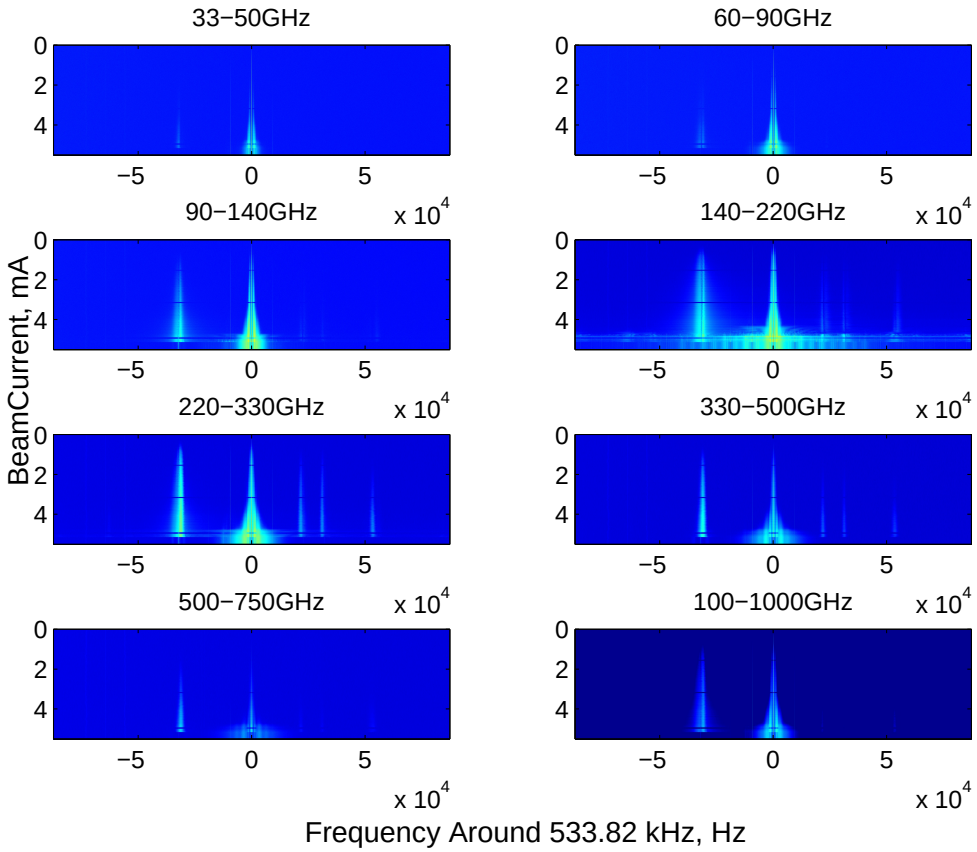


Figure 4.37: The eight spectrograms as seen by the eight detectors during a **low-alpha THz mode** multi-bunch current ramp with 158 bunches with a bandwidth of approximately 87 kHz and where the subfigures are on the same colour-scale.

bandwidth either side of the 533.820 kHz revolution frequency. It is in the sidebands that the CSR bursting is witnessed. Initially the blue sidebands appear to create an even tunnel around the central frequency, however the sidebands begin to widen as the current increases. This is due to a increase in the power produced from the CSR. Focusing solely on the red curve representing the signal observed at the revolution frequency, there is an increase across all frequency bands with respect to current. In four of the detectors this increase is gradual with minimal change in the slope (90-500 GHz). With regards the other four (33-50 GHz, 69-90 GHz, 500-750 GHz and 100-1000 GHz), the slope increases more sharply. As well as an increase in slope, the sidebands which are parallel to one another begin to spread out forming more of a cone shape. This growth of the sidebands demonstrates that there is activity. It is known that true bursting has happened when the sidebands step-change to more erratic behaviour.

For the low-alpha THz mode multi-bunch case all eight detectors display activity in

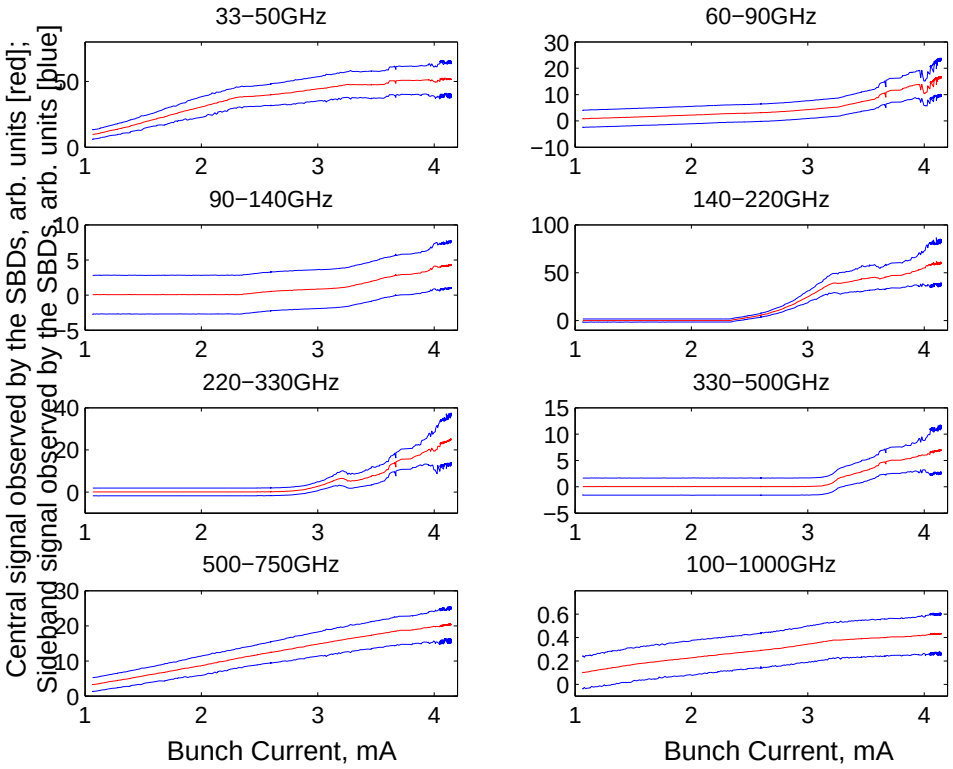


Figure 4.38: The signal observed at the revolution frequency by each of the detectors during a **normal mode** single bunch current ramp depicted in red and the activity in the sidebands under the same conditions depicted in blue against the beam current. The combined RF cavity voltage was 2.2 MV as opposed to the usual 2.5 MV.

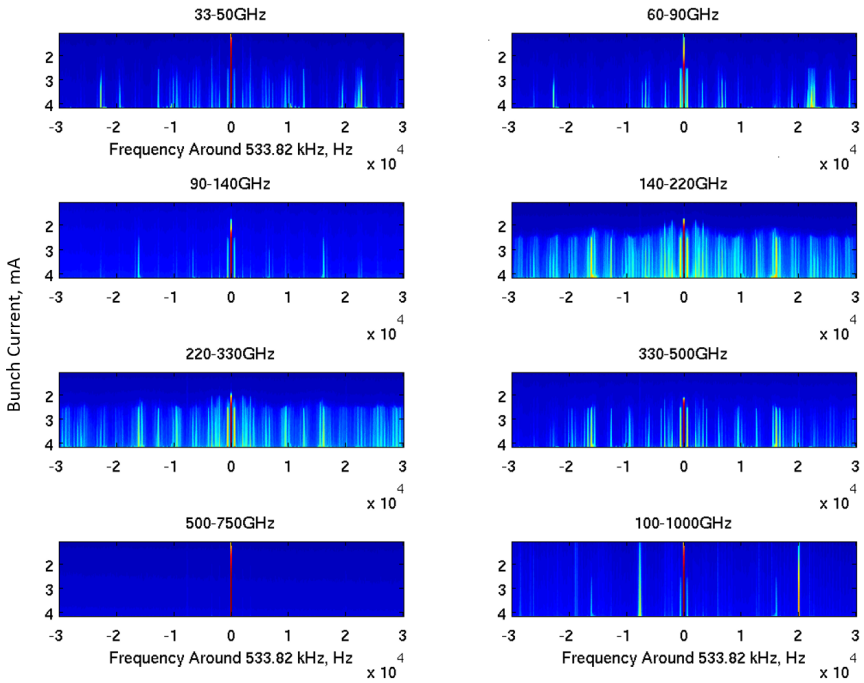


Figure 4.39: The spectrograms observed by each detector during a **normal mode** single bunch current ramp with a bandwidth of 30 kHz. The combined RF cavity voltage was 2.2 MV as opposed to the usual 2.5 MV.

their sidebands. This can been seen in Figure 4.36 where the blue sidebands form a cone around the red curve as opposed to a parallel tunnel. Low-alpha THz mode is designed to create signal in the THz regime and thus it is expected that each of the eight detectors observe signal outside the central curve of the revolution frequency. The 140-220 GHz detector undergoes a change at $\sim$5 mA, which represents the increase in sideband activity as shown in the corresponding spectrograms of Figure 4.37. The sideband activity can be defined as the increase in signal in the 87.4 kHz of bandwidth either side of the revolution frequency. Unfortunately, data capture ceased before significant bursting could be observed (Figs. 4.36 and 4.37). However it is seen for each detector that the sidebands are beginning to spread just as the experiment ended, this can be deemed as proof that chaotic bursting was almost ignited. Data capture was ended prior to 6 mA in order to protect the synchrotron and thus could not be reinvestigated under these conditions. Nevertheless in the case of Figure 4.38, where the conditions were normal mode single bunch, the step-change can be observed and this is also reflected in its corresponding spectrograms shown in Figure 4.39. This is particularly apparent for the more active 140-500 GHz bands.

In the case of low-alpha THz mode a different 'turn on' pattern is seen. This is to be expected as low-alpha mode is designed to create CSR unlike normal mode. The most stark contrast is that the 500-750 GHz detector, which had been one of the first in normal mode, is now the last and most reluctant to observe signal in low-alpha THz mode. The order of initial observation contrasts from normal mode and can be seen in Figures 4.40 - 4.42, where the figures depict the 'turn on' of the detectors in low-alpha THz mode with three different bunch values (207, 158 and 50 bunches). The sequence is as follows with the 140-220 GHz band detector first, then the 90-140 GHz detector, 60-90 GHz detector, 33-50 GHz detector, 220-330 GHz detector, 100-1000 GHz detector, 330-500 GHz detector and finally the 500-750 GHz detector. The 220-330 GHz detector does change its sequence, first surpassing the 33-50 GHz detector at approximately 2.7 $\mu$A and observing similar strength signal as the 60-90 GHz detector above 1 $\mu$A. These three figures show solely the signal observed at the revolution frequency in low-alpha THz mode current ramps. The three figures only differ in the number of bunches used and the range of beam currents explored. Figure 4.40 can be thought of a zoomed-in section of Figure 4.41 as the former only reaches a beam current of just over 0.6 mA unlike the latter which almost

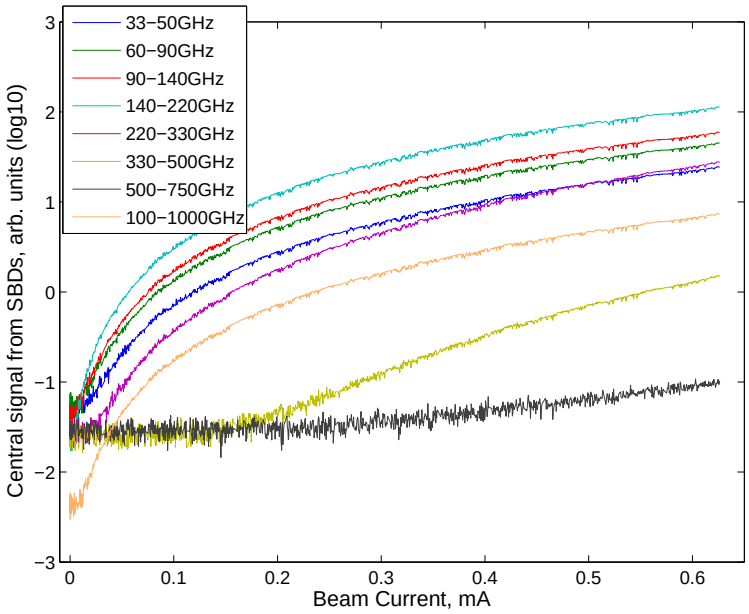


Figure 4.40: The signal at the revolution frequency of the ring as observed by the eight detectors during a **low-alpha THz mode** ultra low current ramp with a multi-bunch fill of **207** bunches.

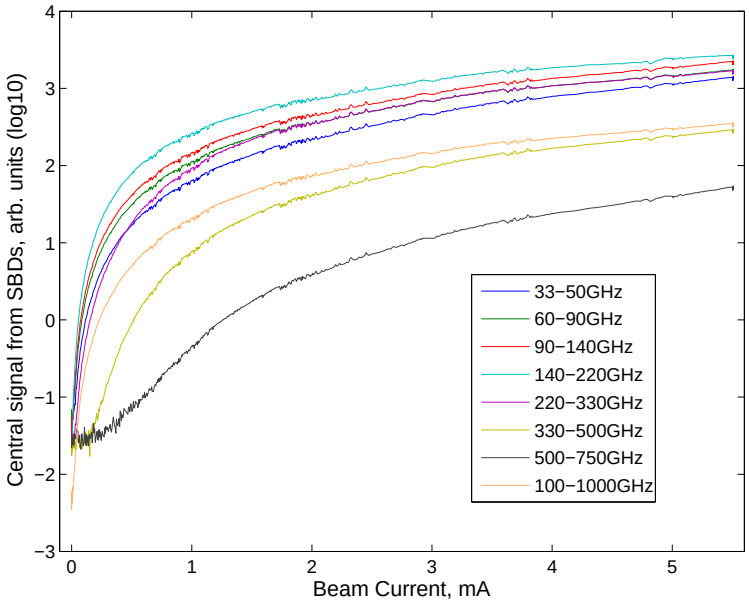


Figure 4.41: The signal at the revolution frequency of the ring as observed by the eight detectors during **low-alpha THz mode** ultra low current ramp with a multi-bunch fill of **158** bunches.

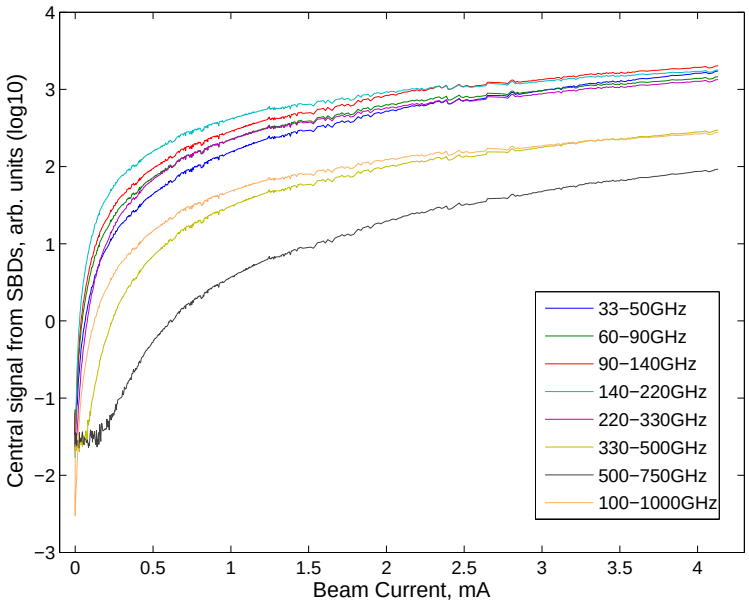


Figure 4.42: The signal at the revolution frequency of the ring as observed by the eight detectors during **low-alpha THz mode** ultra low current ramp with a multi-bunch fill of **50** bunches.

reaches 6 mA. Comparing Figure 4.37 with Figure 4.43 the sideband activity at corresponding beam currents is not the same, this can be attributed to the different number of bunches depicted in each figure with Figure 4.37 taken with 158 bunches compared to the 50 bunches used for Figure 4.43, so though the overall beam current was the same, the individual bunch current was not and it can be seen by comparing these two figures that the higher the bunch current the more activity and bursting will occur.

Despite the different orders of 'turn on' detection for the different modes, the WR5.1ZBD detector (140-220 GHz) observes the most activity. This detector is also the only one operating with a conical horn antenna. When observing the data live as the experiment is being carried, no sensitivity factors (Section 3.4) and this band is seen to be the most active, with the second most active frequency band being 220-330 GHz across both normal and low-alpha modes. When the sensitivity factor has been applied, the 140-220 GHz band still remains the most active. It is key to point out that experimentally determined sensitivity value of the WR5.1ZBD and its horn antenna combination is the highest of all eight detectors at 2261.8 V/W (see Table 3.6) and also the sensitivity value given for just the detector from the manual is also the highest.

As the array is made of separate detectors, it has the ability to truly observe what

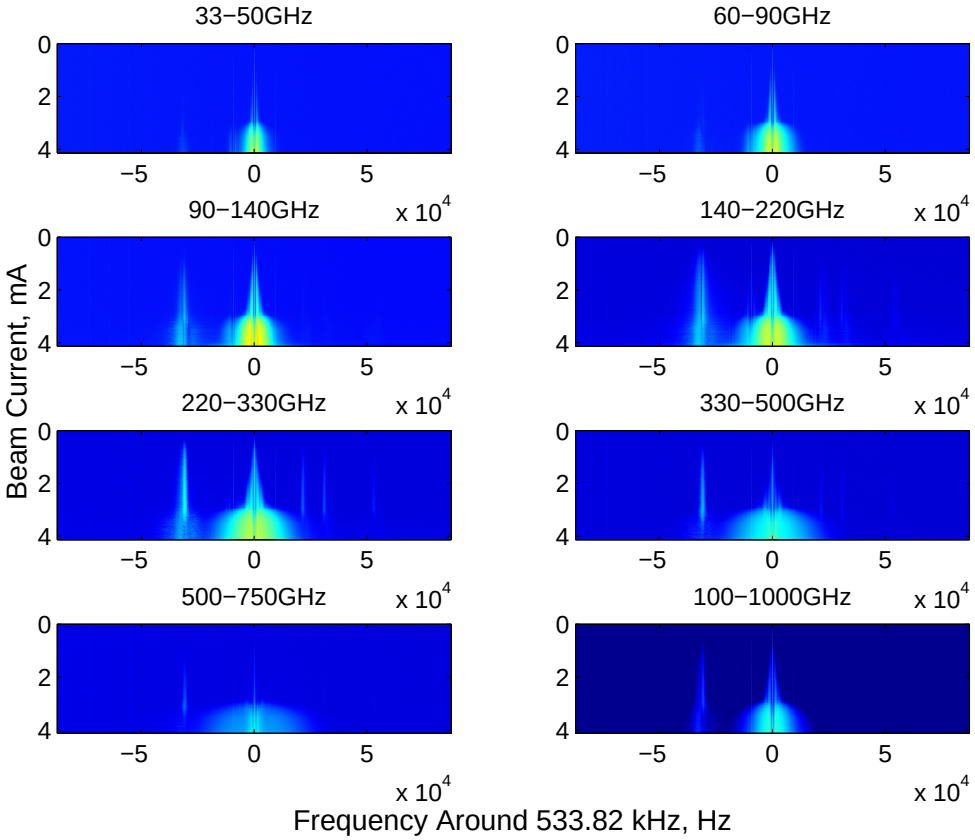


Figure 4.43: The spectrograms observed by each detector during a **low-alpha THz mode** multi-bunch current ramp with 50 bunches with a bandwidth of approximately 87 kHz and where the subfigures are on the same colour-scale.

is happening at different frequencies or more specifically within frequency bands. This is one of the novel capabilities of the detector. Of course, different filters could be employed when using a broadband detector however multiple filters could not be applied simultaneously in order to obtain a series of frequency band data. By observing the activity within each of the frequency bands, more about the bunch dynamics can be ascertained. The higher the frequency, the smaller the length scale of the micro-bunches.

### 4.11.1 CSR Strength

The Vlasov-Fokker-Planck (VFP) equation can be used to describe MBI. In particular, it expresses the interactions within a bunch; of the electrons and their emitted CSR [66]. Using a VFP solver [127] and a linearised Vlasov equation, the MBI threshold can be determined [128]. Considering a beampipe as a pair of parallel plates with distance apart of $2g = h$, it was determined by [128] that shielded CSR only requires two dimensionless parameters to describe the system - the CSR strength, $S_{CSR}$, and shielding parameter, $\Pi$.

$$S_{CSR} = \frac{I_n \rho^{1/3}}{\sigma_{z0}^{4/3}} \tag{4.2}$$

$$\Pi = \frac{\sigma_{z0}\sqrt{\rho}}{g^{3/2}} \tag{4.3}$$

$$with\ I_n = \frac{I_b \sigma_{z0}}{\gamma \alpha \sigma_{\delta,0}^2 I_A}, \tag{4.4}$$

where $I_n$ is the current, $\sigma_{z0}$ is the natural bunch length, $\gamma$ the beam energy, $I_b$ the average bunch current, $\sigma_{\delta,0}$ the nominal energy spread, $\alpha$ the momentum compaction factor and $I_A$ the Alfvén current, which is equal to 17045 A. Moreover, the MBI instability is normally defined as a strong instability, Bane et al [128] show that this is the case and thus determine the threshold for shielded CSR to be:

$$(S_{CSR})_{th} = 0.5 + 0.12\Pi \tag{4.5}$$

In Figure 4.44, the solid lines show the values of $S_{CSR}$ for both the low-alpha THz (blue) and normal optics (green) modes with the cyan diamonds depicting the values of $S_{CSR}$

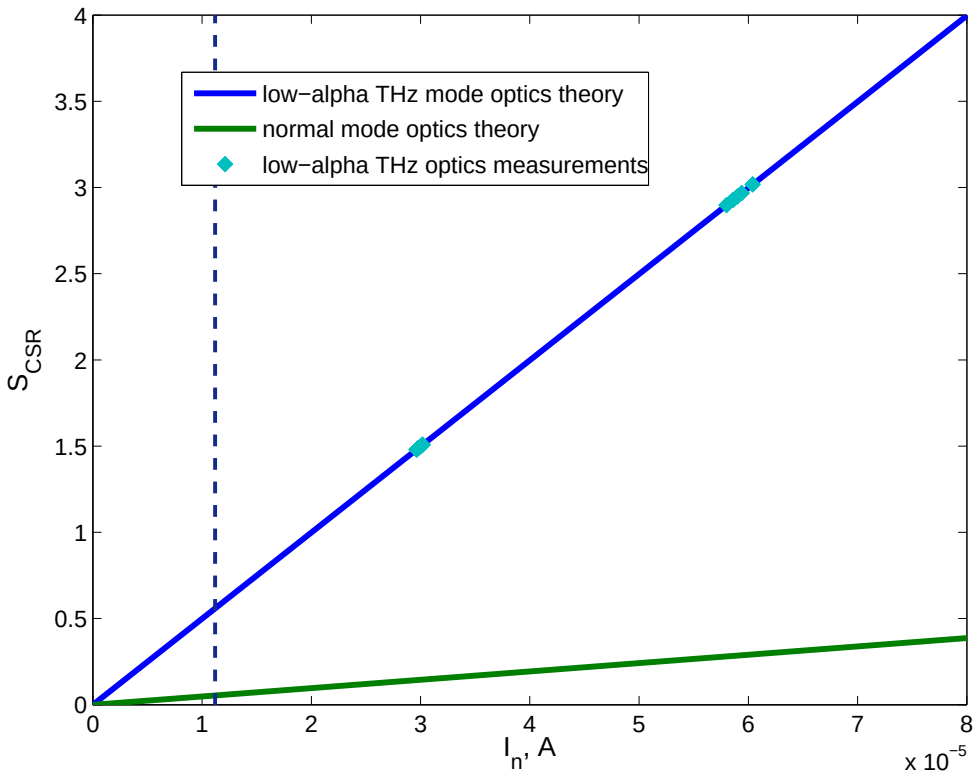


Figure 4.44: The CSR strength, $S_{CSR}$, is shown against the bunch current, $I_n$. The two solid lines represent the values as calculated using Equations 4.2- 4.4, while the cyan diamonds depict the values determined from the real data. The dashed navy line marks the threshold for low-alpha THz mode, $(S_{CSR})_{th}$.

from real data. It is easy to note that $S_{CSR}$ increases more rapidly with respect to the current for low-alpha THz mode compared to normal mode. This is unsurprising as low-alpha THz mode is specifically designed to generate CSR and thus the CSR should be more powerful than during normal optics as depicted in the figure. Using Equation 4.5, the threshold was determined to be $(S_{CSR})_{th} = 0.5598$, which corresponds to a bunch current of $1.1202 \times 10^{-4}$ A, as illustrated on Figure 4.44.

The shielding parameters for low-alpha THz and normal modes are $\Pi = 0.4986$ and $\Pi = 2.8751$, respectively. Bane et al [128] state that when $\Pi \lesssim 2$, the shielding has minimal effect in stabilising the beam while when larger it is effective. These remarks correspond with the shielding parameters determined just above as we know that during low-alpha THz mode, the chosen optics have been implemented specifically to avoid shielding. Moreover, in the case of normal mode, the shielding of CSR is expected and not avoided.

Chapter 5

# Discussions

This chapter summarises the work presented throughout this thesis, proposes changes to both the detector array and beamport as well as highlighting future experiments. Simply put, the main question being asked is: does the spectrometer that has been designed and developed to investigate MBI at Diamond work? The answer is that the spectrometer does operate as intended and this is confirmed by the signal observed at the revolution frequency of the ring.

## 5.1 Summary & Conclusions

In this thesis, the development and use of a single shot spectrometer for the study of MBI by way of detecting the CSR produced by the instability has been presented. The spectrometer is made up of eight individual detectors, collectively encompassing a frequency range of 33-1000 GHz. SBDs are known for their use in millimetre-wave applications and are the selected detector here due to their high sensitivity and fast speeds. They operate at room temperature allowing for simplicity. Seven of the SBDs have set frequency ranges as a result of their waveguide packaging, the eighth SBD is a wide-ranging detector using a log-periodic antenna [123] and silicon lens. Each of the SBDs and corresponding antennas were individually characterised to determine their respective responsivities in the forward direction in free space. Using this knowledge, the power of the signal observed by the SBDs can be determined. The SBDs were combined as an array and the spectrometer was installed at the dedicated viewport tangential to the Diamond storage ring.

Familiarity with the beam and set-up was paramount. At the viewport a variety of different commissioning studies were initiated, whereby the spectrometer was subjected to millimetre wavelengths (CSR) generated at bending magnet B06 of Diamond. The commissioning involved the investigation of the beam's growth and the optimal positions of the SBD array determined by way of raster scans in the xy-plane for various distances from the viewport window. The conditions to produce CSR are known and thus Diamond was configured in this way for the experiments.

Employing a fast oscilloscope, it was proven that two neighbouring bunches acted independently of each other and also that turn-by-turn data capture was sufficient and thus bunch-by-bunch unnecessary. By probing the square-law and linear detection regimes of the SBDs, the optimal filling pattern for the spectrometer was confirmed to be a multi-bunch fill. A multi-bunch fill either in one continuous train or spread throughout the ring allowed for the overall peak power to remain below the threshold of the diodes keeping them within their square-law detection zone.

During three different user runs, the evolution of the beam in the millimetre regime can be seen in each case. As expected in a normal user run with 300 mA, there is minimal CSR emission, with only the 33-50 GHz detector observing a believable beam. Moreover the WR3.4ZBD (220-330 GHz) is encountering real signal. This is in keeping with said detector always detecting one of the highest signal powers in normal mode (and low-alpha). For both low-alpha THz and pulse modes, each SBD observes a true signal as low-alpha mode results in the compression of bunches giving rise to CSR emission and can lead to CSR emission due to MBI. As anticipated the low-alpha THz mode produced a higher power spectral density than the other user runs because it is especially designed to produce a higher CSR flux.

In single bunch normal mode, a selection of RF cavity voltages were explored to show the relationship between an increasing RF voltage and decreasing bunch size thus resulting in additional CSR emission. Naturally, during low-alpha user mode the ring is operated with a higher RF combined cavity voltage than amid a normal user run.

Collimators are known to affect the impedance of the machine and thus can alter the CSR emission and progression of MBI. It has been seen in the previous chapter that this is only meaningful in the case of normal mode whereby the CSR impedance is one

of many impedances, contrary to low alpha-mode where the bunch is shorter and the CSR impedance dominates. In low-alpha mode the signal obtained during a current ramp corresponded with that during a current decay using collimators.

Therefore it can be concluded that the aims of this thesis have been achieved; a spectrometer has been developed in order to study MBI. With the characterisation of each SBD, the spectrometer is able to determine the power of signal received for each frequency range. The spectrometer has been characterised by the steady state emissions from the revolution frequency of the ring and is fully functional. It has provided evidence for what is expected in terms of CSR production at a storage ring. Not only useful for the investigation of MBI, the spectrometer is also able to monitor the variation in spectra during the change of certain machine parameters. The SBD array remains installed at Diamond as a permanent diagnostic tool. Furthermore, the data it captures is now being continually archived, several times an hour.

## 5.2 Further Improvements of Detector Array

The first and foremost improvement to the detector array would be to characterise the remaining detectors experimentally using a relevant source. The sensitivity factors of WR2.2ZBD (330-500 GHz) and WR1.5ZBD (500-75 GHz) had to be calculated using the results from the other detectors and the values given per model on the manufacturers data sheets. The QOD was calibrated on the test bench but its entire range was unable to be reached.

Currently the detector array is composed of many posts, post holders and screws as well as some specifically machined detector holder for individual detectors. This was beneficial when creating the detector array as the positions and amount of detectors were regularly changing. Now that the detector array has been established and characterised it would be favourable for one piece of metal to be specifically machined in order to hold all detectors at their required positions. This would mean that there would be less chance for unwanted movement e.g. loosening of a screw or difficulty in re-assembling the array.

The voltage acceptance for each of the channels is determined by the multi-channel simultaneous digitiser. An improvement to the set-up as a whole would be to introduce

warnings to alert the user that the diodes or more specifically the channels are approaching saturation levels. To go another step further, the voltage acceptances for channels could be automatically changed in accordance with the signal presence. This change of range allowance would be carried out and recorded in the data. Currently, the values at which to set the ranges for each lattice and beam current arrangement have been determined via trial and error and are now known. This was helped by displaying regular snapshots of the raw bit signal as the Fourier transformed data was being streamed, where the digitiser accommodates $2^{15} = 32768$ bits.

## 5.3 Further Improvements of Beampipe Set-Up

The beamport at Diamond dedicated to the investigation of micro-bunching instabilities was originally used to guide visible light and was hence designed and constructed to allow for the output of visible wavelengths. When the beamport was re-purposed to work in the mm-wavelengths, no major changes were implemented. The beamport allows for the emission of mm-wavelengths, nevertheless it was never optimised for this. The beamport's design and hence dimensions affects the beam in many ways. The effect is the size of the apertures within the beamport which do not allow for the millimetre wavelengths to spread out but rather restricts the spread and causes reflections. The first issue is the presence of the slit absorbers which create an 11.5 mm vertical aperture 532 mm from the source. Then 1142 mm from the source point there is a horizontal limit of 20.7 mm. Furthermore, the radiation leg has been designed for x-ray radiation with a fixed vertical dimension of 33 mm and initial horizontal size of 39 mm. It is at the first aperture where the mm-radiation is affected and subsequently thereafter.

All beamlines at Diamond are unique, however B22, a beamline dedicated to THz and IR spectroscopy, is even more so. Starting where the radiation generation and separation from the electron beam occurs, the dipole vessel for B22 has an alternative and most obviously larger shape. Most significantly, there are no slit absorbers within the dipole. After the dipole magnet the B22 beampipe expands at the required rate to allow for the mm-wavelengths to pass through without interruption, e.g. there are no crotch absorbers.

Across the world, there are many beamlines at synchrotron light sources that spe-

Table 5.1: Acceptance Apertures of THz Beamlines [73, 76, 129, 130]

| **Beamline** | **Horizontal Aperture mrad** | **Vertical Aperture mrad** |
|---|---|---|
| B06 | 21.6 | 10 |
| B22 | 50 | 30 |
| IRIS | 60 | 40 |
| MLS THz | 65 | 43 |

cialise is using terahertz radiation to carry out experiments, such beamlines include those at MLS and IRIS at BESSY-II. Both beamlines have been designed with THz in mind and thus have much larger apertures than a typical synchrotron radiation beamline which is key when working with mm-wavelength. The acceptance apertures are depicted in Table 5.1 where the vertical aperture is the most significant with regards these longer wavelengths. By increasing the acceptance aperture of the beampipe from B06, the CSR would be less affected when approaching the SBD array. It can be seen from Table 5.1 that the aperture of B06 is significantly smaller than the dedicated beamlines.

On another note, in an ideal world, there would be nothing to hinder the movement of the SBD array in a raster scan. Currently there are water cooling pipes for the storage ring which results in scans closer to the beamport i.e. longitudinally, being curbed.

## 5.4 Further Experiments

In physics and research as a whole, there is never an end; more ideas and hypothesis spring out of the data and one could be carrying out experiments forever. At some point though, a thesis must be written and the work concluded, however as is the nature many further investigations could have been carried out. Throughout this section, future experiments are expressed.

SBDs are sensitive to the plane of polarisation and thus must be orientated correctly to observe the desired data. The SBD array in this thesis was installed accordingly. An interesting experiment would be to turn the array by ninety degrees and capture data. In theory, there should be no results however, it could show activity within the beam along an unexpected plane.

With the interesting results obtained by the 500-750 GHz detector especially in normal mode (Section 4.9), another higher frequency detector could be acquired, characterised and added to the array. A WR1.0ZBD (750-1100 GHz) detector could be attained to investigate if these anomalies exist at even higher frequencies or filters used to further restrict the frequency ranges of the current detectors.

Since the SBD array has been successfully functioning, it has been used to monitor the changes (or lack there of) that might arise during low-alpha user runs when the collimators or insertion devices are being adjusted. It has been a beneficial tool for the operation of Diamond as whole. The detector array is to remain installed at Diamond's B06 beamport. Hence, it will continue to be used in the commissioning of future low-alpha lattices and watching for changes to the spectra emitted when certain parameters or settings are altered.

## 5.5 Comparisons to Simulations

It is the desire of many to be able to model a light source's true behaviour and also to accurately simulate MBI. The data obtained with the SBD array have been used to provide more information on MBI, the beam as a whole at Diamond, the characteristics of different beam modes and the effects of micro-bunching instabilities. As outlined in Section 1.5, these data can be used to confirm the fidelity and accuracy of the simulations. Currently several doctoral students in conjunction with Diamond are working on improved models to predict the behaviour of MBI. They have been using the data obtained for this thesis and by the SBD array outlined in these pages as a comparison between what they have modelled and what is actually observed [64, 65].

# Bibliography


[1] J P Blewett. Radiation losses in the induction electron accelerator. *Physical Review*, 69(3-4):87–95, 1946.

[2] F R Elder, A M Gurewitsch, R V Langmuir, and H C Pollock. Radiation from electrons in a synchrotron. *Physical Review*, 71(11):829–830, 1947.

[3] J Larmor. On the Theory of the Magnetic Influene on Spectra; And on the Radiation from Moving Ions. *Phil. Mag.*, 44:503–512, 1897.

[4] H Winick. *Synchrotron Radiation Sources: A Primer*. World Scientific, 1994.

[5] R P Walker. Commissioning and Status of the Diamond Storage Ring. In *2007 Asian Particle Accelerator Conference*, pages 66–70, 2007.

[6] Diamond Light Source. www.diamond.ac.uk.

[7] S Baird. Accelerators for Pedestrians. (AB-Note-2007-014 OP), 2007.

[8] E Wilson. *An Introduction to Particle Accelerators*. Oxford University Press, 2001.

[9] N Marks, J A Clarke, and D J Holder. Magnetic Design of the Dipole Magnets for the Diamond Synchrotron Source. In *Proc. EPAC*, pages 2364–2366, 2002.

[10] R Bartolini, C P Bailey, M P Cox, N P Hammond, J Kay, E C Longhi, S Mhaskar, T Pulampong, and R P Walker. Novel Lattice Upgrade Studies for Diamond Light Source. *Proc. IPAC 2013*, pages 240–242, 2013.

[11] R P Walker, M Apollonio, C P Bailey, M P Cox, R T Fielder, N P Hammond, M T Heron, J Kay, I P S Martin, S P Mhaskar, G Rehm, E C M Rial, B Singh, V Smaluk, A Thomson, R Bartolini, and T Pulampong. The Double-Double Bend Achromat (DDBA) Lattice Modification for the Diamond Storage Ring. In *Proc. IPAC 2014*, pages 331–333, 2014.

[12] S Y Lee. *Accelerator physics*, volume 35. 2nd edition, 2004.

[13] EPICS and Open-Source. www.aps.anl.gov/epics/.

[14] M Venturini, R L Warnock, R Ruth, and J Ellison. Coherent synchrotron radiation and bunch stability in a compact storage ring. *Physical Review Special Topics - Accelerators and Beams*, 8(1):014202, 2005.

[15] G Rehm, A F D Morgan, R Bartolini, I P S Martin, and P Karataev. Ultra-fast mm-wave detectors for Observation of Microbunching Instabilities in the Diamond Storage Ring. In *Proc. DIPAC*, pages 369–371, 2009.

[16] M Abo-Bakr, J Feikes, K Holldack, D. Ponwitz, G. Wüstefeld, and H. W. Hübers. Coherent mm-Radiation Experiments At The BESSY II Storage Ring. *Proceedings of EPAC 2000*, pages 720–722, 2000.

[17] M Abo-Bakr, J Feikes, K Holldack, G Wüstefeld, and H-W Hübers. Steady-State Far-Infrared Coherent Synchrotron Radiation detected at BESSY II. *Physical Review Letters*, 88(25):254801, 2002.

[18] P Kuske. Investigation of the Temporal Structure of CSR-Bursts at BESSY II. In *Proc. PAC*, pages 4682–4684, 2009.

[19] A R Hight Walker, U Arp, G T Fraser, T B Lucatorto, and J Wen. New Infrared Beamline at the NIST SURF II Storage Ring. *Proc. SPIE 3153*, 3153:42–50, 1997.

[20] G L Carr, J D Laveigne, D H Reitze, D B Tanner, S L Kramer, and J B Murphy. Evidence for millimeter-wave Coherent Emission from the NSLS VUV Ring. *US Government Reports*, 2(3), 1999.

[21] B Podobedov, G L Carr, S L Kramer, and J B Murphy. Longitudinal Density modulation of Unstable Bunches Emitting Coherent IR. In *Proc. PAC*, volume 3, pages 1921–1923, 2001.

[22] G L Carr, S L Kramer, J B Murphy, R. P S M Lobo, and D B Tanner. Observation of Coherent Synchrotron Radiation from the NSLS VUV Ring. *Nuclear Instruments and Methods in Physics Research, Section A: Accelerators, Spectrometers, Detectors and Associated Equipment*, 463(1-2):387–392, 2001.

[23] J M Byrd, W P Leemans, A Loftsdottir, B Marcelis, Michael C Martin, W R Mckinney, F Sannibale, T Scarvie, and C Steier. Observation of Broadband Self-Amplified Spontaneous Coherent Terahertz Synchrotron Radiation in a Storage Ring. *Physical Review Letters*, 89(22):224801, 2002.

[24] A Mochihashi, M Hosaka, M Katoh, M Shimada, and S Kimura. Observation of THz synchrotron Radiation Burst in UVSOR-II Electron Storage Ring. In *Proc. EPAC*, pages 3380–3382, 2006.

[25] A Andersson, M S Johnson, and B Nelander. Coherent Synchrotron Radiation in the Far Infrared from a 1-mm Electron Bunch. *Optical Engineering*, 39(12):3099, 2000.

[26] B E Billinghurst, J C Bergstrom, C Baribeau, T Batten, T E May, J M Vogt, and W A Wurtz. Longitudinal Bunch Dynamics Study with Coherent Synchrotron Radiation. *Physical Review Accelerators and Beams*, 19(2):020704, 2016.

[27] J L Hesler and T W Crowe. NEP and Responsivity of THz Zero-Bias Schottky Diode Detectors. *2007 Joint 32nd International Conference on Infrared and Millimeter Waves and the 15th International Conference on Terahertz Electronics*, pages 5–6, 2007.

[28] R Han, Y Zhang, Y Kim, D Y Kim, H Shichijo, E Afshari, and Kenneth K O. Active Terahertz Imaging Using Schottky Diodes in CMOS: Array and 860-GHz Pixel. *IEEE Journal of Solid-State Circuits*, 48(10):2296–2308, 2013.

[29] S L Kramer. Direct Observation of Beam Impedance Above Cutoff. *Physical Review Special Topics - Accelerators and Beams*, 5(11):8–17, 2002.

[30] R J Smith and R C Dorf. *Circuits, Devices and Systems*. John Wiley & Sons Inc., 5th edition, 1992.

[31] B E Billinghurst, J C Bergstrom, C Baribeau, T Batten, L Dallin, T E May, J M Vogt, W A Wurtz, R Warnock, D A Bizzozero, and S L Kramer. Observation of Wakefields and Resonances in Coherent Synchrotron Radiation. *Physical Review Letters*, 204801(114):1–5, 2015.

[32] A Finn, P Karataev, and G Rehm. A Multi-Band Single Shot Spectrometer for Observation of mm-Wave Bursts At Diamond Light Source. *Proc. of IPAC*, 2015.

[33] A Schmid, M Brosi, E Bründermann, K Ilin, B Kehrer, A Kuzmin, M Caselle, E Hertle, N Hiller, B Kehrer, A-S Müller, J Raasch, P Schönfeldt, M Schuh, M Siegel, J L Steinmann, S Wuensch, and S A Kuznetsov. Non-Interferometric Spectral Analysis of Synchrotron Radiation In The THz Regime at ANKA. In *Proc. IPAC*, 2016.

[34] N Erickson. A Fast and Sensitive Submillimeter Waveguide Power Meter. In *Tenth International Symposium on Space Terahertz Technology*, pages 501–507, 1999.

[35] http://www.terahertz.co.uk/.

[36] M Caselle, M Brosi, S Chilingaryan, T Dritschler, E Hertle, V Judin, A Kopmann, A-S Müller, J Raasch, M Schleicher, N J Smale, J Steinmann, M Vogelgesang, S Wuensch, M Siegel, and M Weber. Commissioning Of An Ultra-Fast Data Acquisition System For Coherent Synchrotron Radiation Detection. In *Proc. of IPAC*, 2014.

[37] M. Castellano, V. Verzilov, L. Catani, a. Cianchi, G. Orlandi, and M. Geitz. Measurements of coherent diffraction radiation and its application for bunch length diagnostics in particle accelerators. *Physical Review E*, 63(5):056501, apr 2001.

[38] M Abo-Bakr, J Feikes, K Holldack, P. Kuske, W. Peatman, U. Schade, G. Wüstefeld, and H.-W. Hübers. Brilliant, Coherent Far-Infrared (THz) Synchrotron Radiation. *Physical Review Letters*, 90(9):094801, 2003.

[39] M Klein, N Hiller, A-S Müller, K G Sonnad, and P Tavares. Analysis Of THZ Spectra And Bunch Deformation Caused By CSR At ANKA. In *Proc. IPAC*, pages 1925–1927, 2010.

[40] C Evain, J Barros, A Loulergue, M-A Tordeux, R Nagaoka, M Labat, L Cassinari, G Creff, L Manceron, J-B Brubach, P Roy, M E Couprie, and Saint Aubin. Microbunching Instability Studies At SOLEIL. In *Proc. IPAC*, pages 709–711, 2011.

[41] J Barros, C Evain, L Manceron, J B Brubach, M A Tordeux, P Brunelle, L Nadolski, A Loulergue, M E Couprie, S Bielawski, C Szwaj, and P Roy. Coherent Synchrotron Radiation for Broadband Terahertz Spectroscopy. *Review of Scientific Instruments*, 84(3), 2013.

[42] W Shields, P Karataev, R Bartolini, A F D Morgan, and G Rehm. Longitudinal Beam Profile Monitor for Investigating the Microbunching Instability At Diamond Light Source . In *Proc. IBIC*, pages 143–146, 2013.

[43] J Steinmann, E Hertle, N Hiller, V Judin, A-S Müller, P Schönfeldt, M Schuh, P Schütze, and E Bründermann. Spectral Analysis Of Micro-Bunching Instabilities Using Fast THz Detectors. In *Proc. IPAC*, 2014.

[44] I P S Martin, G Rehm, C A Thomas, and R Bartolini. Experience with Low-Alpha Lattices at the Diamond Light Source. *Physical Review Special Topics - Accelerators and Beams*, 14(4):040705, 2011.

[45] I P S Martin, C Bloomer, L M Bobb, A Finn, G Rehm, and R Bartolini. Reconstruction of Electron Bunch Motion During CSR Bursts using Synchronised Diagnostics. In *Proc. IPAC*, 2015.

[46] N Hiller, E Huttel, A-S Mueller, A Plech, P Peier, and V Schlott. A Setup For Single Shot Electro Optical Bunch Length Measurements at the ANKA Storage Ring. In *Proc. IPAC*, pages 1206–1208, 2011.

[47] F Müller, P Peier, V Schlott, B Steffen, T Feurer, and P Kuske. Electro-optical measurement of sub-ps structures in low charge electron bunches. *Physical Review Special Topics - Accelerators and Beams*, 15(7):1–9, 2012.

[48] N Hiller, A Borysenko, E Hertle, E Huttel, V Judin, B Kehrer, S Marsching, A-S Müller, M J Nasse, A Plech, M Schuh, N J Smale, B Steffen, P Peier, and V Schlott. Electro-Optical Bunch Length Measurements at the ANKA Storage Ring. *Proc. IPAC*, (05):500–502, 2013.

[49] N Hiller, A Borysenko, E Hertle, V Judin, B Kehrer, S Marsching, A-S Müller, M J Nasse, P Schönfeldt, M Schuh, N J Smale, and J Steinmann. Status Of Single-Shot EOSD Measurement At ANKA. In *Proc. IPAC*, 2014.

[50] E Roussel, C Evain, M Le Parquier, C Szwaj, S Bielawski, Phlam Cerla, Villeneuve Ascq, L Manceron, J Brubach, M Tordeux, J Ricaud, L Cassinari, M Labat, M Couprie, P Roy, and Synchrotron Soleil. A New Scheme For Electro-Optic Sampling At Record Repetition Rates : Principle And Application To The First ( Turn-By-Turn ) Recordings Of THz CSR Bursts At SOLEIL. *Proc. IPAC*, 2014.

[51] E Roussel, C Evain, M Le Parquier, C Szwaj, S Bielawski, Phlam Cerla, Villeneuve Ascq, L Manceron, J-B Brubach, M-A Tordeux, J Ricaud, L Cassinari, M Labat, M-E Couprie, and P Roy. Single-Shot Electro-Optic Sampling Combined With Photonic Time-Stretch : Detailed Results At Soleil. In *Proc. IPAC 2015*, pages 795–797, 2015.

[52] J Feikes, K Holldack, P Kuske, and G Wuestefeld. Compressed Electron Bunches For THz Generation - Operating BESSY II in a Dedicated Low Alpha Mode. In *Proc. EPAC*, pages 2290–2292, 2004.

[53] J Feikes, P Kuske, R Müller, and G Wüstefeld. Orbit Stability in the 'Low Alpha' Optics of the Bessy Light Source. *Proc. EPAC*, pages 3308–3310, 2006.

[54] A-S Müller, I Birkel, B. Gasharova, E. Huttel, R. Kubat, Y-L Mathis, D. a. Moss, W. Mexner, R. Rossmanith, M. Wuensch, P. Wesolowski, F. Pérez, M. Pont, and

C. J. Hirschmugl. Far Infrared Coherent Synchrotron Edge Radiation at ANKA. In *Proc. PAC*, pages 2518–2520, 2005.

[55] R Müller, A Hoehl, A Serdyukov, G Ulm, J Feikes, M Ries, and G Wüstefeld. THz Studies at a Dedicated Beamline at the MLS. *2011 International Particle Accelerator Conference*, pages 2933–2935, 2011.

[56] J Feikes, M Von Hartrott, M Ries, P Schmid, G Wüstefeld, A Hoehl, R Klein, R Müller, and G Ulm. Metrology Light Source: The First Electron Storage Ring Optimized for Generating Coherent THz Radiation. *Physical Review Special Topics - Accelerators and Beams*, 14(3):1–10, 2011.

[57] X Huang, J Safranek, J Corbett, Y Nosochkov, J Sebek, A Terebilo, and M Park. Low Alpha Mode for SPEAR3. In *PAC*, pages 1308–1310, 2007.

[58] I P S Martin, R Bartolini, G Rehm, J H Rowland, and C A Thomas. Low Alpha Operation of the Diamond Storage Ring. In *Proc. IPAC*, pages 4599–4601, 2010.

[59] G Stupakov and S A Heifets. Beam Instability and Microbunching due to Coherent Synchrotron Radiation. *Physical Review Special Topics - Accelerators and Beams*, 5(5):054402, 2002.

[60] G Stupakov. Theory and Observations Of Microbunching Instability In Electron Machines. In *Proc. of PAC*, pages 102–106, 2003.

[61] G Stupakov and R L Warnock. Microbunch Instability Theory and Simulations. *ICFA Beam Dynamics Newsletter*, 2005.

[62] E Roussel, C Evain, C Szwaj, and S Bielawski. Microbunching Instability in Storage Rings: Link between phase-space structure and terahertz coherent synchrotron radiation radio-frequency spectra. *Physical Review Special Topics - Accelerators and Beams*, 17, 2014.

[63] M Klein, A-S Müller, and K G Sonnad. Simulations of the Microbunching Instability at ANKA Using a Vlasov-Fokker-Planck Solver. In *Proc. IPAC*, pages 2232–2234, 2011.

[64] T Chanwattana, M Atay, R Bartolini, G Cinque, M Frogley, E Koukovini Platia, I P S Martin, L M Bobb, and A Finn. THz Coherent Synchrotron Radiation From Ultra-Low Alpha Operating Mode at Diamond Light Source. In *Proc. IPAC*, pages 3–5, 2016.

[65] M Atay, R T Fielder, I P S Martin, and R Bartolini. Comparison of Measurements and Simulations of Single Bunch Instabilities at Diamond. In *Proc. IPAC*, 2015.

[66] M Brosi, E Blomley, E Bründermann, N Hiller, B Kehrer, A Müller, M Schedler, P Schönfeldt, M Schuh, and J L Steinmann. Systematic Studies of Bunch-Length Bursting at ANKA. In *Proc. IPAC 2016*, number 1, pages 1–4, 2016.

[67] R P Walker. Synchrotron Radiation. In *CERN Accelerator School: Course on General Accelerator Physics*, pages 437–459. 1992.

[68] Klaus Wille. *The Physics of Particle Accelerators: An Introduction*. Oxford University Press, 2000.

[69] R L Warnock. Shielded coherent synchrotron radiation and its possible effect in the next linear collider. *Particle Accelerator Conference, 1991. Accelerator Science and Technology., Conference Record of the 1991 IEEE*, (7):1824–1826, 1991.

[70] R Bartolini, P Karataev, and G Rehm. Observation Of Longitudinal Microbunching Instabilities. *Proc. PAC*, pages 4–6, 2009.

[71] A P Potylitsyn, M I Ryazanov, M N Strikhanov, and A A Tishchenko. *Diffraction Radiation from Relativistic Particles*. Springer, 2010.

[72] H Wiedemann. *Synchrotron Radiation*. Springer, 1st edition, 2003.

[73] M Abo-Bakr, J Feikes, K Holldack, Ullrich Schade, and G Wüstefeld. Powerful, Steady State, Coherent Synchrotron Radiation at BESSY II. *Proc. EPAC*, pages 778–780, 2002.

[74] G Wüstefeld. Short Bunches in Electron Storage Rings and Coherent Synchrotron Radiation. In *Proc. EPAC*, pages 26–30, 2008.

[75] W Shields. *Coherent Synchrotron Radiation Diagnostics for Investigating the Longitudinal Microbunching Instability at Diamond Light Source*. PhD thesis, Royal Holloway, University of London, 2016.

[76] K Holldack, P Kuske, G. Wuestefeld, and H-W Huebers. Coherent Synchrotron Radiation Experiments at BESSY II. *Proc. PAC*, pages 839–841, 2003.

[77] R Bartolini, G Cinque, I P S Martin, G Rehm, and C A Thomas. CSR and THz Emission Measurements at the Diamond Light Source. In *Proc. IPAC*, pages 3050–3052, 2011.

[78] I P S Martin, G Cinque, G Rehm, C A Thomas, and R Bartolini. Operating the Diamond Light Source in Low Alpha Mode for Users. *Proc. IPAC*, pages 246–248, 2013.

[79] M Ries. *Nonlinear momentum compaction and coherent synchrotron radiation at the Metrology Light Source*. PhD thesis, 2014.

[80] J M Byrd. Ultrashort Radiation Pulses from Storage Rings, 2004.

[81] I P S Martin. *Short Pulse X-Ray Generation in Synchrotron Radiation Sources*. PhD thesis, 2011.

[82] I P S Martin, R Bartolini, J Rowland, B Singh, and C A Thomas. A Low Momentum Compaction Lattice For The Diamond. *Proc. PAC*, 2009.

[83] S A Heifets and G Stupakov. Beam Instability and Microbunching Due to Coherent Synchrotron Radiation. *SLAC-PUB-9425*, 5(August):39–42, 2002.

[84] J K Pijanka, N Stone, G Cinque, Y Yang, A Kohler, K Wehbe, M Frogley, G Parkes, J Parkes, P Dumas, C Sandt, D G Van Pittius, G Douce, G D Sockalingum, and J Sulé-Suso. FTIR Microspectroscopy of Stained Cells and Tissues. Application in Cancer Diagnosis. *Spectroscopy*, 24(1-2):73–78, 2010.

[85] J Dudala, M Bialas, A Surowka, M Bereza-Buziak, A Hubalewska-Dydejczyk, A Budzynski, M Pedziwiatr, M Kolodziej, K Wehbe, and M Lankosz. Biomolecu-

lar Characterization of Adrenal Gland Tumors by means of SR-FTIR. *The Analyst*, 140(7):2101–6, 2015.

[86] A L M Batista de Carvalho, M Pilling, P Gardner, J Doherty, G Cinque, K Wehbe, C Kelley, L A E Batista de Carvalho, and M P M Marques. Chemotherapeutic Response to Cisplatin-like Drugs in Human Breast Cancer Cells Probed by Vibrational Microspectroscopy. *Faraday Discuss.*, 00:1–26, 2016.

[87] E Anderson, M J Almond, W Matthews, G Cinque, and M D Frogley. Analysis of Red Pigments from the Neolithic sites of Catalho yuk in Turkey and Sheikh-e Abad in Iran. *Spectrochimica Acta - Part A: Molecular and Biomolecular Spectroscopy*, 131:373–383, 2014.

[88] V Beltran, N Salvadó, S Butí, and G Cinque. Micro Infrared Spectroscopy Discrimination Capability of Compounds in Complex Matrices of Thin Layers in Real Sample Coatings from Artworks. *Microchemical Journal*, 118:115–123, 2015.

[89] M R Ryder, B Civalleri, T Bennett, S Henke, S Rudie, Gi Cinque, F Fernandez-Alonso, and J C Tan. Identifying the Role Of Terahertz Vibrations on Metal-Organic Frameworks: From Gate-Opening Phenomenon to Shear-Driven Structural Destabilization. *Physical Review Letters*, 113(21):1–6, 2014.

[90] A Greenaway, B Gonzalez-Santiago, P M Donaldson, M D Frogley, G Cinque, J Sotelo, S Moggach, E Shiko, S Brandani, RF Howe, and P A Wright. In Situ Synchrotron IR Microspectroscopy of CO2 Adsorption on Single Crystals of the Functionalized MOF Sc2(BDC-NH2)3. *Angewandte Chemie - International Edition*, 53(49):13483–13487, 2014.

[91] U Schade, K Holldack, P Kuske, G Wüstefeld, and H W Hübers. THz Near-Field Imaging Employing Synchrotron Radiation. *Applied Physics Letters*, 84(8):1422–1424, 2004.

[92] A Finn, P Karataev, and G Rehm. Design, Development and Use of the Spectrometer for Investigating Coherent THz Radiation Produced by Micro-Bunching Instabilities at Diamond Light Source. *IoP Conference Series*, 2016.

[93] W Shields, G Boorman, and P Karataev. Observations of Microbunching Instabilities from a THz Port at Diamond Light Source. In *Proc. IPAC*, pages 3114–3116, 2012.

[94] CLRC. Diamond Synchrotron Light Source: Report of The Design Specification. Technical report, 2002.

[95] G Rehm, A F D Morgan, R Bartolini, I P S Martin, and P Karataev. Ultra-Fast mm-Wave Detectors for Observation of Microbunching Instabilities in the Diamond Storage Ring. In *2009 European Workshop on Beam Diagnostics and Instrumentation for Particle Accelerators*, page TUPD32, 2009.

[96] Diamond Light Source. Private Communication with Mechanical Engineering, 2016.

[97] R Feynman, M A Gottlieb, and R Pfeiffer. The Feynman Lectures on Physics-Modes. In *The Feynman Lectures on Physics*. Basic Books, online edition.

[98] Arne Hoehl. Private Communication, 2016.

[99] S A Maas. *Nonlinear Microwave and RF Circuits*. ARTECH House Ltd, 2nd edition.

[100] A Aryshev, S Araki, P Karataev, T Naito, N Terunuma, and J Urakaw. Fast Microwave Detection System for Coherent Synchrotron Radiation Study at KEK: Accelerator Test Facility. *Nuclear Instruments and Methods in Physics Research A*, 580:1544–1551, 2007.

[101] Millitech. DXP Detector Specifications. Technical report, Millimeter-Wave Technology & Solutions.

[102] Millitech. DET Detector Specifications. Technical report, Millimeter-Wave Technology & Solutions.

[103] Virginia Diodes Inc. VDI User Guide. Technical report.

[104] Ron Pratt. Characterisitics and Applications of Diode Detectors. *Hewlett Packard, RF & Microwave*.

[105] Rick Cory. Schottky Diodes. Technical Report February, Skyworks Solutions, Inc., 2009.

[106] Skyworks Solutions Inc. Mixer and Detector Diodes (Application note 200826A). *Application note 200826A*, pages 1–18, 2008.

[107] Agilent Technologies. Designing Detectors for RF / ID Tags Application Note 1089. Technical Report 1089, Agilent Technologies, 1999.

[108] Skyworks. Silicon Schottky Diodes - Infineon. Technical report, Skyworks Solutions, Inc.

[109] Avago Technologies. Schottky Barrier Diode Video Detectors Application Note 923. *Current*, pages 1–12.

[110] Hewlett Packard. Square Law and Linear Detection. Technical Report September, Hewlett Packard, 1981.

[111] Agilent Technologies. Schottky Detector Diodes Technical Data. *Technical Data*, pages 1–12.

[112] Thomas Milligan. *Modern Antenna Design, 2nd Ed.* Wiley, 2005.

[113] A P King. The Radiation Characteristics of Conical Horn Antennas. *Proc. IRE*, 38:249–251, 1950.

[114] A W Love. The Diagonal Horn Antenna. *Microwave Journal*, V:117–122, 1962.

[115] ANITA-Hawaii. Antenna Introduction / Basics 1., 2007.

[116] ZEISS. Zeiss AxioVision Optical Microscope.

[117] Millitech. SGH Specifications. Technical report.

[118] ECE. ECE Tutorials - Schottky Barrier Diodes, 2016.

[119] Virginia Diodes Inc. Private Communication, 2016.

[120] Millitech Inc. Private Communication, 2016.

[121] Thomas Keating LTD. Thomas Keating Power Meter Manual. Technical report, 2010.

[122] Millitech. Detector Specifications. Technical report, Millimeter-Wave Technology & Solutions.

[123] J L Hesler, L Liu, H Xu, Y Duan, and R M Weikle. The Development of Quasi-Optical THz Detectors. *33rd International Conference on Infrared and Millimeter Waves & the 16th International Conference on Terahertz Electronics, 2008, IRMMW-THz 2008*, 2008.

[124] A F D Morgan, G Rehm, and I Uzun. First Tests of the Transverse Multibunch Feedback at Diamond. *Proc. DIPAC*, pages 295–298, 2007.

[125] L M Bobb. Private Communication, 2016.

[126] A Finn, P Karataev, and G Rehm. Using a Single Shot Spectrometer to Determine the Spectral Characteristics of the Beam as a Result of Micro-Bunching Instabilities. In *Proc. IPAC*, 2016.

[127] R L Warnock and James A Ellison. A General Method For Propagation of the Phase Space Distribution , With Application to the Saw-Tooth Instability. Technical report, 2000.

[128] K. L F Bane, Y. Cai, and G Stupakov. Threshold studies of the microwave instability in electron storage rings. *Physical Review Special Topics - Accelerators and Beams*, 13(10):1–6, 2010.

[129] NP Hammond, K Kay, and G Rehm. Developments in the Diamond Storage Ring. In *Proceedings of MEDSI 2008*, 2008.

[130] G Wüstefeld, J Feikes, M Von Hatrott, M Ries, A Hoehl, R Klein, R Mueller, A Serdyukov, and G Ulm. Coherent THz Measurements at the METROLOGY LIGHT SOURCE. In *2010 International Particle Accelerator Conference*, volume 3, pages 2508–2510, 2010.

“From stardust we come, and to stardust we will go”